

Dissertation
submitted to the
Combined Faculties for the Natural Sciences and for Mathematics
of the Ruperto Carola University of Heidelberg, Germany
for the degree of
Doctor of Natural Sciences

presented by
M.Sc. - Physics: Marcel Dorf
born in: Bad Mergentheim

Oral examination: 21.12.2005

**Investigation of
Inorganic Stratospheric Bromine
using Balloon-Borne DOAS Measurements
and Model Simulations**

Referees: Prof. Dr. Klaus Pfeilsticker
Prof. Dr. Frank Arnold

Investigation of Inorganic Stratospheric Bromine using Balloon-Borne DOAS Measurements and Model Simulations

Inorganic bromine is the second most important halogen effecting stratospheric ozone [WMO 2003]. Although the concentration of bromine in the stratosphere is about two orders of magnitude lower than the concentration of chlorine, it currently contributes about 25% to global ozone loss due to its much greater ozone depletion efficiency (factor of around 45) compared to chlorine.

In this study, stratospheric balloon-borne DOAS (Differential Optical Absorption Spectroscopy) measurements of bromine-monoxide (BrO) were analysed and interpreted using the 3-D CTM (Chemical Transport Model) SLIMCAT [Chipperfield and Pyle 1998] and a 1-D photochemical model. Photochemical changes were calculated along air mass trajectories which match the balloon data with SCIAMACHY (SCanning Imaging Absorption spectroMeter for Atmospheric CHartography) satellite observations in order to produce a set of BrO profiles suitable for SCIAMACHY validation. Furthermore, DOAS BrO observations were used to infer the trend of total inorganic stratospheric bromine, which peaked around 1998 at 21 ± 3 pptv and is consistently 3.5 to 5 pptv higher than the known trend in organic bromine precursors (halons and methyl bromide) can account for. This discrepancy, the non-zero amount of inorganic bromine observed around the tropopause and the rapid increase above the tropopause, all indicate that short-lived organic bromine source gases have to be taken into account. These results were confirmed by comparing the DOAS BrO data with different SLIMCAT model runs.

Moreover, previous discrepancies between DOAS OClO measurements and model comparisons [Fitzenberger 2000] were removed and detailed model studies were used to investigate ozone loss on specific days and the consistency of the known stratospheric photochemistry.

Untersuchung des Anorganischen Stratosphärischen Bromgehalts mittels DOAS Ballonmessungen und Modellrechnungen

Anorganische Bromverbindungen sind die zweitwichtigsten Halogenverbindungen für den stratosphärischen Ozonabbau [WMO 2003]. Obwohl die Bromkonzentration in der Stratosphäre fast zwei Größenordnungen kleiner als die Chlorkonzentration ist, trägt Brom zur Zeit mit ca. 25% zum weltweiten Ozonverlust bei, da es eine größere Effizienz im Zerstören von Ozone hat (ca. 45 mal so groß) als Chlor.

Die vorliegende Arbeit befaßt sich mit stratosphärischen DOAS (Differentielle Optische Absorptions Spektroskopie) Ballonmessungen von Brommonoxid (BrO). Diese wurden mit Hilfe des dreidimensionalen Chemischen Transport Modells SLIMCAT [Chipperfield and Pyle 1998] und eines eindimensionalen photochemischen Modells interpretiert. Um die Ballonmessungen mit SCIAMACHY (SCanning Imaging Absorption spectroMeter for Atmospheric CHartography) Satellitenmessungen vergleichen zu können, wurden die photochemischen Änderungen entlang Luftmassentrajektorien berechnet, und es wurde ein Satz an BrO Profilen erzeugt, der zur Validierung von SCIAMACHY geeignet ist. Darüberhinaus wurden DOAS BrO Messungen dazu verwendet, den Trend des anorganischen Gesamtbromgehalts in der Stratosphäre zu bestimmen, welches 1998 mit 21 ± 3 pptv seinen Maximalwert erreichte und durchweg 3.5 bis 5 pptv größer ist als der bekannte Trend der bromierten organischen Vorläufersubstanzen (Halone und Methylbromid) es erwarten läßt. Diese Diskrepanz, zusammen mit dem beobachteten nicht verschwindenden Anteil an anorganischem Brom an der Tropopause und dem raschen Anstieg darüber, deuten an, daß kurzlebige bromierte organische Quellgase berücksichtigt werden müssen, was auch durch Vergleiche mit verschiedenen SLIMCAT Modellläufen bestätigt wurde.

Weiterhin konnten bisher bestehende Unterschiede zwischen DOAS OClO Messungen and Modellvergleichen [Fitzenberger 2000] beseitigt werden. Die Konsistenz der bekannten stratosphärischen Photochemie wurde mit detaillierte Modellrechnungen überprüft und der Ozonverlust an einzelnen Tagen berechnet.

Contents

1	Introduction	1
2	Stratospheric Photochemistry and Dynamics	5
2.1	Dynamics of the Polar Stratosphere	8
2.1.1	Potential Temperature	8
2.1.2	Potential Vorticity	9
2.1.3	The Vortex Edge	10
2.1.4	The Northern and Southern Polar Vortex	10
2.1.5	Planetary Waves	11
2.1.6	Stratospheric Warmings	12
2.2	Stratospheric Chemistry	12
2.2.1	Ozone Chemistry	13
2.2.2	Stratospheric Nitrogen Chemistry	15
2.2.3	Halogen Chemistry and Source Gases	18
2.2.4	Heterogeneous Chemistry on PSCs - The Ozone Hole	25
2.2.5	Heterogeneous Chemistry on Sulfate Aerosoles	29
3	Methodology	31
3.1	Basics of the Atmospheric Radiative Transfer	31
3.1.1	Definitions	31
3.1.2	Photochemical Effects	32
3.1.3	Scattering	32
3.1.4	Absorption	33
3.2	Solar Radiation and the Solar Spectrum	34
3.3	DOAS - Differential Optical Absorption Spectroscopy	35
3.4	Spectral Retrieval	36
3.4.1	Sources of Errors	39
4	Instrumentation	45
4.1	The LPMA/DOAS Balloon Payload	45
4.1.1	The LPMA Fourier Transform Interferometer	45
4.1.2	The DOAS Balloon Spectrograph	46
4.1.3	mini-DOAS	50
4.2	Instrumental Effects and Sun-Tracker Correlations	51
4.2.1	Instrumental Deficits	51
4.2.2	Sun-Tracker Correlations	53

5	Laboratory Reference Spectra	57
5.1	Experimental Setup	58
5.2	O ₃ Reference	60
5.3	BrO Reference	61
5.4	NO ₂ and HONO Reference	62
5.5	OCIO Reference	65
5.6	Summary and Effect on Retrieval	65
6	Stratospheric BrO Profiling	69
6.1	Experimental Details of the BrO Evaluation	69
6.1.1	The DOAS BrO-Retrieval	69
6.1.2	Langley Plot	73
6.1.3	BrO-Retrieval Error	76
6.2	Profile Retrieval	76
6.2.1	Inversion Techniques	77
6.2.2	Errors of the Raytracing	79
6.2.3	BrO Profile Inversion and Errors	79
6.3	Discussion of LPMA/DOAS Balloon Flights	82
6.3.1	LPMA / DOAS Flight on August 21/22, 2001 at Kiruna	85
6.3.2	LPMA / DOAS Flight on March 23, 2003 at Kiruna	90
6.3.3	LPMA / DOAS Flight on October 09, 2003 at Aire sur l'Adour	95
6.3.4	LPMA / DOAS Flight on March 24, 2004 at Kiruna	99
6.3.5	LPMA / DOAS Flight on June 17, 2005 at Teresina	103
7	Validation of SCIAMACHY BrO Limb Profiles	107
7.1	Balloon-Borne and Satellite BrO Measurements	108
7.1.1	Resonance Fluorescence BrO Measurements	108
7.1.2	SAOZ BrO Measurements	109
7.1.3	SCIAMACHY BrO Profile Retrieval	109
7.2	Modelling	110
7.2.1	Trajectory Modelling	110
7.2.2	Chemical Modelling	112
7.3	Further Constraints on the Photochemical Modelling	114
7.3.1	Photochemical Modelling and its Constraints	115
7.4	Results and Discussion	119
7.5	Conclusions	123
8	Stratospheric OCIO	129
8.1	OCIO Evaluation	130
8.2	The LPMA / DOAS Measurements at Kiruna on February 14, 1997	135
8.3	The LPMA / DOAS Measurements at Kiruna on February 10, 1999	139
8.4	The LPMA / DOAS Measurements at Kiruna on February 18, 2000	148
8.5	Conclusions	154
9	Total Stratospheric Bromine	155
9.1	Stratospheric Bromine Trend	155
9.1.1	Bry Inferred from Stratospheric DOAS BrO Measurements	157
9.2	Contribution of Very Short-Lived Organic Bromine Species	164
9.2.1	First Tropical BrO Profile	171
9.3	Correlation between Tracers and Bry	171
9.4	Summary	176

10 Conclusion	179
Publications	181
List of Figures	183
List of Tables	187
References	189
Acknowledgements	203

Chapter 1

Introduction

The stratospheric ozone layer, centred at around 25 km altitude effects life on Earth in several ways. The ozone molecule contains strong UV absorption bands that turn incoming solar UV radiation into heat, causing the characteristic temperature structure of the stratosphere. Its strong infrared absorption bands effect the radiation back from Earth into space. This alters the temperature structure of the troposphere and thus influences the climate. Stratospheric ozone protects life on Earth by shielding it from the full amount of solar UV radiation that can damage life forms and materials. The role of stratospheric ozone is different to that of tropospheric ozone, which is mainly a product of pollution and effects human health.

Although it was already known in the early 1970s that anthropogenic emissions of nitrogen and halogen compounds influence the stratospheric ozone budget [*Crutzen 1970; Molina and Rowland 1974*], the discovery of a dramatic ozone loss over Antarctica was surprising [*Farman et al. 1985*]. It was found, that this phenomenon of almost 100% ozone reduction at altitudes between 12 km and 20 km, referred to as the Antarctic ozone hole, occurs each austral spring in the southern hemisphere. Observations showed that the analogous ozone depletion in the arctic regions has not been as severe, although substantial late winter / spring ozone losses were observed during unusually cold stratospheric winters in the 1990s [*WMO 2003*].

The anthropogenic emissions of organic halogen compounds (mainly chlorofluorocarbons (CFCs) and halons) and the subsequent release of chlorine and bromine into the stratosphere were soon identified as the likely cause of the spring time ozone depletion in the polar regions. The Montreal Protocol on Substances that Deplete the Ozone Layer was agreed in 1987, leading to the phase-out of many ozone-depleting substances. Based on increasingly strong scientific evidence, the Protocol has since been strengthened by a number of amendments and adjustments (London, 1990; Copenhagen, 1992; Vienna 1995; Montreal, 1997; Beijing, 2000).

The mechanisms responsible for the formation of the Antarctic (and Arctic) ozone hole are now quantitatively understood. The dynamic prerequisite is the formation of a strong wintery cyclone over the pole - the polar vortex. Inside the polar vortex, temperatures can drop below 196 K and polar stratospheric clouds (PSCs) can form [*Toon et al. 1986; Crutzen and Arnold 1986*]. Heterogenous chemical reactions on the surface of PSCs convert stable inorganic halogen compounds, such as HCl, ClONO₂ or BrONO₂ into more reactive species Cl₂, HOCl, and BrCl [*Solomon et al. 1986*]. After polar night, when the sunlight returns, the latter species photodissociate and destroy ozone through catalytic cycles.

Strong dynamic disturbances make the Arctic vortex generally less stable than the Antarctic vortex and prevent temperatures from being as low. Therefore, the potential for PSC formation and ozone depletion is much reduced but ozone loss can be as high as 70% at around 20 km [*EORCU 2000*]. In addition to the stratospheric ozone depletion over the poles, a statistically significant negative trend in ozone can be also observed in both hemispheres at mid and high latitudes during all seasons. The increased

bromine and chlorine loading of the stratosphere also primarily contributes to mid-latitudinal ozone loss, as some heterogeneous reactions that occur in the polar regions can take place on background aerosol in the tropopause region [WMO 2003].

Although most of the key processes involved in ozone depletion are well understood, discernible discrepancies can be observed when comparing the predictions of chemical model calculations with atmospheric measurements. Neither the ozone destruction observed during the Arctic winter nor the mid-latitudinal trend can be explained quantitatively by models [EC-Report 2001a; WMO 2003].

One of the questions concerning the future evolution of the ozone layer is the amplitude of the recovery that may have started already, well after the peak halogen loading in the stratosphere has been reached. As the stratosphere is also expected to cool in the future because of increased radiative cooling by greenhouse gases, it is important to understand when chlorine and bromine levels will drop in order to predict whether severe ozone depletion can occur in a northern hemisphere polar winter. In any case, as it is uncertain how the dynamics of the stratosphere may change, it is important to reduce emissions as much as possible and to monitor the temporal trend of chlorine and bromine in the stratosphere.

The differential optical absorption spectroscopy (DOAS) [Platt *et al.* 1979] is a well-established technique for the sensitive detection and quantification of atmospheric trace gases. Within the scope of this study, UV spectra recorded with a balloon-borne DOAS instrument, installed on the LPMA¹ / DOAS balloon gondola, were analysed for BrO and OClO absorption signatures. In total, thirteen flights have been performed since 1996 at different geolocations and times. The lastest five flights were conducted within the scope of this study and results are presented for the first time. The eight earlier flights were re-analysed (see e.g. Harder [1999] or Fitzenberger [2000]) and new findings are presented here.

During daylight the most abundant stratospheric bromine species is BrO, which accounts for 60 – 70 % of total Br_y [Lary 1996; Lary *et al.* 1996]. Fortunately, BrO is also the most feasible inorganic bromine species to detect. Detection of atmospheric BrO in the past relied on (1) resonance fluorescence of Br atoms formed by reaction with excess NO added to the probed air [Brune *et al.* 1989] or (2) UV/visible spectroscopy of either (2a) scattered skylight analysed from the ground, (2b) direct sunlight observed from balloon payloads and (2c) backscattered skylight detected from space [Fish *et al.* 1995; Harder *et al.* 1998; Wagner and Platt 1998; Van Roozendaal *et al.* 2002; Pundt *et al.* 2002].

Direct sunlight observations of BrO performed by the balloon-borne DOAS presented in this study are used to examine inorganic stratospheric bromine and its chemistry in detail. DOAS BrO observations in combination with comparisons with the 3-D chemical transport model SLIMCAT [Chipperfield and Pyle 1998] allow conclusions to be drawn about total inorganic bromine in the stratosphere and about the composition of the organic bromine source gases. Observations from all flights are used to study the trend in inorganic bromine over the covered time period and to compare it with the known amount of organic bromine source gases. This is especially important as the Montreal protocol and its amendments have to be monitored to see if they are having an impact and to see if the stratospheric bromine load is levelling off, decreasing or will even increase in future.

Since satellite instruments are becoming more important and are well suited for global coverage and trend analysis over a perennial time period, high-precision DOAS BrO profiles are used to validate BrO limb profiles from the new SCIAMACHY² satellite instrument. Lagrangian box model calculations on isentropic trajectories are used to match the photochemical conditions of the satellite measurement with the balloon observations.

The reaction of BrO with ClO produces OClO which was also detected during arctic winter flights and which is an indicator for chlorine activation in the polar vortex. DOAS OClO observations during three arctic winters, in combination with LPMA measurements, are therefore well suited to investigate the consistency of the known stratospheric photochemistry and to calculate the ozone loss during that time.

Chapter 2 gives an overview of the stratospheric dynamics and the chemistry, and emphasises the importance of the halogens. Descriptions of the measurement technique and the DOAS instrument are

¹LPMA = Limb Profile Monitor of the Atmosphere

²SCIAMACHY = SCanning Imaging Absorption spectroMeter for Atmospheric CHartographY

given in chapters 3 and 4 respectively. Laboratory measurements of absorption cross-sections used in the DOAS evaluation of BrO and OCIO are presented in chapter 5. Recent balloon flights and BrO profiling are both described in chapter 6. Chapter 7 shows how a set of SCIAMACHY BrO validation profiles is inferred from balloon observations. OCIO measurements of three DOAS balloon flights and studies on the photochemistry of the stratosphere are given in chapter 8. Major findings on total inorganic stratospheric bromine, its trend and the composition of the bromine source gases are dealt with in detail in chapter 9, before this study ends with the conclusions - chapter 10.

Chapter 2

Stratospheric Photochemistry and Dynamics

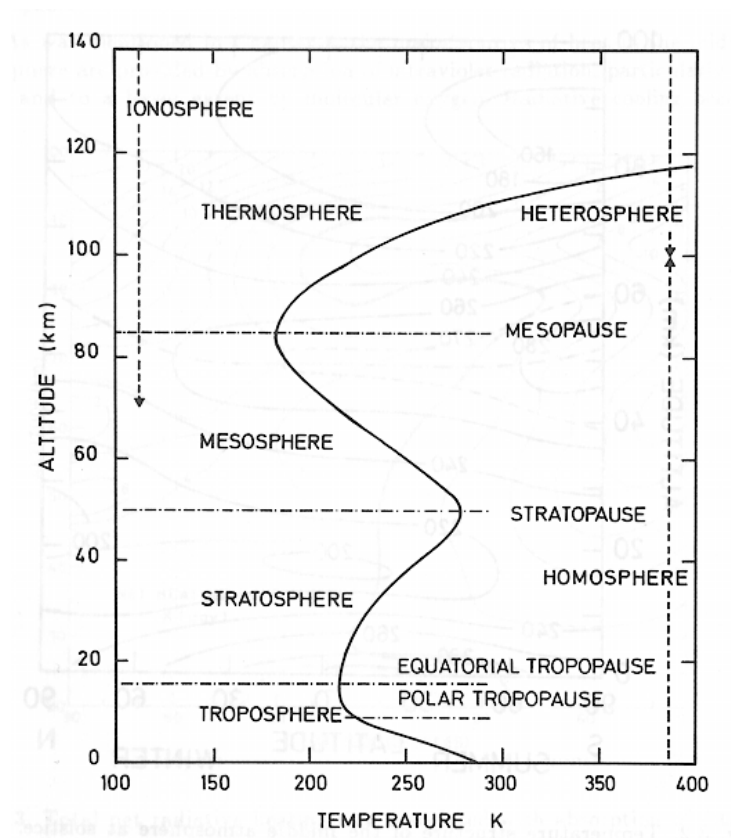


Figure 2.1: Vertical structure of the Earth's atmosphere. Adopted from Brasseur and Solomon [1986]

The atmosphere can be divided into a number of generally defined horizontal layers, distinguished mainly by the temperature gradients. The pattern roughly consists of three relatively warm layers (near the surface; between 50 and 60 km; and above 120 km) which are separated by two rather cold layers

(between 10 and 30 km; and 80 - 100 km) (see Figure 2.1).

The *troposphere*, the lowest layer of the atmosphere, is the zone where weather phenomena and atmospheric turbulence are most marked. It contains about 75 % of the total mass of the atmosphere and virtually all the water vapour and aerosol. The temperature generally decreases with height throughout the troposphere, at a mean lapse rate of $6.5^{\circ}\text{C}/\text{km}$. This decrease is due to the adiabatic expansion of rising air and the consequent cooling. Additional cooling occurs in the upper troposphere by radiative cooling in the infra-red wavelength range mainly by water vapour, CO_2 , CH_4 and O_3 [Goody and Yung 1989]. Furthermore, the troposphere is heated mainly by turbulent heat transfer (latent and sensible) from the surface and not by absorption of radiation. It is topped in most places by a temperature inversion level and in others by a zone that is isothermal with height. This so called tropopause acts as a ‘roof’ that effectively limits convection and keeps the troposphere self-contained to a large extent. There is a distinct variation in the altitude of the tropopause, from 18 km in the tropics, where there is great heating and convective turbulence, to only 8 km at the poles. This variation is correlated to different sea level temperatures and pressures and therefore depends on the latitude, season and daily changes of surface pressure.

The *stratosphere* is the second major atmospheric layer and extends from the tropopause to about 50 km, including about 20 % of the atmospheric mass. Although the stratosphere contains most of the atmospheric ozone, with the maximum concentration at around 22 km, the maximum temperatures associated with the absorption of the sun’s UV radiation by ozone occur at the *stratopause*. The air density at the stratopause is much lower, so even limited absorption produces a large temperature increase, causing temperatures that may exceed 0°C . Generally temperatures increase with height in summer, with the lowest temperature at the equatorial tropopause. During the winter, the structure is more complex with very cold air (around -80°C) at the equatorial tropopause, which is highest at this time. Similar low temperatures occur in the lower stratosphere at the poles, whereas over $50-60^{\circ}\text{N}$ there is a warm region with nearly isothermal conditions at about -45 to -50°C . Seasonal changes of temperature affect the stratosphere (see also section 2.1). The cold polar winter stratosphere often undergoes dramatic *sudden warmings* (see section 2.1.6) associated with subsidence due to circulation changes in late winter or early spring. During this time, temperatures at about 25 km may change from -80 to -40°C over a 2-day period, whereas the cooling in autumn is a more gradual process. In the lower and middle tropical stratosphere, there is a quasi-biennial (26 month) wind regime, with easterlies and westerlies in the layer from 18 to 30 km alternating every 12 to 13 months [Labitzke and van Loon 1988]. The reversal starts at high levels and takes approximately 12 months to descend from 30 to 18 km.

The temperature field in the stratosphere is caused by a balance between radiative and dynamic heating or cooling. The major source of radiative heating is the absorption of ultraviolet radiation mainly by ozone and molecular oxygen. Radiative cooling occurs through infrared emissions of CO_2 , H_2O and O_3 . Dynamic heating is caused by vertical (diabatic) motion, which occurs partly in response to the annual varying solar insolation. A substantial part of the vertical motion occurs due to forces arising from the breaking and dissipation of so-called Rossby waves, planetary waves with a typical wavelength of the Earth’s diameter [Andrews et al. 1987]. The dominant features of the global stratospheric wind system are the strong mean zonal winds. They can generally be understood as thermal winds. The tropical lower stratosphere and the equatorial tropopause region are cold in comparison to the summer polar stratosphere, which is subject to strong radiative heating. As a consequence of the temperature difference, a geostrophic easterly wind forms. The opposite is true for the winter hemisphere. Due to the low solar radiation, the winter polar stratosphere cools down and a westerly flow regime develops (see section 2.1).

The overall feature of the annual mean stratospheric meridional circulation is well described by the Brewer-Dobson circulation. Based on global water vapour and ozone observations they suggested a circulation exhibiting rising motion only in the tropics, and descending motion at extra-tropical latitudes [Brewer 1949; Dobson 1956]. This classical picture of the Brewer-Dobson circulation has been refined considerably in recent years [WMO 2003]. Stratospheric transport and mixing reveals a number of

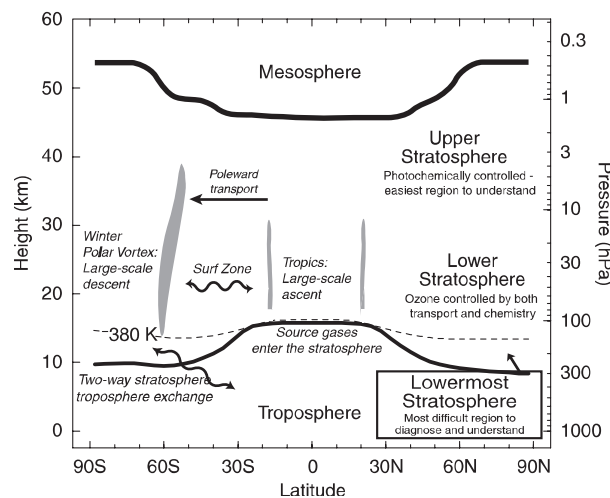


Figure 2.2: Schematic diagram showing the structure of, and transport within, the stratosphere. Adopted from WMO [2003]

distinct regions, depicted in Figure 2.2. In the winter hemisphere, one has to distinguish between the ‘surf zone’ of mid-latitudes, which is largely influenced by breaking of Rossby waves, and the polar vortex, which is relatively undisturbed. The wave breaking process is associated with erosion of the vortex through extraction of air from the vortex edge. This air is typically stretched out into filaments. The surf zone also has a subtropical edge, isolating the tropics from the surf zone. Erosion processes similar to those seen at the vortex edge are evident. The summer hemisphere is generally characterised as a region of very weak meridional transport. Diabatic heating rates calculated from the UKMO (United Kingdom Meteorological Office) analysis show atmospheric cooling (sinking air) poleward of 50° N below 20 km and atmospheric heating (rising air) poleward of 60° N between 25 km and 30 km altitude in July. The latitude and latitude of the boundaries between heating and cooling differs for different analyses [Cordero and Kawa 2001]. The rising motion of air masses in summer at high latitudes leads to a summer to winter pole flow in the upper stratosphere and mesosphere.

In contrast to the region above, the region referred to as ‘lowermost stratosphere’ is bounded on the side facing the equator by the tropopause rather than by the tropical stratosphere and it seems that the distinction between surf zone and vortex does not exist. The isentropic surfaces of the lowermost stratosphere intersect the mid-latitude tropopause and as a result rapid isentropic exchange is possible, which is though hindered by conservation of potential vorticity (section 2.1.2). It should be emphasized that a combination of radiative, chemical and dynamical processes maintains the global distribution of ozone and other species. Their distribution is a result of a balance between these processes. The nature of the balance may differ, depending on location and season. In addition to examining the chemistry, transport effects also need to be considered [Rosenlof 1999; Cordero and Kawa 2001]. Variations of species such as CH_4 or N_2O , which are relatively long-lived in the (lower) stratosphere, can be used to examine transport processes.

The mesosphere, between about 50 and 90 km (or 1 hPa to 0.01 hPa), has temperatures as low as -130°C at around 80 to 90 km in summer. Above this height, temperatures begin to rise again with molecular oxygen and ozone absorption contributing to the heating process. This inversion is referred to as the mesopause. In this region *noctilucent clouds* are observed at high latitudes in summer [Lübken et al. 1996]. Their formation is thought to be related to the production of water vapour through the oxidation of atmospheric methane.

The *thermosphere* stretches from around 100 to 500 km. Its lower section, up to 200 km, comprises mainly nitrogen (N_2) and oxygen in molecular (O_2) and atomic (O) form. Above 200 km atomic oxygen predominates over nitrogen (N_2 , N). Owing to the absorption of extreme ultraviolet radiation by molecular and atomic oxygen, temperatures rise with height, reaching more than 1000 K at 350 km. Above 100 km the atmosphere is increasingly affected by cosmic radiation, solar X-rays and ultraviolet radiation, which cause ionization. Therefore the term *ionosphere* is commonly applied to layers above 80 km.

The *exosphere* has its base between 500 and 750 km. Here the atmosphere consists of atomic oxygen, hydrogen and helium, of which about 1% is ionised. Hydrogen and helium atoms can escape into space, as the chance of molecular collisions deflecting the atoms downwards lessens with increasing height. Hydrogen is produced by the breakdown of water vapour near the mesopause, while helium is produced by the action of cosmic radiation on nitrogen and from the breakdown of radioactive elements.

2.1 Dynamics of the Polar Stratosphere

The temperature distribution in the polar winter stratosphere has crucial influence on the formation of polar stratospheric clouds (*PSCs*) and thus on ozone depletion. It is determined by the general airflow on the horizontal scale of 10^3 to 10^4 km.

During the polar night, the lack of solar radiation causes the air to cool, resulting in a large scale descent of air masses forming the so called *polar vortex*. As a result of the descent, the adiabatic compression of air counteracts a further cooling and descent of the air masses. Although the descent should result in an adiabatic heating, there is a marked cool region inside the polar vortex. This is due to the fact that no solar radiation is absorbed during polar night and radiative cooling occurs through infrared emissions of CO_2 , H_2O and O_3 . Overall the radiative cooling outbalances the adiabatic heating. Therefore, during winter the stratosphere at the pole is much colder than at low- or mid-latitudes, resulting in a meridional pressure gradient $\vec{\nabla}p$. In a first approximation, friction can be neglected in the stratosphere and the assumption can be made that the air motion is solely determined by the pressure gradient force \vec{F}_p and the Coriolis force \vec{F}_c . The resulting air flow is a geostrophic wind. If the velocity is non-zero the flow will be diverted by the Coriolis force, giving the velocity a component perpendicular to the pressure gradient. The flow is further accelerated until an equilibrium of the pressure gradient and the Coriolis force is reached (see Figure 2.3). The resulting geostrophic wind flows parallel to the isobars and can be described by:

$$\vec{v}_g \times \vec{\Omega} = \frac{1}{2 \cdot \rho} \vec{\nabla}p \quad (2.1)$$

with the density ρ , the pressure gradient $\vec{\nabla}p$ and the angular velocity of the Earth $\vec{\Omega}$. Thus, during winter a polar jet stream at around 60° latitude builds up which characterises the edge of the polar vortex. The polar vortex is cyclonal and anticyclonal at the northern and southern hemisphere, respectively. Due to the strong zonal flow, the air masses of the polar vortex are largely isolated from air masses at mid-latitudes.

2.1.1 Potential Temperature

For the polar stratosphere winter we can assume that transport processes on the time scale of a couple of days are adiabatic. Thus the flow of air can be described by means of isentropic surfaces which are defined in this section.

Since the atmosphere is a compressible gas, neither the temperature nor the density are an adequate measure for the layering. We therefore use the *potential temperature* Θ which is the temperature an air parcel would have if it was moved adiabatically i.e. without change in entropy, to a reference pressure level,

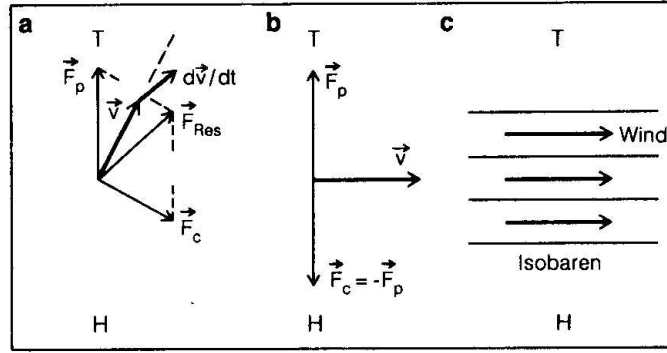


Figure 2.3: **a-c:** Formation of the geostrophic wind. **H** and **T** denote high and low pressure areas, respectively. **a:** Intermediate state when there is not yet an equilibrium of the pressure gradient force \vec{F}_p and the Coriolis force \vec{F}_c . The resulting force \vec{F}_{res} further accelerates the flow, with a component in the direction of the velocity (resulting in an increase of its absolute value) and a component perpendicular to it (changing the direction of the velocity and \vec{F}_c towards the equilibrium state). **b:** Equilibrium case. **c:** The resulting geostrophic wind parallel to the isobars is indicated. (Adapted from [Roedel 1992].)

which is simply defined as the normal pressure $p_0 = 1013$ hPa. The potential temperature is therefore defined by:

$$\Theta = T \cdot \left(\frac{p_0}{p} \right)^{\frac{\kappa-1}{\kappa}} \quad (2.2)$$

where T is the temperature, p the pressure as a function of height, p_0 the normal pressure and $\kappa = c_p/c_v$ (i.e. $\frac{\kappa-1}{\kappa} = 0.286$) is the ratio of specific heat at constant pressure and constant volume, respectively. If the atmospheric layering is stable, the potential temperature increases monotonically and can be used as a substitute for the geometrical altitude as a vertical component. The corresponding surfaces of constant potential temperature (or entropy) are called isentropic planes. Θ is therefore a conservative property in any adiabatic air parcel displacement and is often used to evaluate air parcel trajectories.

2.1.2 Potential Vorticity

The polar vortex or the edge of the vortex can be defined by means of the *potential vorticity* (PV). A measure for the vorticity of a horizontal air flow \vec{v} is the vertical component (here the z -component) of the vector $rot \vec{v}$.

$$\xi = rot_z \vec{v} = \frac{\partial v_y}{\partial x} - \frac{\partial v_x}{\partial y} = \vec{\nabla}_h \times \vec{v} \quad (2.3)$$

ξ points in negative z -direction for anticyclones and in z -positive direction for cyclones. The vorticity is non-zero for curved flows or for linear flows with horizontal wind shears, or a combination of both. In reference to the inertial system Earth the described vorticity is simply the relative vorticity. In order to obtain the absolute vorticity η the fraction of the Earth's rotation, given by the Coriolis parameter $f = 2\vec{\Omega} \sin \varphi$ has to be added:

$$\eta = \xi + f = \vec{\nabla}_h \times \vec{v} + 2\vec{\Omega} \sin \varphi \quad (2.4)$$

As the vorticity is a conserved parameter, a continuity equation can be defined in the absence of external forces:

$$\frac{d\eta}{dt} + \eta \cdot \vec{\nabla}_h \cdot \vec{v} = 0 \quad (2.5)$$

$$\text{with } \frac{d\eta}{dt} = \frac{\partial\eta}{\partial t} + \frac{\partial\eta}{\partial x}v_x + \frac{\partial\eta}{\partial y}v_y \quad (2.6)$$

The *potential vorticity* combines the conservation of vorticity and the conservation of mass. On the condition that there is no friction and the process is adiabatic, the potential vorticity in the atmosphere is a mass conserving parameter. Its definition according to Ertel is

$$Q = \eta \cdot \frac{\nabla\Theta}{\rho} \quad (2.7)$$

where η is the absolute vorticity, ρ the density and Θ the potential temperature. The unit of Ertel's potential vorticity is

$$1\text{PVU (Potential Vorticity Unit)} = 10^{-6}\text{Km}^2\text{kg}^{-1}\text{s}^{-1}.$$

The potential vorticity is thus well suited to describe the polar vortex, since its potential vorticity is higher than that of the surrounding mid-latitude air.

2.1.3 The Vortex Edge

Simultaneous to the descent of the air masses inside the polar vortex, slow vertical transport of stratospheric trace gases occurs. The vertical displacement of trace gases outside the vortex is impeded by planetary waves, which cause meridional mixing of the air masses. Considering the absolute altitude, it seems that air masses inside the vortex compared to outside, are shifted downwards by 2 to 3 km [Schöberl *et al.* 1992]. The polar vortex can therefore be defined by the gradient of long-lived trace gases such as nitrous oxide (N_2O), ozone (O_3), water vapour (H_2O) or methane (CH_4). Therefore the vortex edge is not clearly confined but rather stretched over a zone in the order of 10^1 to 10^2 km.

Besides its chemical characteristics the vortex edge can also be localised by dynamic components [e.g. Nash *et al.* 1996 or Tao and Tuck 1994]. Different methods use either the potential vorticity or the zonal wind. Due to the vortex, polar air masses have a significantly higher PV than air masses of mid and low-latitudes. Since maximum values of the PV gradient occur at the vortex edge, it can be defined accordingly. An example of the northern hemispheric polar vortex at the 675 K potential temperature level is shown in figure 2.4. Data are for March 24, 2004 the day of an LPMA/DOAS balloon flight carried out at Kiruna in northern Sweden. The potential vorticity is colour coded in units of PVU and the edge of the vortex can clearly be recognised. The vortex during that winter was not very distinct and different filaments can be seen. The map was generated with the GMT (*Generic Mapping Tool*) available at <http://gmt.soest.hawaii.edu> using ECMWF (*European Centre for Medium-Range Weather Forecasts*) data.

2.1.4 The Northern and Southern Polar Vortex

In the southern hemisphere the polar vortex evolves basically unperturbed according to the mechanisms described at the beginning of section 2.1. Shape and flow pattern of the Antarctic polar vortex are mostly stable and are not perturbed by wave activity in the stratosphere. The whole vortex is zonally symmetric around the pole. Due to the unperturbed conditions, air inside the vortex can cool down significantly. Therefore, every winter the temperature falls below the critical temperature for the formation of PSC-particles (see also section 2.2.4).

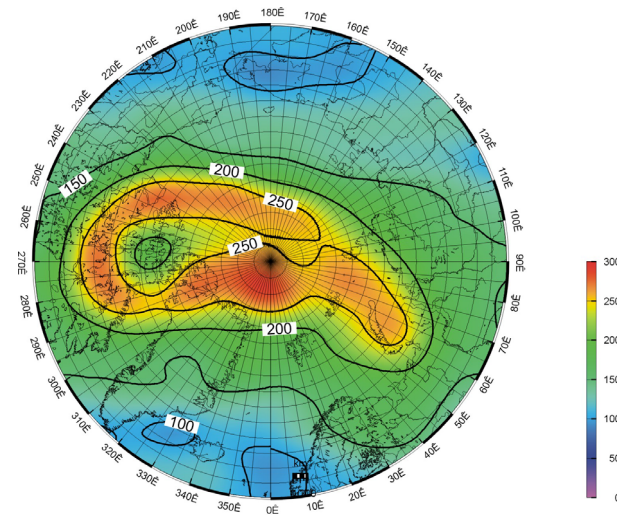


Figure 2.4: Example of the northern hemispheric polar vortex. The 675 K potential temperature level is plotted for March 24, 2004 at 00 UT. The potential vorticity is colour coded in units of PVU ($10^{-6}\text{Km}^2\text{kg}^{-1}\text{s}^{-1}$).

Such a distinct vortex is the exception rather than the rule in the northern hemisphere. Although a low pressure system also builds up in the Arctic, it is not centered above the pole. In the lower parts of the stratosphere (around 100 hPa), the cold vortex is surrounded by a belt of warm areas, caused by the winter jet streams in the upper troposphere. The strongest jet streams are found in the Western Pacific, where the highest temperatures occur. These high temperatures are responsible for the Alëuten anticyclone in the northern hemispheric stratosphere. This quasi-stationary anticyclone, named after the Alëuten Islands in the Northern Pacific, has a strong influence on dynamics of the northern stratosphere since it causes a displacement of the polar vortex towards Europe. As a result, the vortex is not centered over the pole and the temperature distribution is influenced as the cold area of the polar vortex is shifted to Northern Europe. On average, the low temperature and the vortex centre are located over Spitzbergen. The asymmetry of the Arctic polar vortex is crucial for the dynamics of the northern hemisphere.

2.1.5 Planetary Waves

Whereas the Antarctic continent is centred around the pole and surrounded solely by water, the topography of the northern hemisphere is more complex. The northern polar region is not only surrounded by the Pacific and Atlantic Ocean, but also by the land masses of the American and Eurasian continents. As a result of the different heat capacity of land and water and the continental distribution in the northern hemisphere, temperature and pressure gradients build up and induce planetary waves in the atmosphere (see e.g. *Shindell et al.* [1997]). These planetary waves propagate into the stratosphere where they disturb and destabilise the polar vortex. Among other effects they cause warm air to be transported from mid-latitudes to the polar region, which counteracts the radiative cooling of the polar vortex. Due to the orthographic conditions, the activity of planetary waves is significantly larger in the northern than in the southern hemisphere. As an overall result, temperatures in the Arctic polar vortex are on average higher than in the Antarctic polar vortex. The low temperatures necessary for the formation of PSCs are often only reached for a short time and are very regional [*Pawson et al.* 1995]. There is also a high variability between winters, mainly caused by sudden *stratospheric warmings*.

2.1.6 Stratospheric Warmings

Sudden stratospheric warmings occur during almost every northern hemispheric winter and hardly at all during southern hemispheric winters. The stratospheric warmings are caused by perturbances in the circulation due to planetary waves. One factor that stimulates these waves is the large mountain ranges in the northern hemisphere. Planetary waves propagate through the troposphere into the stratosphere, where they have larger amplitudes due to the decreasing air density. Local instabilities cause the wave energy to dissipate, resulting in a warming of the stratosphere [MyIntyre and Palmer 1983]. Different stratospheric warmings can be identified, depending on the size of the temperature increase and the stability of the polar vortex.

Minor Warmings

Minor warmings are characterised by a sudden temperature increase of at least 25 K within a week, in any stratospheric layer and any region of the winter hemisphere. They can be very intense and invert the temperature gradient, but do not result in a turnover of the circulation at 10 hPa or below. Such minor warmings occur in different strengths during almost every winter in the northern hemisphere. They are also observed in the southern hemisphere, but only rarely.

Canadian Warmings

In the northern hemisphere there is an additional form of stratospheric warming called Canadian warmings. They often occur during early winter and originate from an amplification of the Alëuten anticyclone, which is thereby shifted towards the pole. Canadian warmings can temporarily invert the temperature gradient and the wind direction without causing a breakup of the polar vortex.

Major Midwinter Warmings

Besides heating the polar region and inverting the temperature gradient between 60° and 90° latitude at 10 hPa or below, major midwinter warmings are characterised by the breakup of the polar vortex. The breakup is defined by the turnover of circulation from westerlies to easterlies at the 10 hPa level between 60° and 90° latitude. As a result, the centre of the polar vortex then lies south of 65° to 60° latitude and the vortex itself is shifted and can split into one or more parts. After the major warming the polar vortex rebuilds. In the Arctic, major midwinter warmings usually occur at most once per winter in January to February. In the Antarctic such warmings do not occur due to the colder and more stable polar vortex.

Final Warmings

During spring the turnover from winter westerlies to summer easterlies appears in connection with the final warmings. The characteristics are the same as for the major midwinter warmings, with the difference that the polar vortex does not rebuild after its breakup. Early and late final warmings can be identified, depending on the time of their occurrence. The change from winter to summer circulation, that is, the time of the final warming, occurs on average 2 months later in the southern hemisphere. While the northern hemispheric polar vortex often breaks up as early as March, the Antarctic vortex mostly remains stable and cold till the end of October [Labitzke 1999], allowing for a longer period of ozone depletion.

2.2 Stratospheric Chemistry

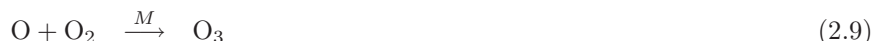
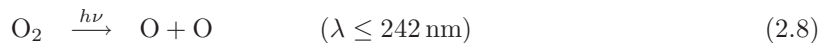
One of the most important stratospheric species is ozone. Although ozone is present in the atmosphere in all layers, the bulk of ozone resides in the lower stratosphere with the concentration maximum at ~ 22 km, referred to as the *stratospheric ozone layer*. In addition to its role in stratospheric heating, the UV absorption of ozone is essential for the protection of living organisms on Earth from the short

wavelength solar radiation. All solar radiation between 200-300 nm is intercepted in the mid and lower stratosphere due to the presence of ozone. Furthermore, ozone is a so-called greenhouse gas. It is infrared active and contributes to the radiative transfer in the long wavelength regime of the terrestrial radiation. Ozone is primarily produced at mid-latitudes and in the tropics by photodissociation of molecular oxygen by hard ultraviolet radiation (< 242 nm) and is transported toward the poles by the Brewer-Dobson circulation resulting in an annual cycle in ozone. Because of the stronger Brewer-Dobson circulation in the Northern Hemisphere (NH), the Arctic is both warmer and has larger column ozone amounts than the Antarctic. In the NH, the amount of column ozone is greatest in late winter/early spring. During the pre ozone-hole era there was less annual variation of O_3 at the poles. In recent years, the annual cycle has been modified by polar ozone depletion, most obviously in the Southern Hemisphere (SH).

This section first focuses on the chemical processes which are responsible for the current distribution of stratospheric trace gases, in particular ozone, nitrogen and halogen compounds. It then carries on to the processes leading to the so-called *stratospheric ozone hole*.

2.2.1 Ozone Chemistry

A chemical scheme for the formation and destruction of ozone in the stratosphere involving only oxygen species was first proposed by *Chapman* [1930]. The photodissociation of molecular oxygen by ultraviolet radiation produces atomic oxygen, which can react with molecular oxygen via a three-body reaction to form ozone:



The photodissociation of ozone followed by reactions of atomic oxygen with either another oxygen atom or with ozone, represent the processes with ozone loss.



Due to the strong attenuation of the short wavelength radiation, the photolysis of O_2 (reaction 2.8) and thus the production of ozone occurs mainly in the upper stratosphere. The photolysis of ozone (reactions 2.10 and 2.12) below 50 km represents only a gross loss process over timescales of days, since almost all atomic oxygen forms ozone again within a few seconds or less (reaction 2.9). An important aspect of atmospheric chemistry is the family concept. If we define the O_X family as the sum of the odd-oxygen such as ozone, $O(^3P)$, and $O(^1D)$ ¹ then a number of reactions only convert one species of the O_X family into another without changing the total O_X concentration. An important consequence is the difference in lifetime. While the lifetime of the individual species is short (e.g. $\sim 10^{-8}$ s for $O(^1D)$ at 30 km) the lifetime of the O_X family as a whole is several weeks.

According to the photochemical model of ozone production, the rate of O_2 photodissociation and hence the O_3 production is at a maximum with overhead sun. As a consequence the greatest ozone production is found in the equatorial region, but even at 60° latitude the production rate is still effective. As a result of transport and mixing processes, the average global distribution of ozone deviates substantially from the pure photochemical predictions. Hence, the global distribution strongly depends on latitude and season with the highest concentrations found at high latitudes during spring.

The stratospheric ozone profile can be explained qualitatively by the Chapman theory, based on pure

¹Accordingly, HO_X , ClO_X , BrO_X , and NO_X families can be defined

oxygen chemistry. Even the existence of the concentration maximum in the lower stratosphere is predicted correctly, but a quantitative comparison with the measured ozone profile shows that the concentrations are largely overestimated. It soon became clear that stratospheric ozone was chemically not only destroyed by reactions with atomic oxygen but also by catalytic reactions, involving OH (HO_X-cycle [Bates and Nicolet 1950]), NO (NO_X-cycle [Crutzen 1970; Johnston 1971]), Cl (ClO_X-cycle [Molina and Rowland 1974]) and Br (BrO_X-cycle [Wofsy *et al.* 1975]):



where X represents one of the radicals OH, NO, Cl, or Br. The radical X is regenerated by reaction 2.16 and is once more available for another ozone destruction cycle until removed by a sink process. Thus, a small concentration of the catalyst X already has a large impact on ozone concentration. Even in the absence of atomic oxygen, the OH radical can destroy ozone by:



This cycle is particularly important at lower altitudes where less atomic oxygen is available. Another type of catalytic cycle involving species of different families is:



where X=OH and Y=Cl, X=OH and Y=Br or X=Br and Y=Cl. Since no atomic oxygen is involved, this cycle is important in the lower stratosphere, where catalytic ozone destruction cycles involving species of only one family are suppressed.

The relative contributions of the various cycles to ozone depletion are shown in Figure 2.5. Values are calculated for mid-latitude conditions (60°N) in October. The relative contributions vary strongly with altitude. While the ozone loss in the lower stratosphere is dominated by the HO_X cycle with a small contribution by the ClO_X+BrO_X cycle, the O₃ loss between 25 and 40 km is almost solely caused by the NO_X cycle. Recent findings e.g. by [Salawitch *et al.* 2005] indicate a more important role of the ClO_X+BrO_X cycle at low altitudes, also discussed in chapter 9. Above 40 km, the catalytic cycles involving halogens play the dominant role. The relative contributions for other latitudes or seasons will differ from the calculations shown in the figure and hold only true outside the polar vortex (see section 2.1). As discussed in section 2.2.3, the dramatic ozone loss during polar spring is caused by cycles involving chlorine and bromine.

It became clear that anthropogenic emissions of long-lived trace gases such as N₂O, CH₄, chlorofluorocarbons (CFCs) or halons have a crucial impact on the stratospheric ozone concentration, since these gases can react to species which serve as catalysts in the ozone destruction cycles [e.g. Crutzen 1970; Molina and Rowland 1974]. Therefore the total global ozone column has decreased in recent years. Between 1997 and 2001, the global average was ~ 3% below pre-1980 values [WMO 2003]. The lowest annual average total column since the beginning of systematic global observations in the mid-1960s occurred in 1992-1993 with values 5% below the pre-1980 average. However, the ozone trends differ for different seasons and latitudes. In the tropics (25°N – 25°S), no significant trend could be observed in the 1980-2000 period, but only a decadal variation of ~ 3% peak-to-peak approximately in phase with the 11-year solar cycle. Total column ozone loss becomes statistically significant in the 25° – 35° latitude bands of each hemisphere. In mid-latitudes 35° – 60°, the total column in the 1997-2001 period is below

the pre-1980 average. Furthermore there are also discussions as to whether mid-latitude ozone loss can be partly explained by polar effects (transport of polar air to mid-latitudes) or circulation changes such as changes in the tropopause height. However, there are still difficulties in quantitatively understanding the mid-latitude ozone loss [WMO 2003].

Due to the predicted decrease in stratospheric chlorine loading over the next 50 years, the total global ozone column is expected to increase. For the present, the ozone values are expected to level out, but, because of the year-to-year variability, it could take as long as a decade to obtain unambiguous measurements. For a quantitative prediction of the O_3 recovery, several effects are relevant besides the halogen abundances. For example, stratospheric cooling, mainly due to further CO_2 increases, is predicted to amplify future ozone increases in the upper stratosphere. According to model calculations, a recovery to pre-ozone-hole values (before 1980) is predicted to be significant by 2050.

2.2.2 Stratospheric Nitrogen Chemistry

Nitrogen species play an important part in stratospheric chemistry with respect to ozone. They are responsible for ozone depletion (NO_x cycle) and can transform ozone-destructive halogen species into passive reservoir species. The dominant net source of stratospheric NO_x ($=NO+NO_2$) is the reaction of $O(^1D)$ atoms with nitrous oxide (N_2O):



The natural sources of N_2O (oceans and tropical forests) are twice as large as the anthropogenic ones. As a consequence of biomass burning and the use of artificial fertilizers, the N_2O level has increased from pre-industrial levels of $\sim 260 - 285$ ppb to $315 - 317$ ppb in January 2001 [Prinn *et al.* 2000; Hall *et al.* 2002]. At present, its rate of increase is ~ 0.75 ppb per year, with some interannual variability [WMO 2003]. N_2O is an inert gas with a lifetime of 120 (97 – 137) years, for which no destruction processes in the lower stratosphere are known. The only concurring loss process to reaction 2.25 is the photolysis of N_2O , which accounts for $\sim 90\%$ of its removal.

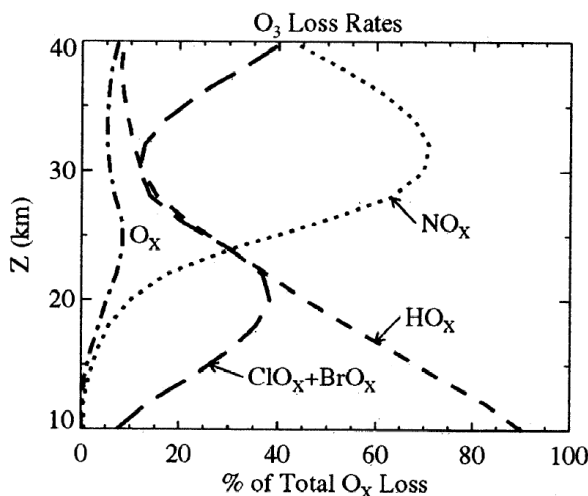
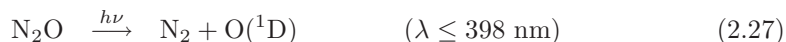


Figure 2.5: The O_3 loss rates due to catalytic cycles involving NO_x , HO_x , $ClO_x + BrO_x$, and O_x reactive families as a percentage of total O_3 loss rates for $60^\circ N$ in October computed for the 1990s using JPL-97 [DeMore *et al.* 1997] values. Adapted from Portmann *et al.* [1999].

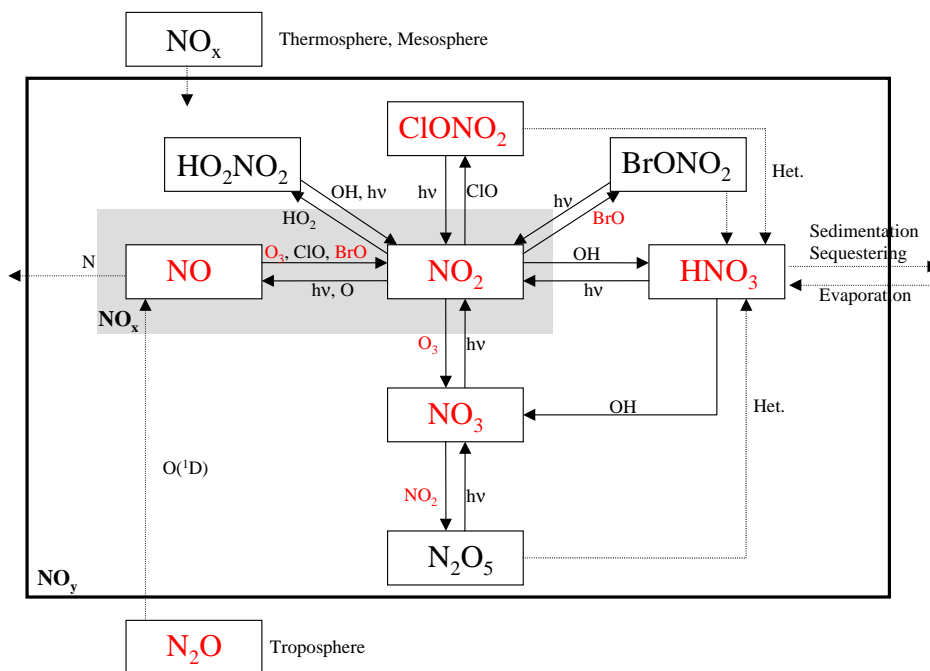
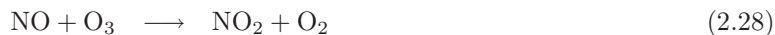


Figure 2.6: Principle components, sources, sinks, and pathways of the NO_Y family. The dotted lines indicate heterogenous pathways. The red marked species can be measured with the instruments onboard the LPMA/DOAS balloon gondola. Adopted from Bösch [2002]

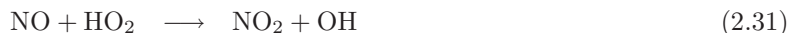
Another significant but highly variable source of NO_Y ² in the mesosphere and lower thermosphere is due to solar proton events, galactic cosmic rays and energetic electron precipitation, which produce atomic nitrogen through dissociations, predissociations or dissociative ionizations in collisions with N_2 . NO_x , formed in the mesosphere and thermosphere, partly descends into the stratosphere during winter and early spring, when there is downward atmospheric transport at mid to high-latitudes. During daytime, NO and NO_2 are in a photochemical steady-state mostly via the reactions



and the photodissociation of NO_2



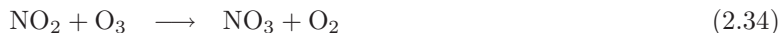
The conversion of NO to NO_2 can also take place with oxidants other than O_3 .



In the stratosphere, the only relevant organic peroxy radical RO is CH_3O_2 , which is formed by the oxidation of CH_4 . The Leighton ratio ($\frac{\text{NO}}{\text{NO}_2}$) is close to one in most of the stratosphere during daytime,

² NO_Y is the sum of the reactive nitrogen species, i.e. $\text{NO}_Y = \text{NO} + \text{NO}_2 + \text{NO}_3 + 2\text{N}_2\text{O}_5 + \text{HNO}_3 + \text{ClONO}_2 + \text{HO}_2\text{NO}_2 + \text{BrONO}_2$

but increases rapidly above 40 km because of the increasing atomic oxygen densities. At dusk, NO is rapidly converted to NO₂, which reacts with ozone to build up NO₃, an important nighttime nitrogen species.



During daytime, NO₃ is rapidly destroyed by photolysis:



NO₃ can react with NO₂ to form the *reservoir species* N₂O₅, a species that does not destroy odd-oxygen.



N₂O₅ is destroyed through collisional decomposition



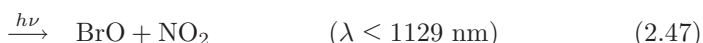
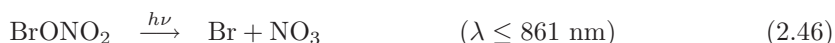
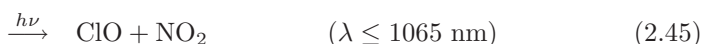
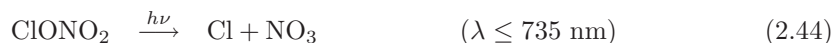
or through photolysis during the day.



The fast photolysis of NO₂ together with the slow photolysis of N₂O₅ is responsible for the typical diurnal variation of NO₂. As the photolysis begins at sunrise, a strong decrease of the NO₂ concentration is observed. During the day, the NO₂ concentration slowly increases due to N₂O₅ photolysis. At dusk the decreasing NO₂ photolysis causes a fast increase in concentration. The distribution of odd nitrogen shows rising concentration with increasing latitude in summer, while in winter the abundance decreases polewards of 40°N – 50°N [Noxon 1979; Coffey *et al.* 1981]. The tendency for NO_X to increase at high latitudes in summer can be understood in terms of atmospheric transport in a similar manner as for ozone. The observed decrease in the winter season at high latitude is the result of the combined effects of dynamics and chemistry. As a consequence of the reduced solar radiation during the polar winter, most of the nitrogen has formed reservoir species and the NO_X concentrations are smallest (*denoxification*). In addition, the formation of the polar vortex (see section 2.1) prevents the poleward transport of NO_X-rich mid-latitude air. NO₂ plays an ambiguous role in stratospheric ozone chemistry. On the one hand, it participates in ozone destruction (NO_X - cycle), on the other hand, it is involved in a number of reactions forming reservoir species.



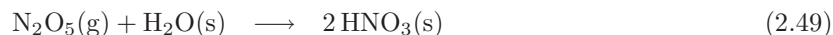
The catalysts can be released by photolysis



or by reactions with OH



Since the formation and decline of HNO_3 are slow processes, HNO_3 has only a small impact on the diurnal variation of NO_x . As a result of its long lifetime, HNO_3 builds up large concentrations, which generally exceed concentrations of total NO_x below 25 km. Another important production channel of HNO_3 is the heterogeneous hydrolysis of N_2O_5 occurring on the surfaces of stratospheric aerosols such as aqueous sulfate aerosol or ice (see section 2.2.5).



During polar winter, HNO_3 is the dominant NO_y species. This can be explained by heterogeneous processes (reaction 2.49), which continuously convert N_2O_5 into HNO_3 and by the inefficiency of reactions 2.43 and 2.48 [e.g., *Wetzel et al. 1995; Toumi et al. 1993*].

Total reactive nitrogen, NO_y , has a long photochemical lifetime in the middle and lower stratosphere. In the upper stratosphere NO_y is removed via the following reaction



where N is produced by the photolysis of NO . Since N_2O is the major source of stratospheric NO_y , the distributions of NO_y and N_2O in the stratosphere are photochemically linked. Below 30 km, the mixing ratio of NO_y has been found to be almost linearly anti-correlated with N_2O [*Loewenstein et al. 1993; Kondo et al. 1994; Kondo et al. 1996; Keim et al. 1997*]. The gradient of this lower stratospheric correlation is controlled by a combination of photochemistry and dynamics. At higher altitudes (30 – 70 km) the shape of the correlation curve is overwhelmingly influenced by the rapid loss of NO_y via reaction 2.50. At these altitudes the correlation becomes nonlinear as it approaches a maximum. Above ~ 70 km, NO_y increases rapidly with altitude and is predominately composed of NO [*Michelson et al. 1998*].

2.2.3 Halogen Chemistry and Source Gases

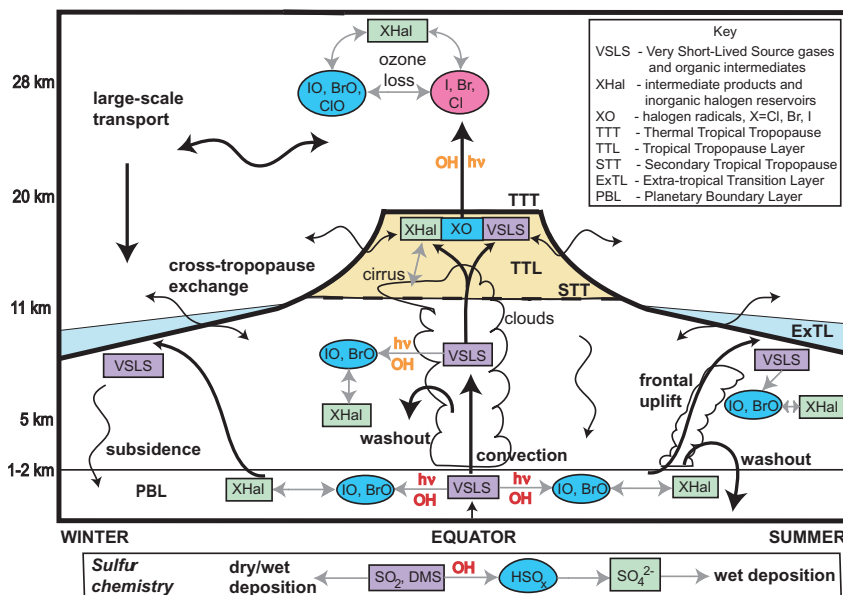


Figure 2.7: Chemical and dynamical processes affecting very short lived (VSL) substances in the troposphere and stratosphere. Adapted from WMO[2003]

Halogen species play an important role in stratospheric ozone destruction and are mainly responsible for the formation of the polar ozone hole. Due to their strong bonding, fluorine species (HF) are very

stable and do not play a role in ozone depletion. The source gases get less stable from chlorine through bromine to iodine and, thus, their Ozone Depletion Potential (ODP)³ increases. Due to its high stratospheric abundance (~ 3.6 ppbv around 20 km), chlorine contributes about 60% to ozone destruction under ozone hole conditions. Bromine plays an important role since its much lower abundance ($\sim 0.6\%$ of chlorine) is compensated by an ODP that is ~ 50 times higher. The contribution of iodine species is still not fully clear as exact measurements of its stratospheric load do not exist. Although iodine participates in ozone destruction, the iodine-containing gases are largely removed in the troposphere before they can reach the stratosphere. Upper limits of IO and OIO and the implications for total gaseous iodine and stratospheric ozone have been inferred by *Bösch et al.* [2003].

Figure 2.7 demonstrates the dynamic and chemical processes, that affect very short-lived source gases (VSLS) in the troposphere and the stratosphere. Source gases with a longer lifetime basically undergo the same processes, but have a higher chance of reaching the stratosphere. Once emitted at the Earth's surface by human activities and through natural processes, halogen source gases accumulate in the atmosphere and are distributed throughout the lower atmosphere by winds and other air motions. They are either removed from the atmosphere or undergo chemical conversion. Gases with the shortest lifetimes (e.g. HCFCs or CHBr_3) are destroyed to a great extent in the troposphere, therefore only a fraction of these gases reaches the stratosphere. Halogen source gases with longer lifetimes accumulate in the troposphere and are transported to the stratosphere, where they are converted to reactive halogen gases (e.g. Br, BrO, Cl, ClO) by UV sunlight and other chemical reactions. Reactive halogen gases cause chemical depletion of stratospheric ozone throughout the globe. At polar regions, polar stratospheric clouds increase ozone depletion by reactive halogen gases during winter and spring (section 2.2.4). Eventually, air that contains reactive halogen gases returns to the troposphere, where the gases are removed by precipitation. The following sections give brief descriptions of the relevant chlorine and bromine chemistry and their source gases. A description of the iodine chemistry can be found in e.g. *Bösch* [2002].

Halogen Source Gases

Stratospheric ClO_x ⁴ and BrO_x ⁵ has a variety of sources, all of which are associated with the release of Cl and Br atoms from halogenated organics by direct photolysis or reactions with OH and $\text{O}(^1\text{D})$. Figure 2.8 summarizes the primary source gases of chlorine and bromine for the stratosphere in 1999. Methyl chloride (CH_3Cl) is the only important natural chlorine source species. The most prominent artificial sources are the chlorofluorocarbons (CFCs). CFCs are chemically inert gases which are photostable and have a low solubility in water. Thus the lifetime of CFCs in the troposphere is very high, varying from years to centuries and resulting in an almost uniform distribution in the troposphere. CFCs, along with carbon tetrachloride (CCl_4) and methyl chloroform (CH_3CCl_3) are the most important chlorine-containing gases. Table 2.1 gives an overview of atmospheric lifetimes and the ODP of the most important chlorine and bromine source gases.

The major source of bromine is CH_3Br which provides more than 50% of the total bromine content [*Wamsley et al.* 1998]. CH_3Br is released by natural (biomass burning, oceans) and anthropogenic (agricultural fumigants, gasoline additives, etc.) processes and has a lifetime of 0.7 years. It is believed that the natural processes account for approximately 60 – 80% of the total CH_3Br load. Measurements of Antarctic firn air indicate a positive trend of Br_Y from CH_3Br of 2 – 2.5 ppt in the 1950-1995 period [*Sturges et al.* 2001]. Methyl bromide peaked in 1998 and has since declined by nearly 5% [*Montzka et al.* 2003]. Another important source of bromine are the man-made halons. Halons are halogenated hydrocarbon gases originally developed to extinguish fires. They are widely used to protect large computers, military hardware and commercial aircraft engines. Halon-1211 and Halon-1301 are the most

³The ODP is calculated on a 'per mass' basis for each gas relative to CFC-11, which has an ODP defined to be 1. A gas with a larger ODP has a greater potential to destroy ozone over its lifetime.

⁴ $\text{ClO}_x = \text{Cl} + \text{ClO} + 2 \cdot \text{Cl}_2\text{O}_2$

⁵ $\text{BrO}_x = \text{Br} + \text{BrO}$

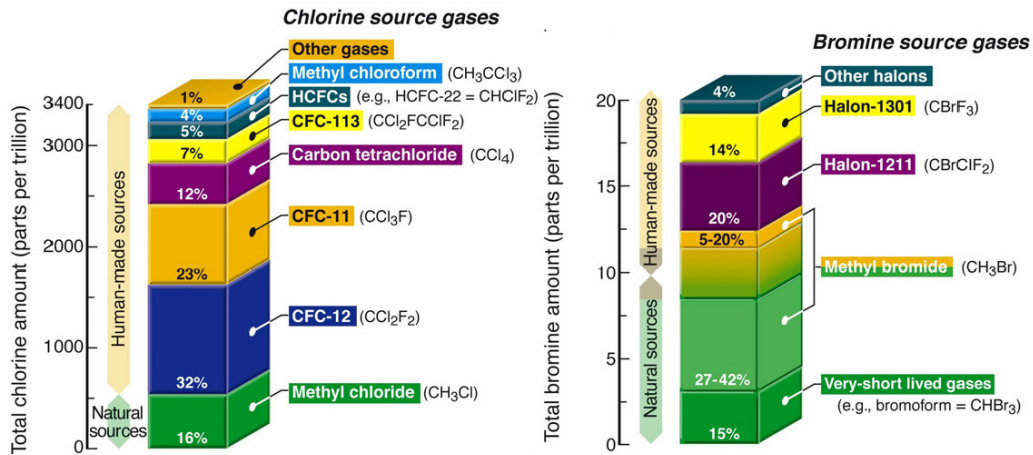


Figure 2.8: Primary source gases of chlorine and bromine for the stratosphere in 1999. Adapted from WMO[2003]

abundant halons emitted by human activities. Although controlled by the Montreal Protocol, their global mean is still increasing slightly, due to the use of large halon stocks and the continued production in developing countries, by a mean annual rate of 0.1 ppt which is much slower than was observed in the mid-1990s [Montzka *et al.* 2003]. Consequently, the sum of Br_Y from the most abundant halons and CH_3Br peaked in 1998 and declined thereafter in the troposphere at a mean annual rate of -0.25 ± 0.09 pptv (mean over

Table 2.1: Atmospheric lifetimes, emissions, and Ozone Depletion Potentials of halogen source gases. Anthropogenic and natural sources are included. Adapted from WMO[2003]

Halogen Source Gas	Lifetime (years)	Global Emissions in 2000 (gigagrams per year) ^b	Ozone Depletion Potential (ODP)
Chlorine			
CFC-12	100	130-160	1
CFC-113	85	10-25	1
CFC-11	45	70-110	1
Carbon tetrachloride	26	70-90	0.73
HCFCs	1-26	340-370	0.02-0.12
Methyl chloroform	5	~20	0.12
Methyl chloride	1.3	3000-4000	0.02
Bromine			
Halon-1301	65	~3	12
Halon-1211	16	~10	6
Methyl bromide	0.7	160-200	0.38
Very short-lived gases	Less than 1	^c	^c

^a Includes both human activities and natural sources.

^b 1 gigagram = 10^9 grams = 1000 metric tons.

^c No reliable estimate available.

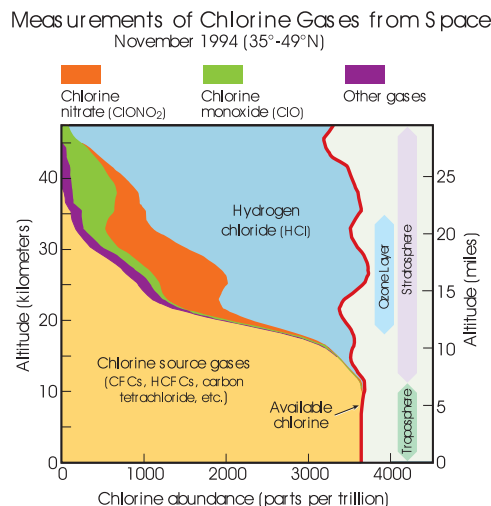


Figure 2.9: *Reactive chlorine gas observations from space. In the stratosphere, reactive chlorine gases increase with altitude and chlorine source gases decrease with altitude. The available chlorine (Cl_Y^*) determined by the source gases is nearly constant with altitude up to 47km. HCl and $ClONO_2$ are the most abundant chlorine gases in the ozone layer. Adapted from WMO [2003].*

1999-2002, [Montzka *et al.* 2003]). This decline also caused the tropospheric Equivalent Chlorine ($ECl = [Cl] + 45 \cdot [Br]$) to decrease faster than expected in WMO[2003] (see Figure 2.10). Minor bromine source gases are CH_2Br_2 and CH_2BrCl with atmospheric lifetimes of years and tropospheric mixing ratios of 1.1 and 0.14 pptv, respectively. After the Montreal Protocol (1987) and the amendments of Copenhagen (1989), London (1992) and Beijing (1999) the industrial production of CFCs and halones was limited and finally stopped (see Figure 2.11). The CFCs were replaced by partly halogenated substitutes (the so-called HCFCs), which are less stable and hence have a shorter atmospheric lifetime. The loading of inorganic chlorine in the unperturbed stratosphere has recently stabilized in response to the production regulations and will decrease [WMO 2003]. These measurements are consistent with the trends for chlorinated organic trace gases measured at the Earth's surface. The stratospheric total inorganic bromine (Br_Y) for early 1999 in 5.6 - year old air is estimated at 21.25 ± 3 pptv from DOAS BrO measurements and ~ 16 pptv

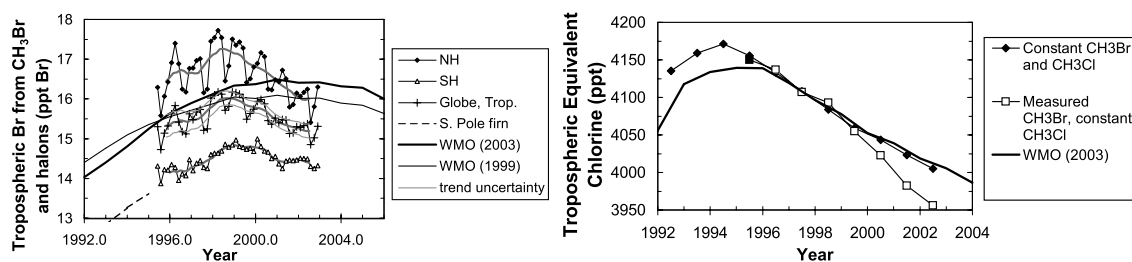


Figure 2.10: *Right panel: Mean tropospheric organic Br from NOAA-CMDL flask measurements of CH_3Br and the most abundant halons, and in recent WMO scenario calculations. Trend uncertainty only shown for the smoothed global results. Left panel: Changes in the global tropospheric load of both brominated and chlorinated ozone-depleting gases in recent years expressed as equivalent chlorine (where $ECl = [Cl] + 45 \cdot [Br]$). The first scenario assumes constant mixing ratios for CH_3Br and CH_3Cl , the second assumes constant CH_3Cl and measured changes in CH_3Br and the third assumes the WMO scenario. Adapted from Montzka *et al.* [2003].*

from organic precursor measurements (Br_Y^{org}) of CH_3Br and halons. The discrepancy is due to the influx of short lived organic bromocarbons or a possible direct transport of (Br_Y) from the troposphere. Chapter 9 discusses the stratospheric bromine trend as deduced from DOAS BrO measurements and compares it to organic precursor measurements (Br_Y^{org}). An average annual increase of Br_Y of 0.7 pptv is found by balloon-borne DOAS measurements in the years 1996–2000 (*Harder et al.* [1998]; [2000]; *Fitzenberger et al.* [2000] and *Pfeilsticker et al.* [2000]) which is broadly consistent with the increase of tropospheric organic bromine over this time period. *Salawitch et al.* [2005] suggest that inorganic Br_Y at and above the tropopause is 4–8 pptv greater than assumed in models used in previous trend assessment studies. This study concludes that enhanced Br_Y causes photochemical loss of ozone below 14 km to change from being controlled by HO_X catalytic cycles (primarily $\text{HO}_2 + \text{O}_3$) to a situation where loss by the $\text{BrO} + \text{HO}_2$ cycle is also important.

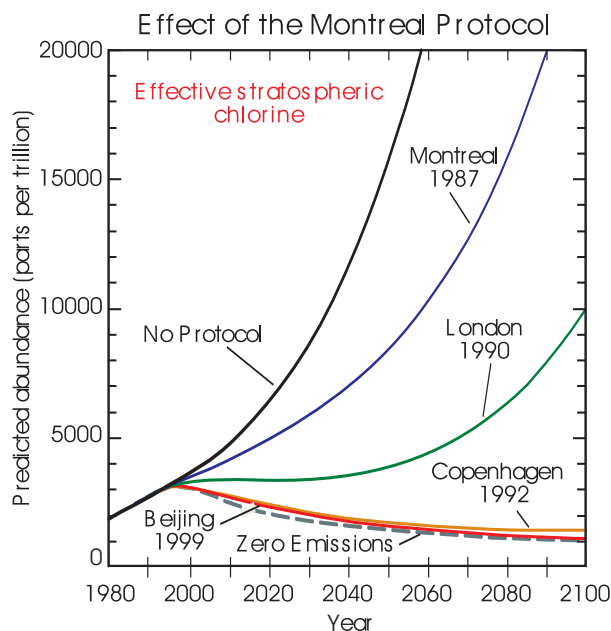
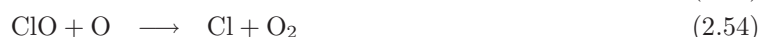


Figure 2.11: *Effect of the Montreal Protocol. The city names and years indicate where and when changes to the original 1987 Protocol provisions were agreed upon. The zero emissions line shows stratospheric abundances if all emissions were reduced to zero beginning in 2003. Effective stratospheric chlorine as used here accounts for the combined effect of chlorine and bromine gases. Adapted from WMO[2003]*

Stratospheric Chlorine Chemistry

Once chlorine is released from its source gases, it undergoes a variety of reactions. Similar to NO_X , ClO_X is dominated by the rapid cyclic transformation between Cl and ClO by the following reactions



and the photolysis of ClO.



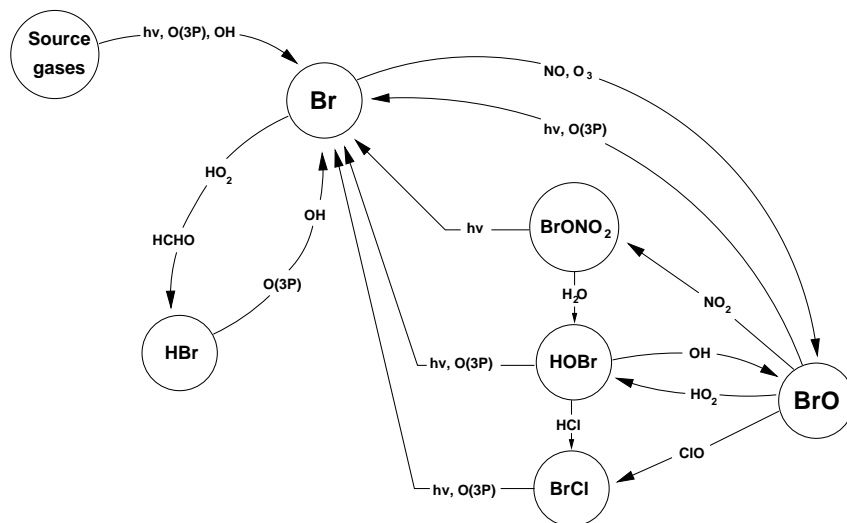
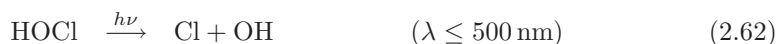


Figure 2.12: Stratospheric bromine chemistry scheme [Lary 1996; Lary et al. 1996]

The main temporary reservoir species of ClO_X are formed through the reactions with NO_2 , HO_2 and CH_4



The active forms are regenerated again from ClONO_2 and HOCl by photolysis,



or from HCl by reaction with OH

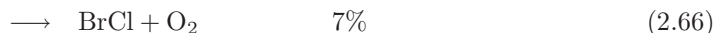


Since the absorption of HCl is limited to $\lambda \leq 205 \text{ nm}$ its photolysis is extremely inefficient. Since only the photolysis of HOCl is efficient, most of the chlorine is present in its inactive forms HCl and ClONO_2 . A significant re-conversion to ClO_X occurs only between 30 km and 45 km. At altitudes around 50 km almost all chlorine resides as HCl [Solomon 1999]. As a result, the impact of chlorine on the stratospheric ozone content is restricted to the upper stratosphere in unperturbed conditions (see Figure 2.5). For so-called ozone-hole conditions, heterogenous processes lead to an efficient release of active ClO_X and a subsequent ozone destruction (see section 2.2.4). For low temperatures, the activation of chlorine can also occur on liquid sulfate aerosols at mid-latitudes and polar regions [Webster et al. 1998; Solomon et al. 1998].

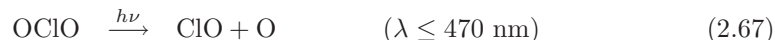
Stratospheric Bromine Chemistry

The second important halogen catalytic cycle is the bromine cycle. An overview of the bromine chemistry according to Lary [1996] and Lary et al. [1996] is presented in this section (see also Figure 2.12). The

impact of bromine is most effective during high chlorine activation inside the polar vortex, since the combined cycle of BrO and ClO can effectively destroy ozone.



Percentage yields for the three branches at 195 K using JPL 2002 kinetics [Sander *et al.* 2003] are noted. Because of the fast photolysis of BrCl and the collision-induced decay of ClOO to Cl and O₂, the reaction of BrO with ClO leads to coupled catalytic bromine-chlorine ozone-depletion cycle. The third pathway is the only known production channel of OCIO in the lower stratosphere. Subsequent loss of OCIO is nearly all due to the fast photolysis,



which prevents the build up of large concentrations during daytime. Nevertheless, OCIO is an important indicator of chlorine activation and ozone depletion [e.g., Solomon *et al.* 1987; Erle 1999; Fitzenberger 2000; Wagner *et al.* 2001]. Recent findings by Canty *et al.* [2005] highlight the importance of accurate knowledge of BrO+ClO reaction kinetics and suggest an increase of the BrCl yield from 7% (JPL 2002 value) to 11% (near the upper limit of the uncertainty). Figure 2.13 shows the effect of a dif-

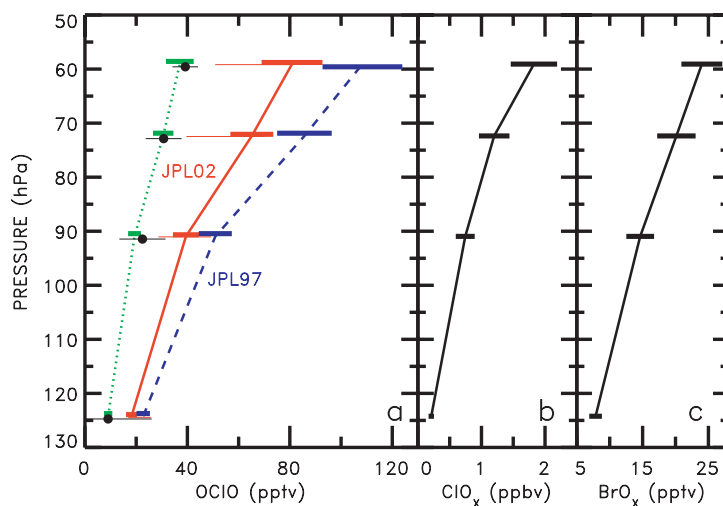
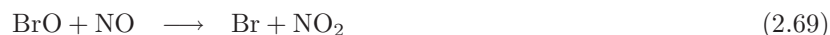
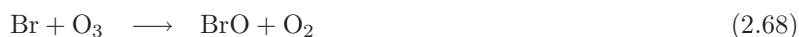


Figure 2.13: (a) Calculations of OCIO for 18:00 LT using JPL 1997 kinetics (blue dashed curve), JPL 2002 kinetics (red solid), and JPL 2002 kinetics with a BrCl yield of 11% (green dotted) at 68°N for January 23, 2000, from a 10-day isentropic back trajectory photochemical model. Measured OCIO (black dots) above Kiruna (68°N) at 18:00 LT on January 23, 2000, using lunar occultation, is also shown. (b) ClO_x measurement above Kiruna on January 20 and 27, 2000. (c) BrO_x based on DOAS measurements of BrO above Kiruna obtained on February 18, 2000. Adapted from Canty *et al.* [2005]

ferent BrCl yield for OCIO lunar occultation and DOAS BrO solar occultation measurements during the Arctic winter 1999/2000. Chapter 8 presents results from a comparison of DOAS OCIO solar occultation measurements at twilight and model calculations.

The fast BrO/Br conversion is also promoted by other reactions

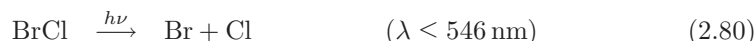




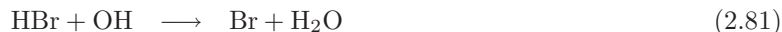
BrO has a short lifetime (~ 1 s) during the day. However, between 40 – 70 % of the total inorganic bromine (Br_Y) can be in the form of BrO, since atomic bromine (Br) reacts very quickly with O_3 . The most important sinks of BrO are its photolysis and reactions with NO, ClO and NO_2 . During sunset, BrO concentrations decrease very rapidly, as the reservoir species become more and more abundant. The main reservoir species are formed in reactions with NO_2 , HO_2 , ClO and CH_2O .



Under non-denoxification conditions (outside the polar vortex), bromine nitrate (BrONO_2) is the most important bromine reservoir species and has a photolytic lifetime of a few minutes. Because of its lower photolytic stability, HOBr can form up to 30 % of the total inorganic bromine during daytime and can be the most important bromine reservoir during the night, when taking into account the increased importance of BrONO_2 hydrolysis on sulphuric acid background aerosols (see section 2.2.5). The active species Br and BrO are released from their reservoirs by photolysis



Due to the relatively long wavelength absorption of these reservoir species, their photodissociation is very efficient throughout the whole stratosphere. Moreover, Br atoms are rapidly regenerated from HBr via



As a result, the partitioning of the total bromine content between active and inactive species is shifted more towards the active forms when compared with chlorine. Thus, bromine is more efficient in destroying ozone than chlorine.

2.2.4 Heterogeneous Chemistry on PSCs - The Ozone Hole

After the discovery of the ozone hole over Antarctica in early 1985 [Farman *et al.* 1985], it was recognized, that the chemical conversion of species related to ozone loss, in the presence of stratospheric particles, is important. These conversions ultimately result in the rapid build up of active ClO_X and BrO_X catalysts which subsequently lead to ozone destruction. The dynamic prerequisite for polar ozone loss is the formation of the wintery polar vortex as described in section 2.1. Temperature, size and persistence of the polar vortex determine the rate of formation of particles referred to as Polar Stratospheric Clouds (PSCs). Water, nitric acid and sulfuric acid are the main constituents of PSCs and appear in various concentrations. PSCs can be liquid or solid. PSCs are often measured with LIDAR (Light Detection And Ranging) instruments and are thus classified with respect to their optical properties of backscatter and depolarization (see Table 2.2). The mechanisms for the formation and the exact constitution of PSCs is still subject of research. It was first believed that PSCs consist mostly of water ice. These stratospheric ice clouds (now referred to as PSC type 2) are usually optically thick and brilliant in

Table 2.2: PSC classification with respect to their optical properties [e.g., David et al. 1998].

Type	Backscatter signal	Depolarization	Shape	Composition	Temperature
PSC 1a	weak	significant	non-spherical	possibly NAT	$< 196\text{ K}$
PSC 1b	very weak	negligible	spherical	possibly STS	$< 196\text{ K}$
PSC 2	large	strong	non-spherical	ice	$< 188\text{ K}$

color. They can occur when the temperature falls below the freezing point ($T_{ice} < 188\text{ K}$). They have been observed with concentrations between 10^{-4} and 10 cm^{-3} and diameters ranging from 2 to $25\text{ }\mu\text{m}$ [WMO 2003]. McCormick et al. 1982 also observed optically thinner PSCs at warmer temperatures (type 1 PSCs). It was suggested by Crutzen and Arnold [1986] and Toon et al. [1986] that these particles are formed by solid nitric acid trihydrate (NAT = $\text{HNO}_3 \cdot 3\text{H}_2\text{O}$). Laboratory measurements of Hansen and Mauersberger [1988] supported the theory and showed that the NAT crystal is stable a few degrees above the ice frost point ($T_{NAT} < 196\text{ K}$) under stratospheric conditions. These particles, referred to as type 1a PSCs, can exist a few Kelvin above the freezing point of ice but below the NAT threshold of 196 K. Nitric acid dihydrate (NAD = $\text{HNO}_3 \cdot 2\text{H}_2\text{O}$) could also form stable particles up to 2.5 K below the NAT threshold. Typical size distributions of type 1a particles show diameters in the range of 2 to $5\text{ }\mu\text{m}$ and concentrations below 0.1 cm^{-3} [WMO 2003]. HNO_3 containing particles with diameters around $15\text{ }\mu\text{m}$ have been observed and are believed to be NAT (or NAD) particles ('NAT-rocks') [Fahey et al. 2000].

In addition to solid NAT particles, liquid particles can appear for temperatures above the freezing

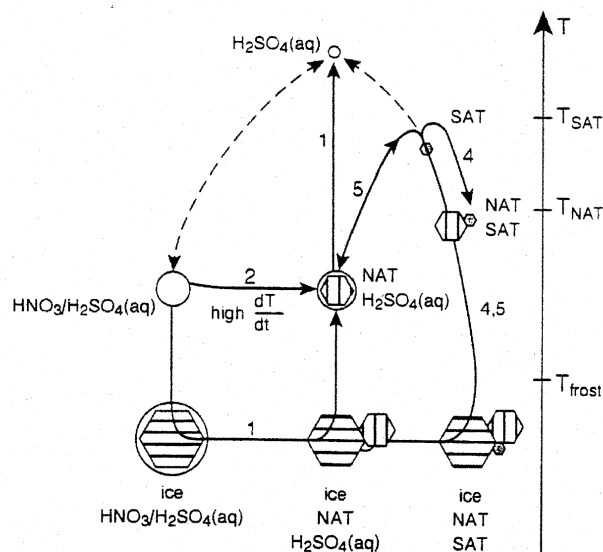


Figure 2.14: Simplified scheme of the NAT formation. Liquid particles are indicated as circles, whereas solid particles are marked by hexagonals. Adapted from Carslaw et al. [1999]

point of ice [Browell et al. 1990]. These particles are called type 1b PSCs. They are typically found with diameters smaller than $1\text{ }\mu\text{m}$ and concentrations of 10 cm^{-3} [WMO 2003], where the particle volume increases strongly for temperatures of 3 to 4 K below the NAT threshold. These liquid particles are interpreted as supercooled ternary ($\text{HNO}_3/\text{H}_2\text{SO}_4/\text{H}_2\text{O}$) solutions (STS) formed by the ubiquitous Stratospheric Sulfate Aerosol (SSA) particles, i.e. $\text{H}_2\text{SO}_4/\text{H}_2\text{O}$ solutions, taking up large amounts of

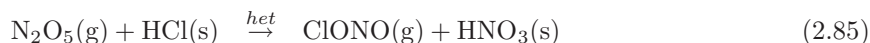
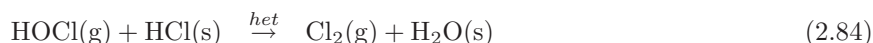
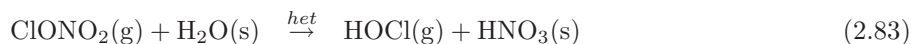
HNO₃ at temperatures below 193 K.

Different particle types do not necessarily occur in distinct PSCs. Liquid and solid particles can coexist in the same cloud [e.g. *Tsias et al.* 1999]. This was confirmed by balloon-borne in situ measurements of PSCs by *Voigt et al.* [2000], who also presented the first direct evidence for the existence of NAT particles. A simplified scheme of the possible pathways is given in Figure 2.14.

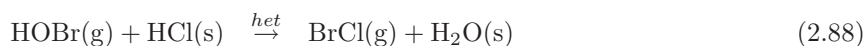
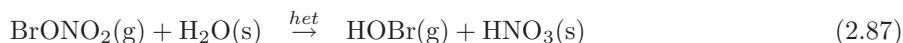
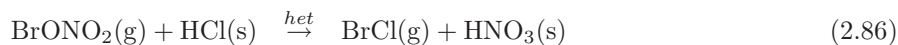
Temperatures in the Antarctic polar vortex are usually very low and often below the freezing point of ice for months. Thus, over Antarctica synoptic scale type 2 PSCs are often observed. The Arctic polar vortex is warmer and less stable (see also section 2.1), with temperatures below the freezing point of ice only for a few days or weeks. Nevertheless, mesoscale processes such as gravity waves caused by mountains can generate vertical air motions that are large enough to adiabatically cool the air parcels below the frost point of ice, leading to the formation of PSCs (lee-wave PSCs) [*Carslaw et al.* 1998; *Rivière et al.* 2000].

Further prerequisites for a strong and long lasting ozone depletion leading to the formation of an ozone hole are denoxification and denitrification (see section 2.2.2). In the absence of sunlight, NO_x is converted to N₂O₅ and via hydrolysis to HNO₃ (denoxification). Therefore the conversion of active chlorine, ClO_x, to ClONO₂ through reaction 2.56 is suppressed. The sedimentation of large PSC particles containing HNO₃ to lower altitudes leads to an irreversible removal of NO_y at higher altitudes (denitrification) and to extended ozone depletion during polar spring (see e.g. *Schlager and Arnold* [1990]).

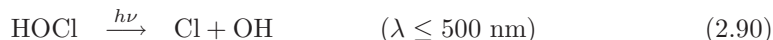
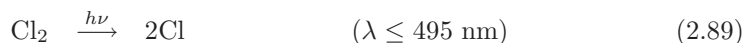
PSCs provide the surface for a number of heterogeneous reactions converting the chlorine reservoir species HCl and ClONO₂ to the more reactive species Cl₂ and HOCl:



Bromine species are activated by



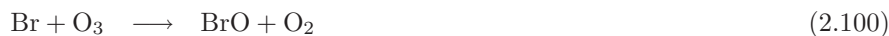
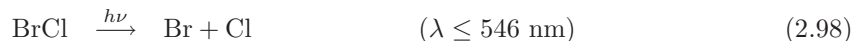
As soon as the sunlight returns at the beginning of the polar spring, the photochemically unstable compounds Cl₂ and HOCl photodissociate rapidly



The destruction of O₃ occurs primarily by two gas-phase catalytic cycles, the ClO-dimer cycle [*Molina and Molina* 1987] and the ClO/BrO cycle [*McElroy et al.* 1986]:



and



This ClO/BrO cycle is also effective at higher temperatures and even in darkness. The abundance of BrO determines the removal rate by the ClO/BrO cycle. It is less important in the Antarctic with higher chlorine activation but may account for up to 60% of the Arctic ozone loss in cold winters [Chipperfield and Pyle 1998]. In contrast to ClO, the abundance of BrO is not greatly affected by reactions involving PSCs since less than half of the available inorganic bromine budget is sequestered in reservoirs such as BrNO₃ and HBr. With the beginning of the *renoxification* in early polar spring, i.e.

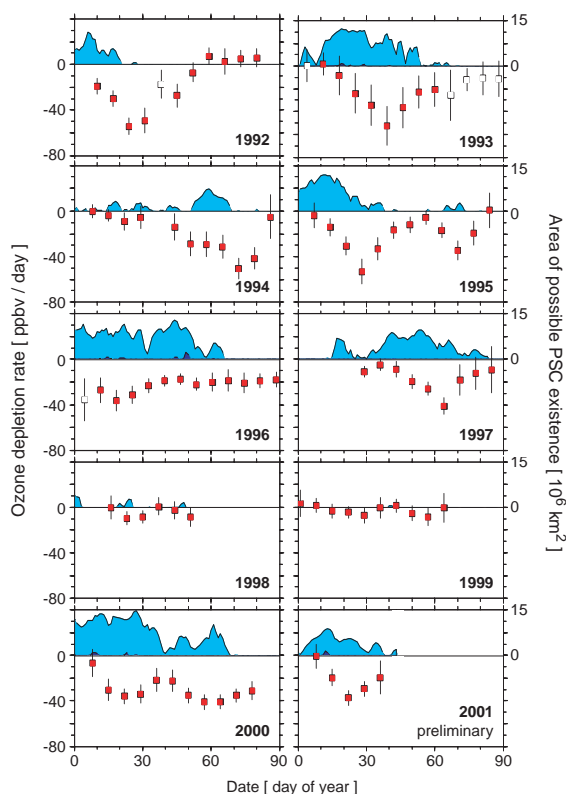


Figure 2.15: Ozone loss rates at 475 K for various winters (red squares) and area of possible PSC existence (blue shaded areas) for the northern hemisphere. Adopted from WMO [2003]

the conversion of nitrogen reservoir species to NO_x, the ozone depletion slows down and finally ends. In the case of denitrification, the ozone depletion continues until the break-down of the polar vortex and the subsequent mixing with ozone-rich, mid-latitude air. The vertical distribution of the ozone loss is extremely non-uniform. While ozone is often totally destroyed between 13 and 20 km, it remains essentially unaffected in the middle and upper stratosphere [e.g. Hoffmann *et al.* 1997]. In Antarctica, with its stable wintery conditions and cold temperatures (below the 195 K threshold for PSC formation), the

ozone level is directly linked to the halogen loading in the stratosphere. The same processes that lead to ozone loss in Antarctica certainly occur in the Arctic, but the meteorology of the northern hemisphere is more variable, with large interannual differences in the strength of the vortex and the duration of low temperatures. Thus, the development of the ozone level in the Arctic not only depends on the future trend of the halogen loading but also on climate change. Figure 2.15 shows Arctic ozone loss rates at 475 K for various winters.

2.2.5 Heterogeneous Chemistry on Sulfate Aerosols

Significant ozone loss can also occur at mid-latitudes. It was soon clear that this loss could not be attributed to dilution of polar air masses with low ozone at the end of the polar winter/spring [Sze *et al.* 1989]. Fahey *et al.* [1993] explained these mid-litudinal phenomena by heterogeneous chemistry on liquid stratospheric sulphuric acid aerosols, with the latter increasing dramatically after volcanic eruptions [Avallone *et al.* 1993; Solomon *et al.* 1996]. After the eruption of Mount Pinatubo in June 1991, it was possible to study the effect of enhanced aerosol loading of the PSC-free stratosphere in terms of chlorine activation on the background aerosols. The aerosol *Junge-Layer* in altitudes of 10 – 30 km consists mainly of $\text{H}_2\text{SO}_4/\text{H}_2\text{O}$ droplets, which are distributed globally in the lower stratosphere (*background aerosol*) [Roedel 1992].

Sulphuric species are emitted anthropogenically (direct SO_2 emissions, fossil fuel burning) as well as

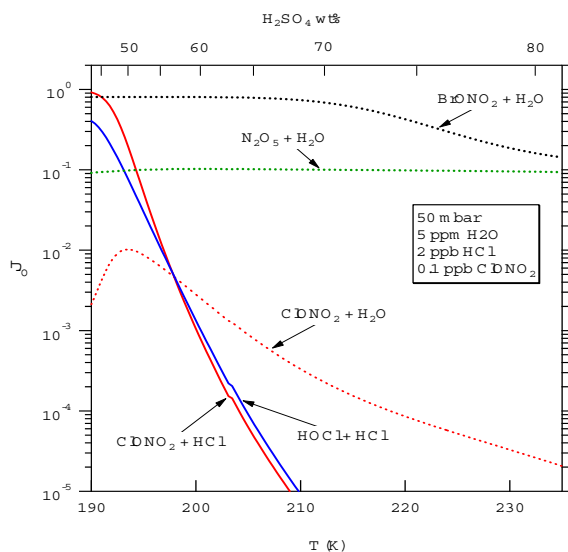


Figure 2.16: Reactive uptake coefficients as a function of temperature of the key stratospheric heterogeneous processes on sulfuric acid aerosols. Calculations are shown for a background pressure of 50 mbar and background water vapor and HCl mixing ratios of 5 ppmv and 2 ppbv, respectively. Adapted from Sander *et al.* [2003].

naturally (organic sulphur species, dimethyl sulfid (DMS), COS and H_2S from the ocean, volcanic eruptions). Direct entry of SO_2 into the stratosphere is negligible, while long-lived sulphur species reach the stratosphere, where they lead to the production of sulphuric acid



and subsequently form hydrate aerosols in connection with water [Roedel 1992]. Typical aerosol surfaces are about $1 - 10 \mu\text{m}^2\text{cm}^{-3}$ in the lower stratosphere under non-perturbed conditions.

The N_2O_5 hydrolysis was the first reaction found to be relevant not only on PSCs but also on sulphuric acid aerosol surfaces [Mozurkewich and Calvert 1988; Tolbert et al. 1988]. This reaction leads to a reduction of NO_x and is therefore indirectly responsible for an increase in reactive chlorine. The same holds true for the BrONO_2 hydrolysis. BrONO_2 hydrolysis also has a large influence on the bromine chemistry, since it converts BrONO_2 to HOBr , which photolyses faster. After the eruption of Mount Pinatubo and El Chichon, model studies [Brasseur and Granier 1992; Lary 1996; Tie and Brasseur 1996] and measurements [Solomon et al. 1994; Slusser et al. 1997] showed how important these reactions are at both high and mid-latitudes. Figure 2.16 summarizes the reaction probabilities for the different reactions. The loss of ClONO_2 , BrONO_2 , HOCl and HOBr on HCl is not important for temperatures above 200 K and background aerosol conditions. The time constant (or lifetime) for the different heterogeneous reactions can be calculated from the aerosol surface area A , the reaction coefficient γ and the mean thermal velocity v_{th} - see for example Finlayson-Pitts and J. N. Pitts [1986]. $v_{th} = \sqrt{\frac{8k_b T}{\pi m}}$ - where k_b is the Boltzmann constant, T the temperature and m the molecular mass.

$$\tau = \frac{4}{\gamma \times v_{th} \times A} \quad (2.105)$$

$$k_{het} = \tau^{-1} \quad (2.106)$$

The ClONO_2 hydrolysis has a time constant of 3 weeks for a typical aerosol surface area of $A = 1 \frac{\mu\text{m}^2}{\text{cm}^{-3}}$ and $\gamma = 0.01$. Therefore it is clear that most heterogeneous reactions do not lead to chlorine activation at temperatures above 210 K. However, they cannot be neglected for $T = 200 - 210$ K, when aerosol levels are slightly increased. Bromine reaction coefficients are higher by 1 – 3 orders of magnitude than respective chlorine reactivities, explaining why the effect of bromine is comparable to that of chlorine, although bromine is about 100 times less abundant than chlorine.

Chapter 3

Methodology

3.1 Basics of the Atmospheric Radiative Transfer

A photon traversing the Earth's atmosphere can undergo a variety of processes. It can be Rayleigh or Raman scattered on air molecules, Mie scattered on aerosols, cloud droplets or ice particles, or it can be absorbed by them. Since the absorption by aerosols and cloud droplets is negligible in the UV/vis/NIR¹ wavelength range ($\sim 300 - 800$ nm), only the gaseous absorption of molecules will be considered in this study. This section describes the different scattering processes and molecular absorption in more detail and lists the definitions of some basic quantities in radiative transfer.

3.1.1 Definitions

The incident radiant energy per time dW_λ at wavelength λ on an arbitrary orientated area element dA is represented by the spectral *irradiance* E_λ

$$E_\lambda = \frac{dW_\lambda}{dA} \quad (3.1)$$

Taking into account the orientation of the area element and the solid angle Ω of the incident radiation, the spectral *radiance* L_λ , often simply called intensity I_λ , is obtained by

$$L_\lambda = \frac{dW_\lambda}{dA_\perp d\Omega} \quad (3.2)$$

where $dA_\perp = dA \cos \vartheta$ and ϑ is the angle between the incident beam and the normal of the area element. The irradiance can be calculated by integrating L_λ over the half sphere, considering the factor $\cos \vartheta$:

$$E_\lambda = \int_{2\pi} L_\lambda \cos \vartheta d\Omega \quad (3.3)$$

For isotropic radiation, the integration yields $E_\lambda = \pi L_\lambda$. The *actinic flux* F_λ is of major importance for the photochemistry. It is obtained by integrating L_λ over the whole sphere

$$F_\lambda = \int_{4\pi} L_\lambda d\Omega . \quad (3.4)$$

¹UV: ultraviolet; vis: visible; NIR: near infrared

3.1.2 Photochemical Effects

Absorption of ultraviolet and visible radiation by atmospheric molecules can cause the molecule to photodissociate. The photodissociation rate of a molecule A is

$$\frac{dn(A)}{dt} = -j_A \cdot n(A) \quad (3.5)$$

where $n(A)$ is the concentration of the molecule and j_A the photodissociation probability or coefficient. The photodissociation coefficient can be calculated by integrating the product of the absorption cross section σ , which refers to the ability of a particular molecule to absorb a photon of a particular wavelength, the actinic flux F and the quantum yield ϵ . The quantum yield describes the probability of photodissociation after absorption of a photon.

$$j_A = \int \epsilon(\lambda) \sigma(\lambda) F(\lambda) d\lambda \quad (3.6)$$

The spectral distribution of the absorption cross section and the quantum yield is determined in the laboratory and can vary with temperature and pressure (see e.g. chapter 5). In most cases, the quantum yield is close to unity but can be smaller, especially near the dissociation limit. This limit corresponds to the minimum energy required to dissociate the molecule. Wavelengths given for photolytical reactions (e.g. in section 2.2) indicate the dissociation limit.

3.1.3 Scattering

Rayleigh Scattering

Rayleigh scattering occurs if the dimension of the scatterer is small compared to the wavelength of the incident radiation (e.g. air molecules). The scattered light can be treated as radiation emitted by an oscillating dipole, excited by the oscillating field of the incident electromagnetic wave. The scattering cross section has a λ^{-4} dependency for light frequencies smaller than the natural frequency of the oscillator (see e.g. [Feynman et al. 1965]). An accurate empirical formula for the total cross section, taking into account the polarizability and the anisotropy of air molecules, is given e.g. by [Brasseur and Solomon 1986]

$$\sigma_{Rayl} = \frac{4.02 \cdot 10^{-28}}{\lambda^{3.916+0.074\lambda+\frac{0.05}{\lambda}}} \text{ cm}^2 \quad (3.7)$$

with λ given in μm . Other empirical formulas are found in literature, e.g. by Nicolet [1984]. The phase function for unpolarized light is

$$p(\theta) = \frac{3}{4} (1 + \cos^2 \theta) \quad (3.8)$$

It describes the angular dependence of Rayleigh scattered radiation with the angle θ between incident and scattered radiation. When taking into account the anisotropy of the molecules [Pennedorf 1957] it can be written as:

$$p(\theta) = 0.7629 (1 + 0.932 \cos^2 \theta) \quad (3.9)$$

Mie Scattering

Mie scattering occurs when the dimension of the scattering particle is equal to or greater than the wavelength of the incident light. In this case, the emission of a large number of excited dipoles in the particles has to be considered. The resulting interference leads to a strong emphasis of the forward direction of the scattered light. This scattering characteristic can be approximated by the Henyey Greenstein phase function:

$$p(\theta) = \frac{1 - g^2}{(1 + g^2 - 2g \cos \theta)^{\frac{3}{2}}} \quad (3.10)$$

with the asymmetry factor

$$g = \langle \cos \theta \rangle = \frac{1}{2} \int_{-1}^{+1} p(\theta) \cdot \cos \theta \, d(\cos \theta). \quad (3.11)$$

For atmospheric aerosols an asymmetry factor in the range of 0.6 to 0.7 is usually assumed. As a mixture of different size aerosols is found in the atmosphere, the macroscopic extinction coefficient is used instead of the scattering cross section. This macroscopic extinction coefficient is defined as the integral over the particle size distribution times the scattering cross section and the particle surface [Van De Hulst 1957]. The size distribution of atmospheric aerosols is described well by the Junge distribution ($\sim r^{-s-1}$) with $s = 3.5 \pm 1$ [Junge 1961] leading to a λ^{3-s} dependence of the macroscopic extinction coefficient.

Raman Scattering

Raman scattering occurs when light is scattered inelastically on molecules. This means that the rotational or rotational-vibrational state of the molecule and thus the energy of the scattered photon changes during the scattering process. Consequently, the scattered light consists of the Rayleigh line (due to elastic scattering contributions) accompanied by several closely spaced vibrational Raman bands, each consisting of several rotational Raman lines. Detailed calculations of the Raman cross section for air molecules (O_2 and N_2) can be found e.g. in Bussemer [1993] and Funk [2000].

For measurements of scattered sunlight, a consequence of Raman scattering lies in the ‘filling’ of Fraunhofer lines. This effect is referred to as the *Ring effect* [Grainger and Ring 1962] (see section 3.4.1). Strong atmospheric absorption lines can also be affected by the Ring effect [Fish and Jones 1995].

3.1.4 Absorption

An atom or molecule can be excited from its current energy state to a higher energy state by absorption of a photon, if the energy difference of the two states equals the energy of the absorbed photon. The transition probability depends linearly on the energy density of the radiation field with a proportionality factor called *Einstein coefficient* of absorption. Atoms or molecules can change their internal state by absorption and stimulated or spontaneous emission where an Einstein coefficient is assigned to each process. The strength of the absorption is thus given by the Einstein coefficient obtained by quantum mechanical calculations (see e.g. [Bransden and Joachain 1983]). Besides energy conservation, certain *selection rules* for the transitions have to be obeyed. The selection rules can be inferred by considering the symmetry properties of the wave functions of the atomic or molecular states. The absorption characteristics of an atom or molecule are expressed in terms of an absorption cross section, which is a measure of the probability of absorption at a certain wavelength.

While only electronic transitions are possible for atoms, molecules also have rotational and vibrational transitions. Molecular absorption spectra in the UV/vis wavelength range ($\sim 300 - 700$ nm) consist of rotational-vibrational spectra of different electronic transitions. Examples of some absorption spectra in the UV/visible wavelength range are shown in Figure 4.2 and 4.3.

The spectral lines of the transitions are broadened by Doppler and pressure broadening. Under atmospheric conditions, the natural line width, associated with the radiative lifetime of the excited state, is negligible compared to the Doppler and pressure broadening. Because of the thermal motion of atoms and molecules the statistically distributed Doppler shift of the absorption frequency causes the spectral line to broaden, resulting in a Gaussian line shape. In the case of pressure broadening, the interaction with neighbouring atoms or molecules causes the energy levels to shift. The amount of shift depends on the energy level itself and the distance between the collision partners. For statistically distributed distances the broadened line has a Lorentzian line shape. In general the line shape of atmospheric absorption lines is dominated by pressure broadening. Doppler broadening only becomes important at low pressures. Both broadening effects can be accounted for by a Voigt profile, which is obtained by convolving a Gaussian with a Lorentzian profile.

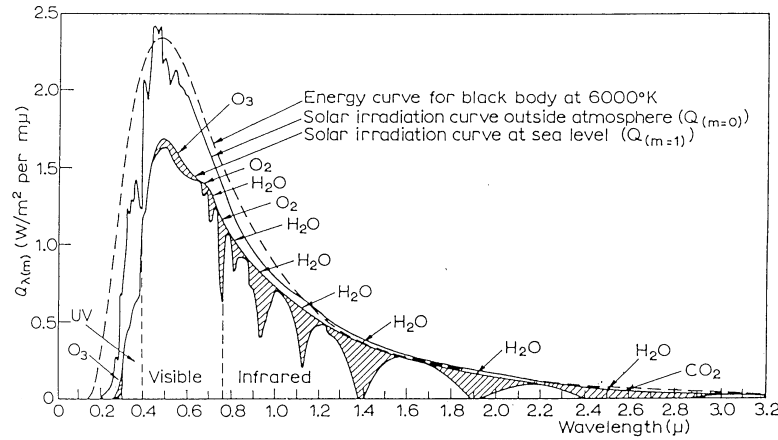


Figure 3.1: Extraterrestrial and sea level solar spectrum. The dashed line indicates the spectrum of a black body at $T=6000\text{ K}$. Shaded areas indicate the absorptions of O_3 , H_2O , CO_2 and O_2 . Adapted from Steingger [1999].

3.2 Solar Radiation and the Solar Spectrum

Solar radiation ranges from X-rays through ultraviolet to far radio radiation. Almost all of the solar radiation is emitted from the so called *photosphere*, a thin layer that is a few hundred kilometers thick. Increases of temperature and pressure towards the inner layers causes a superposition of the emission of layers with different temperatures. Since the outer layers absorb radiation emitted by the inner layers and temperature decreases towards the outer layers, only a thin layer contributes to the solar emission spectrum. This continuous spectrum is superimposed by a large number of absorption lines, the *Fraunhofer lines*, which originate from higher layers of the sun's atmosphere. Analysing the Fraunhofer lines gives information about the chemical composition and physical conditions, such as pressure and temperature. At least 63 elements have been identified in the solar photosphere, hydrogen and helium (H and He) being the most abundant.

A variety of other solar effects and characteristics exists. One of them is the *solar centre to limb darkening*. It refers to the decrease of the observed intensity from the centre towards the edge of the solar disc. A detailed description can be found e.g. in Bösch [2002]. The total irradiance E of the Sun is obtained by integrating the spectral intensity over the half sphere and all wavelengths. The *solar constant* S is the irradiance at a mean distance d_{E-S} ($= 1\text{ AU}^2$) from the earth to the sun:

$$S = \frac{ER_{Sun}^2}{d_{E-S}^2} = 1.37\text{ kWm}^{-2} \tag{3.12}$$

where the solar radius $R_{sun} = 696000\text{ km}$. Interpreting the solar irradiance according to Stefan-Boltzmann's law, an effective temperature T_{eff} of 5780 K can be assigned to the Sun. The solar irradiance is subject to fluctuations such as those caused by the *sun spot cycle* which has a period of 11 years. Sun spots are dark areas with an effective temperature of about 3500 K and a diameter in the order of $\sim 10^4\text{ km}$. The occurrence of the sun spots is accompanied by several other phenomena such as prominences and plagues, which overcompensate the reduced radiation of the sun spots. The mean energy per unit time and area arriving at the top of the Earth's atmosphere is represented by:

$$S_0 = S \frac{\pi R_{Earth}^2}{4\pi R_{Earth}^2} = \frac{S}{4} \tag{3.13}$$

²Astronomical unit (AU) = 149598000 km

where R_{earth} is the radius of the Earth. The mean radiance S_0 in combination with the conversion of energy in the earth-atmosphere system is the most important driving force of atmospheric processes. S_0 is subject to significant temporal variations as a result of quasi-periodical changes of astronomical parameters controlling the Earth's trajectory [Milankovitch 1920].

On the Earth's surface only radiation with wavelengths larger than 300 nm can be observed. Due to the strong absorptions of ozone in the Hartley band and the subsequent O_2 , N_2 and O absorptions, the earth's atmosphere is impermeable for radiation below 300 nm. In the infrared wavelength region there are strong absorption bands of H_2O and CO_2 (see figure 3.1).

3.3 DOAS - Differential Optical Absorption Spectroscopy

The extinction of light with a spectral intensity $I(\lambda)$ passing through an infinitesimally thin layer dl is given by

$$dI(\lambda) = -I(\lambda) \alpha(\lambda) dl \quad (3.14)$$

in the case that emission of light and scattering of light from an arbitrary direction in the direction of the considered light beam is neglected. $\alpha(\lambda)$ is the extinction coefficient and can be separated into the scattering and absorption coefficients $\alpha_s(\lambda)$ and $\alpha_a(\lambda)$, respectively.

$$\alpha(\lambda) = \alpha_s(\lambda) + \alpha_a(\lambda) \quad (3.15)$$

Neglecting inelastic Raman scattering, the coefficient $\alpha_s(\lambda)$ includes Mie scattering on aerosols and droplets and Rayleigh scattering by molecules:

$$\alpha_s(\lambda) = \sigma_{Ray}(\lambda) \cdot n_{Ray} + \sigma_{Mie}(\lambda) \cdot n_{Mie} \quad (3.16)$$

σ being the scattering cross section and n the density of the scatterers. The absorption coefficient $\alpha_a(\lambda)$ is the sum of all absorbers i with a non-zero absorption cross section σ_i at wavelength λ and density n_i

$$\alpha_a(\lambda) = \sum_i \sigma_i(\lambda) \cdot n_i . \quad (3.17)$$

Integration of equation 3.14 along the light path L yields the *Beer-Lambert law*

$$I(\lambda) = I_0(\lambda) e^{-\int_L \alpha(\lambda) dl} \quad (3.18)$$

The optical density τ can be introduced

$$\tau(\lambda) = -\ln \left[\frac{I(\lambda)}{I_0(\lambda)} \right] \quad (3.19)$$

to express equation 3.18 as

$$I(\lambda) = I_0(\lambda) e^{-\tau(\lambda)} . \quad (3.20)$$

If an intensity I at a certain wavelength is measured, the determination of the absorption of a species requires exact knowledge of the extraterrestrial intensity I_0 and the extinction due to Rayleigh and Mie scattering. Few measurements of the extraterrestrial solar spectra exist (e.g., the quasi-extraterrestrial measurement of Kurucz[1984] and [Gurlit et al. 2005]). Applying them to the used instrument introduces large errors due to e.g. the different resolution and wavelength calibration. A further complication is the absorption of other species at the same wavelength, which have to be separated. However, if a continuous spectrum is measured instead of only a single wavelength, the Differential Optical Absorption Spectroscopy (DOAS) technique can be applied and the above limitations can be avoided [Platt et al. 1979; Platt 1994]. The DOAS technique is based on the fact that Rayleigh and Mie scattering vary weakly in wavelength, while molecular or atomic absorption cross sections usually consist of narrow absorption bands (often overlaid by a broad continuum).

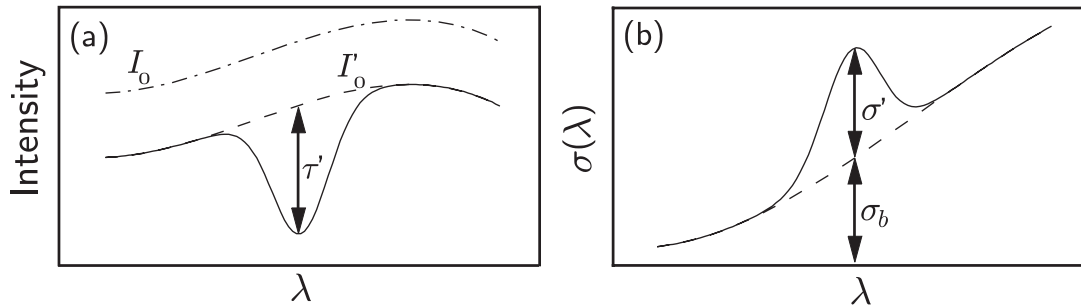


Figure 3.2: *Illustration of the DOAS principle. The absorption cross section σ can be split into a broad band σ_b and a narrow band component σ' . Adopted from Stutz [1996]*

The absorption cross section σ of a certain species can be separated into a low and a high frequency component or a broad band and a differential absorption cross section σ_b and σ' , respectively (for illustration see figure 3.2):

$$\sigma = \sigma_b + \sigma' \quad (3.21)$$

Accordingly, the absorption coefficient α_a can be split into a broad and a narrow band component $\alpha_{a,b}$ and α'_a . Equation 3.18 can then be rewritten as:

$$I(\lambda) = I_0(\lambda) e^{-\int_L (\alpha_s(\lambda) + \alpha'_a(\lambda) + \alpha_{a,b}(\lambda)) dl} = I'_0(\lambda) e^{-\int_L \alpha'_a(\lambda) dl} \quad (3.22)$$

The *differential optical density* τ' can be defined according to equation 3.19:

$$\tau'(\lambda) = -\ln \left[\frac{I(\lambda)}{I'_0(\lambda)} \right] = \int_L \alpha'_a(\lambda) dl = \sum_i \tau'_i(\lambda) \quad (3.23)$$

Broad band structures can simply be removed by high pass filtering. In practice, a so-called *Fraunhofer reference spectrum* $I_0(\lambda)$; that is, the measured spectrum with the smallest absorptions, is used. For the balloon measurements this is the spectrum at balloon float recorded at the smallest solar zenith angle. The absorber amounts in the Fraunhofer reference spectrum have to be determined by using other methods (see section 6.1). The broad band components in the retrieval $\int_L (\alpha_s(\lambda) + \alpha_{a,b}(\lambda)) dl$ are approximated by a polynomial. Assuming constant pressure and temperature along the light path, the differential absorption cross section $\sigma'_{i,a}(\lambda)$ for species i is independent of the light path and the differential optical density τ'_i can be expressed as

$$\tau'_i(\lambda) = \sigma'_{i,a}(\lambda) \cdot \int_L n_i dl = \sigma'_{i,a}(\lambda) \cdot SCD_i \quad (3.24)$$

where SCD is the *slant column density*. The SCD is the quantity obtained when performing a DOAS-retrieval. One of the shortcomings of this technique is the assumption that the pressure and temperature are constant, which is usually not fulfilled. Section 3.4.1 includes a detailed discussion on the temperature and pressure dependence of the absorption cross sections.

3.4 Spectral Retrieval

The recording of a spectrum I^* with a grating spectrograph is represented mathematically by a convolution of the continually and perfectly resolved incoming intensity spectrum I , with the instrument slit function W of the apparatus.

$$I^*(\lambda) = I(\lambda) \circ W = \int I(\lambda - \lambda') \cdot W(\lambda') d\lambda' \quad (3.25)$$

$W(\lambda)$ can be approximated the spectrum of an atomic emission line from a low pressure lamp (e.g. a mercury or cadmium lamp). Since the spectrum is recorded with a detector, the covered wavelength range is mapped onto N discrete pixels n , each integrating the light in a wavelength interval $\Delta\lambda(n)$ around the centre wavelength $\lambda(n)$

$$I(n) = \int_{\lambda(n) - \frac{\Delta\lambda(n)}{2}}^{\lambda(n) + \frac{\Delta\lambda(n)}{2}} I^*(\lambda') d\lambda' \quad (3.26)$$

Similar to equation 3.24 we can write

$$\ln[I(n)] = \ln[I_0(n)] - \left(\sum_{i=1} SCD_i \cdot \sigma_i(n) + R(n) + N(n) + A(n) \right) \quad (3.27)$$

where $\sigma_i(n)$ are the convolved cross sections of the m absorbers. The broad band components of Mie and Rayleigh scattering are represented by $R(n)$. The detector and the photon noise are described by $N(n)$, and any structures caused by the spectrograph or the detector are summarized by $A(n)$.

The spectral retrieval is the determination of the slant column densities SCD_i . Therefore, an appropriate model function $F(n)$, with input parameters $\sigma_i(n)$ and $I_0(\lambda)$ (the cross sections and the Fraunhofer reference spectrum), is used for the approximation of $\ln[I(n)]$.

$$F(n) = \ln[I_0(n, d_{00}, d_{01} \dots)] - \left(\sum_{i=1} a_i \cdot \sigma_i(n, d_{i0}, d_{i1} \dots) + P_r(n) \right) \quad (3.28)$$

The value of the fit parameter a_i corresponds to the slant column density of species i and the broad band structures are approximated by a polynomial $P_r(n)$ of degree r . To account for possible differences in the wavelength-pixel mapping of $I_0(n)$ and $\sigma_i(n)$ compared to $I(n)$, the reference spectra $I_0(n)$ and $\sigma_i(n)$ can be shifted and squeezed, expressed by the spectral alignment parameters d_{ik} . The parameter d_{i0} describes a shift in the wavelength-pixel mapping by d_{i0} pixels. d_{i1} represents a linear squeeze i.e., pixel n is shifted by $d_{i1}(n - n_c)$ pixels, where n_c is the centre pixel of the spectral range in question. For $k > 1$ the parameter d_{ik} describes a squeeze of higher order. The values d_{0k} for the Fraunhofer reference spectrum $I_0(\lambda)$ are often kept fixed and instead the measured spectrum $I(\lambda)$ is shifted and squeezed. In general, the shift and squeeze are required to compensate the misalignment of spectra as a result of different measurement conditions (e.g., temperature, pressure) and optical effects.

The spectral analysis consists of a *linear least square fit* to derive the parameters a_i and the parameters of the polynomial and a successive *non-linear Levenberg-Marquardt fit* to determine the values $d_{i,k}$ in order to minimize

$$\chi^2 = \sum_{n=0}^N \left(\frac{\ln I(n) - F(n)}{\epsilon_n} \right)^2. \quad (3.29)$$

N is the number of pixels in the retrieval range and ϵ_n is the measurement error of the n^{th} diode. Usually, a constant measurement error is assumed for all diodes, i. e. $\epsilon_n = \epsilon = \text{const}$. The fitting procedure starts with a linear least-square fit where initial values for d_{jk} are assumed. The retrieved values for a_j and the polynomial coefficients are then input parameters for a non-linear Levenberg-Marquardt fit. After performing one iterative step, the obtained new values d_{ik} are in turn used as input for the linear fit. The iterative loop of successive linear and non-linear fit is stopped if one of several abortion criteria of the Levenberg-Marquardt fit is fulfilled (e.g., convergence of the fit, represented by very small changes of χ^2 between two steps).

In contrast to the linear least-square fit, the Levenberg-Marquardt method is an iterative numerical procedure. The reference spectra $\sigma_i(n)$ and $\ln I_0(n)$ are aligned to the measured spectra $\ln I(n)$ by varying d_{ik} in order to minimize χ^2 . Therefore $\sigma_i(n)$ and $\ln I_0(n)$ have to be recalculated for the new wavelength-pixel mapping, which is done by cubic spline interpolation. The Levenberg-Marquardt method also gives an estimate of the errors of the alignment parameters. As the alignment parameters are input data for the linear fit, their errors will influence the results of the linear fit. A numerical method is used to obtain the dependence on the errors. Thus a spectrum is calculated which consists of the various reference

spectra which are scaled, shifted and squeezed according to the results of the linear fit. In addition, this spectrum is shifted and squeezed as given by the errors of the alignment parameters. The results of the linear fit performed with the original spectrum and the spectra additionally shifted and squeezed allows to infer the errors of the linear parameters caused by the errors of the alignment. Assuming that this error is independent of the statistical error of the linear fit, the total error is obtained by Gaussian error propagation.

The least-square solution for the linear fit can be found analytically [Albritton *et al.* 1976; Stutz 1996]. However, the fitting procedure will only give the best possible results including realistic errors if the model function $F(n)$ is well suited to describe the measurements $\ln I(n)$. Fit results will be incorrect if the model lacks relevant processes or describes them inaccurately. Prerequisites for the validity of the fitting procedure are independence of the measurement errors ϵ_n , linear independence of the σ_i and measurement errors with a mean value of zero and a finite variance.

The linear least-square procedure also gives an estimate of the measurement error per pixel $\hat{\sigma}$. If ϵ_n is not explicitly given, $\hat{\sigma}$ is used as measurement error instead. A significant overestimation of the real measurement errors ϵ_n (estimated by considering the different noise contributions) is an indication of an inadequate model function or of systematic errors. $\hat{\sigma}$ is equal to the root-mean-square (rms) of the remaining residual $Res(n) = \ln I(n) - F(n)$, if the number of pixels N in the fitting range is larger than the number of linear parameters of the fitting procedure (the number of cross sections σ_i plus the degree of the polynomial r).

The statistical errors of the parameters a_i and the parameters of the polynomial are given by the diagonal elements of the *covariance matrix* V . The first order covariance matrix is defined by

$$V_{vw} = cov(a_p, a_q) \equiv \langle (a_p - \bar{a}_p)(a_q - \bar{a}_q) \rangle \quad (3.30)$$

where \bar{a} is the mean. The *correlation coefficients* C_{pq} can be derived by

$$C_{pq} = \frac{V_{pq}}{\sqrt{V_{pp}V_{qq}}} \quad (3.31)$$

The correlation matrix is normalized in a way that all diagonal elements are equal to one. All other elements are between ± 1 . The correlation of two parameters p and q is given by the correlation coefficients C_{pq} where an absolute value close to 1 indicates strong correlation.

Usually, the remaining residual structure $Res(n) = \ln I(n) - F(n)$ of the fitting procedure does not consist of pure noise. A pure noise spectrum is characterized by fully independent pixel intensities which is equivalent to structures of a width of one pixel. However, a real residuum often shows groups of adjacent pixels, changing their intensities simultaneously in a random way (statistical residual structures), indicating interdependency between the pixels. The dependency of the measurement errors is described by the variance-covariance matrix. If the covariance matrix is known the linear fit procedure can be extended in such a way that the calculation of the fit results also accounts for the error interdependency [Albritton *et al.* 1976]. If the matrix is not known, a numerical method can be used to examine the influence of the residual structures on the fit results [Stutz and Platt 1996]. By smoothing a pure noise spectrum with a running mean, a spectrum can be created that shows similar structures to the residuum. The covariance matrix can then be calculated by varying the width of the smoothing filter until the width of the generated structures are of the same order as the width of the residual structures. However, this covariance matrix has to be recalculated for every measured spectrum, which is a very time-consuming and tedious procedure. Therefore, empirical correction factors for errors given by the fitting procedure were inferred and can be found in Stutz and Platt [1996].

The occurrence of systematic residual structures is not described by this method. Systematic errors influence the fitting procedure in two ways. First, residual structures can be misinterpreted as molecular absorptions and second, the fitting errors can be estimated incorrectly. A method to investigate the impact of spectral artifacts on the DOAS evaluation can be found in Hausmann *et al.* [1999]. However, this method is restricted to irregular, non-reproducible structures generated within the optical setup, and it is not valid for reproducible structures. Spectral structures result from non-identified absorbers or

instrumental errors.

The theoretical *detection limit* is an important quantity for the characterization of the quality of a trace gas measurement. It can be defined as the lowest measurable value of the fit parameter a_i or as the smallest detectable average optical density $\bar{\tau}_{limit}$ (for the definition of τ see equation 3.19). For the latter, an average optical density $\bar{\tau}_i$ of a reference spectrum is defined by three times the standard deviation of the reference spectrum $\sigma_i(n)$:

$$\bar{\tau}_i = 3 \cdot \left[\frac{1}{N-1} \sum_{n=1}^N (\sigma_i(n) - \bar{\sigma}_i)^2 \right]^{1/2} \quad (3.32)$$

where N is again the number of pixels. As the estimation of the detection limit requires time-consuming Monte-Carlo calculations, only the linear problem is considered (ignoring the uncertainties of the wavelength-pixel mapping) allowing the derivation of the detection limit to be simplified. Defining the detection limit \bar{a}_i as the value of a_i with a relative error of 0.5 yields

$$\bar{a}_i = 2 \cdot \sqrt{V_{ii}} \quad (3.33)$$

This means that the covariance matrix V has to be calculated, i.e. the evaluation has to be carried out. In this study the software packages *WinDOAS* [Van Roozendael and Fayt 2000] and *MFC* [Gomer et al. 1995] were used for the spectral evaluation, both providing the fitting procedure described above. An additional feature of *WinDOAS* is the correction of instrumental stray light caused by reflections inside the spectrograph. The correction is performed by including an intensity offset $O(n)$ described by a polynomial of maximal 2^{nd} order. The left side of equation 3.27 therefore reads:

$$\ln[I(n) - O(n)] = \ln[I_0(n)] - \left(\sum_{i=1} SCD_i \cdot \sigma_i(n) + R(n) + N(n) + A(n) \right) \quad (3.34)$$

The coefficients of the polynomial are additional parameters in the non-linear fit. Another important feature of *WinDOAS* is that it allows single scaling parameters a_i to be predefined in the model function $F(n)$. The Fraunhofer reference spectrum $I_0(n)$ is also scaled with a fitting parameter determined by the linear fit. The scaling parameter for the Fraunhofer reference spectrum has to be set to one. One shortcoming of *WinDOAS* is that it does not consider the error propagation of the uncertainties of the non-linear parameters for estimating the errors of the linear parameters, as *MFC* does.

3.4.1 Sources of Errors

The accuracy of the results is determined by the noise of the measured intensities. If the described procedure works well and the prerequisites are fulfilled, the accuracy is given by the estimated errors of the scaling parameters. Several effects are inaccurately treated by the model function described above. They result in systematic errors which contribute to the accuracy of the measurement and distort the estimation of the fitting error. For some effects a correction term can be derived which can be included in the model function. The most important effects arising from instrumental shortcomings as well as from physical deficits of the model function, are discussed in this section.

Instrument Noise

Instrument noise is an important parameter in the fitting procedure. The statistical errors of the fitted parameters and therefore the theoretical detection limit are determined by the noise of the measurement. The *photoelectron noise* σ_{ph} is caused by the statistical distribution of the number of electrons generated by the photons which illuminate the detector pixel. Since the number of photoelectrons is distributed according to Poisson statistics, the noise is given by

$$\sigma_{ph} = \sqrt{\alpha \cdot N_{e,total}} \quad (3.35)$$

where $N_{e,total}$ is the maximum number of photoelectrons and α the degree of saturation. $N_{e,total}$ can be calculated from the semiconductor capacity and the charge voltage.

The *dark-current noise* σ_{dc} of a single detector photodiode is caused by the statistical variance of the dark current across the junction. The dark current electrons are Poisson distributed and thus for an integration time t and a mean number of dark current electrons per time n , the noise is obtained by

$$\sigma_{dc} = \sqrt{n \cdot t} \quad (3.36)$$

The mean number of dark current electrons depends strongly on the temperature of the photodiode and the saturation level - nonlinearity of the dark current (see Figure 4.6).

Another important noise contribution is the *electronic offset noise* σ_{off} . The electronic offset is added to the photoelectron current before it is A/D converted to ensure positive values. Furthermore, there are several electronic noise contributions, e.g. caused by the readout process σ_r of the preamplifier, or by the analog-to-digital converter σ_{adc} . All these noise contributions are random noise and, thus, decrease when several spectra are added up. The total noise σ_{tot} is therefore given by:

$$\sigma_{tot} = \sqrt{\sigma_{ph}^2 + \sigma_{dc}^2 + \sigma_{off}^2 + \sigma_r^2 + \sigma_{adc}^2} \quad (3.37)$$

For short integration times, the dark current noise can usually be neglected. Consequently, the total noise consists of the signal-dependent photoelectron noise, which is the most dominant contribution for high saturation α , and the offset noise. The signal-to-noise ratio can be increased by co-adding subsequently recorded spectra, i.e. by increasing $N_{e,total}$.

Solar I_0 Effect

The convolved cross sections used in UV/visible spectroscopy need to be corrected since the I_0 spectrum in the sunlight measurements is the highly-structured solar Fraunhofer spectrum, whereas in most cases the I_0 used to measure the laboratory absorption cross sections is almost flat. In DOAS sunlight spectroscopy, the Fraunhofer structures are removed by forming the log ratio of a spectrum to a reference spectrum with minimal absorptions (i.e. for our balloon measurements, that is the first spectrum at balloon float at the smallest solar zenith angle), thus retaining the absorptions by atmospheric absorbers. Since both spectra forming the ratio are measured using the same instrument and have therefore been filtered by the instrument slit function, complete removal of the Fraunhofer structures is not possible.

Assuming no absorption, the reference spectrum I_{Ref} according to equation 3.25 is

$$I_{Ref}(\lambda) = I_0(\lambda) \circ W = \int I_0(\lambda') W(\lambda - \lambda') d\lambda' \quad (3.38)$$

where the I_0 spectrum here is the solar Fraunhofer spectrum and $W(\lambda)$ is the normalized instrument slit function. Similarly, a spectrum with absorptions of optical density τ (see equation 3.19) can be written as

$$I_{Spec}(\lambda) = \int I_0(\lambda') e^{-\tau(\lambda')} W(\lambda - \lambda') d\lambda' . \quad (3.39)$$

The negative log ratio of the measurement spectrum I_{Spec} to the reference spectrum I_{Ref} does not completely remove the I_0 term unless $I_{Ref}(\lambda)$ or $\tau(\lambda)$ are constant over the integration interval, i.e. the full width of the instrument slit function. This is only approximately the case for broadly-structured cross sections like O_4 , but not for NO_2 , BrO or O_3 in the Huggins bands.

The above restrictions can be avoided by using a so-called *I_0 corrected cross section* $\sigma_{corr}(\lambda)$ [Johnston 1997]. In order to generate absorption cross sections that include the solar I_0 effect, synthetic spectra with an optical density $\tau(\lambda) = \sigma(\lambda)SCD$, where SCD is the slant column density, are calculated. This leads to the following definition:

$$\sigma_{corr}(\lambda) = \frac{1}{SCD} \ln \left[\frac{\int I_0(\lambda') e^{-\tau(\lambda')} W(\lambda - \lambda') d\lambda'}{\int I_0(\lambda') W(\lambda - \lambda') d\lambda'} \right] \quad (3.40)$$

I_0 corrected cross sections can be obtained directly with the programme *WinDOAS*, if a high-resolution cross section of the absorber and of the solar spectrum is available. However, as shown by *Huppert* [2000], the use of convolved cross sections results in larger residual structures compared to cross sections recorded with the instrument itself. Thus, in this study cross sections of strong absorbers recorded with the same instrument in the laboratory were mainly used for the spectral retrieval (see chapter 5). To account for the I_0 effect, a I_0 correction was calculated and added to the measured cross section (see section 6.1). Therefore, the measured cross section had to be calibrated with the convolved cross section taken from literature.

Absolute Value and Temperature Dependence of Absorption Cross Sections

Most absorption cross sections in the UV/visible show a strong temperature dependence, i.e. the absolute value and the shape of the cross section change according to temperature. The temperature dependence can directly affect the retrieval of the fit parameters a_i due to the change of the absolute value, and the variation of the shape can result in large residual structures. Hence, if the temperature dependence of the cross section of a strong absorber is not taken into account, it may not be possible to detect underlying weak absorbers. Here the cross sections of NO_2 , O_3 , O_4 , BrO and OClO were used. Their temperature and possible pressure characteristics is discussed briefly.

The temperature dependence of the NO_2 cross section has been the subject of a number of studies (see e.g.

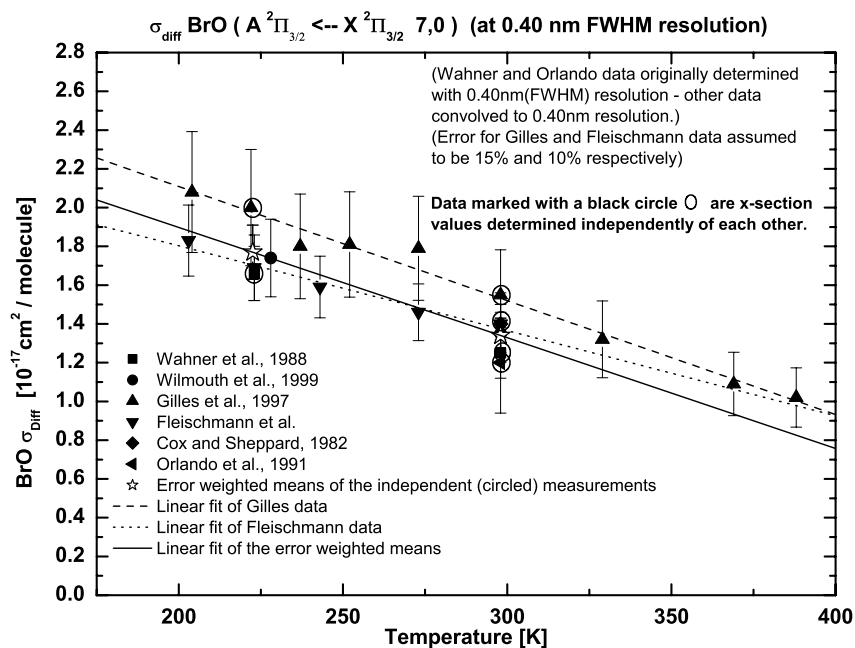


Figure 3.3: Temperature dependence of the differential BrO cross section. The vibrational band 7,0 of the $A^2\Pi_{3/2} \leftarrow X^2\Pi_{3/2}$ electronic transition is plotted for a FWHM resolution of 0.4 nm. Data was taken from *Wahner et al.* [1988], *Wilmouth et al.* [1999], *Gilles et al.* [1997], *Fleischmann et al.* [2001], *Cox et al.* [1982] and *Orlando et al.* [1982].

Orphal [2003]; *Harder et al.* [1997]; *Kirmse et al.* [1997]; *Pfeilsticker et al.* [1999]). The NO_2 cross section can be described as a bell-shaped envelope with a superimposed differential structure. The temperature effect on the cross section is a slight broadening of the envelope with increasing temperature while the amplitude of the superimposed fluctuations decrease. The effect of broadening of the envelope is largest for the red tail of the cross section, whereas for the UV the envelope does not change significantly with

temperature. Thus, the integrated cross section is only dependant to a limited extent on the temperature. The differential cross section shows an asymmetric increase with decreasing temperatures. The differential cross section has a smaller negative temperature coefficient in the region of the peaks and a larger positive coefficient in the region in between. The magnitude of this temperature variation depends on the wavelength and the spectral resolution of the instrument used. For a resolution of 0.54 nm (FWHM) the differential cross section at 448 nm increases almost linearly with decreasing temperature by almost 40 % from 298 K to 200 K [Pfeilsticker *et al.* 1999]. In addition, at very high spectral resolution the differential cross section shows large changes with changing pressure. For the low spectral resolution used in this work, this effect is not of importance.

A detailed study of the temperature dependence of the ozone absorption in the Chappuis band (410 – 760 nm) can be found in Burkholder and Talukdar [1994] or more recently for the wavelength range 230 - 850 nm in Voigt *et al.* [2001]. Near the peak of the Chappuis band (550 – 650 nm) the cross section varies slightly ($< 1\%$), while at wavelengths outside the peak it decreases with decreasing temperature. For example, at 420 nm the absorption cross section decreases by 40% when the temperature decreases from 298 K to 220 K. A pressure dependence is not observed.

The temperature and pressure dependence of the O₄ absorption was investigated by Osterkamp [1997] and Pfeilsticker *et al.* [2000]. They found that the shape of the O₄ collisional pair absorption cross section does not depend on pressure or temperature, while the magnitude of the cross section decreases by about 11 % when increasing the temperature by 50 K.

The cross section of OClO consists of a series of absorption bands overlaid with a broad continuum (see Figure 5.10). The continuum decreases when the temperature is lowered, while the individual bands become sharper and the peak cross sections increase. The error of the OClO absorption cross section is estimated to be about 10 % and its temperature dependance between 204 and 298 K is 10 – 20 % [Wahner *et al.* 1987; Kromminga *et al.* 2003].

The temperature dependence of the differential BrO absorption cross section is shown in Figure 3.3. All literature values available are compared for 0.40 nm FWHM resolution and the 5 independent measurements are marked with circles. The differential BrO absorption cross section decreases by $\sim 15\%$ when the temperature increases from 200 K to 250 K. Its absolute error at a given temperature is $\sim 10\%$ and therefore the largest independent error source in the DOAS BrO retrieval. In future it will be necessary to measure the BrO cross section with higher accuracy.

Since the light measured by the spectrograph has traversed several atmospheric layers with different temperatures, the absorption seen in the spectrum is a composition of absorptions taking place at different temperatures. Accordingly, the residual of the fitting procedure can be decreased by using several cross sections (in general two or three cross sections are used) recorded at different temperatures for the same species [Sanders 1996]. The temperatures should be in the range of the temperatures of the absorbing trace gas.

Correlations of Cross Sections

Correlations between the cross sections included in the fit can lead to systematic structures in the fit residual. Their effect on the quality of the fit is hard to quantify, e.g. residual structures as a measure of the quality of the DOAS evaluation can get smaller when structures are fitted incorrectly by correlating cross sections. Correlations may occur between weakly-structured absorbers like e.g. O₄ and the polynomial. Therefore the degree of the polynomial must be as low as possible and the fit parameters must be checked to ensure they have a reasonable order of magnitude, e.g. not negative. Correlations can also be present when including both a pseudo-absorber (like the Ring effect) and an additive intensity offset to correct for instrumental stray light. This can be avoided by using only one of them. Since both effects are real, exclusion of one leads to a larger residual.

Two (or more) cross sections of the same absorber at different temperatures are quite similar in structure and, thus, strongly correlate. This can be avoided by using a mathematical orthogonalization procedure which makes the cross sections linearly independent. But cross sections of different absorbers can also show cross correlations or can correlate with the spectrum itself (see also equation 3.31). Generally,

correlations increase with the degrees of freedom of the fit and decrease with increasing fit range, i.e. number of pixels. They vary largely between different wavelength ranges.

Ring Spectrum

For scattered light measurements, the depth of the Fraunhofer lines changes with solar zenith angle caused by the filling in effect of Raman scattering (see section 3.1.3). Usually, this is corrected by including a further spectrum in the fitting process [Solomon *et al.* 1987]. This so-called Ring spectrum can be obtained by polarization measurements or by model calculations [Funk 2000]. For direct sun light measurements the Ring effect is negligible [Bauer 1997; Pundt *et al.* 1998] and therefore not applied.

Center-to-Limb Darkening Correction

The DOAS technique is based on the assumption that the structures of the Fraunhofer spectrum I_0 remain constant for all measurements. In this case, the strong solar lines, with optical densities 100 – 1000 times larger than the atmospheric absorption structures, can be removed properly from the measured spectrum and the trace gas absorptions can be evaluated. This assumption is not valid for measurements of direct sunlight during sunrise or sunset. As the solar disk has a diameter of 0.55° when seen from the Earth without refraction, the zenith angles and hence the atmospheric air masses are different for rays leaving the upper edge, center or lower edge of the Sun. This effect becomes more important as the solar zenith angle increases. The optical densities of the solar Fraunhofer lines vary across the solar disk and the resulting shift of the radiance-weighted average of the sun from the solar disk center to its upper edge causes a change of the optical densities of the Fraunhofer lines over the course of the occultation measurements (sunrise or sunset). Unfortunately, the relative change of the different solar lines is non-uniform and therefore an exact treatment of this effect is difficult. Bösch [2002] investigated the Centre to Limb Darkening effect in detail and derived a correction factor that is used in this study for the OC10 DOAS evaluation in the 362 – 390 nm wavelength range (see chapter 8).

Further Sources of Error

Changes in the wavelength-pixel mapping of the measured spectra and the molecular cross sections, with respect to the solar reference spectrum, are compensated by shifts and squeezes. As the cross sections are given on a discrete grid, the shifted and squeezed spectra are obtained by (spline) interpolation. The approximation is better for higher sampling ratios, given by the number of grid points per full width at half maximum (FWHM) of the instrument function. Roscoe *et al.* [1996] pointed out, that interpolation errors are small for sampling ratios > 4.5 . This criterium is fulfilled for the instrument used here. A detailed investigation of this undersampling effect for the UV spectrograph can be found in Vrdelis [1998] and Ferlemann *et al.* [2000].

Systematic structures can be caused by changes in the instrumental resolution. Pressure and temperature variations can displace optical components of the spectrograph thus altering the instrumental resolution. Each Fraunhofer line and, to a smaller degree, each absorption band, will cause a positive (negative) large peak at the center of the band and smaller negative (positive) dips at the wings in the residual of the fitting procedure. A misalignment of one of the absorption cross sections also results in systematic structures. In this case an almost symmetrical structure with a large positive and negative peak at the wings of the band occurs in the residual. Both effects impact the scaling factors a_i as well as the estimated errors [Ferlemann 1998].

The fitting procedure requires absorption cross sections with the resolution given by the instrument function. Therefore, a mathematical convolution of a highly resolved cross section with the measured instrument function is performed. However, the instrument function is not constant over the entire spectral range. This means that the convolved cross sections deviate from cross sections recorded

directly with the instrument (see chapter 5), causing systematical residual structures.

There are several instrumental shortcomings which can result in additional residual structures if they are not taken into account. Differences in the sensitivity of the detector diodes lead to errors if a shift and squeeze is applied in the fitting procedure. The sensitivity of the diodes can be obtained by measuring the broadband emission spectrum of a halogen lamp. The differences of the diode sensitivity can be corrected by dividing of the measured spectra by the broadband emission spectrum. Further structures can be caused by the used grating itself. These structures depend on the wavelength and can not be removed easily.

Spectrometer stray light is caused by internal reflections of light from higher orders of the grating or from wavelengths not detected by the diode array. The stray light also occurs as an offset added to the measured intensity, an effect which changes the optical densities of the Fraunhofer lines and of the molecular absorption lines significantly. The stray light can be reduced but not totally suppressed by using filters and light traps for higher orders of the grating. By including an additional intensity offset (see section 3.4) the instrumental stray light can be accounted for in the fitting procedure.

The influence of the Memory effect, which causes strong structures of one spectrum to also appear in a successively recorded spectrum and the Etalon effect, which is caused by multiple reflections on thin parallel surfaces, were investigated by *Bauer* [1997] and found to be small for the used instrument. When using glass fibres to conduct the light into the spectrograph, structures can be caused by slight variations of the exposure of the fibre entrance and thus the stimulation of different modes. Due to inhomogeneities of the fibre the transmissions of the modes differ. By using e.g. a diffuser plate in front of the fibre steady exposure is achieved and this effect can be avoided.

Chapter 4

Instrumentation

The measurements presented in this study have been performed with a DOAS UV/vis double spectrograph installed on the LPMA/DOAS¹ balloon gondola during a series of balloon flights conducted since 1996. The DOAS spectrograph and the LPMA infrared Fourier Transform spectrograph (FTIR) both perform direct sunlight measurements during balloon ascent and solar occultation.

4.1 The LPMA/DOAS Balloon Payload

The LPMA/DOAS balloon gondola is based on a gondola developed for astronomical observations by the Observatoire de Genève and was optimised for atmospheric measurements by *Camy-Peyret et al.* [1995] (Figure 4.1). In order to perform direct sun measurements, the gondola can be stabilised in azimuthal direction with an accuracy of about 3-1° in the lower stratosphere and 1° - or better at balloon float altitude. Therefore the gondola is aligned to the Earth's magnetic field with a gyroscope. The gondola can be rotated with respect to the larger balloon. The rotational energy is converted to frictional heat through the torque of a special joint that connects the gondola with the balloon. The fine-pointing is performed by a suntracker [*Hawat et al.* 1995], which provides the infrared Fourier Transform spectrograph and the DOAS UV/vis spectrograph with a parallel solar beam. Since 2002, a mini-DOAS instrument has been installed on the gondola as well, taking measurements of scattered sunlight in nadir and limb (90° to the sun) geometry [*Weidner* 2005]. Furthermore the gondola is equipped with pressure and temperature sensors, GPS antennas and an on-board chemical ozone sonde.

4.1.1 The LPMA Fourier Transform Interferometer

The FTIR operated by the french LPMA team is based on a DA2 Michelson type interferometer manufactured by BOMEM and customised for balloon operations. It has an effective aperture of 45 mm and produces a maximum path difference of $\Delta_{max} = 50$ cm leading to an apodised resolution of $\frac{1}{\Delta_{max}} = 0.020$ cm⁻¹. The interferometer is equipped with two channel optics with two detectors cooled using liquid nitrogen. The spectral signatures of ClONO₂, HNO₃, O₃, CH₄, N₂O, NO and H₂O are covered by a HgCdTe detector (mid-IR) and those of HCl, O₃, NO₂, CH₄ and HF by an InSb detector (near-IR) [*Camy-Peyret et al.* 1995; *Payan et al.* 1998; *Payan et al.* 1999]. The instrument has also been used to measure H₂O and O₂ in the 920 nm and 760 nm regions, respectively, to retrieve CCl₂F₂ in the lower stratosphere and to obtain CO₂ in the 13 μm region [*Camy-Peyret et al.* 1999]. A multifit algorithm [*Carlotti* 1988] associated with an efficient minimization of the Levenberg-Marquardt type is used for the retrieval of vertical mixing ratio profiles from ascent and occultation measurements. The algorithm allows the information contained in several micro-windows to be combined. The molecular parameters used in

¹LPMA = Limb Profile Monitor of the Atmosphere

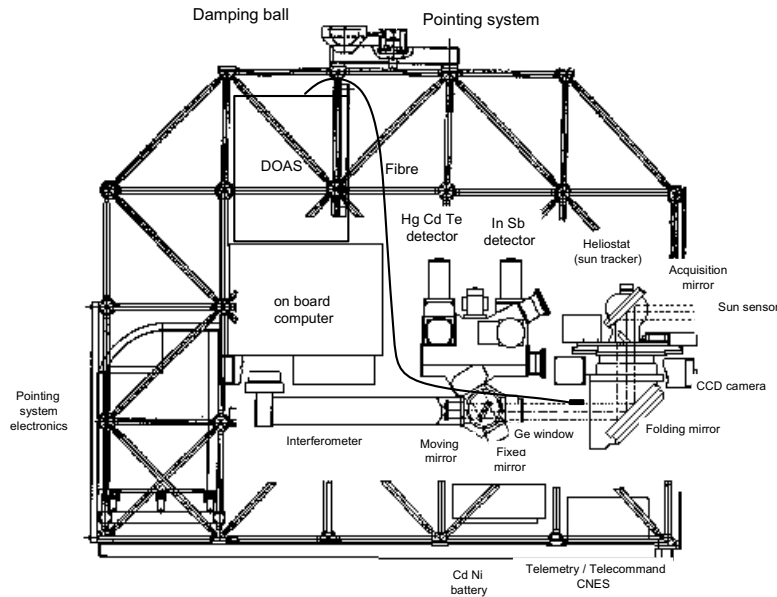


Figure 4.1: Schematic drawing of the LPMA/DOAS balloon gondola. Direct sunlight is directed into the gondola by a suntracker and is subsequently analysed by the FTIR and the DOAS instrument.

the forward model are extracted from the HITRAN database [Rothman *et al.* 2003]. For more details on the LPMA instrument and retrieval, see Dufour *et al.*[2005] and Butz *et al.*[2005].

4.1.2 The DOAS Balloon Spectrograph

A DOAS instrument optimized for airborne applications was designed and described, for example, by Ferlemann [1998], Harder [1999] and Ferlemann *et al.* [2000]. The basic features of the instrument are low weight, low power consumption, stable spectral imaging and insignificant thermal drift of the spectroscopic system.

The instrument consists of two spectrographs in one housing, which analyse the UV and the visible part of the sunlight separately (see Figure 4.4). The light enters each of the two spectrographs via a quartz fibre bundle, which forms a rectangular entrance slit at the fibre end on the spectrograph side. Telescope optics are mounted on the other end of the fibre bundles, intended to average the light received from the sun, to limit the spectral transmission range of the incoming light and to match the f -number of each spectrometer. Coming from the entrance slit, the light reaches a holographic grating, which disperses the light of the respective wavelength range in 1st-order onto the detector (UV: 316.5 – 417.3 nm and visible: 399.9 – 653.0 nm). The light is detected with Peltier cooled photodiode arrays. The width of the entrance slit was chosen to fulfill the sampling criteria given by Roscoe *et al.* [1996], i.e. the FWHM of the instrument function should be sampled with more than 4.5 detector pixels. The instrumental resolution is found to be 0.55 nm (= 5.5 detector pixels) and 1.48 nm (= 5.7 detector pixels) for the UV and the visible spectrometer, respectively. The whole spectrometer housing is evacuated and thermally stabilized by a surrounding vessel filled with a water-ice mixture. Keeping the spectrograph at a stable temperature of 0°C avoids spectral shifts. In addition, a refrigerant circulates in a cooling circuit to regulate the temperature of the optical components and to cool the warm side of the photodiode Peltier elements. Low spectrometer stray light is achieved by suppressing the higher-order and zero-order grating reflections by using light traps and, for some flights, by including a dispersive prism preanalyzer for

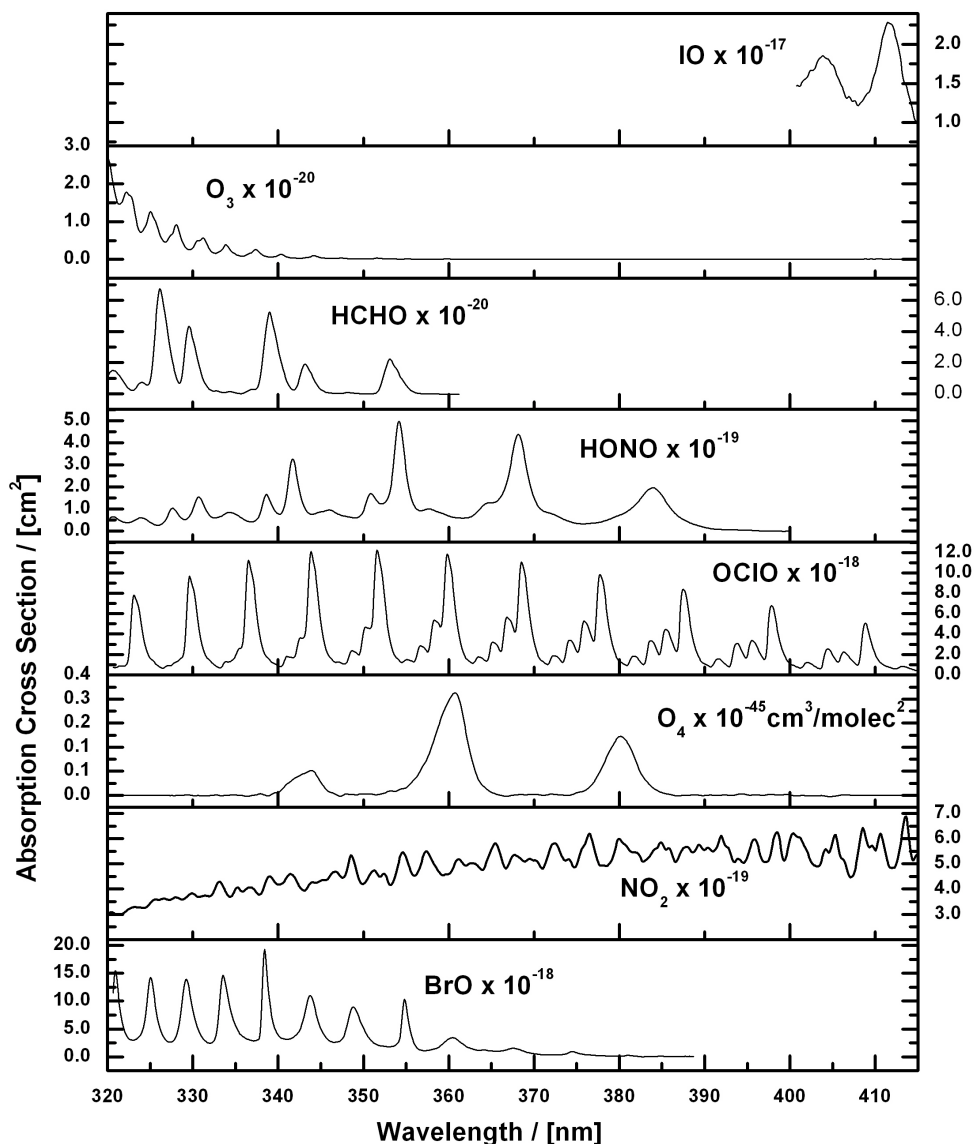


Figure 4.2: Absorption cross sections in the UV wavelength range. Top to bottom: IO [Harwood et al. 1997], Ozone [Voigt et al. 2001], HCHO [Cantrell et al. 1990], HONO [Stutz et al. 2000], OCIO [Wahner et al. 1987], O_4 [Greenblatt et al. 1990], NO_2 [Voigt et al. 2002] and BrO [Wahner et al. 1988]. For O_4 , the collisional pair absorption cross section is shown. Absorption cross sections are convolved to the resolution of the spectrograph.

the UV spectrograph [Vradelis 1998]. A detailed description of the DOAS spectrograph can be found in Bauer [1997].

In the wavelength range covered by the combination of the UV and vis spectrograph, absorption features of several species can be found, e.g. O_3 , BrO, NO_2 , OCIO, HONO, HCHO, O_4 etc. in the UV range and O_3 , NO_2 , H_2O , O_4 , NO_3 , OCIO, IO, OIO etc. in the visible range (see Figure 4.2 and 4.3). The results presented in this study focus on the retrieval of BrO and OCIO from measurements taken with the UV spectrograph. For previous results obtained by evaluating the UV/vis measurements see

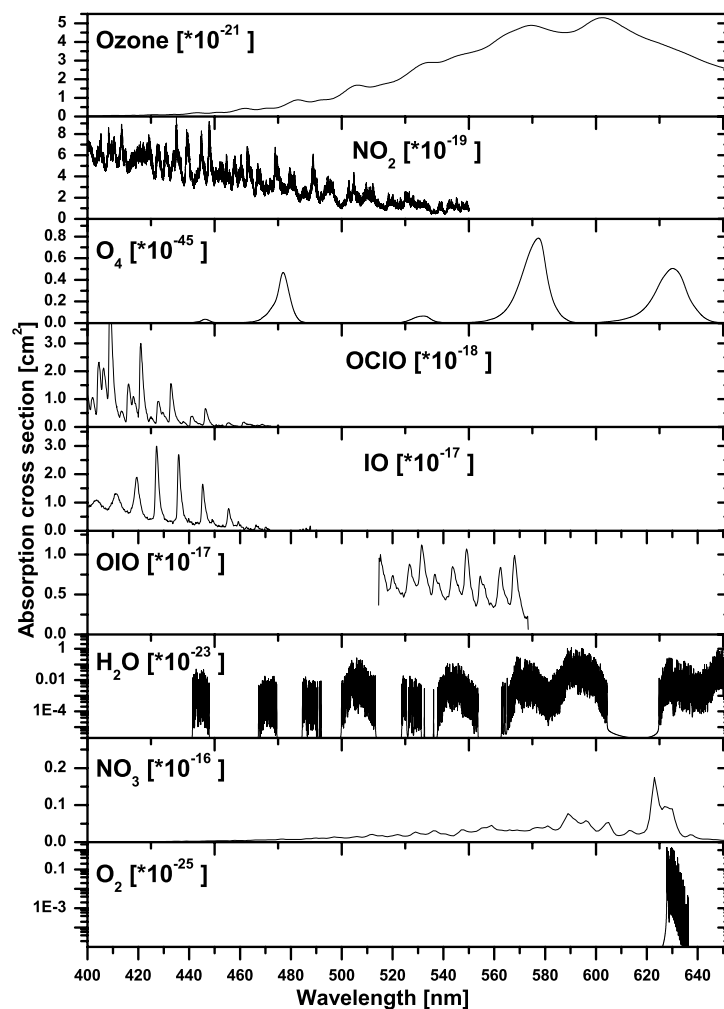


Figure 4.3: Absorption cross sections in the visible wavelength range. Top to bottom: Ozone [Burrows et al. 1999], NO_2 [Harder et al. 1997], O_4 [Greenblatt et al. 1990], OCIO [Wahner et al. 1987], IO [Harwood et al. 1997], OIO [Cox et al. 1999], H_2O [Rothman et al. 2003], NO_3 [Sander 1986] and O_2 [Rothman et al. 1996]. For O_4 , the collisional pair absorption cross section is shown. Absorption cross sections are convolved to the resolution of the spectrograph, except NO_2 , H_2O and O_2 . Adopted from Bösch [2002]

e.g. Ferlemann et al. [1998]; Harder et al. [1998], [2000]; Fitzenberger et al. [2000]; Fitzenberger [2000]; Pfeilsticker et al. [2000]; Bösch [2002] and Bösch et al. [2003].

Modifications on the DOAS balloon spectrograph since 2001

Some minor repairs and modifications were carried out to improve the performance of the DOAS spectrographs.

- To reduce the weight, the original stainless steel housing was replaced with an aluminum housing, reducing the total weight by 6 kg.
- The contaminated holographic UV grating was replaced with a new one of the same type (Jobin Yvon 52300080).

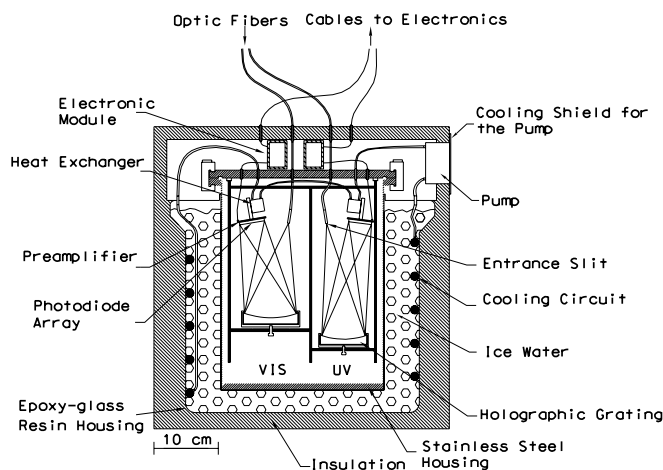


Figure 4.4: Schematic drawing of the DOAS instrument. Two holographic grating spectrographs (UV and visible) are integrated into a vacuum-sealed aluminum housing. The light enters the spectrographs through two quartz fibre bundles which form an apparent rectangular slit at the end. Photodiode array detectors cooled with Peltier elements detect the light. The aluminum housing is surrounded by an Epoxy-glass resin vessel which contains a water-ice mixture. A refrigerant is pumped through a cooling circuit to regulate the temperature of the optical components and to cool the warm side of the Peltier elements.

- Visible grating was readjusted to cover spectral range from 400 – 653 nm (previously 417 – 671 nm) to include OCIO absorption band (see Figure 4.2 and 4.3).
- Partially broken fibre bundles replaced with new ones. The diameter was increased from 125 μm to 150 μm to obtain a better sampling.
- A new *Swagelok* connection was implemented between fiber and flange to prevent leakage. New leakage rate of the spectrograph is $\sim 1.5 \cdot 10^{-7} \frac{\text{mbar}\cdot\text{l}}{\text{s}}$. Teflon gaskets were initially used, but were later replaced with nylon gaskets, which compensate thermal expansion and contraction much better.
- Adaptors for the electrical connectors on top of the flange were built to thermally decouple the connectors from the 0°C cold housing, in order to avoid condensation of water and thus possible short circuits. The 5 cm high adaptors were placed on the existing connector drillings and flange mounted. New vacuum connectors which have a larger spacing between individual pins were chosen to avoid short circuits.
- The valve, which is integrated in the flange, was replaced since the screw thread was worn out.

As the fibre bundles and the UV grating had to be replaced, and the visible grating readjusted, the whole optical alignment between entrance slit, grating, photodiode array and light traps had to be renewed for both spectrographs. Therefore a new set of reference spectra had to be recorded in the laboratory (see chapter 5).

Recommendation for future balloon flights

A dispersive prism preanalyser for the UV spectrograph [Vradelis 1998] was used during balloon flights between 1997 and 2000. Although it was possible to reduce the spectrometer stray light, the strong light attenuation and the resulting longer integration times and fewer recorded spectra, greatly reduced the

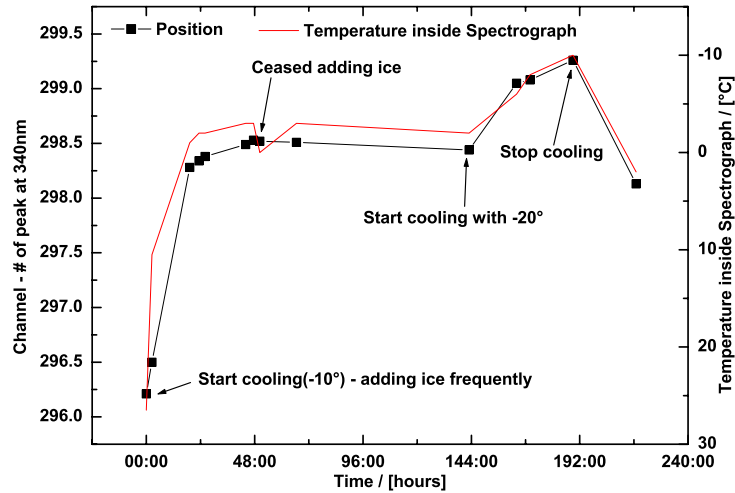


Figure 4.5: Spectral shift depending on the temperature of the spectrograph. The channel number at the peak of a cadmium line at 340 nm is plotted for different cooling scenarios - see text for details. On the right axis the temperature inside the spectrograph is shown for comparison.

quality of the trace gas retrieval. For at least one of the flights the preanalyser was subject to a shift and vibrations, which influenced the imaging and the spectral retrieval. The inclusion of the intensity offset in the WinDOAS software (see section 3.4) means that it is no longer necessary to correct for the small (see [Ferlemann 1998]) spectrographic stray light mechanically. The preanalyzer was not used after 2001, which lowered the integration time per spectrum. The low integration time between $\sim 150 - 250$ ms (for the UV spectrograph, depending on altitude and SZA) allows (20 – 30) scans to be added up before a spectrum is transmitted. Almost no height resolution is lost since the transmission and processing of one spectrum takes ~ 5 seconds, but the signal to noise is increased.

Up to 2001 all the water surrounding the spectrograph was frozen until an ice block formed and then it was allowed to defrost slowly to obtain a water-ice mixture. By doing so the spectrograph was not in a perfect thermal equilibrium, as demonstrated in Figure 4.5. Here the position of the peak of a cadmium emission line was recorded and compared for different spectrograph temperatures. First the spectrograph was cooled to 0°C by adding ice frequently into the vessel surrounding the housing. After 2 days the spectrograph was in a thermal equilibrium which was maintained for almost 3 days. Afterwards, the water ice mixture was cooled with a cryostat, so a ice block formed slowly. The temperature further decreased, down to -10°C inside the spectrograph, which caused an additional shift of the emission line. Letting the ice block melt slowly resulted in the opposite effect and again showed a deviation from thermal equilibrium. Since spectral shifts are to be avoided, it is strongly recommended to use a water ice mixture to cool the spectrograph and to keep it at thermal equilibrium.

4.1.3 mini-DOAS

Since 2002 a new light-weight mini-DOAS has been installed on the LPMA/DOAS gondola [Weidner 2005 and Weidner et al. 2005]. The new mini-DOAS spectrometer has been designed for low weight (~ 5 kg) and low power consumption (7.5 W), with particular emphasis being put on stable optical imaging and a reasonably large signal-to-noise ratio. Its light weight and small size allow versatile applications on different platforms and under several observation geometries (scanning and fixed limb, nadir and direct sunlight). Skylight radiances in the UV/visible range between 330 and 550 nm are observed. The recorded spectra are analysed for column densities of O_3 , NO_2 , BrO , H_2O and O_4 along the line of sight. For the limb and nadir measurements Radiative Transfer (RT) calculations are used to simulate the measured

quantities and infer vertical profiles of the measured species. The new method of atmospheric trace gas profiling by balloon-borne UV/vis limb scatter measurements has been tested against simultaneous measurements of the same parameters available from in-situ, or UV/vis/near IR solar occultation observations performed by the LPMA and DOAS instruments onboard the same payload. Scanning limb observations provide time-resolved profile information of radicals during sunset.

4.2 Instrumental Effects and Sun-Tracker Correlations

Within the framework of the ENVISAT / SCIAMACHY (ENVIronment SATellite / SCanning Imaging Absorption spectroMeter for Atmospheric CHartography) satellite validation, solar irradiance spectra are measured absolutely with the LPMA and DOAS instruments at balloon float altitude. After accounting for the atmospheric extinction due to Rayleigh scattering and gaseous absorption (O_3 , and NO_2), the measured solar spectra can be compared with previous observations by e.g. *Kurucz et al.* [1984] or *Thuillier et al.* [1997]; [1998]. Details of the absolute calibration and results can be found in *Gurlit et al.* [2005] and *Lindner* [2005] and are not discussed in any more detail here. During initial tests for the absolute calibration and a first data evaluation, some instrumental effects were observed and measured. These effects are presented in this section.

4.2.1 Instrumental Deficits

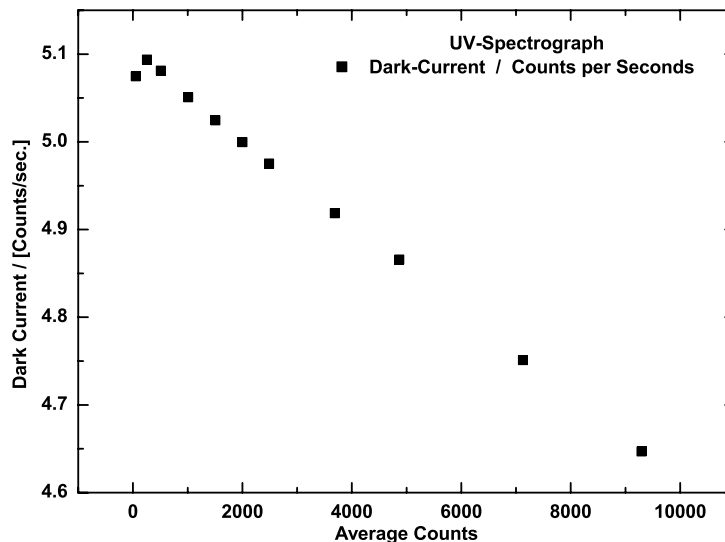


Figure 4.6: Nonlinearity of the dark current for the UV spectrograph at $-10^{\circ}C$ photodiode array temperature. Counts are averaged over the total 1024 pixels of the photodiode array.

Since the balloon-borne LPMA/DOAS spectrometers analyse the solar light from a parallel beam of 10 cm diameter, a sun simulator for laboratory test measurements was developed at the *University of Bremen*. The sun simulator consists of a small passively-cooled reflective diffuser plate of 9.2 mm diameter which is uniformly illuminated by 4 stabilised 250 W reflector Quartz Tungsten Halogen (QTH) lamps. The small diffuser plate is imaged into infinity through a 200 mm diameter, $f = 1000$ mm, off-axis parabolic mirror. It produces a collimated beam with a divergence of about 0.52° . The diffuser plate is installed in the focus of the collimating mirror for the emission of a virtually homogeneous beam across its principal axis [*Gurlit et al.* 2005]. Long integration times (up to 25 minutes for the UV spectrograph) are necessary since the UV/visible output of this source is relatively low. With an average of $\sim 5 \frac{\text{counts}}{\text{s}}$

the dark current of the photodiode array can make up to $\sim 30\%$ of the total signal at an average saturation level of $\sim 50\%$ of the lamp spectrum. That means that exact knowledge of the dark current is mandatory. Unfortunately the dark current shows nonlinear behaviour at constant temperature, i.e. it depends on the saturation level of the photodiode. It is usually assumed that the dark current is independent of the discharge of the photodiode. However, it can be shown that it strongly depends on the present charge in the barrier layer capacity and, therefore, on the voltage at the barrier layer (see *Stutz* [1991]). Figure 4.6 shows the nonlinear behaviour of the UV spectrograph's dark current at a temperature of the photodiode array of -10°C .

Another prerequisite for absolute calibration is the linearity of the detector response (photodiode and

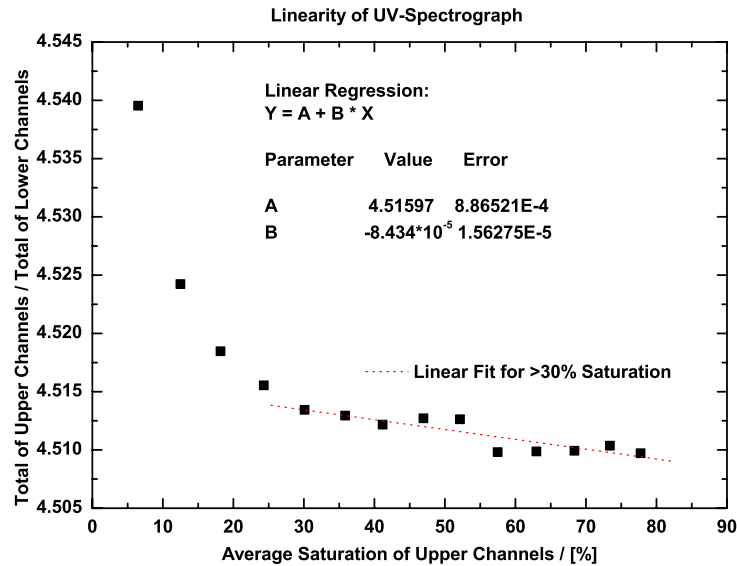


Figure 4.7: Test of the detector's linearity response (photodiode and electronics). The figure shows the ratios of two sums of photodiode readouts for direct sun observations from ground, as a function of the average saturation level of the upper channels. The two clusters of channel readouts are from the centre and from the far wing of the Fraunhofer calcium line at 393 nm, where 7 and 11 photodiodes were considered, respectively. The linear fit is for data points with a saturation level greater than 30 % but less than 80 %, which is the typical maximum saturation level during measurements. The resulting curve represents linearity of the detector electronics $((8.4 \pm 1.5) \times 10^{-5})$.

electronics). It was tested using the method suggested by *Ferlemann et al.* [2000] but values at different saturation levels were weighted equally and only between 30 % and 80 % saturation level. Direct sun observations from the ground were used to calculate the ratio of two clusters of photodiode readouts from the centre and from the far wing of the Fraunhofer calcium line at 393 nm. It is assumed that the calcium absorption line in the Fraunhofer spectrum remains constant over the period of the measurements. The advantage of this method is that the ratio is independent of the integration time and fluctuations in the intensity of the light source. The ratio is plotted in Figure 4.7 as a function of the average saturation level of the upper channels. The ratio is expected to be constant which is the case for saturation levels $> 30\%$. The results obtained are similar to the previous measurements of *Ferlemann et al.* [2000].

While performing measurements with a constant light source, it became clear that the exposure time was not set or transmitted correctly. The UV and the visible spectrograph contain independent single-board computers (MC68332 CPU module - also known as 68k) [*Ferlemann* 1998]. The program written in the EPROM² of the 68k module controls the read-out and the temperature regulation of the photodiode

²EPROM = Electrically Programmable Read Only Memory

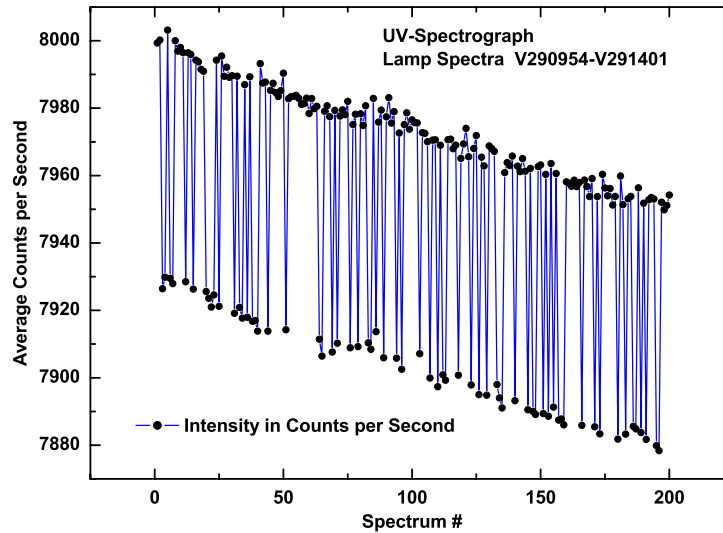


Figure 4.8: Illustration of the single-board computer MC68332 timing problem (see text for details). The average counts per second for 200 successive lamp spectra recorded with the UV spectrograph are plotted. Two domains can be distinguished: one for correctly and one for incorrectly transmitted exposure time. The overall decrease of the intensity is due to a decrease in the lamp output.

arrays and their Peltier elements. Unfortunately, in the previous version of the program in some cases an additional start signal, which initializes the exposure of the photodiode, was sent 10 ms after the first one. Therefore for a specified exposure time it was possible to actually receive a spectrum that was exposed 10 ms less. This behaviour is demonstrated in Figure 4.8 where the average counts per second for successive lamp spectra, which were recorded with the UV spectrograph, are plotted for a specified constant exposure time. Two domains can clearly be distinguished, where the overall decrease of the intensity is due to the decrease in lamp output.

During balloon flights the 68k module is operated in automatic mode. This means that the exposure time is calculated for each scan from the signal of the former scan in order to reach the optimum of 80 % of the maximum signal, which avoids nonlinearity effects. This procedure has to be performed since the signal changes constantly during the course of a balloon flight. In the previous version of the program, used until 2001, the new exposure time was calculated with an accuracy of one millisecond, although the internal timing of the 68k module is only in 10 ms steps. Therefore the wrong (with 1 ms accuracy) exposure time was stored with the transmitted spectrum. In the latest version of the program these deficiencies have been removed.

4.2.2 Sun-Tracker Correlations

During a first evaluation of the absolutely calibrated spectra for the flight at Aire sur l'Adour in October 2003, the intensity in counts per second, of 30 diodes at around 350 nm, is plotted against time. As can be seen in Figure 4.9 the development of the intensity is not smooth, but shows a break from around 15:50 to 16:15 UT. The increase in intensity until the balloon reaches float altitude at 16:35 UT, is due to decreasing absorption and scattering of light, mainly of NO_2 and O_3 and of Rayleigh scattering. After reaching float altitude, observed air masses increase again as the Sun is setting, which leads to a decrease of intensity. For details of the flight profile see section 6.3.3.

The observed increasing intensity is due to a change in the position of the acquisition mirror of the sun-tracker (see Figure 4.1). Since the gondola is stabilised in azimuth direction, the acquisition mirror

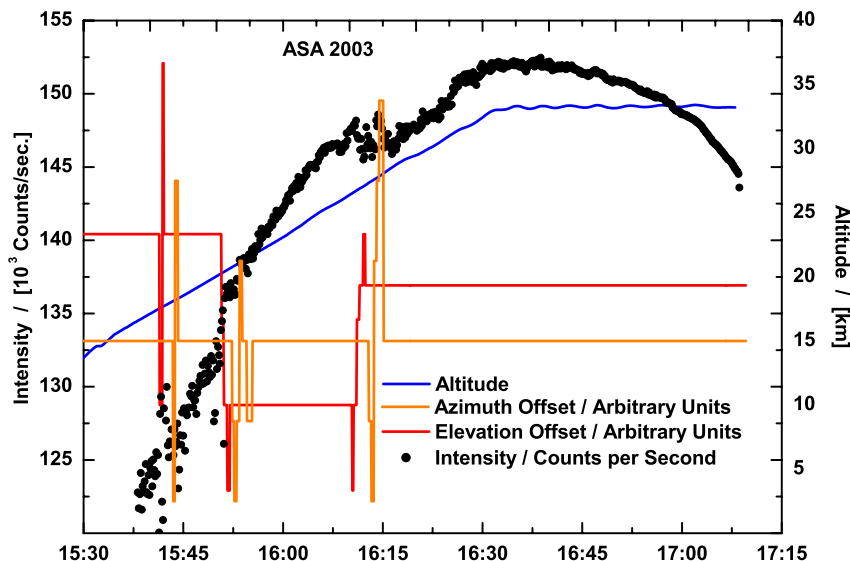


Figure 4.9: Dependence of the average intensity of 30 photodiodes of the UV spectrograph, on the sun-tracker position for the balloon flight at Aire sur l'Adour on 9 October 2003. The thick red and magenta line are the elevation and azimuth offset position, respectively. Black dots denote the averaged intensity in counts per second. A correlation between the sun-tracker position and the recorded intensity can be seen, especially between 15:50 UT and 16:15 UT. The increase in intensity until the balloon reaches float altitude at 16:35 UT, is due to decreasing absorption and scattering of light. As a result of the setting Sun, observed air masses increase again, leading to a decrease in intensity.

mainly compensates for changes in elevation angle in order to guarantee a perfect pointing towards the Sun. This behaviour is caused by an electronic offset applied to the pointing system of the sun-tracker acquisition mirror. Since the LPMA fourier transform spectrometer has a very narrow field of view, the signal can be optimised by observing a different section of the Sun. Therefore, the pointing can be changed from the nominal position, by applying a fixed angular offset to either the azimuth or elevation position of the acquisition mirror. This is done by adding an electronic offset to the signal send to the stepper motors which control the position. The conversion from electronic signal to actual angle in degrees is given by equations 4.1 and 4.2.

$$0.023 \cdot Offset_{Elevation} = \Delta(Elevation)^{\circ} \quad (4.1)$$

$$0.0047 \cdot Offset_{Azimuth} = \Delta(Azimuth)^{\circ} \quad (4.2)$$

To further investigate this effect, ground measurements were performed during the tropical campaign in Teresina, Brazil in November 2004. The DOAS instrument was fully integrated into the balloon gondola and direct sun light measurements were performed with the sun tracker during sunset. During measurements the offset position of the acquisition mirror was changed in positive and negative elevation and azimuth direction. Figure 4.10 shows the results of a typical BrO retrieval (see section 6.1) performed with these recorded spectra. The root mean square (RMS) of the residual is used as an indication of the quality of the DOAS fit. The overall increase of the RMS is due to the change in elevation by tracking the setting sun. The first few data points show regular retrieval in nominal mirror position (18:50 to 18:54 UT). Between 18:55 and 19:06 UT the elevation offset was changed gradually up to $\sim 0.7^{\circ}$ in both directions. Afterwards an azimuth scan was performed in the same way up to $\sim 0.33^{\circ}$ from 19:06 to 19:20 UT. It can clearly be seen that a change in elevation or azimuth offset position has a strong influence on

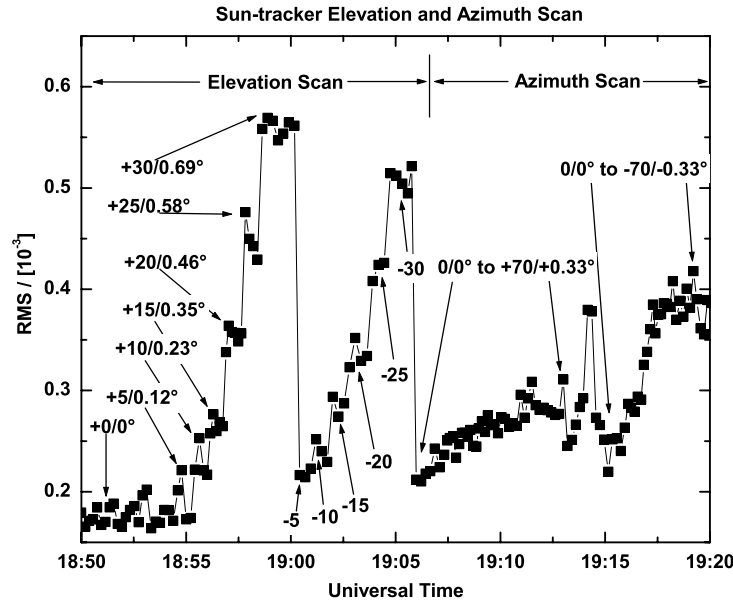


Figure 4.10: Root mean square (RMS) of the residual as an indicator for the quality of a BrO retrieval, from direct sun light ground measurements, for different elevation and azimuth offset positions of the sun-tracker acquisition mirror. Measurements were taken during the tropical balloon campaign at Teresina, Brasil. The overall increase of the RMS is due to the change in elevation by tracking the setting sun. Changes are given relative to zero position in arbitrary electronic offset units, as used by the LPMA team and in angular degrees. Sensitivity to elevation changes is more distinct than for azimuth.

the RMS and that changes in elevation seem to effect the residual more severely than changes in azimuth. Figure 4.11 shows the field of view of the UV telescope as measured in the laboratory. Although the

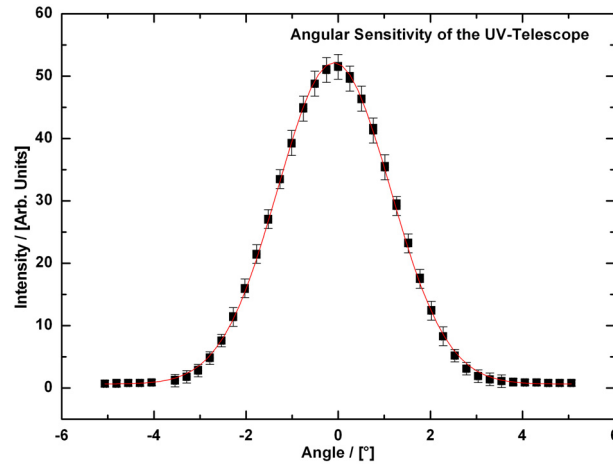


Figure 4.11: Field of view of the UV telescope.

FWHM with about 3° is larger than the flare angle of the Sun disk, which is 0.53° , the UV telescope shows a strong sensitivity to changes in the optical axis (see also [Lindner 2005]). Therefore, the behaviour of the intensity as observed in Figure 4.9 can easily be explained. Here, the elevation offset of the sun tracker

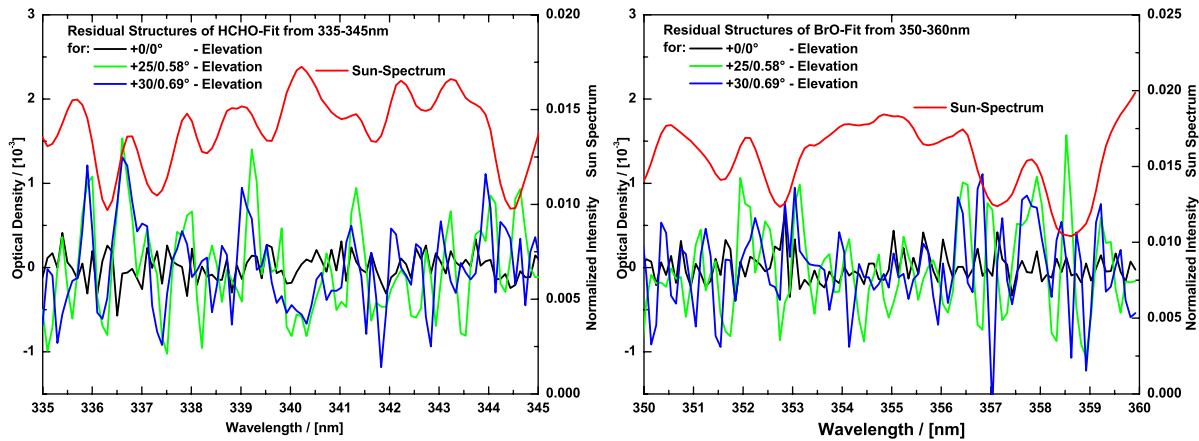


Figure 4.12: Optical densities of the residual structures for HCHO and BrO retrieval (left and right panel, respectively), from direct sunlight ground measurements, for different elevation offset positions of the sun-tracker acquisition mirror. Left panel shows the 335 – 345 nm wavelength range of the HCHO fit window (335 – 360 nm) and the right panel shows the 350 – 360 nm wavelength range of the BrO fit window (346 – 360 nm). Three cases are plotted for an elevation offset angle of 0° , 0.58° and 0.69° , in black, green and blue respectively. For comparison a normalised Sun spectrum is shown in red. It can be seen that with increasing elevation offset angle, the residual structures get significantly larger and correlate with the Fraunhofer absorption lines.

was changed to -0.23° between 15:50 UT and 16:15 UT. Such behaviour was not observed for the Vis spectrograph.

A change in intensity alone does not explain the degradation of the DOAS-fit as observed in Figure 4.10. This indicates that there is also a wavelength-dependent factor, which changes the imaging of the UV spectrograph. Figure 4.12 shows residual structures of HCHO and BrO retrieval for the ground measurements performed during the tropical campaign in Teresina, Brazil in November 2004. In the left panel a sub window of the HCHO fit window from 335 – 345 nm is plotted for 3 elevation offset angles: 0° , 0.58° and 0.69° . The right panel shows the respective residual structures in the 350 – 360 nm sub window of the BrO fit, for the same angles. For comparison, the reference Sun spectrum is also shown. It can be seen that as the elevation offset increases, the residual shows large systematic structures that correlate with the Fraunhofer lines.

A possible explanation is the wavelength-dependent reflectivity of the sun-tracker mirror, which varies with the angle of incidence. Corresponding measurements performed by the French SOPRA company can be found in Lindner [2005]. Polarisation effects might also be of importance. This behaviour and possible causes have to be investigated further during future campaigns.

Chapter 5

Laboratory Reference Spectra

In order to optimise the DOAS retrieval for the different species that can be measured with the balloon spectrograph, a series of reference spectra of the main absorbers was measured in the laboratory. These reference spectra proved to be particularly valuable for the DOAS-retrieval of weak absorbers (BrO and OCIO), which mainly depends on the accurate removal of strong absorbers like O₃ and NO₂ from the measured spectra. Although nowadays high resolution cross sections of all relevant absorbers exist and can be convolved to the resolution of the balloon spectrograph, it is difficult to determine the exact instrumental slit function W in the desired wavelength range. It is also virtually impossible to consider variation of W with wavelength. The recording of a spectrum I^* with a grating spectrograph is represented mathematically by a convolution of the continually and perfectly resolved incoming intensity spectrum $I(\lambda)$, with $W(\lambda)$ of the apparatus (for a detailed description see e.g. *Stutz* [1996]).

$$I^*(\lambda) = I(\lambda) \circ W = \int I(\lambda - \lambda') \cdot W(\lambda') d\lambda' \quad (5.1)$$

The instrumental slit function can be obtained experimentally by recording the spectrum of an atomic emission line. With a full width at half maximum (FWHM) of typically 10⁻³nm, the emission lines can be regarded as delta peaks compared to the typical resolution of 0.1 - 1 nm for a DOAS spectrograph. The emission spectra of mercury, cadmium and neon are commonly used. When performing the convolution with a computer, the highly-resolved cross section and the emission line spectrum have to be discretised, i.e. they have to be interpolated on a linear dispersion. The advantage of recording reference spectra with the spectrograph, which is used later for taking measurements, is that the described processes of interpolation and convolution are no longer necessary. Another advantage is that the wavelength-pixel mapping can be compared more easily for the measured and reference spectra.

An example of the effect of different instrument slit functions on the resulting reference spectrum is shown in Figure 5.1, where a high resolution O₃ (see *Voigt et al.* [2001]) cross section with a temperature of 246 K was convolved. The different instrument slit functions used in this study were all derived from the same cadmium emission line at 340.4 nm but unequally interpolated and corrected for baseline. The figure shows the results for the 346 - 360 nm BrO evaluation wavelength range. It can be seen that especially at the large absorption bands at ~ 347 nm and ~ 351.5 nm the results vary significantly. Since even small changes in the reference spectra of the strong absorbers have a significant influence on the evaluation and thus the detection limit of the weak absorbers, a new set of reference spectra was taken in the laboratory after minor changes in the optical setup of the spectrograph had been carried out (see section 4.1.2). A list of all the spectra recorded for different temperatures is given in table 5.1 and table 5.2, for the visible and the UV channels respectively. In addition, spectra of nitrous acid (HONO) were taken in the UV channel.

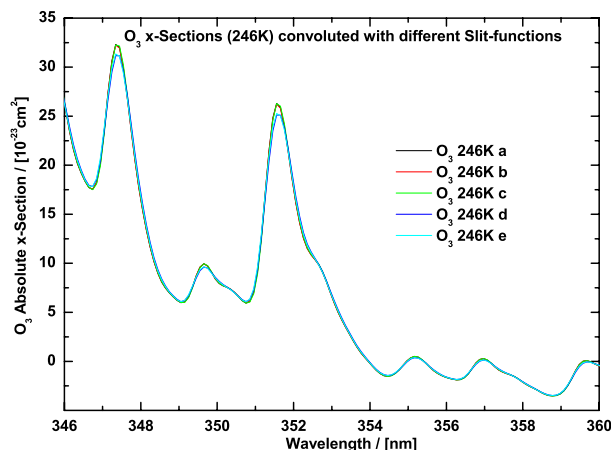


Figure 5.1: High resolution O_3 cross section at 246 K [Voigt et al. 2001] convolved with different instrument slit functions in the 346 nm - 360 nm BrO evaluation window. The case scenarios a to e correspond to instrument slit functions derived from the same 340.4 nm cadmium emission line.

5.1 Experimental Setup

The measurements were taken at the Institut für Umweltp Physik using a cylindrical flow tube 1.22 m in length and 3.4 cm in diameter (see Figure 5.2). A coolant is pumped through a second concentric glass cylinder, allowing the temperature inside the flow tube to be varied between 350 K and 195 K. A vacuum was created in a third concentric cylinder to thermally insulate the tube. For details regarding the experimental setup see the diploma theses of *Hönninger* [1999] and *von König* [1996].

An evacuated cell with Suprasil quartz glass windows is flanged to each end of the flow tube. Suprasil is well suited for this purpose because it has a transmission coefficient of more than 90 % for a path length of 2 mm between 200 nm and 1000 nm. An OSRAM XBO 450 W xenon lamp was used as a light source for the UV measurements as it has a high output in the 280 nm to 380 nm wavelength range and shows

Table 5.1: Overview of Laboratory reference spectra taken with the balloon spectrograph for the visible channel (400 to 650 nm) at 1.3 nm resolution. The label of the spectra follows the balloon group internal numbering

Vis T / K ± 3K	O_3 - Spectrum #	NO_2 - Spectrum #	OCIO - Spectrum #
280	V258765 – V258767		
273		V258327 – V258329	V258198 – V258199
258		V258359 – V258360	
253			V258176 – V258177
244	V258850 – V258851		
240		V258435 – V258436	
233	V259066 – V259069		V258160 – V258161
224			
221	V259109 – V259111	V258449 – V258479	
212			V258100 – V258101
207	V259194 – V259196	V258582 – V258587	
197			V258020 – V258021

Table 5.2: Overview of Laboratory reference spectra taken with the balloon spectrograph for the UV channel (317 to 418 nm) at 0.5 nm resolution. The label of the spectra follows the balloon group internal numbering

UV T / K	\pm 3K	O ₃ - Spectrum #	NO ₂ - Spectrum #	OCIO - Spectrum #	BrO - Spectrum #
293		V255306 – V255314			
273		V255334 – V255337	V254532 – V254534	V257438 – V257441	V256182 – V256183
253		V255373 – V255377	V254537 – V254539	V256945 – V256947	V256192 – V256194
240		V255396 – V255394			
233		V255401 – V255410	V254588 – V254590	V256962 – V256963	
224			V254606 – V254608	V257039 – V257048	
221		V255420 – V255422			V256203 – V256205
216			V254699 – V254702		
212		V255426 – V255442			
207		V255442 – V255443	V254745 – V254747	V257058 – V257063	
201			V254799 – V254800		
197		V255460 – V255461			V256217 – V256220

almost no spectral structures. For the measurements in the visible channel, an OSRAM XENOPHOT HLX 150 W lamp was used which has no significant spectral structures over the whole wavelength range. To create a parallel light beam through the flow tube, the spiral-wound filament was imaged by a lens onto a pin hole (1 mm in diameter) which served as a point light source and was placed in the focus of a second lens (see Figure 5.3). The diameter of the second lens determines the diameter of the light beam and in this case was 20 mm. The telescopes of the balloon spectrograph were mounted on the opposite side of the flow tube.

Before each series of measurements for a species at different temperatures, the flow tube was evacuated down to $\sim 10^{-3}$ hPa and then flushed with O₂ or O₃ to remove possible contamination and avoid surface reactions. It was especially important to pump water vapor out of the tube to avoid reactions with H₂O and condensation of H₂O on the tube and side windows. During the whole measurement process which lasted about 6 weeks, the balloon spectrograph was kept stable at 0° C by adding ice frequently into the surrounding water ice reservoir. This ensured that spectral shifts between the series of measurements of different species could be avoided. Before each measurement for a certain temperature an emission line

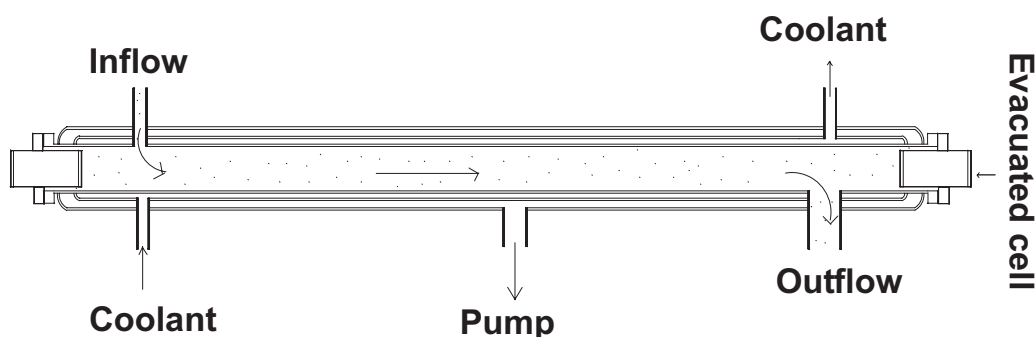


Figure 5.2: Sketch of the flow tube. The inner tube is used to synthesize and measure the trace gases. A coolant can flow through the middle tube to vary the temperature and a vacuum can be created in the outer tube to serve as thermal insulation. Adapted and modified from Hönninger [1999]

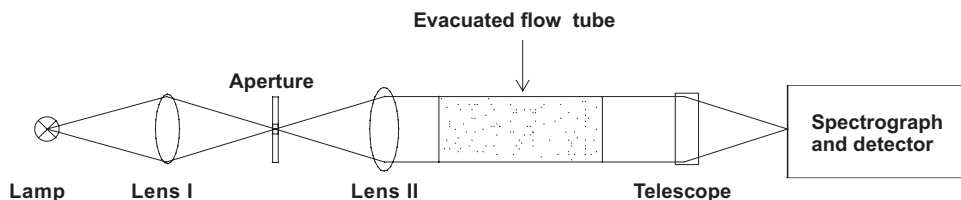


Figure 5.3: *Experimental setup for taking reference spectra: The spiral-wound filament of the lamp is imaged by lens I on a pin hole (1 mm in diameter). Lens II creates a parallel beam through the flow tube. The telescope collects the light and couples it into the spectrograph.*

spectrum of a mercury-cadmium lamp was taken. When comparing emission line spectra from different measurements or days, no spectral shifts could be observed, i.e. they were smaller than 0.03 pixels. Keeping the spectrograph stable in this way proved to be very useful for the further processing of the spectra, since no relative spectral shift between the absorbers, especially the main absorbers (O_3 and NO_2), had to be applied.

Before and after the flow tube was filled with a chemical species and an absorption spectrum at a certain temperature was taken, a reference spectrum of the lamp was recorded, without absorber in the light path. Furthermore, the temperature inside the tube was monitored to ensure it was stable. It was left to stabilize for 20 minutes before starting a measurement. The following section gives a short description of the measurement of each species and its particularities and shows examples of recorded reference spectra in the UV channel.

5.2 O_3 Reference

Ozone was produced using an ozoniser. Its mode of operation is based on the Siemens principle, in which molecular oxygen is dissociated by impacts with electrons. Molecular and atomic oxygen react to ozone. The ozoniser consists of two concentric glass tubes. A 0.5 mm strong copper foil is fixed around the outer tube and inside the inner tube, to serve as electrodes. O_2 flows through the gap between the tubes. The outer electrode is grounded and voltage pulses of 14 kV at a frequency of 50 Hz are connected to the inner one (for details see e.g. *Hönninger* [1999]). Since the discharge occurs at a fixed frequency, the amount of oxygen atoms and therefore ozone molecules produced per time unit is fixed. The maximum concentration that can be obtained under standard conditions is around 6%, since an excess of ozone will be destroyed inside the ozoniser itself. Such an ozone production rate can only be achieved at low flow rates.

Teflon tubes and stainless steel joints are used to connect the ozoniser with the flow tube to reduce ozone loss by surface reactions. A constant air flow rate of approximately 41/hour was chosen. Figure 5.4 shows recorded O_3 cross sections plotted after they were processed and fitted to a high resolution absorption cross section of *Voigt et al.* [2001] which was convolved to the resolution of the ballon spectrograph. The laboratory cross section at $T_{lab} = 197\text{ K}$, $T_{lab} = 207\text{ K}$ were fitted to a convolved cross section at $T_{lit} = 203\text{ K}$, the $T_{lab} = 223\text{ K}$ was fitted to $T_{lit} = 223\text{ K}$ and $T_{lab} = 240\text{ K}$ and $T_{lab} = 253\text{ K}$ were fitted to $T_{lit} = 246\text{ K}$ respectively. Therefore the cross sections scatter around three regimes corresponding to the three temperatures of the literature cross sections. Figure 5.4 shows a section of the Huggins band from 345 nm to 360 nm, which is also the BrO retrieval range. Around 346 nm, 350 nm and 357 nm the temperature dependence of the O_3 absorption cross section can clearly be observed.

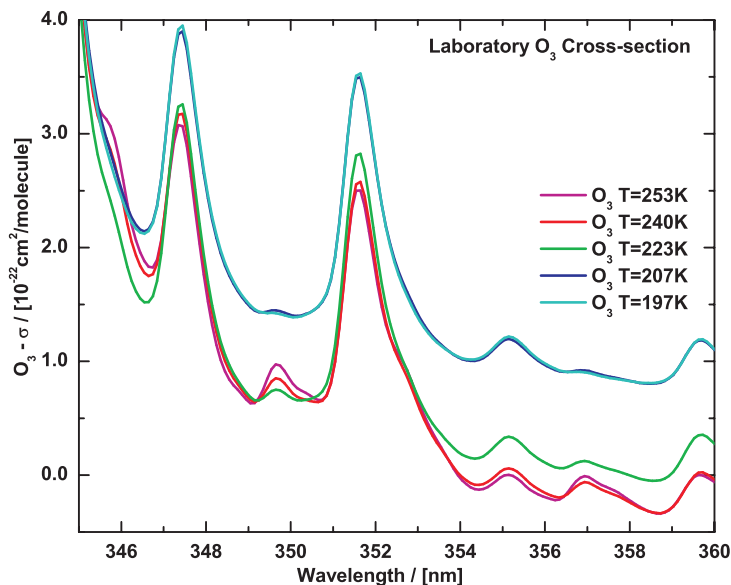


Figure 5.4: O_3 laboratory absorption cross section determined at the Institut für Umweltphysik. The 345 nm - 360 nm wavelength range is shown for five temperatures. The reference spectra were fitted (see text for details) to convolved high resolution absolute absorption cross section at $T = 203$ K, $T = 223$ K and $T = 246$ K Voigt et al. [2001]. Therefore, three different regimes [197 K/207 K, 223 K, 240 K/253 K] are displayed respectively and absolute values are shown. Strong temperature effects can clearly be observed at 346 nm, 350 nm and 357 nm.

5.3 BrO Reference

As BrO is a radical, it has to be produced permanently during observations. Here, BrO was produced by reacting bromine with ozone. At room temperature bromine (Br_2 , from FlukaChemie with a purity $\geq 99.5\%$) is a reddish brown fluid with a vapour pressure of 200 mbar. In order to obtain a constant

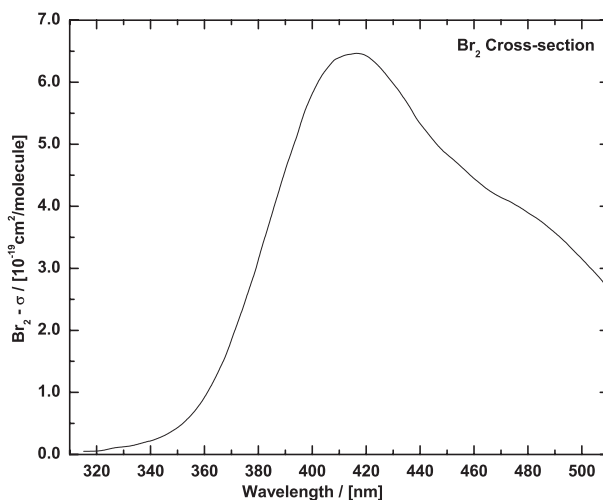
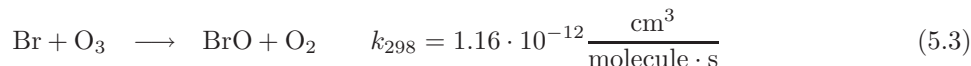


Figure 5.5: Br_2 literature absorption cross section as determined by Seery and Britton [1964]

and well defined amount of Br₂, an adjustable flow of oxygen was channeled over liquid bromine, which was kept constant at 0° C inside a washing flask. At 0° C, Br₂ has a vapour pressure of 82 mbar. The O₂ pressure was kept constant at ~1000 mbar. O₃ was produced by an ozoniser as described in section 5.2. By merging the separate flows of O₂/O₃ and O₂/Br₂ before the flow tube, a mixture of O₂, O₃ and Br₂ is formed. For a detailed description see *Hönninger* [1999]. BrO is mainly produced by the following reactions (see e.g. *Wahner et al.* [1988]) inside the flow tube:



As only low concentrations of BrO could be obtained, the recorded BrO cross sections are quite noisy.

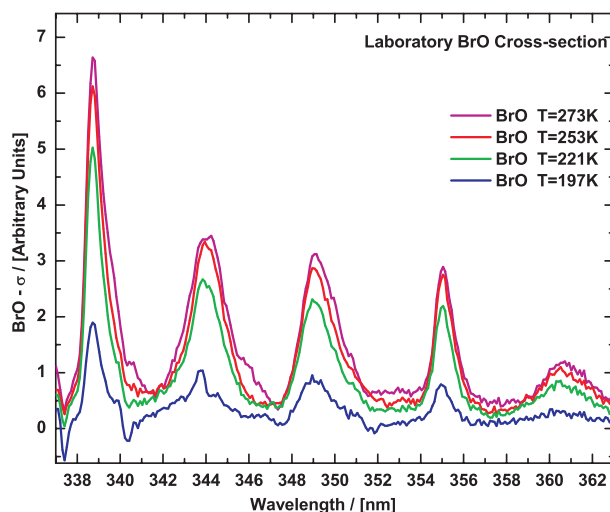
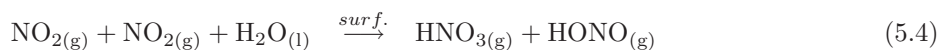


Figure 5.6: BrO laboratory absorption cross section determined at the Institut für Umweltp Physik. The 337 nm - 363 nm wavelength range is shown for four temperatures between 197 K and 273 K in arbitrary units.

Nevertheless they are very useful in determining the correct shift that has to be applied in the DOAS evaluation for example for the convolved *Wahner et al.* [1988] BrO absorption cross section. The recorded spectra have to be corrected for O₃ and Br₂ (see Figure 5.5) absorptions. The results are shown in Figure 5.6 in the 337 nm - 363 nm wavelength range for 4 different temperatures between 197 K and 273 K. Note that arbitrary units are plotted and that the decreasing cross section with decreasing temperature is due to the lower concentration inside the flow tube and not the temperature of the BrO absorption cross section.

5.4 NO₂ and HONO Reference

To record NO₂ reference spectra, the flow tube was first evacuated and then filled from a connected NO₂ gas cylinder. After filling the flow tube with NO₂ up to a pressure of ~ 25 mbar, the tube was sealed, allowing no flow. Unfortunately, nitrous acid (HONO) forms in the tube since the surface to volume ratio is rather high and remnants of water were still present in the inner tube. The cooling of the flow cell in particular favours the condensation of water on the inner tube's surface. HONO is formed by heterogeneous reactions on surfaces. For a detailed description of the HONO chemistry see e.g. *Stutz* [1996] and *Trick* [2000].



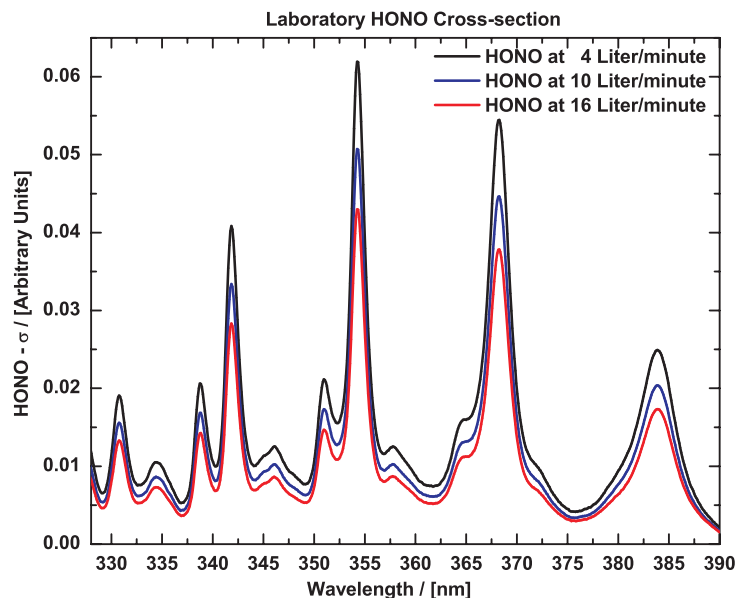


Figure 5.7: HONO laboratory absorption cross section determined at the Institut für Umweltphysik. The 328 nm - 390 nm wavelength range is shown for three different production rates (see text for details) in arbitrary units.

The subscripts l and g denote the liquid and gas phase respectively. Since the adsorption of NO₂ on H₂O is unlikely, the production of HONO is probably favoured by the reaction on aqueous atmospheric aerosols and surfaces as follows:



The nitrous acid subsequently escapes into the gas phase. At low temperatures the strongly temperature dependent equilibrium is shifted in favour of the dimer N₂O₄.

As both N₂O₄ and HONO have significant absorption structures in the UV range it was necessary to correct the measured UV absorption spectra of NO₂ for both. The N₂O₄ structure is broad banded (see Figure 5.8) and can be removed by fitting a polynomial to the NO₂ spectra. For HONO the spectra had to be recorded using the UV spectrograph in the laboratory. For this purpose, a glass apparatus developed to produce HONO at the *Forschungszentrum Karlsruhe* and based on the work of *Nash* [1976] was used. A 0.065 % sulphuric acid (H₂SO₄) and a 0.01 molar potassium nitrite dilution (KNO₂) was pumped at a constant rate via flexible tube pumps into a reaction tray. At equilibrium a pH-value of ~ 2 adjusts. Under these conditions the two dilutions form nitrous acid and potassium hydrogen sulphate.



The quantities of NO and NO₂ produced can be ignored. On the surface of the 800 mm high and 40 mm in diameter glass downpipe, the reactant dilutions further react with each other and are collected in a glass reaction tray. N₂ at a constant rate of about 10 l min⁻¹ was blown over the product dilution. Therefore, outflowing gas contained HONO concentrations well above the equilibrium concentration. The product dilution had to be pumped out of the tray with a second flexible tube pump to obtain stable conditions and a constant filling level. For a detailed description and a picture of the apparatus see *Trick* [2000]. Figure 5.7 shows the recorded HONO spectra in the 328 nm - 390 nm wavelength range for 3 different flow rates adjusted with the reactant pump. The NO₂ spectra corrected for N₂O₄ and HONO are shown

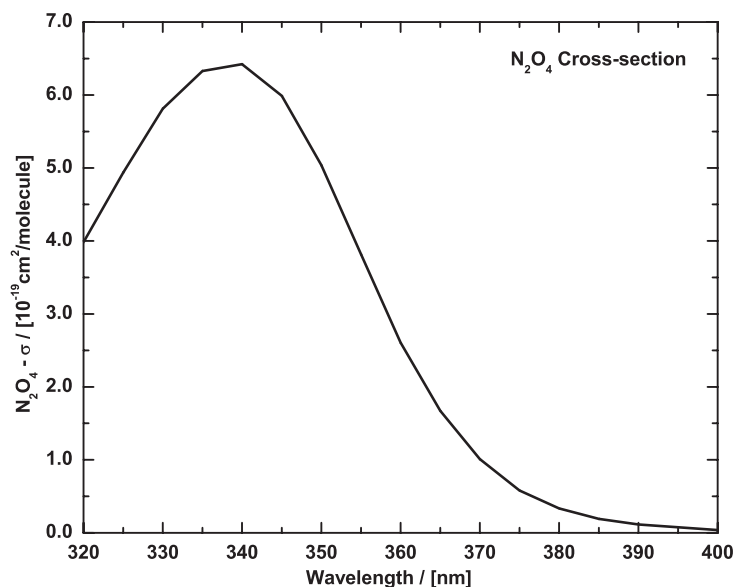


Figure 5.8: N_2O_4 literature absorption cross section as determined by Harwood and Jones [1994] for $T = 213$ K

in Figure 5.9 in the 360-390 nm wavelength range for temperatures of 207 K and 223 K. The reference spectra were fitted to a convolved high resolution absolute absorption cross section at $T = 223$ K published by Voigt *et al.* [2002]. Therefore absolute values are shown. Note that temperature effects can be seen throughout the range.

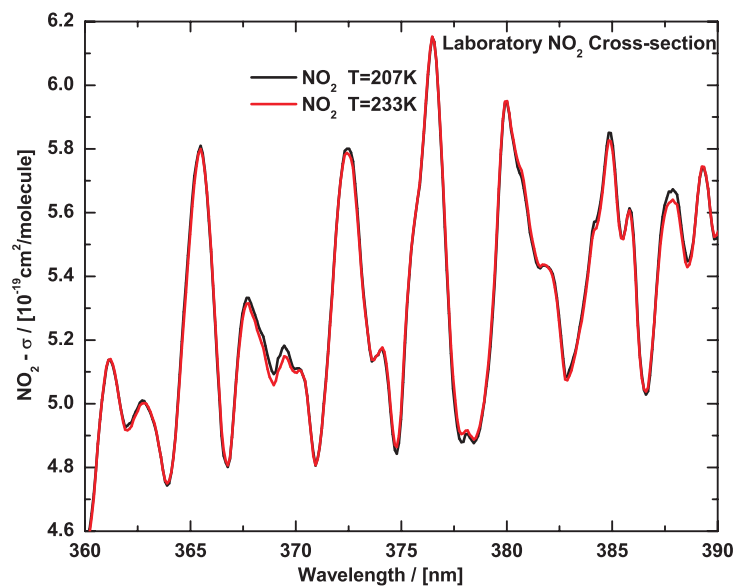


Figure 5.9: NO_2 laboratory absorption cross section determined at the Institut für Umweltphysik. The 360-390 nm wavelength range is shown for temperatures of 207 K and 223 K. The reference spectra were fitted (see text for details) to a convolved high resolution absolute absorption cross section at $T = 223$ K [Voigt *et al.* 2002]. Therefore absolute values are shown. Note that temperature effects can be seen.

5.5 OCLO Reference

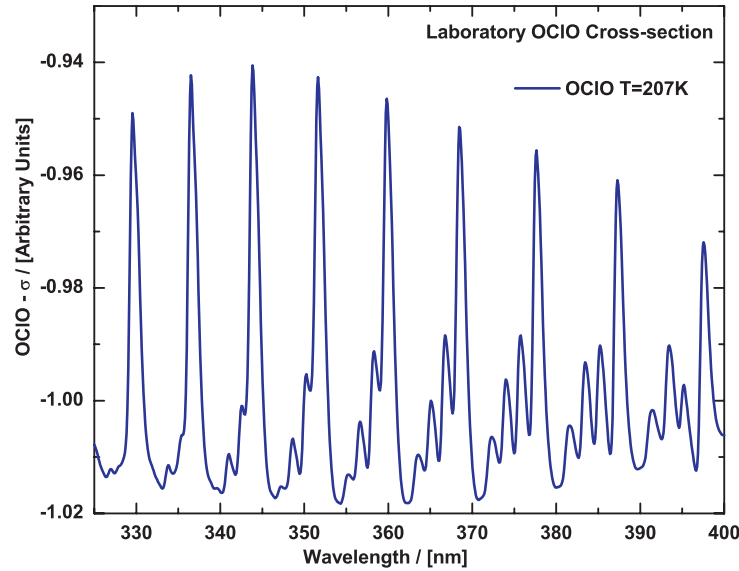


Figure 5.10: *OCLO laboratory absorption cross section determined at the Institut für Umweltphysik. The 325 to 400 nm wavelength range is shown for a temperature of $T = 207$ K in arbitrary units.*

OCLO is formed and can be observed inside the vortex during the polar winter. To produce OCLO in the laboratory a small vessel containing potassium chlorate (KClO_3) was placed inside a horizontally mounted glass cylinder. The cylinder was closed at both ends with shot plugs which have small openings in the middle to connect teflon tubes. Before the cylinder was sealed, highly concentrated sulphuric acid (H_2SO_4) was dripped on the potassium chlorate. O_2 was blown through the glass cylinder at a constant rate to transport the produced OCLO and the other reaction products into the flow cell. An example of a measured OCLO absorption cross section can be seen in Figure 5.10 for the 325 to 400 nm wavelength range at a temperature of $T = 207$ K.

5.6 Summary and Effect on Retrieval

The recording of reference spectra in the laboratory with the balloon spectrograph has proved to be important and useful. Especially for the retrieval of BrO and OCLO it is of utmost importance to remove the absorption features of the strong absorbers O_3 and NO_2 thoroughly. Keeping the spectrograph stable over the whole measurement period in the laboratory, and therefore avoiding spectral shifts, makes it possible to perform a relative wavelength alignment between the reference spectra independent of literature values. Thus, incorrect wavelength calibrations as for the *Wahner et al.* [1988] BrO cross section can be easily compensated. Several studies have been carried out on incorrect wavelength calibrations and the effect on the retrieval of for example BrO, see e.g. *Mohamed-Tahrin et al.* [2001] and *Aliwell et al.* [2002]. Figure 5.11 shows, using the example of the Kiruna 1997 balloon flight, how different NO_2 and O_3 reference spectra influence the BrO retrieval. In panels a) - h) the development of the slant column densities and important fit parameters for the BrO retrieval wavelength range (346-360 nm) are plotted. The standard retrieval with laboratory absorption cross sections of O_3 and NO_2 and convolved literature absorption cross sections of OCLO [*Kromminga et al.* 2003], O_4 [*Hermans* 2002] and BrO [*Wahner et al.* 1988] are plotted. The results of a retrieval are shown for comparison, where the O_3 and the NO_2 absorption cross sections were replaced with convolved literature absorption cross sections

of Voigt *et al.* [2001] for O_3 and Voigt *et al.* [2002] for NO_2 at almost the same temperatures. All other fit parameters were the same. Especially in the occultation part of the measurements, starting at 14:00 UT, there are significant discrepancies between the two retrievals and the root mean square of the residual (panel a) in the case of self-recorded references is much lower. In the development of the $OCIO$ -, O_4 -

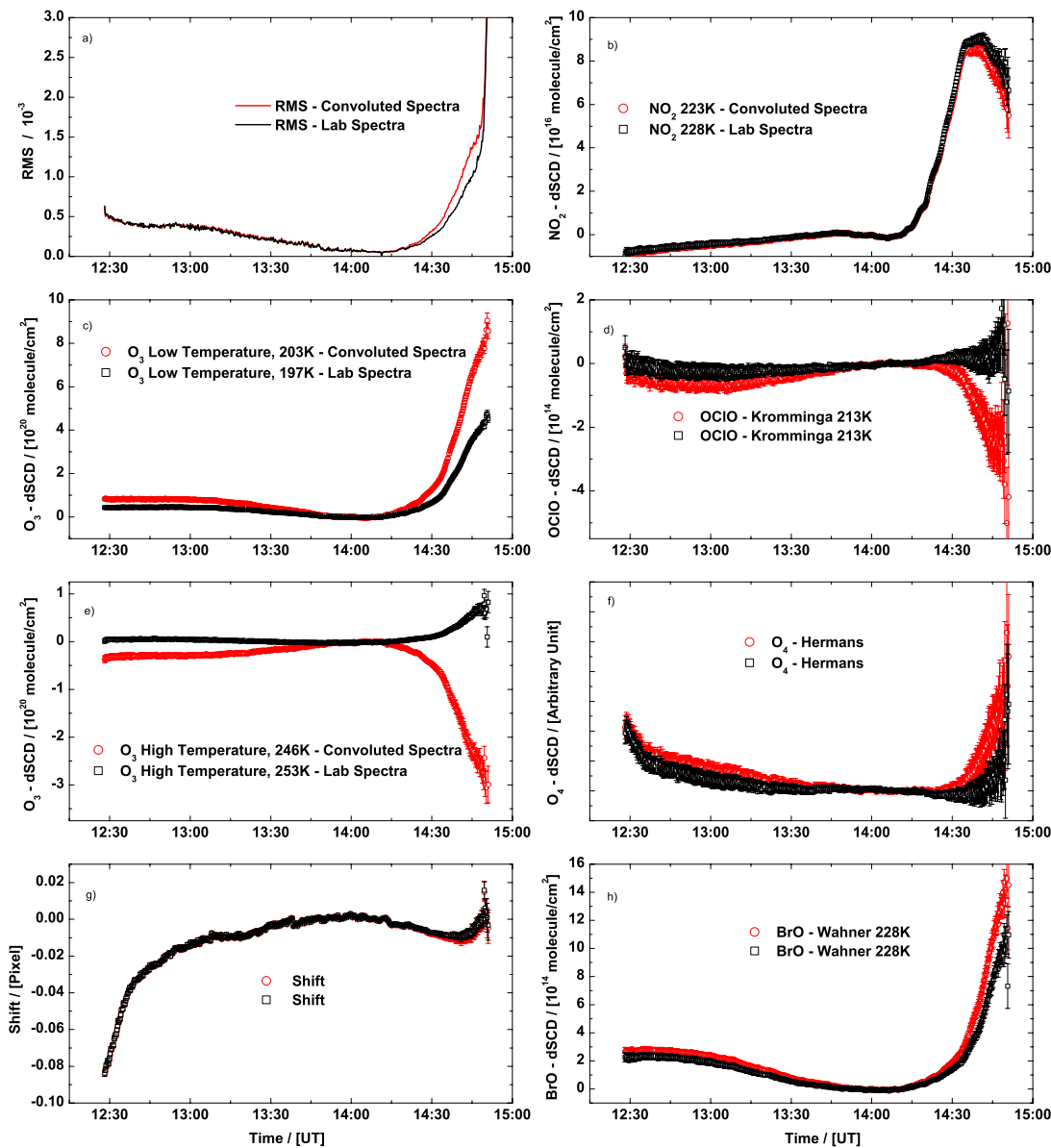


Figure 5.11: Development of the slant column densities and important fit parameters for the BrO retrieval in the 346 nm - 360 nm wavelength range for the 1997 Kiruna balloon flight. Two scenarios are compared: In black the standard retrieval with laboratory absorption cross sections of O_3 at $T = 197$ K and $T = 253$ K and NO_2 at $T = 228$ K and in red a retrieval where the O_3 and NO_2 cross sections were replaced by convoluted literature absorption cross sections at $T = 203$ K and $T = 246$ K [Voigt *et al.* 2001] and $T = 223$ K [Voigt *et al.* 2002], respectively.

and BrO - differential slant column densities (panels d), f) and h)) gives more realistic values in the case of self-recorded references. For the retrieval of weak absorbers, especially in the UV channel, the use of absorption cross sections recorded with the balloon spectrograph is recommended to accurately remove the spectral features of strong absorbers.

Chapter 6

Stratospheric BrO Profiling

BrO slant column densities (SCDs) are retrieved by applying the DOAS method to the spectra recorded during balloon flights, as described in detail in section 6.1. Stratospheric BrO profiles can be obtained from BrO - SCDs with different inversion methods, which are explained in section 6.2. So far, 13 DOAS balloon flights have been performed. The latest 5, which have not been discussed in detail in previous publications, are presented in section 6.3.

6.1 Experimental Details of the BrO Evaluation

The theoretical details of the DOAS evaluation are described in section 3.4. The actual input parameters and resulting errors are summarized here. All spectra measured during a balloon flight are corrected for offset and dark current prior to the DOAS evaluation. Offset and dark current spectra are either recorded on the ground before balloon launch or at balloon float after sunset. An important aspect of the DOAS evaluation is the exact wavelength calibration of both the measured spectra and the fitted trace gas cross-sections. In general, literature cross-sections measured with Fourier Transform (FT) spectrometers have a very precise wavelength calibration.

6.1.1 The DOAS BrO-Retrieval

The BrO evaluation was performed in the wavelength range 346 to 360 nm as recommended by *Aliwell et al.* [2002]. This wavelength range contains the UV vibration absorption bands (4–0 at 354.7 nm, and 5 – 0 at 348.8 nm) of the $A(^2\Pi) \leftarrow X(^2\Pi)$ electronic transition of BrO. This set of reference spectra used contained a NO₂ reference spectrum for T= 207 K, mainly for Arctic winter flights, or T= 233 K, where indicated. Two ozone spectra at T= 197 K and T= 253 K were fitted simultaneously to account for temperature effects (see e.g. section 3.4.1), where the two cross-sections are orthogonalized to each other. As described in chapter 5, the NO₂ and O₃ spectra were all recorded with the balloon spectrograph in the laboratory. The NO₂ spectra were calibrated, with respect to wavelength and the absolute value, with the NO₂ cross-sections given by *Voigt et al.* [2002]. For this purpose, the high resolution cross-section of *Voigt et al.* [2002] was convolved to our instrumental resolution using the standard convolution tool of *WinDOAS*. An I_0 -corrected convolution was also performed and the differences between both calculated. This I_0 -correction was then added to the measured and calibrated NO₂ reference spectra. The relative wavelength alignment and calibration of the O₃ reference spectra were performed correspondingly with the convolved high-resolution cross-section of *Voigt et al.* [2001].

For the O₄ absorptions, the measured laboratory spectrum of *Hermans* [2002] was used. The O₄ reference spectrum is not an absolute cross-section but a collision pair absorption cross-section. From measurements in the laboratory it is known that the absorption of O₄ per unit length can be written as $A = \alpha \times [O_2]^2$,

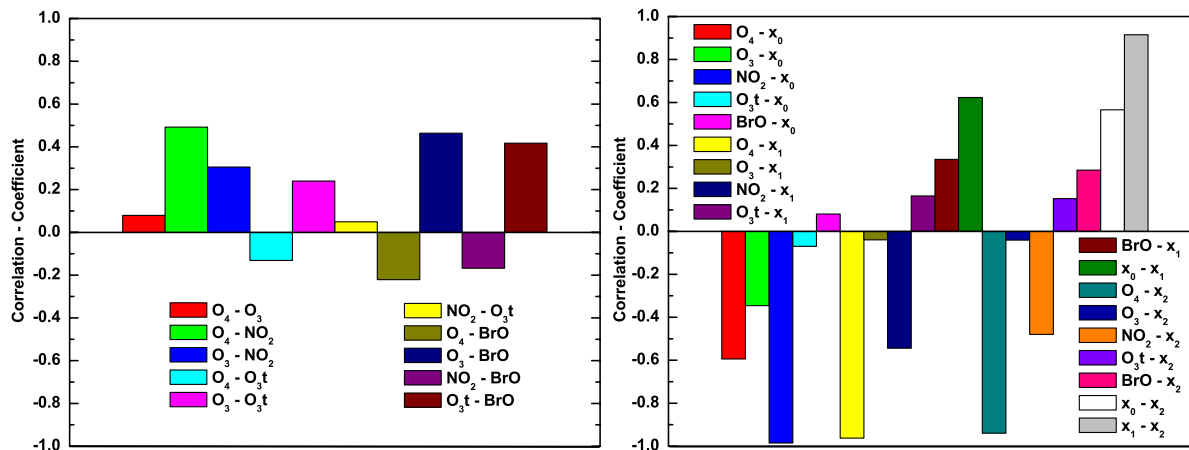


Figure 6.1: Correlation coefficients for the BrO evaluation for flights after Kiruna 2001 (see text for details). The coefficients of the polynomial are denoted by x_0 , x_1 and x_2 .

where α is the collision pair absorption cross-section in units of $\frac{cm^5}{molecule^2}$. The BrO reference used is the absolute cross-section measured by *Wahner et al.* [1988], measured with a spectral resolution of 0.4 nm. The wavelength calibration was taken from our own laboratory measurements. As observed in the laboratory spectra the Wahner spectrum has to be shifted by ~ 0.19 nm, which is in accordance with the measurements of *Wilmouth et al.* [1999], who deduced a shift for the 4-0 and 5-0 vibrational absorption bands of 0.07 – 0.19 nm relative to the Wahner BrO cross section.

A 2nd- degree polynomial was used to approximate the broad-band components. Additionally an intensity offset - an additive 1st- degree polynomial - was included in the fit to account for the spectrometer stray light. The spectrum that was recorded immediately after the balloon float altitude had been reached was used as the Fraunhofer reference spectrum.

The whole package of trace gases was then aligned to the Fraunhofer spectrum. For this purpose, a solar spectrum was evaluated with large NO_2 and O_3 absorptions using the set of reference spectra, which was allowed to be shifted. The coefficients obtained for the shift and squeeze were then used for the evaluation of the whole flight where only the measured spectra were allowed to shift and squeeze.

The correlation coefficients for this set of reference spectra in the 346 – 360 nm range, together with the polynomial are shown in Figure 6.1. A correlation coefficient in the range of ± 1 indicates a strong correlation, while a value around zero is an indication of a weak correlation. It can be seen that the small correlations between BrO and the polynomial and the other trace gas cross-sections are negligible. However, significant correlations exist between the polynomial and O_4 , which is very broad banded.

Figure 6.2 shows an example of a BrO DOAS evaluation for a spectrum that was recorded during balloon ascent at Kiruna on March 24, 2004. Details of the flight can be found in section 6.3.4. Differential optical densities for trace gas absorptions of O_3 (at 197 K), NO_2 (at 207 K), O_4 and BrO are shown. It can be seen that the differential optical density of BrO ($\sim 0.5 \cdot 10^{-3}$) is more than one order of magnitude smaller than the dominating absorption of O_3 . Although the remaining residual is close to the residual structure of $\sim 0.5 \cdot 10^{-4}$ expected in theory, it still shows some systematic structures. A comparison of spectra recorded in succession shows similar residuals. The cause is either unknown spectrometer structures or shortcomings in describing the atmospheric absorptions [*Ferlemann et al.* 2000]. These shortcomings can result from an incorrect characterisation of the known absorbers (e.g. temperature effects), or contributions of unknown absorbers, which might be present especially in the troposphere.

In order to avoid correlations, the degrees of freedom of a fit (number of fit parameters) has to be kept as low as possible. This is especially important for the degree of the polynomial and the intensity offset. Different wavelength ranges for the retrieval each have unique correlations.

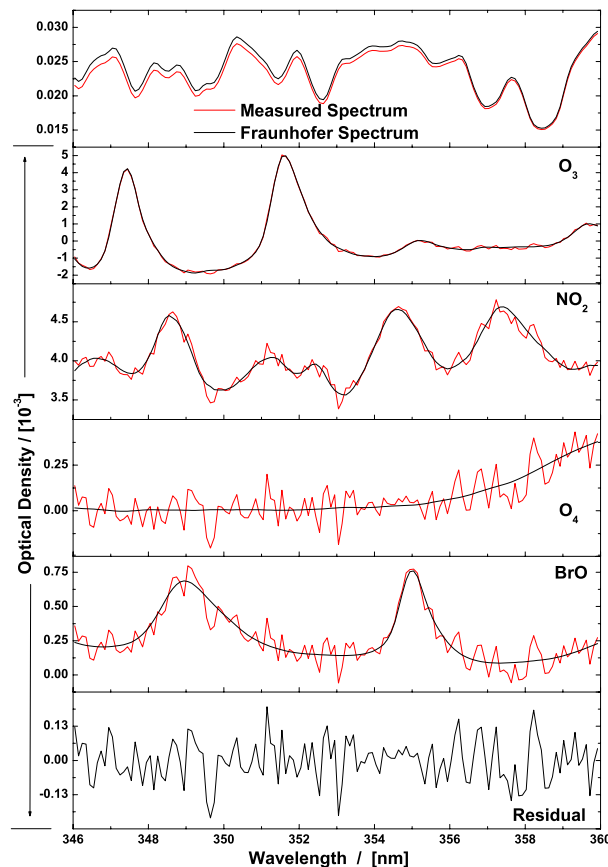


Figure 6.2: BrO DOAS evaluation in the 346 – 360 nm wavelength range for a spectrum recorded during the ascent of the balloon at Kiruna on March 24, 2004. The spectrum was recorded at 17.36 km at 79.70° SZA (15:07:53 UT) with 22 scans and a total exposure time of 5.5 seconds. The upper panel shows the Fraunhofer spectrum (black line) and the measured spectrum (red line). In the panels below the retrieved trace gas absorptions of O_3 (at 197 K), NO_2 (at 207 K), O_4 and BrO as described in the text are plotted. A 2^{nd} - degree polynomial was included in the fit. The black lines indicate the spectral absorptions and the red line represents the sum of the spectral absorption and the residual of the fit. The lowest panel displays the remaining residual structure.

The whole development of dSCDs (differential slant column densities) for all absorbers fitted in the BrO retrieval for the Kiruna 2004 balloon flight can be found in Figure 6.3, together with important fit parameters such as the root mean square (RMS) and shift and squeeze of the spectra. The fluctuating values between 15:30 and 15:45 UT are due to a sun tracker scan (see section 4.2.2) as performed by the LPMA team to improve the response of their instrument. The oscillations that can be seen between 16:15 and 17:00 UT, especially for the RMS, the O_4 SCD and the squeeze, are due to oscillations of the gondola and therefore oscillations of the sun tracker acquisition mirror.

Several wavelength ranges were considered for the detection of BrO. Extending the range to larger wavelengths ($\lambda > 360$ nm) is of no avail, since the strength of the absorption bands is about an order of magnitude smaller than for $\lambda < 360$ nm. At smaller wavelengths ($\lambda < 346$ nm) the O_3 absorption cross-section increases significantly and dominates the fit. Although the fit error can be reduced by including further BrO absorption bands at lower wavelengths, such a retrieval was not used for a number of reasons. The fit error decreases as more (4 or 5) BrO absorption bands are included in the fit and correlations

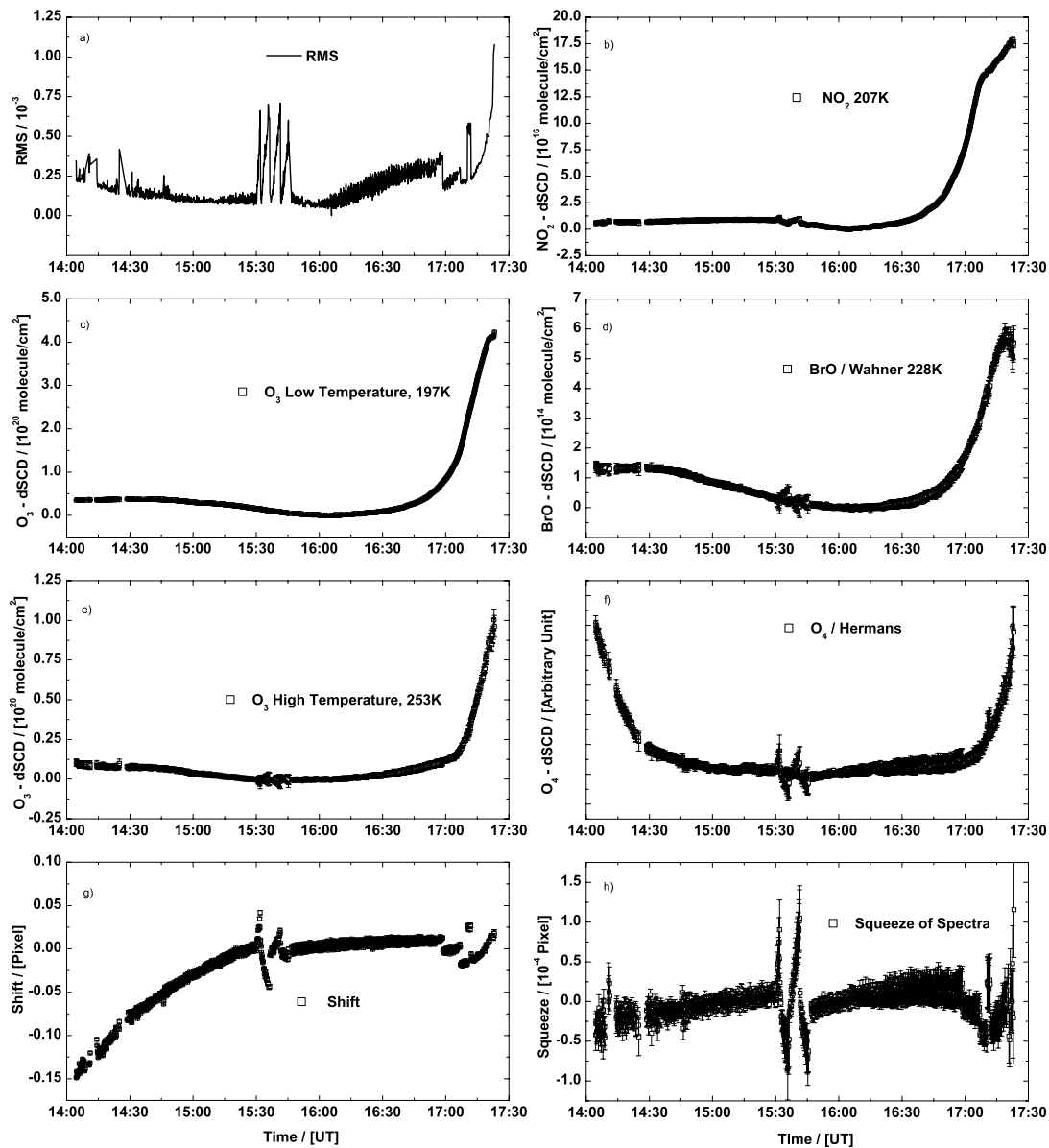


Figure 6.3: Development of the slant column densities and important fit parameters for the BrO retrieval in the 346 – 360 nm wavelength range for ascent and sunset measurements of the balloon flight at Kiruna on March 24, 2004. Laboratory absorption cross-sections of O_3 at $T = 197\text{ K}$ and $T = 253\text{ K}$ and NO_2 at $T = 207\text{ K}$ were used together with literature cross-sections of BrO and O_4 as described in the text (panels b - f)). In panel a) the resulting root mean square (RMS) of the fit is plotted. Panels g) and h) represent the shift and squeeze of the fitted spectra respectively.

are reduced. The problem is that the fit error does not account for systematic errors caused by larger systematic residual structures. By extending the wavelength range it becomes more difficult to remove the strong absorbers precisely, especially O_3 . This is complicated even further by the strongly increasing O_3 absorption below 346 nm. Inaccurate removal of O_3 causes large systematic residual structures, which

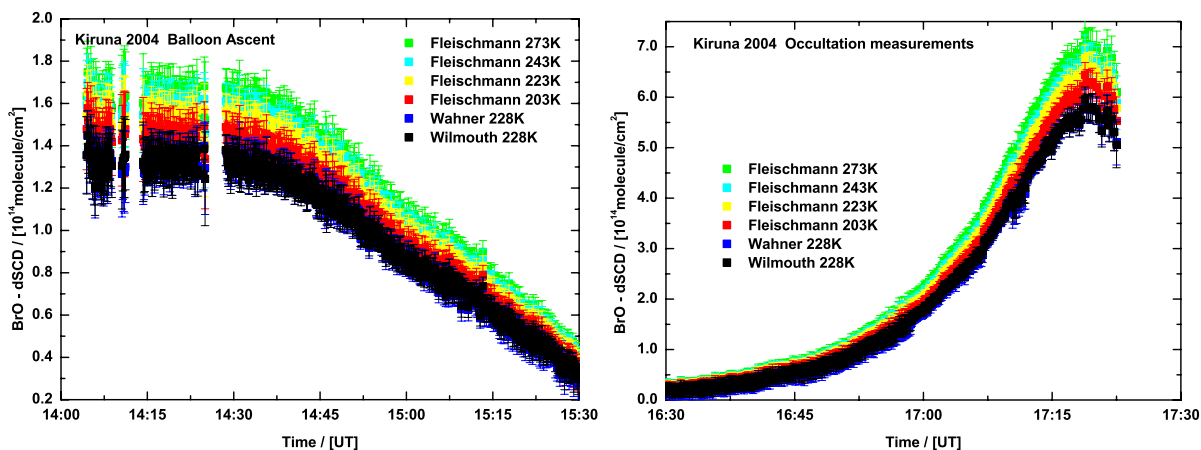


Figure 6.4: BrO SCD retrieval for different BrO cross-sections available in literature from Wahnert *et al.* [1988], Wilmouth *et al.* [1999] and Fleischmann *et al.* [2001] (see also section 3.3). Results are shown for balloon ascent (left panel) and solar occultation (right panel) for the Kiruna 2004 flight.

in turn cause unrealistic results for small underlying absorbers, like BrO. Therefore, a fit that departs from the ‘classical’ BrO retrieval range as recommended by Aliwell *et al.* [2002] was not performed. This also has the advantage of a better consistency and comparability with previous retrievals and BrO observations from other groups. Unfortunately it has become common practice by other groups to deviate from the recommendations obtained during a comparison campaign presented by Aliwell *et al.* [2002].

The BrO cross-section of Wahnert *et al.* [1988] was also chosen for better consistency and comparability between measurements and because it is used by models (e.g. SLIMCAT) to calculate the photolysis rate of BrO. A comparison was performed for BrO cross-sections of Wahnert *et al.* [1988], Wilmouth *et al.* [1999] and Fleischmann *et al.* [2001]. As expected from the values shown in Figure 3.3, the cross-sections of Wahnert *et al.* [1988] and Wilmouth *et al.* [1999] (in blue and black) give similar results and the Fleischmann *et al.* [2001] cross-section results in higher SCD values, although recorded at an even lower temperature of 203 K. The retrieval for the Fleischmann *et al.* [2001] cross-section shows a higher RMS (not shown here), but allows to investigate the BrO temperature dependence. By performing the fit with BrO cross-sections recorded at temperatures between 203 and 273 K, it can be seen in Figure 6.4 that the SCD values correspondingly increase by $\sim 13\%$ due to the decreasing differential cross-section.

Note that due to changes of the instrument before and after the campaign in August 2001 at Kiruna (see section 4.1.2), there are three different sets of reference spectra for the BrO fit. A new set of reference spectra was recorded in the laboratory and adjusted as described above before and after each change was made.

6.1.2 Langley Plot

The total atmospheric SCD is given by the sum of the SCD retrieved by the fit (the differential SCD) and the amount of absorber in the Fraunhofer reference spectrum, which is usually obtained by a *Langley plot*. Assuming a constant mixing ratio VMR above balloon float altitude, the SCDs obtained for balloon float for $\text{SZA} < 90^\circ$ can be written as

$$\text{SCD} = \text{AMF} \cdot \text{VCD}_{\text{Air}} \cdot \text{VMR} - \text{SCD}_{\text{Fraunh}} \quad (6.1)$$

with the air mass factor AMF, the vertical column density for air VCD_{Air} and the slant column density in the Fraunhofer spectrum $\text{SCD}_{\text{Fraunh}}$. The point of interception with the SCD-axis of a linear fit to

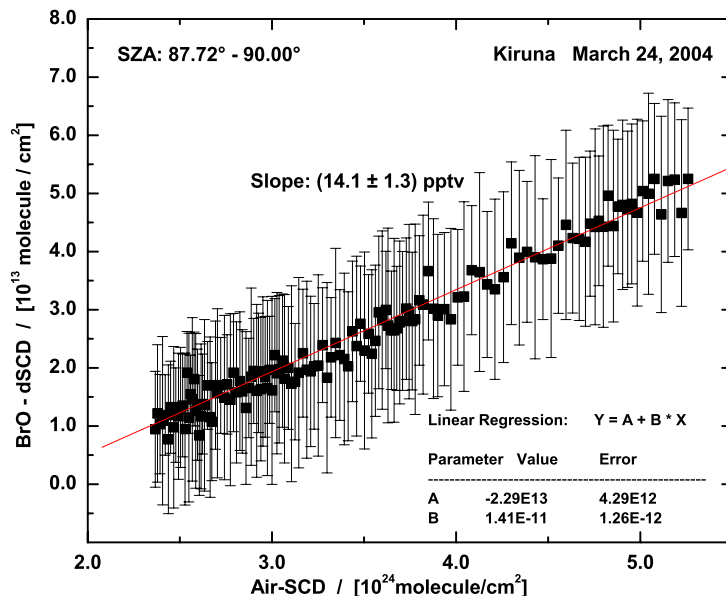


Figure 6.5: Langley plot of the measured BrO absorption as a function of the calculated total air mass. Observations are for a SZA range between $87.72^\circ - 90.00^\circ$ at balloon float (33.2 km) over Kiruna on March 24, 2004.

equation 6.1 yields the amount of the absorber in the Fraunhofer reference spectrum SCD_{Fraunh} . The assumption of a temporally-constant BrO mixing ratio is almost fulfilled since photochemical changes are small during the measurement period considered for the Langley plot. The slope of the linear regression line gives the VMR above float altitude for a constant mixing ratio, which for BrO is generally only the case between about 30 and 40 km.

A typical Langley plot for BrO is shown in Figure 6.5 for the balloon flight at Kiruna on March 24, 2004. Although balloon float altitude was already reached at 85.41° SZA, the first spectra are not used for the Langley plot since they are below the detection limit and scatter around zero. Therefore, these values would be weighted too strongly which leads to unrealistic result in the regression line. It was also considered to average over a whole number of *Brunt - Väisälä*¹ oscillations and not a fraction of them. In cases where not enough data points are available to perform a Langley plot, the amount of BrO absorption present in the Fraunhofer reference spectrum (Fraunhofer offset) can also be determined by comparing the development of the measured differential SCDs with modelled SCDs. The modelled SCDs are obtained by integrating a model concentration field along the line of sight of the balloon observations as shown in Figure 6.6 for the Kiruna 2004 flight (for model description see chapter 7). The offset between the development of the modelled versus the measured SCDs gives the amount of absorber present in the Fraunhofer reference spectrum. This method can be applied to BrO since the chemistry above balloon float altitude (30 – 40 km) is simple and can be modelled easily. It is dominated by the photolysis of BrO and the reaction of Br with O_3 .

Figure 6.7 shows such a case. Since the balloon reached float altitude at 89.1° SZA, not enough spectra are available to perform a proper Langley plot. A rudimentary estimate using a Langley plot gives a Fraunhofer offset of $(6.0 \pm 2.2) \times 10^{13}$ molecule/cm². By comparing the differential SCDs with modelled SCDs, a value of $(7.2 \pm 1.0) \times 10^{13}$ molecule/cm² can be deduced.

Another method exists to obtain the Fraunhofer offset. In principle, two different BrO evaluations can be performed. One evaluation with the Fraunhofer spectrum of the corresponding flight and one with the Fraunhofer spectrum of a previous flight for which the Fraunhofer offset is known. From the offset

¹The balloon at float altitude is oscillates around the equilibrium altitude.

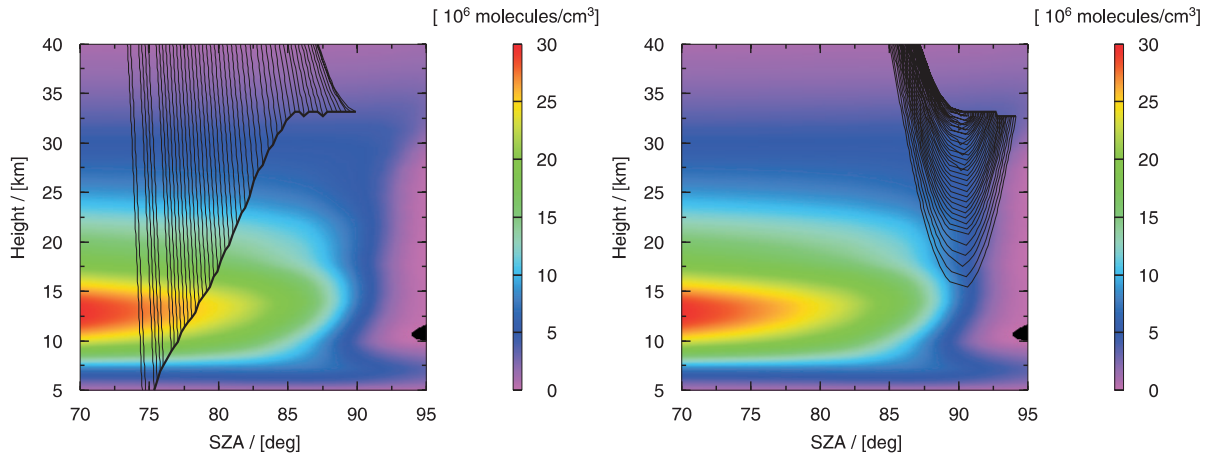


Figure 6.6: Colour-coded model concentration field of BrO at Kiruna (67°N , 22°E) on March 24, 2004, as a function of height and SZA. The thick black line and the thin black lines represent the trajectory of the balloon and the light rays from the sun that reach the balloon instrument, respectively. The left panel only shows measurements during the ascent and the float part of the balloon flight. The right panel shows occultation measurements.

of the linear correlation of the two evaluations and the known amount of BrO in the old Fraunhofer spectrum, the amount of BrO in the Fraunhofer spectrum of the actual flight itself can be obtained. This method has proven to be valuable [Bösch 2002] for the evaluation of NO_2 and O_3 with spectra recorded with the visible spectrograph. Unfortunately, due to the different optical setup and sampling of the UV spectrograph, this method cannot be applied in the UV. Performing the BrO evaluation using a

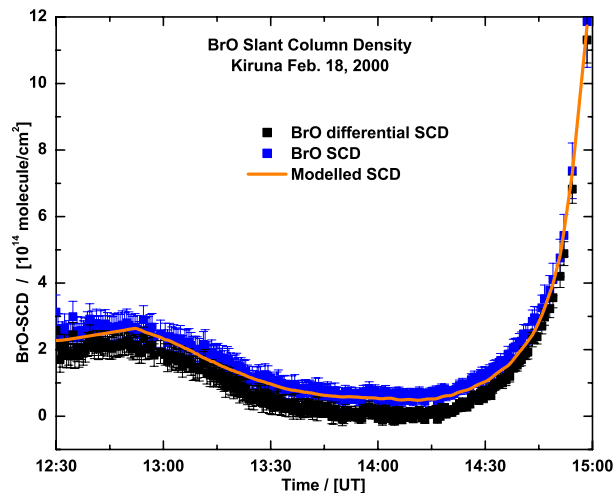


Figure 6.7: BrO SCD development for the balloon flight at Kiruna on February 18, 2000. The black squares are differential SCD values as obtained by the WinDOAS fit programme. Values corrected for Fraunhofer offset ($(7.2 \pm 1.0) \times 10^{13}$ molecule/cm²) are shown in blue. The orange line is the modelled development of SCDs by integrating a BrO concentration model field of the SLIMCAT CTM model, along the line of sight of the balloon measurement (see text for details).

Fraunhofer spectrum of a previous flight, results in up to 6 times higher residual structures, which has a negative effect on the retrieval of BrO.

6.1.3 BrO-Retrieval Error

Spectral retrieval errors can be caused by the wavelength misalignment of the individual reference spectra. A misalignment of the strong absorbers O₃ and NO₂ in particular can lead to systematically higher BrO SCDs. Assuming a misalignment of less than 0.01 nm for the reference spectra, this effect only causes a systematic error of $\pm 3\%$ [Ferlemann *et al.* 1998]. Furthermore, the residual of the fitting process shows systematic features. Since BrO optical densities are generally of the same order of magnitude (see e.g. Figure 6.2) as the residual structures, the fit is systematically influenced. Sensitivity tests showed that a $\pm 10\%$ error has to be assigned to account for the effect of the residual structures.

The error in determining the amount of BrO in the Fraunhofer reference spectrum (section 6.1.2) may arise from uncertainties in the air SCD, photochemical changes in the BrO SCD and from the spectral retrieval. In cases where the amount of BrO in the Fraunhofer reference spectrum is determined by comparison with modelled SCDs (Figure 6.7), the error is defined by the model. Ferlemann *et al.* [1998] deduced a error of $\pm 3.5 \times 10^{12}$ molecule/cm². Since there is high variability between individual flights and the quality of Langley plots, this study uses more conservative error estimates, which are mainly determined by the errors of the Langley plot and / or the comparison with modelled SCDs. A summary of all Fraunhofer BrO offsets and errors is given in Table 6.2

The error due to the absolute BrO cross-section as discussed in section 3.4.1 is $\pm 10\%$ and errors due to its temperature dependence in the temperature range encountered for stratospheric observations is estimated to $\pm 5\%$.

Since the error of the fitting routine is not purely statistical, it already includes systematic errors of the fit ($\sim 10\%$) accounting for the misalignment of the different absorption cross-sections and residual features. Whenever SCDs are shown in this study, the error due to the determination of the amount of BrO in the Fraunhofer reference spectrum and a $\pm 10\%$ cross-section error are added to the fitting error by applying Gaussian error propagation.

6.2 Profile Retrieval

In general, a balloon flight can be divided into three different phases. The balloon ascent, the balloon float and the solar occultation. During the balloon ascent (see Figure 6.8), the balloon climbs vertically through the trace gas profile at solar zenith angles (SZAs) less than 90°. Thus, the change of the measured slant column densities can be attributed directly to the concentration of the crossed height segment. During balloon float (until 90° SZA) and solar occultation (starting at 90° SZA), the balloon remains at a constant altitude. The first measurement taken after reaching maximum altitude (i.e. at the smallest SZA and therefore the smallest observed air mass) is commonly used as the Fraunhofer reference spectrum for the spectral fitting procedure. The float measurements can be used to estimate the amount of trace gas absorption contained in the Fraunhofer reference spectrum with a Langley plot (see section 6.1).

During solar occultation, the light path of the measurement crosses the trace gas profile twice for each layer above the tangent point but below float altitude. Above float altitude each layer is crossed once. At the tangent point the light path has the smallest distance to the Earth's surface. Due to the increasing SZA, the tangent height decreases and the light path crosses an increasing part of the trace gas profile. The concentrations of most chemical species are subject to substantial photochemical changes at twilight. Therefore, the obtained profiles also include photochemical changes, especially for solar occultation measurements. A variety of retrieval techniques is available to derive a trace gas profile from slant column density measurements [e.g. Rodgers 2000]. Profile retrieval techniques used in this study are described here.

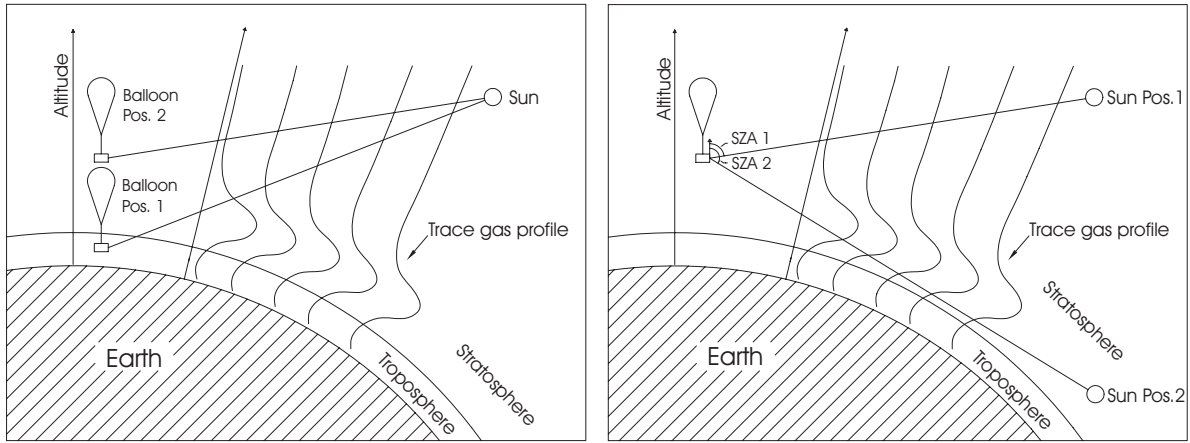


Figure 6.8: Observation geometry of the measurements for balloon ascent (left panel) and solar occultation (right panel).

6.2.1 Inversion Techniques

The atmosphere can be divided into N layers, each with constant pressure, temperature and trace gas concentration. The measured slant column density SCD can then be written as the sum of the contributions of the individual layers:

$$SCD = \sum_{i=1}^N SCD_i = \sum_{i=1}^N AMF_i \cdot VCD_i \quad (6.2)$$

The vertical column density VCD_i of layer i is given by the concentration multiplied by the height of the layer. The VCD_i is connected to the SCD_i of layer i by the (box-)air mass factor AMF_i , which is given for direct light measurements by the ratio of the length of the light path through the layer to the vertical height of the layer. For all M ascent or occultation measurements used for inferring a profile, a system of M linear equations is obtained:

$$\begin{bmatrix} SCD_1 \\ SCD_2 \\ \vdots \\ SCD_M \end{bmatrix} = \begin{bmatrix} AMF_{1,1} & AMF_{1,2} & \dots & AMF_{1,N} \\ AMF_{2,1} & AMF_{2,2} & \dots & AMF_{2,N} \\ \vdots & \vdots & \ddots & \vdots \\ AMF_{M,1} & AMF_{M,2} & \dots & AMF_{M,N} \end{bmatrix} \cdot \begin{bmatrix} VCD_1 \\ VCD_2 \\ \vdots \\ VCD_N \end{bmatrix} \quad (6.3)$$

With the air mass factor matrix \mathbf{AMF} , this can be written as

$$\overrightarrow{SCD} = \mathbf{AMF} \cdot \overrightarrow{VCD} \quad (6.4)$$

The \mathbf{AMF} matrix can be calculated using the raytracing and profile retrieval programme *DAMF* [Schulte 1996]. The raytracing is based on a Runge-Kutta algorithm [Press et al. 1986] considering the spherical geometry and the pressure and temperature-dependent refraction. To take into account the extent of the solar disk, with an apparent diameter of up to 5 km at the tangent point, the air mass factor matrix is calculated for 8 rays. Each ray represents one of 8 equally-sized areas, obtained by splitting the solar disk horizontally. The air mass factor matrix is then obtained by averaging the air mass factor matrices of the 8 individual rays.

The desired profile \overrightarrow{VCD} is obtained by inverting the air mass factor matrix:

$$\overrightarrow{VCD} = \mathbf{AMF}^{-1} \cdot \overrightarrow{SCD} \quad (6.5)$$

Since the number of measurements M is usually much larger than the number of height segments N , the inversion problem is overdetermined and cannot be solved by simple matrix inversion of \mathbf{AMF} . Two different inversion techniques were used - the *Singular Value Decomposition* (SVD) method [Press et al. 1986] and the *Maximum A Posteriori* (MAP) [Rodgers 2000] technique described below.

The SVD method uses a theorem of linear algebra, that a $M \times N$ matrix, where $M \geq N$, can be written as a product of an $M \times N$ orthogonal matrix \mathbf{U} , a $N \times N$ diagonal matrix \mathbf{W} and the transpose of an $N \times N$ orthogonal matrix \mathbf{V} . The diagonal elements of \mathbf{W} are called singular values. Thus the inverse matrix \mathbf{AMF}^{-1} can easily be calculated:

$$\mathbf{AMF}^{-1} = \mathbf{V} [\text{diag}(1/w_j)] \mathbf{U}^T \quad (6.6)$$

The SVD method then gives the best solution for \overrightarrow{VCD} in the least-squares sense. The SVD method offers no termination criteria to avoid over-interpretation of the measured $SCDs$. Stochastic variations of the $SCDs$ in the range of the measurement errors are interpreted as profile information. This becomes apparent by the occurrence of negative entries in the retrieved \overrightarrow{VCD} . The equations for very small singular values map large variations in \overrightarrow{VCD} on small variations in \overrightarrow{SCD} and, analogously, equations with very large $1/w_j$ map small variations in \overrightarrow{SCD} on large variations in \overrightarrow{VCD} . Consequently, for a measured \overrightarrow{SCD} with statistical errors it is necessary to set the smallest singular values and their reciprocals to zero. This is achieved by reducing the *condition number* of the air mass factor matrix, defined as the ratio of the largest to the smallest singular value. Setting small singular values to zero only slightly reduces the vertical resolution, while the propagation of the measurement errors is largely suppressed. The main source of error for the profile retrieval is caused by the errors of the $SCDs$. Gaussian error propagation yields:

$$\Delta VCD_i = \sqrt{\sum_j \left(\sum_i V_{ik} \frac{1}{w_k} U_{jk}^T \right)^2 (\Delta SCD_j)^2} \quad (6.7)$$

Since the measurements do not generally contain information about all height segments of \overrightarrow{VCD} , an initial estimation (*a priori* information) of the profile and its variability can be used for these altitudes in order to get reasonable results at the altitudes the measurements contain information about. According to chapter 4 of Rodgers [2000], a best estimate \overrightarrow{VCD} , which considers the measurements (\overrightarrow{SCD}), the *a priori* information ($\overrightarrow{VCD}_{apr}$) and their errors, can be found by applying the *Maximum A Posteriori* (MAP) method. It can be written as:

$$\overrightarrow{VCD} = (\mathbf{AMF}^T \mathbf{S}_{SCD} \mathbf{AMF} + \mathbf{S}_{apr}^{-1})^{-1} (\mathbf{AMF}^T \mathbf{S}_{SCD} \overrightarrow{SCD} + \mathbf{S}_{apr}^{-1} \overrightarrow{VCD}_{apr}) \quad (6.8)$$

\mathbf{S} is the covariance matrix defined as a diagonal matrix, which contains the squared errors, i.e. $\mathbf{S}_{SCD} = \text{diag}(\Delta SCD)^2$. $\overrightarrow{VCD}_{apr}$ and \mathbf{S}_{apr} are the *a priori* profile and its covariance, respectively, and can be estimated by other measurements or chemical model outputs. The covariance of \overrightarrow{VCD} is defined by

$$\hat{\mathbf{S}} = (\mathbf{AMF}^T \mathbf{S}_{SCD} \mathbf{AMF} + \mathbf{S}_{apr}^{-1})^{-1} \quad (6.9)$$

and its *averaging kernel* matrix $\hat{\mathbf{A}}$ is given by

$$\hat{\mathbf{A}} = (\mathbf{AMF}^T \mathbf{S}_{SCD} \mathbf{AMF} + \mathbf{S}_{apr}^{-1})^{-1} (\mathbf{AMF}^T \mathbf{S}_{SCD} \mathbf{AMF}) \quad (6.10)$$

The averaging kernels contain information about the quality and information content of the retrieved profile. Each row of the averaging kernel matrix states where the information of the corresponding VCD_i is obtained from. The ideal case would be a delta function for each row, i.e. a value of 1 at column i and 0 everywhere else, i.e. the averaging kernel matrix would be the unit matrix. The area of the averaging kernel, i.e. the sum of its elements, should also be close to 1 for altitude levels where the retrieval is accurate. Generally, the area can be seen as a rough measure of the fraction of the corresponding profile point that comes from the measurements, rather than from the *a priori*. The half-width of the

averaging kernel gives information about the altitude resolution and the trace of the averaging kernel matrix corresponds to the number of independent values in the retrieved profile. Therefore the altitude grid can be chosen accordingly. The retrieval method works in a way that it decides whether to take the information from the measurements or from the a priori profile based on the errors given in the respective covariance matrices. The covariance of the measurement is determined by the measurement errors but the error of the a priori can be taken, for example, from climatology. If the a priori covariance is unknown, it has to be chosen carefully. If it is too small the retrieval could disregard information from the measurements. If it is too large or if the a priori profile is selected incorrectly, the algorithm can produce fake features in the retrieved profile that might be mistaken as profile information.

6.2.2 Errors of the Raytracing

Important input parameters required for the raytracing calculations are the atmospheric temperature and pressure profile, the balloon altitude and the solar zenith angle. The uncertainties of these quantities were not considered in the calculation of the profile errors. Temperature and pressure are measured up to balloon float altitude with a Vaisala radio sonde and additional pressure and temperature sensors. The inaccuracy of these measurements is 0.5 hPa for the pressure (between 1060 and 3 hPa) and 0.2 K for the temperature. Above balloon float altitude, the US Standard Atmosphere [NOAA-S/T76-1562 1976], which is only an approximation of the real atmospheric conditions, is scaled to the conditions of the balloon flight. The altitude of the balloon is measured with an onboard GPS which has a vertical uncertainty of ~ 20 m. The solar zenith angle is calculated for a given time and location by a routine provided by ARI (Astronomisches Recheninstitut, University of Heidelberg). For a comparison of different routines see e.g. Bösch [2002].

6.2.3 BrO Profile Inversion and Errors

Figure 6.9 compares the three different profile inversion techniques for BrO measurements taken during the ascent of the balloon flight at Kiruna in 2003. Details of the flight are discussed in section 6.3.2. The upper left panel of Figure 6.9 shows the a priori profile with 100% relative error that is used for the MAP inversion. Resulting averaging kernels are plotted in the upper right panel. Concentration and volume mixing ratio BrO profiles, retrieved with the MAP and the SVD inversion techniques, are shown in the lower panels on a 2 km grid. The three inversion techniques compare well in the 10 to 28 km range. Ascent measurements for this flight started at ~ 4 km and stopped at 30 km, but have two measurement gaps between 4.5 to 6 km and 10.5 to 11.5 km. Therefore, values below 8 km and above 28 km do not contain enough information to be reliable. This is demonstrated clearly by the averaging kernels. They show values of 1 as expected for altitudes where the retrieval is accurate and no a priori information is used in the MAP inversion. Below 8 km and above 30 km they deviate from 1, meaning that a priori information is necessary. Here a value of 1 for the area of the averaging kernels is important - the maximum can deviate from 1, which indicates a smaller height resolution. Furthermore, the half-width, which gives information about the altitude resolution, is clearly higher. Starting at 28 km, the different inversion techniques begin to deviate. For the SVD inversion, oscillations can occur at the boundaries of measurements (here at 32 km) which also influence values retrieved below (28 and 30 km). Thus, it can be useful to use an a priori profile in order to suppress oscillations. The a priori profile and its covariance have to be chosen wisely though as otherwise fake values or even stronger oscillations can result.

The altitude grid is chosen according to results obtained from performing a MAP inversion, i.e. by consulting the half-width of the averaging kernels and the trace of the averaging kernel matrix.

To better estimate the propagation of systematic errors in the BrO profile, inversion is performed twice. First, the BrO SCDs with the errors as given by the DOAS evaluation are inverted. A second inversion is performed with a systematic error added to the BrO-SCDs. This error is estimated by Gaussian error propagation from a 10 % SCD error, which accounts for temperature effects and uncertainties of the BrO cross-section, and the error of the BrO amount in the Fraunhofer reference spectrum (see also section 6.1.3). The difference between these two profiles is added directly to the error bars obtained in the first

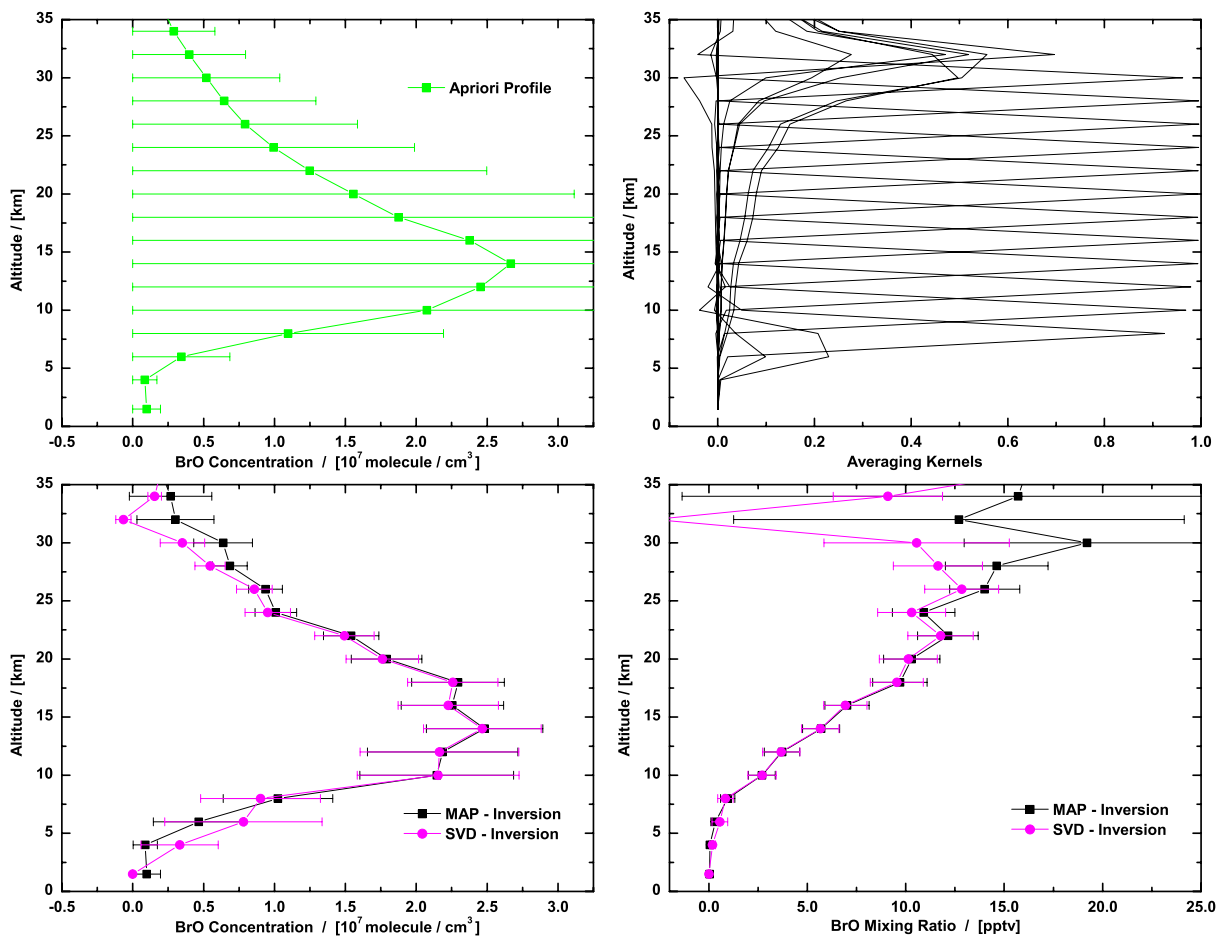


Figure 6.9: Example of a BrO profile inversion for Kiruna 2003 ascent measurements. The upper panels show the a priori profile and averaging kernels of the MAP inversion. Lower panels compare BrO concentration and volume mixing ratio profiles for the MAP and the SVD inversion techniques (see text for details).

inversion. Therefore a conservative estimate of profile errors is obtained.

Radicals like BrO or NO₂ are subject to a distinct diurnal variation. In Figure 6.10 BrO and NO₂ profiles are plotted for solar zenith angles between 60° and 100°. It can be seen that photochemical change is significant especially during solar occultation measurements. The measurement geometry is more complicated for occultation measurements, and SCD values are a composite of the photochemical situation at different SZAs, as indicated in Figure 6.6. Thus, profile inversion is expected to be ambiguous. This is clearest for NO₂. When measurements are taken between 90° and ~95° at balloon float altitude (33 km for Kiruna 2003), the tangent point of the observations decreases from 33 km down to ~8 km. When performing a profile inversion, the strong increase of NO₂ absorption due to photochemical change (at higher altitudes) is misinterpreted as higher profile concentrations at low altitudes (for decreasing tangent point). Therefore occultation profiles are not accurate.

Model output can be used to scale a profile to the photochemical conditions of a specific SZA by introducing the photochemical weighting factor κ_{kj} as described by Butz *et al.* [2005]. When model output is given along the SZA timeline, κ_{kj} can be defined as $\kappa_{kj} = \frac{a_{kj}}{b_j}$. b_j is the modelled trace gas concentration at altitude j and at the SZA that the measurement is scaled to. a_{kj} is the corresponding modelled concentration at altitude j and SZA k of the observation. As shown in Figure 6.6, each point on the line-

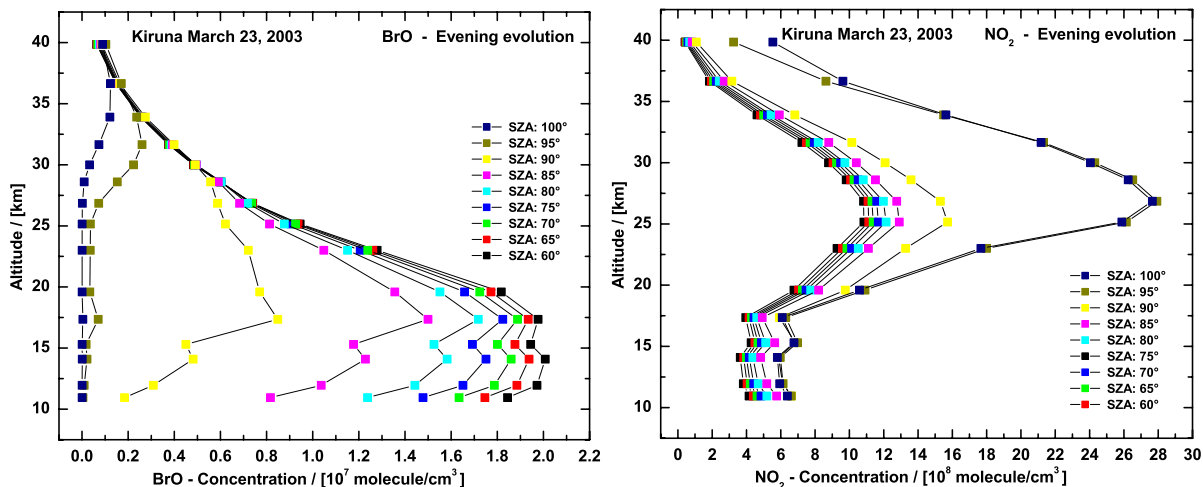


Figure 6.10: Example of a BrO and NO_2 photochemical evening evolution for $SZA = (60^\circ - 100^\circ)$. Model simulations were performed as described in chapter 7 for the balloon flight on March 23, 2003 at Kiruna.

of-sight of the observation can be identified by its altitude and its local SZA. Since a layered atmosphere is assumed in the profile retrieval, the slant path through layer j at local SZA k is multiplied by κ_{kj} . Thus a photochemically-corrected weighting function matrix (here the **AMF** matrix) is obtained. Performing the profile inversion with the photochemically-corrected weighting function matrix, scales the balloon profile to the photochemical conditions of the desired SZA. Such a scaling is only possible if the relative diurnal variation is modelled correctly.

Figure 6.11 corresponds to Figure 6.9 but shows occultation measurements. The same a priori profile was used since changes are minimal above float altitude, where almost no information is contained in the spectra. UV measurements were possible down to $SZA = 94.25^\circ$, corresponding to a tangent height of ~ 14 km. The averaging kernels clearly indicate that no information is taken from the a priori profile from float altitude (33 km) down to 16 km. In the lower panels the ascent profile is shown for comparison. MAP inversion without scaling results in the profile shown as blue triangles. It matches (and is therefore covered) perfectly with a profile inversion scaled to 90° SZA (red circles). This behaviour can be explained by the fact that a) the photochemical change is minimal around float altitude b) the main atmospheric absorption takes place around the tangent point, i.e. at 90° SZA and c) lower concentrations at higher SZAs are compensated by higher concentrations at lower SZA along the line-of-sight, i.e. concentrations decrease linearly with increasing SZA for altitudes below float. Such behaviour is not observed for NO_2 occultation profiles for reasons discussed above. NO_2 occultation profiles show too high values at lower altitudes. The lower panels of Figure 6.11 also show profiles scaled to 92° and 94° SZA, together with modelled profiles for comparison. Error bars shown here are not realistic and only reflect fitting errors. The model underpredicts BrO abundances since NO_2 is overpredicted and consequently too much inorganic bromine exists as $BrONO_2$. Therefore, a second model profile for 90° SZA is shown as green line, which is obtained by scaling NO_2 in the model to simultaneous measurements of the DOAS instrument. SVD inversion for occultation profiles basically results in the same values as obtained by the MAP inversion. Inversion of occultation measurements from other balloon flights and comparison with BrO profiles scaled to 90° SZA resulted in the same conclusion, that BrO occultation profiles without scaling already reflect conditions at 90° SZA.

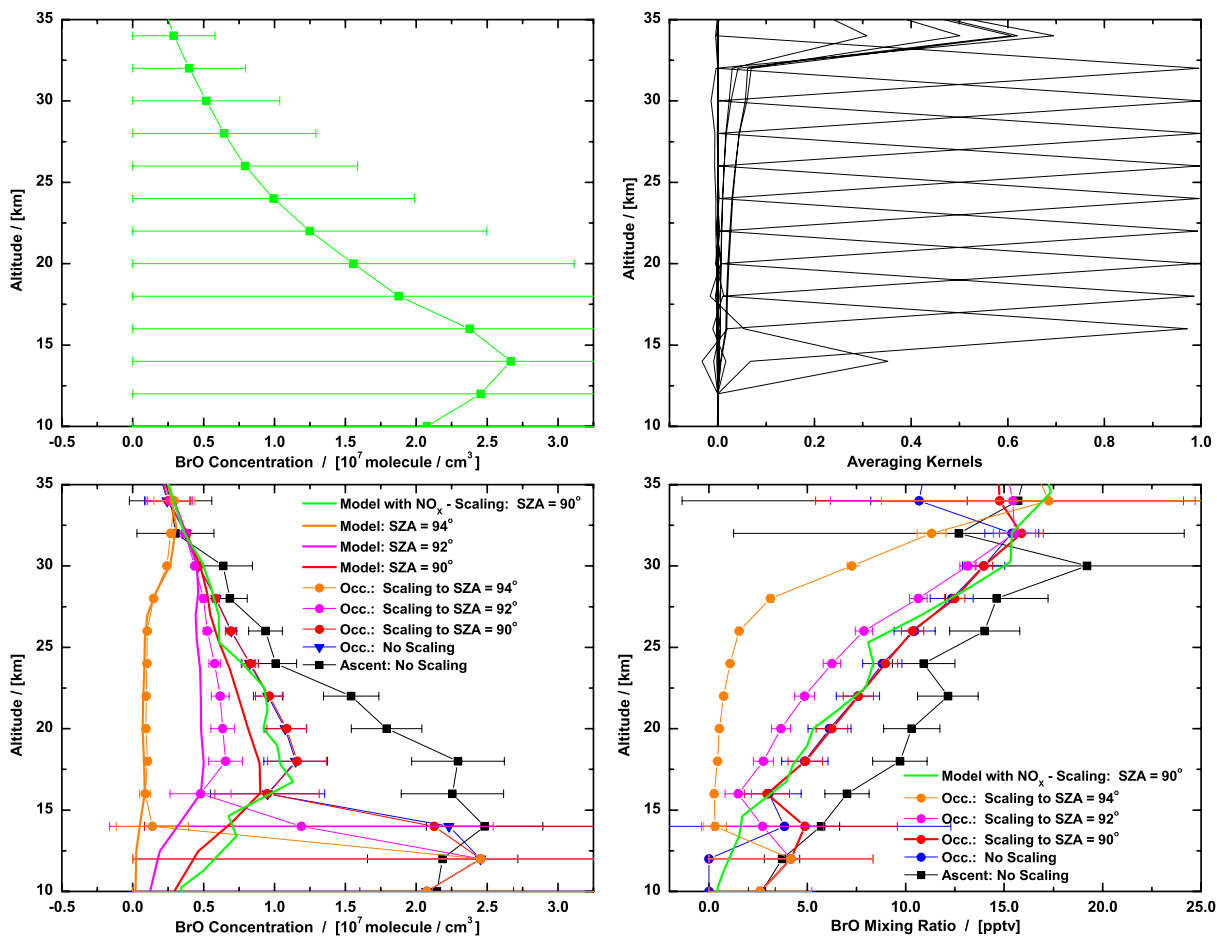


Figure 6.11: Example of a BrO profile inversion for Kiruna 2003 occultation measurements and the scaling of profiles. The upper panels show the a priori profile and averaging kernels of the MAP inversion. Lower panels compare MAP-inverted BrO concentration and volume mixing ratio profiles for different scalings to 90°, 92° and 94° SZA. SLIMCAT model results (concentrations only) and the BrO ascent profile are shown for comparison. Model calculations for constraint NO_2 are shown for 90°. For details see legend and text.

6.3 Discussion of LPMA/DOAS Balloon Flights

Thirteen successful DOAS flights have been performed since 1996, the last five within the framework of this thesis. Although BrO and OCIO UV measurements were reanalysed for flights presented by *Ferlemann* [1998], *Harder* [1999] and *Fitzenberger* [2000], balloon flights performed before 2001 are not discussed here. Necessary information is given whenever results are discussed in the following chapters. For details, see for example the studies of *Bösch* [2002] and *Fitzenberger* [2000]. Tables 6.1 and 6.2 summarise important parameters of measurement conditions and DOAS evaluation in the UV. In Table 6.1 the time, SZA and altitude range during which UV observations were possible, are given for ascent / descent and accordingly for sunset / sunrise. The Fraunhofer reference spectrum, the dark current and the offset spectrum used for the DOAS evaluation and the Fraunhofer offset obtained for each flight are summarised in Table 6.2. The following sections describe DOAS balloon flights performed since 2001 and show results of the DOAS evaluation.

Table 6.1: Summary of all 13 successful flights performed to the end of 2005. The altitude range, corresponding universal time and SZA range, for which useful measurements were performed during the ascent/descent (middle column) and sunset/sunrise part (right column) of the balloon flight. The altitude range for occultation measurements is not indicated since the balloon stays at almost constant height during this time. Descent measurements were only performed during the Gap campaigns in 1997 and 1999. For Kiruna 1998 and 2001, measurements were performed at sunset and on the following morning at sunrise.

Date	Location	Ascent or Descent		Sunset and / or Sunrise	
Place	Geophysical Condition	Time/UT	SZA - Range	Time/UT	SZA - Range
		Altitude/km			
Nov. 23, 1996	42.6° N, 5.7°W	14:55:48 - 16:20:32	74.85° - 86.61°	16:38:12 - 16:53:33	90.00° - 92.97°
Leon	mid-lat. fall	5.06 - 31.05			
Feb. 14, 1997	67.9° N, 21.1°E	12:28:11 - 14:11:15	82.60° - 89.51°	14:15:45 - 14:51:58	90.00° - 94.32°
Kiruna	high lat. winter	6.10 - 30.17			
June 20, 1997	44.0° N, 6.1°E	04:37:40 07:42:32	85.88° - 56.29°	03:30:41 - 04:07:12	94.74° - 90.00°
Gap	mid-lat. summer	39.71 - 31.34			
March 19, 1998	42.6° N, 5.7°W	16:00:58 - 18:06:47	63.81° - 86.82°	18:21:47 - 18:42:47	90.00° - 94.40°
Leon	mid-lat. spring	1.01 - 38.00			
Aug.19/20, 1998	67.9° N, 21.1°E	16:03:07 - 18:21:00	74.85° - 87.35°	18:54:27 - 19:59:54	90.00° - 94.46°
Kiruna	high lat. summer	6.55 - 38.98		01:24:53 - 02:29:21	94.28° - 90.00°
Feb. 10, 1999	67.9° N, 21.1°E	11:49:08 - 13:06:11	83.01° - 86.05°	13:59:42 - 14:47:49	90.00° - 94.21°
Kiruna	high lat. winter	5.11 - 28.67			
June 25, 1999	44.0° N, 6.1°E	04:32:08 08:10:30	86.64° - 50.45°	03:36:45 - 04:08:22	94.34° - 90.00°
Gap	mid-lat. summer	38.98 - 20.65			
Feb. 18, 2000	67.9° N, 21.1°E	12:28:45 - 14:15:32	81.64° - 89.02°	14:24:54 - 14:58:29	90.00° - 93.60°
Kiruna	high lat. winter	4.81 - 30.05			
Aug.20/21, 2001	67.9° N, 21.1°E	15:55:26 - 18:17:50	74.89° - 87.99°	18:42:18 - 19:51:34	90.00° - 95.05°
Kiruna	high lat. summer	5.91 - 38.86		01:19:56 - 02:29:36	95.03° - 90.00°
March 23, 2003	67.9° N, 21.1°E	14:38:30 - 16:28:57	77.90° - 88.78°	16:41:02 - 17:23:50	90.00° - 94.25°
Kiruna	high lat. winter	3.72 - 30.08			
Oct. 9, 2003	43.7° N, 0.3°W	15:32:13 - 16:34:25	70.92° - 81.50°		
Aire sur l'Adour	mid-lat. fall	14.60 - 33.24			
March 24, 2004	67.9° N, 21.1°E	14:04:28 - 16:05:44	74.58° - 85.41°	16:45:40 - 17:23:09	90.00° - 94.41°
Kiruna	high lat. winter	3.16 - 33.08			
June 17, 2005	5.1° S, 42.9°W	18:32:17 20:16:58	60.66° - 83.22°	20:47:06 - 21:05:46	90.00° - 94.20°
Teresina	tropics	1.85 - 33.32			

Table 6.2: Summary of important parameters used for the evaluation of the 13 successful flights performed to the end of 2005. The label of the Fraunhofer reference spectrum, the recording time and corresponding SZA are given for each flight. Furthermore, the retrieved BrO Fraunhofer offset (see section 6.1.2) and the dark current and offset spectrum used for the individual retrievals are listed. The label of the spectra follows the internal numbering of the balloon group. For some flights, successively-recorded spectra were added up and used as the Fraunhofer reference spectrum. Two individual reference spectra were used for the sunset and sunrise retrieval of the Kiruna 1998 flight. For Kiruna 2004 different reference spectra were used for the ascent and occultation retrieval.

Date Place	Reference Spectrum	Time/UT SZA	Fraunhofer Offset / $10^{13} \frac{\text{molecule}}{\text{cm}^2}$	Dark Current Spectrum	Offset Spectrum
Nov. 23, 1996 Leon	V126900	16:20:32 86.61°	3.1 ± 0.4	V126078	V126080
Feb. 14, 1997 Kiruna	V129958	14:11:15 89.51°	8.6 ± 1.5	V131064	V131062
June 20, 1997 Gap	V132825	04:37:32 85.88°	1.4 ± 0.3	V126080	V126078
March 19, 1998 Leon	V150895 - V150899	18:06:47 - 18:07:36 86.82° - 86.99°	1.1 ± 0.5	V135262	V135261
Aug.19/20, 1998 Kiruna	V182047 - V182059 V183382 - V183386	18:20:07 - 18:22:06 87.26° - 87.43° 02:53:31 - 02:54:01 88.19° - 88.15°	1.5 ± 1.0 5.2 ± 2.0	V182608	V182606
Feb. 10, 1999 Kiruna	V196488	13:06:11 86.05°	5.0 ± 0.9	V195189	V195183
June 25, 1999 Gap	V203344 - V203352	04:31:25 - 04:32:08 86.74° - 86.64°	1.5 ± 0.5	V202479	V202477
Feb. 18, 2000 Kiruna	V212529	14:15:32 89.02°	7.2 ± 1.0	V208553	V208551
Aug.20/21, 2001 Kiruna	V246621 - V246633	17:58:01 - 17:59:01 86.26° - 86.35°	2.0 ± 1.5	V228407	V228411
March 23, 2003 Kiruna	V285251 - V285259	16:28:57 - 16:29:28 88.78° - 88.84°	7.2 ± 1.0	V275946	V275940
Oct. 9, 2003 Aire sur l'Adour	V328293	16:34:25 81.50°	1.6 ± 0.5	V309030	V309038
March 24, 2004 Kiruna	V346185 V346191	16:05:44 85.41° 16:06:11 85.46°	2.3 ± 0.4	V335638	V335630
June 17, 2005 Teresina	V428291	20:16:58 83.22°	2.0 ± 0.5	V429080	V429074

6.3.1 LPMA / DOAS Flight on August 21/22, 2001 at Kiruna

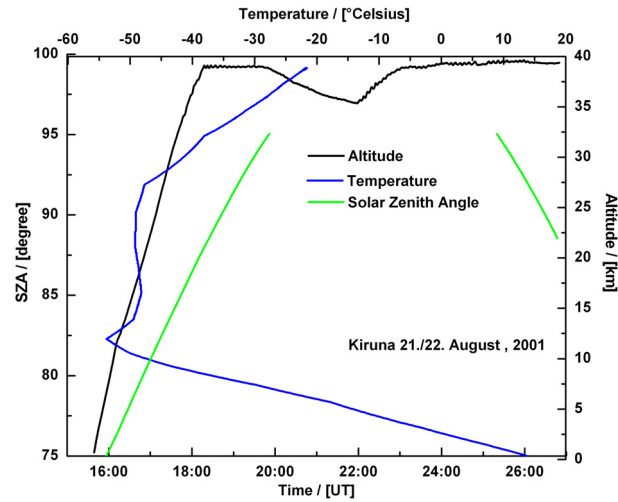


Figure 6.12: Balloon trajectory, temperature and the SZA for UV observations at the position of the balloon for the flight on August 21 and 22, 2001 at Kiruna. Times greater than 24 UT indicate morning measurements on August 22.

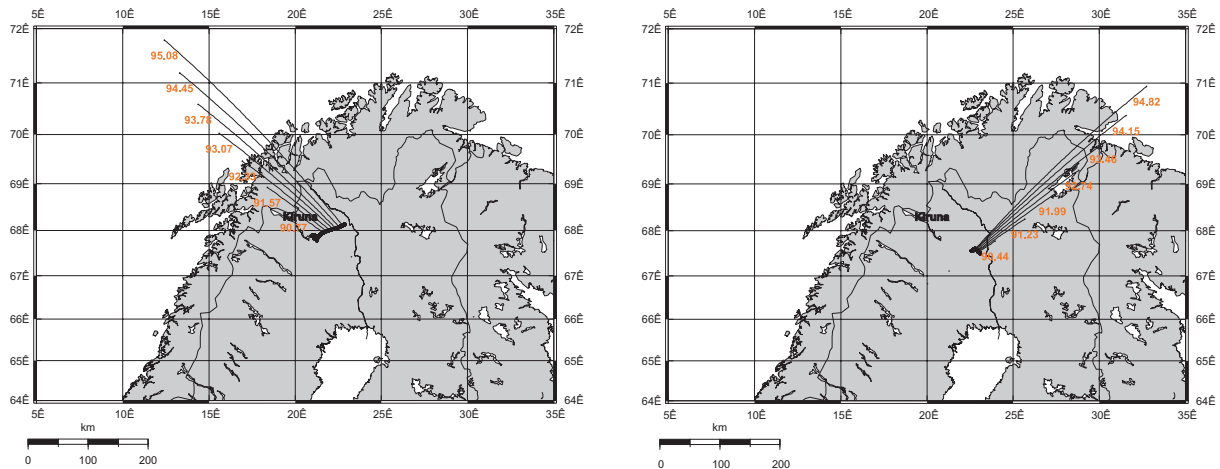


Figure 6.13: Balloon trajectory and observation geometry of the flight at Kiruna on August 21/22, 2001. The trajectory is the thick black line. The thin black lines denote the light rays for occultation measurements, which end at the tangent point. Numbers at the lines indicate the SZA. The left panel shows the observation geometry for ascent and sunset measurements on August 21. The right panel shows corresponding sunrise measurements on August 22.

A strong and steady zonal wind surrounds the pole in summer and suppresses the mixing of polar with mid-latitude air (see chapter 2). At the end of the summer (mid to end August), the circulation pattern breaks down and after a short transition period, the formation of the winter circulation begins. The flight was launched on August 21, 2001 at 15:39 UT and $SZA = 73.3^\circ$ at Kiruna ($67.9^\circ N$, $21.0^\circ E$). The break down of the strong summer circulation had already occurred and the dominant stratospheric

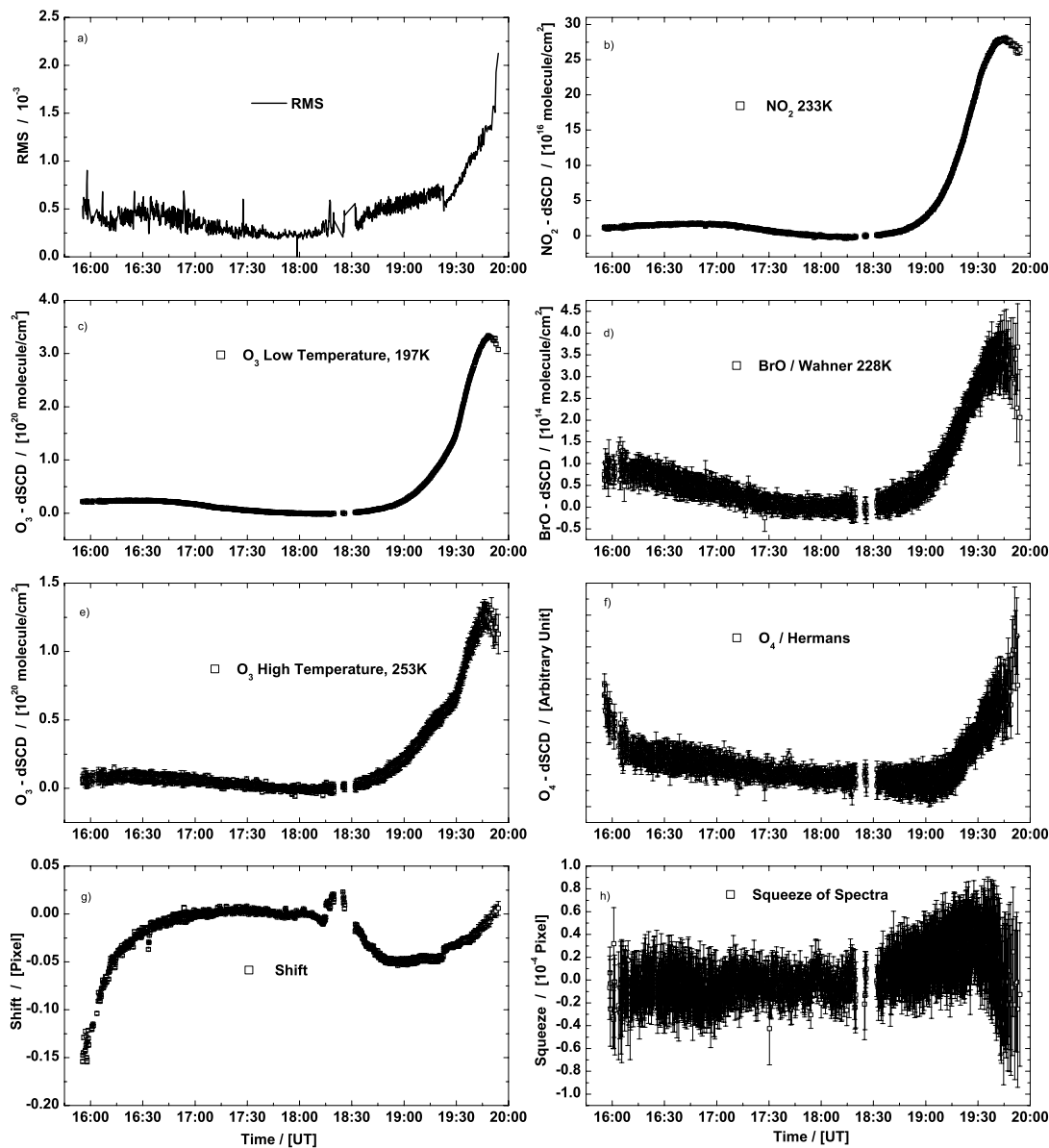


Figure 6.14: Same as Figure 6.3 but for sunset measurements of the balloon flight at Kiruna on August 21, 2001. A laboratory absorption cross-sections of NO_2 at $T = 233\text{K}$ was used here.

winds were weak. Thus, long flights can be performed with almost no drift of the balloon and gondola. For the specific measurement geometry of the LPMA/DOAS instruments, this means that measurements can be taken during sunset and sunrise.

The altitude profile and the corresponding SZA for UV measurements are shown in Figure 6.12, where times greater than 24 UT indicate morning measurements on August 22. After 2 h 40 min, the float altitude of $\sim 39\text{ km}$ was reached at 18:18 UT and $SZA = 88.0^\circ$. From the temperature profile, the tropopause height is estimated at $\sim 11.5\text{ km}$.

There were only low clouds during ascent and the gondola could be stabilised quite early on. Thus measurements with the DOAS spectrographs started at 5.91 km at 15:55:26 UT and $SZA = 74.89^\circ$.

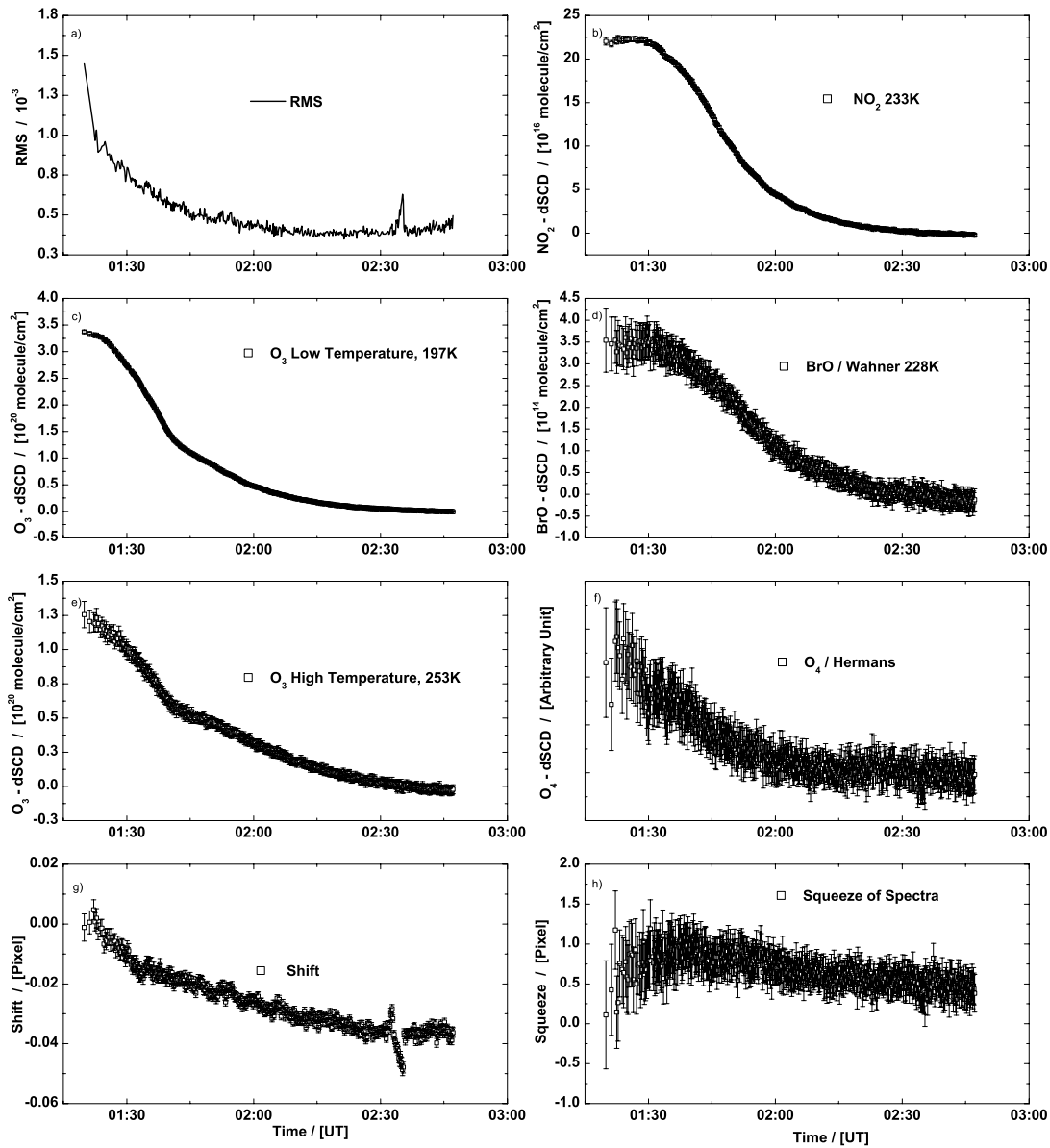


Figure 6.15: Same as Figure 6.3 but for sunrise measurements of the balloon flight at Kiruna on August 21, 2001. A laboratory absorption cross-sections of NO_2 at $T = 233\text{K}$ was used here.

Apart from two small measurement gaps from 7.02 km to 7.49 km (15:58:57 - 16:00:36 UT) and 7.87 km to 8.55 km (16:01:36 - 16:03:35 UT) observations could be performed continuously until float. The mandatory sun-tracker scan, needed to optimise the signal of the LPMA instrument especially for occultation measurements, started immediately after reaching float at 18:19 UT and lasted until 18:32 UT. Occultation data is not affected and measurements in the UV could be performed from 90.00° to 95.05° SZA (18:42:18 - 19:51:34 UT). During the night the balloon descended slowly due to lack of solar heating and consequent cooling of the helium inside the balloon. At 21:58 UT and 35.1 km altitude, ballast was dropped in order to reach around 38 km again before sunrise. Occultation measurements at sunrise started at 01:19:56 UT at 95.03° and lasted until 02:29:36 UT on August 22, 2001. Measurements

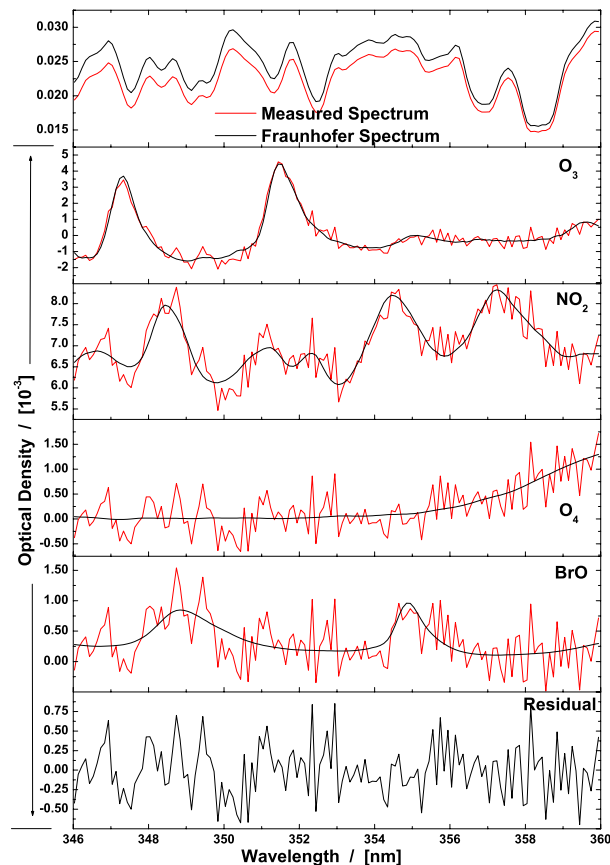


Figure 6.16: Same as Figure 6.2 but for a spectrum recorded during the ascent of the balloon at Kiruna on August 21, 2001. The spectrum was recorded at 12.49 km at 76.99° SZA (16:18:11 UT) with 1 scan and a total exposure time of 0.62 seconds.

continued until the balloon was cut at 02:47:07 UT and 88.55° SZA. For a summary of the observation parameters see Table 6.1.

In Figure 6.13 the trajectory of the balloon is indicated by the thick black line. The thin black lines denote the light rays for occultation measurements, which end at the tangent point. Numbers at the lines indicate the corresponding SZA at the balloon position. The left panel shows the observation geometry for ascent and sunset measurements on August 21. The right panel shows corresponding sunrise measurements on August 22.

Since float altitude was reached at a high SZA and a sun-tracker scan was performed at float, the spectra cannot be used for a Langley plot. Therefore, the absorber amount contained in the Fraunhofer reference spectrum had to be obtained by the model-comparison method described in section 6.1.2. An offset of $(2.0 \pm 1.5) \times 10^{13}$ molecule/cm² of BrO was determined for the reference spectrum obtained by averaging 7 spectra recorded successively between 17:58:01 and 17:59:01 UT (see Table 6.2). Such an early recorded Fraunhofer reference spectrum was chosen since strong oscillations of the gondola during the last part of the ascent prevented correct alignment with the sun and thus had a negative impact on the imaging.

Figure 6.14 shows the development of the slant column densities and important fit parameters for the BrO retrieval in the 346 – 360 nm wavelength range for ascent and sunset measurements. Correspondingly, Figure 6.15 shows the same quantities for sunrise measurements the following morning. Laboratory absorption cross-sections of O₃ at T = 197 K and T = 253 K and NO₂ at T = 233 K were used together

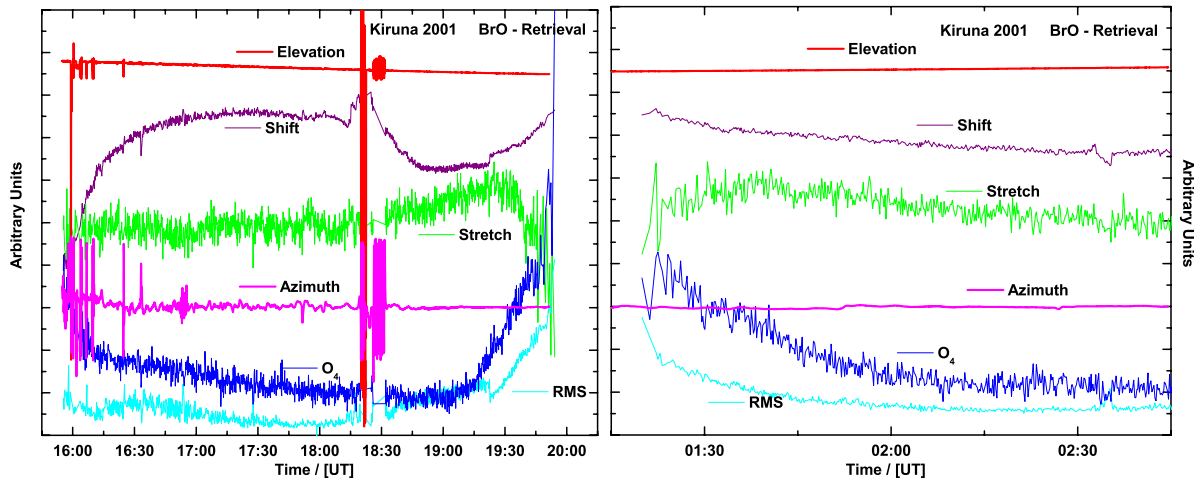


Figure 6.17: Important fit parameters and corresponding elevation and azimuth position of the sun-tracker acquisition mirror for the flight on August 21/22, 2001 at Kiruna. Shown are the total elevation and azimuth positions in arbitrary units (not only the offset as described in section 4.2.2). Ascent and sunset measurements on August 21 are shown in the left panel. The right panel shows the corresponding results for sunrise measurements on August 22.

with literature cross-sections of BrO and O_4 as described in section 6.1.1 (panels b) - f)). In panel a) the resulting root mean square (RMS) of the fit residual is plotted. Panels g) and h) represent the shift and squeeze of the fitted spectra respectively. Float spectra recorded during the sun-tracker scan were removed. Note that the trace gas cross-sections used for the retrieval of the Kiruna 2001 flight differ from the set of references used for flights before 2001 and afterwards. Due to repairs and modifications carried out on the DOAS spectrograph before and after the Kiruna 2001 campaign as described in section 4.1.2. The laboratory spectra recorded especially for this flight are not listed in the tables of chapter 5, but can be found in the internal balloon group laboratory accounts. The calibration and preparation of this set of reference spectra follows the procedure described in section 6.1.1.

A DOAS fit for a spectrum recorded during the ascent of the balloon is plotted in Figure 6.16. The spectrum was recorded at 12.49 km at 76.99° SZA (16:18:11 UT) with 1 scan and a total exposure time of 0.62 seconds. The upper panel shows the Fraunhofer spectrum (black line) and the measured spectrum (red line). In the panels below the retrieved trace gas absorptions of O_3 (at 197 K), NO_2 (at 207 K), O_4 and BrO are plotted. A 2^{nd} - degree polynomial was included in the fit. The black lines indicate the spectral absorptions and the red line represents the sum of the spectral absorption and the residual of the fit. The panel at the bottom displays the remaining residual structure which still shows systematic features. In contrast to the flights performed after 2001, only 1 scan per spectrum was recorded during this flight. Therefore the signal-to-noise ratio is quite low, but can be compensated due to high statistics and about 800 spectra recorded during ascent alone.

In Figure 6.17 important parameters that are sensitive to small changes in the optical imaging and the quality of the fit are shown. The corresponding elevation and azimuth position offsets of the sun-tracker acquisition mirror for the flight on August 21/22, 2001 at Kiruna are shown in arbitrary units as described in section 4.2.2. The sun-tracker scan and its influence on the fit parameters can clearly be observed.

6.3.2 LPMA / DOAS Flight on March 23, 2003 at Kiruna

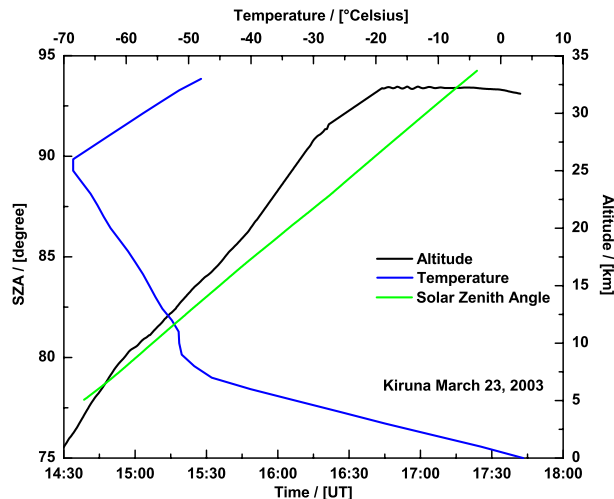


Figure 6.18: Balloon trajectory, temperature and the SZA for UV observations at the position of the balloon for the flight on March 23, 2003 at Kiruna.

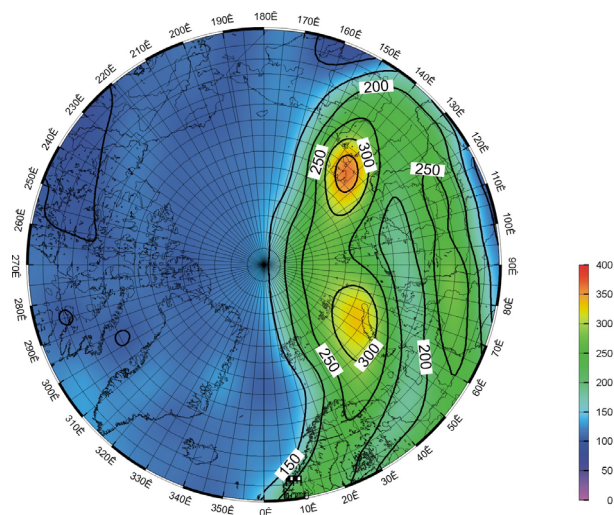


Figure 6.19: Example of the northern hemispheric polar vortex. The 675 K potential temperature level is plotted for March 23, 2003 at 00 UT. The potential vorticity is colour-coded in units of PVU ($10^{-6}\text{Km}^2\text{kg}^{-1}\text{s}^{-1}$).

The flight was launched on March 23, 2003 at 14:28 UT and $SZA = 77^\circ$ at Kiruna (67.9°N , 21.0°E). The altitude profile and the corresponding SZA for UV measurements are shown in Figure 6.18. After 2 h 15 min, the float altitude of ~ 33 km was reached at 16:43 UT and $SZA = 90.2^\circ$. After 1 h at float, the balloon was cut at 17:41 UT and $SZA = 96^\circ$. From the temperature profile, the tropopause height is estimated at 8 km. The position of the polar vortex in the northern hemisphere is shown in Figure 6.19 for March 23, 2003 at 00 UT. The 675 K potential temperature level is colour-coded in units of PVU (Potential Vorticity Units - $10^{-6}\text{Km}^2\text{kg}^{-1}\text{s}^{-1}$). The polar vortex at that time was already disturbed and split caused by warmings that had occurred earlier. Below 675 K (~ 26.7 km) the potential vorticity over Kiruna was very low, which can be seen in Figure 6.20 - note that the scale for the PVU units

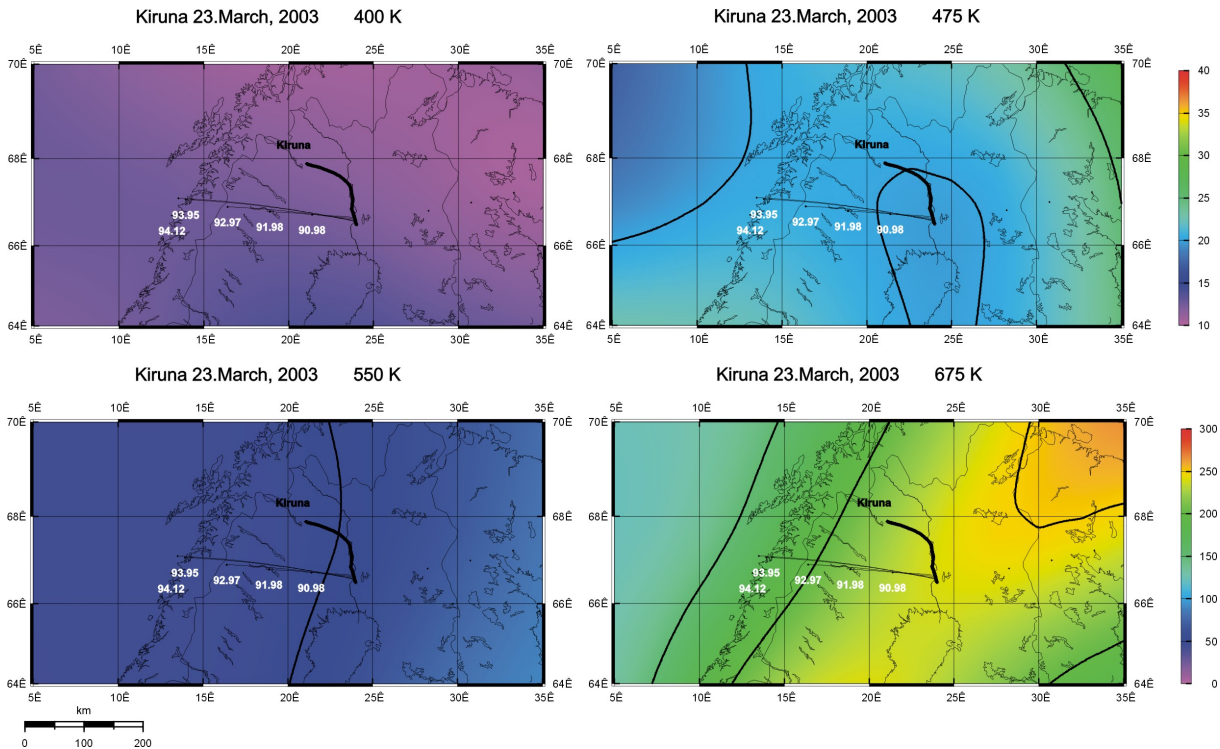


Figure 6.20: Balloon trajectory, observation geometry and potential vorticity of the flight at Kiruna on March 23, 2003. The trajectory is the thick black line. The thin black lines denote the light rays for occultation measurements, ending at the tangent point. Numbers at the lines indicate the SZA. The potential vorticity at March 23, 24 UT is colour-coded in units of PVU ($10^{-6}\text{Km}^2\text{kg}^{-1}\text{s}^{-1}$) and plotted for the 400 K, 475 K, 550 K and 675 K levels.

changes from the upper to the lower panels. Plotted are the 400 K, 475 K, 550 K and 675 K levels. This means that a filament of the vortex reached out over Scandinavia only at higher altitudes in the middle stratosphere. Therefore, measurements were performed at the edge of vortex, observing both air masses outside and inside the vortex at the same time during the ascent of the balloon. During solar occultation the light rays of the direct sun measurements traversed the vortex edge especially for high solar zenith angles. In Figure 6.20 the trajectory of the balloon is indicated by the thick black line. The thin black lines denote the light rays for occultation measurements, ending at the tangent point. Numbers at the lines indicate the corresponding SZA at the balloon position.

Although part of the observed air masses were located inside the vortex, no signs of chlorine activation could be observed. The spectra were analysed for absorption features of OCIO, which is an indicator of chlorine activation, and no absorptions were found (see also chapter 8 for a discussion of OCIO measurements). This is in accordance with other observations and the rather high temperatures during that winter.

Only low clouds were present on March 23, 2003 and the gondola could be stabilised quite early during the ascent. Thus, measurements with the DOAS spectrographs started as early as 3.72 km at 14:38:30 UT and $SZA = 77.9^\circ$. Apart from two small measurement gaps from 4.30 km to 6.09 km (14:40:05 - 14:46:13 UT) and 10.49 km to 11.50 km (15:04:42 - 15:09:52 UT) observations could be performed continuously. Since the launch had been delayed by 15 minutes, float altitude was not reached until 16:43 UT at $SZA = 90.2^\circ$. Therefore, the mandatory sun-tracker scan, needed to optimise the signal of the LPMA instrument especially for occultation measurements, was performed during the last part of the

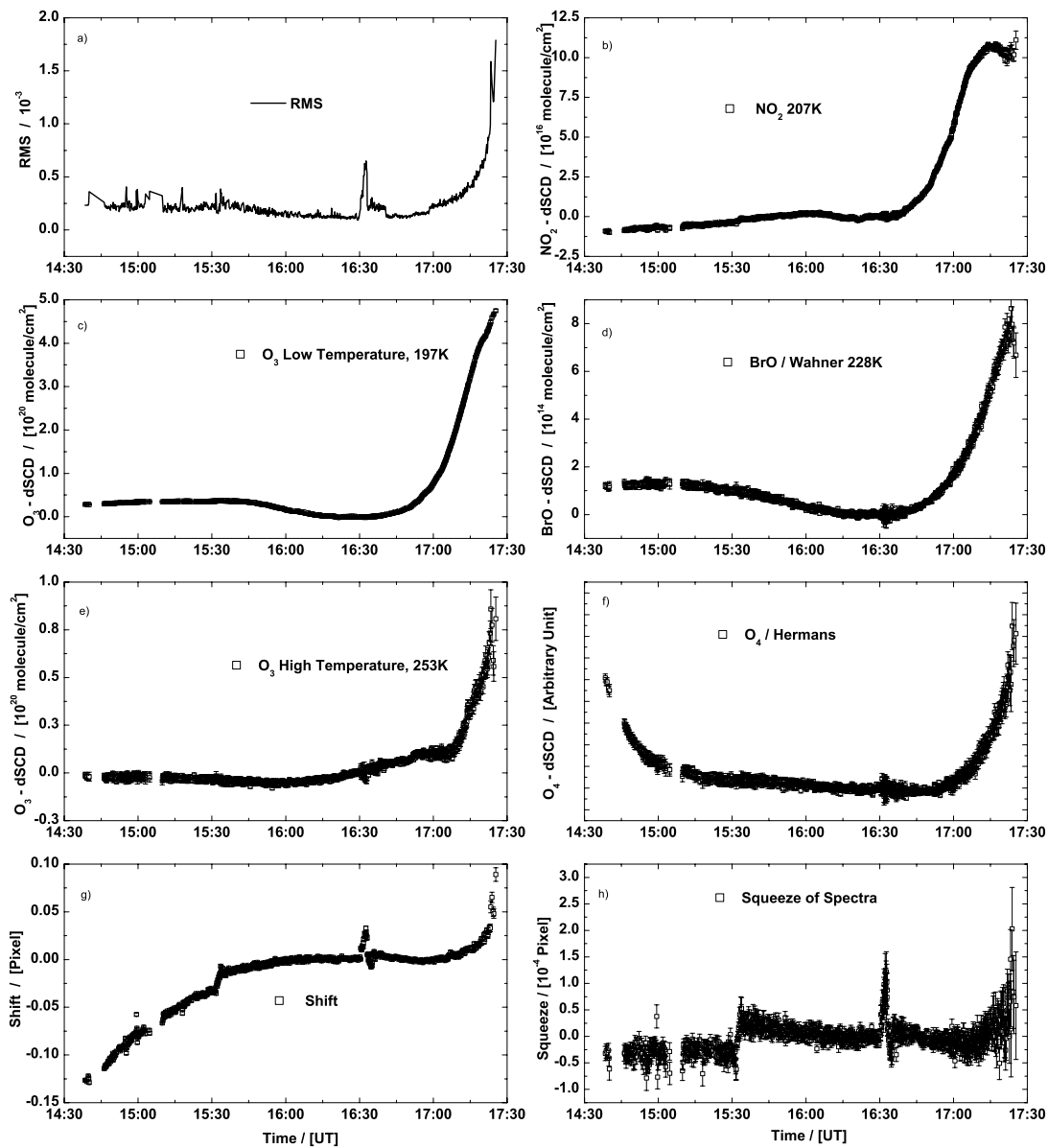


Figure 6.21: Same as Figure 6.3 but for the balloon flight at Kiruna on March 23, 2003.

ascent. Consequently, DOAS UV observations for the ascent can only be used up to 30.08 km reached at 16:28:57 UT and $SZA = 88.78^\circ$. Occultation data is undisturbed and measurements in the UV could be performed from 90.00° to 94.25° SZA (16:41:02 - 17:23:50 UT). For a summary of the observation parameters see Table 6.1.

Since float altitude was reached too late to perform a Langley plot, the absorber amount contained in the Fraunhofer reference spectrum had to be obtained by the model-comparison method described in section 6.1.2. An offset of $(7.2 \pm 1.0) \times 10^{13}$ molecule/cm² of BrO was determined for the reference spectrum obtained by averaging 5 spectra recorded successively between 16:28:57 and 16:29:28 UT (see Table 6.2).

Figure 6.21 shows the development of the slant column densities and important fit parameters for the BrO retrieval in the 346 – 360 nm wavelength range for ascent and sunset measurements. Laboratory

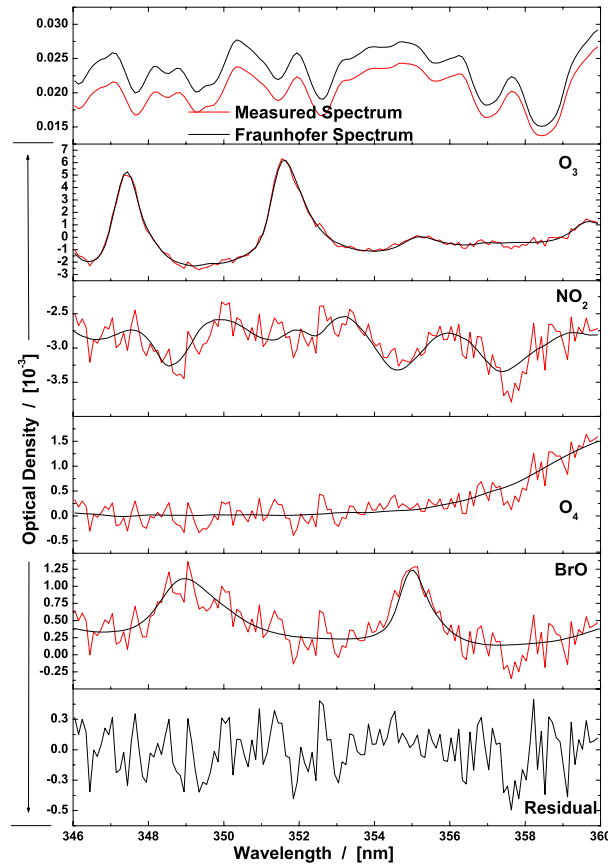


Figure 6.22: Same as Figure 6.2 but for a spectrum recorded during the ascent of the balloon at Kiruna on March 23, 2003. The spectrum was recorded at 11.62 km at 81.04° SZA (15:10:32 UT) with 3 scans and a total exposure time of 0.81 seconds.

absorption cross-sections of O_3 at $T = 197$ K and $T = 253$ K and NO_2 at $T = 207$ K were used together with literature cross-sections of BrO and O_4 as described in section 6.1.1 (panels b) - f)). In panel a) the resulting root mean square (RMS) of the fit is plotted. Panels g) and h) represent the shift and squeeze of the fitted spectra, respectively. The features of the measurement gap and the sun-tracker scan can clearly be seen.

A DOAS fit for a spectrum recorded during the ascent of the balloon is plotted in Figure 6.22. The spectrum was recorded at 11.62 km at 81.04° SZA (15:10:32 UT) with 3 scans and a total exposure time of 0.81 seconds. The upper panel shows the Fraunhofer spectrum (black line) and the measured spectrum (red line). In the lower panels the retrieved trace gas absorptions of O_3 (at 197 K), NO_2 (at 207 K), O_4 and BrO are plotted. A 2^{nd} - degree polynomial was included in the fit. The black lines indicate the spectral absorptions and the red line represents the sum of the spectral absorption and the residual of the fit. The lowest panel displays the remaining residual structure which still shows some systematic features but is comparatively low for this flight.

In Figure 6.23 important parameters that are sensitive to small changes of the optical imaging and the quality of the fit are shown. The corresponding elevation and azimuth position offsets of the sun-tracker acquisition mirror are shown in arbitrary units as described in section 4.2.2. A change of the azimuth and elevation position at around 15:35 UT resulted in a discontinuity in the shift and stretch of the spectra. Also the sun-tracker scan starting at 16:30 UT can clearly be observed and causes the root mean square of the fit to increase significantly.

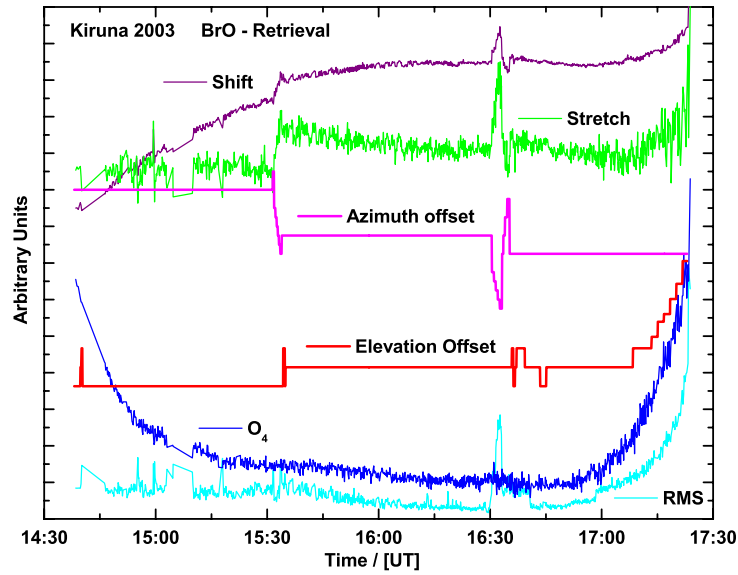


Figure 6.23: Important fit parameters and corresponding elevation and azimuth positions of the sun-tracker acquisition mirror for the flight on March 23, 2003 at Kiruna. Shown are elevation and azimuth offsets in arbitrary units as described in section 4.2.2.

6.3.3 LPMA / DOAS Flight on October 09, 2003 at Aire sur l'Adour

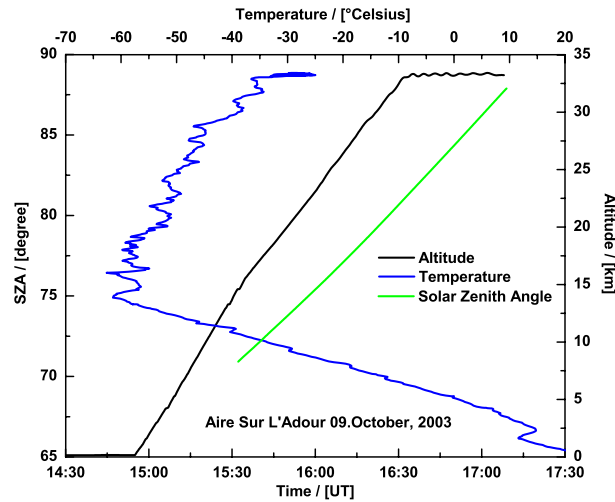


Figure 6.24: Balloon trajectory, temperature and the SZA for UV observations at the position of the balloon for the flight on October 09, 2003 at Aire sur l'Adour.

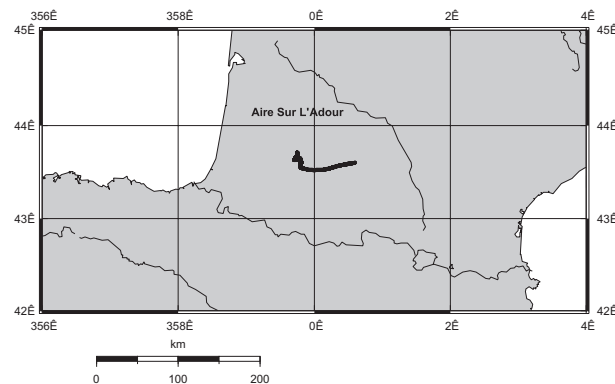


Figure 6.25: Balloon trajectory of the flight on October 09, 2003 at Aire sur l'Adour.

The mid-latitude flight at Aire sur l'Adour, France, was launched on October 9, 2003 from the CNES balloon division headquarters located at 43.7°N , 0.25°W . The flight profile is shown in Figure 6.24 together with the temperature and the SZA at the position of the balloon for UV observations. The height of the tropopause is estimated at ~ 14 km. Launch was at 14:55 UT and $SZA = 65^{\circ}$. After 1 h 37 min float altitude of ~ 33 km was reached at 16:32 UT, half an hour earlier than initially planned. After 30 minutes at float, the balloon had to be cut at 17:08 UT, since it approached the densely populated area of Toulouse. Thus no sunset measurements could be performed.

In Figure 6.25 the trajectory of the balloon is indicated by the thick black line. As the balloon ascended too fast due to uncorrect filling with helium, it reached strong westerly winds in the middle stratosphere earlier than planned. Thus, the early drift towards the east and the ban to overfly highly populated areas prevented occultation measurements. The rapid ascent made the stabilisation of the gondola, and therefore the tracking of the Sun, difficult and measurements did not start before 14.60 km at 15:32:13 UT and $SZA = 70.92^{\circ}$. Apart from a small measurement gap from 14.78 km to 16.54 km (15:33:05 - 15:38:03 UT) observations were performed continuously.

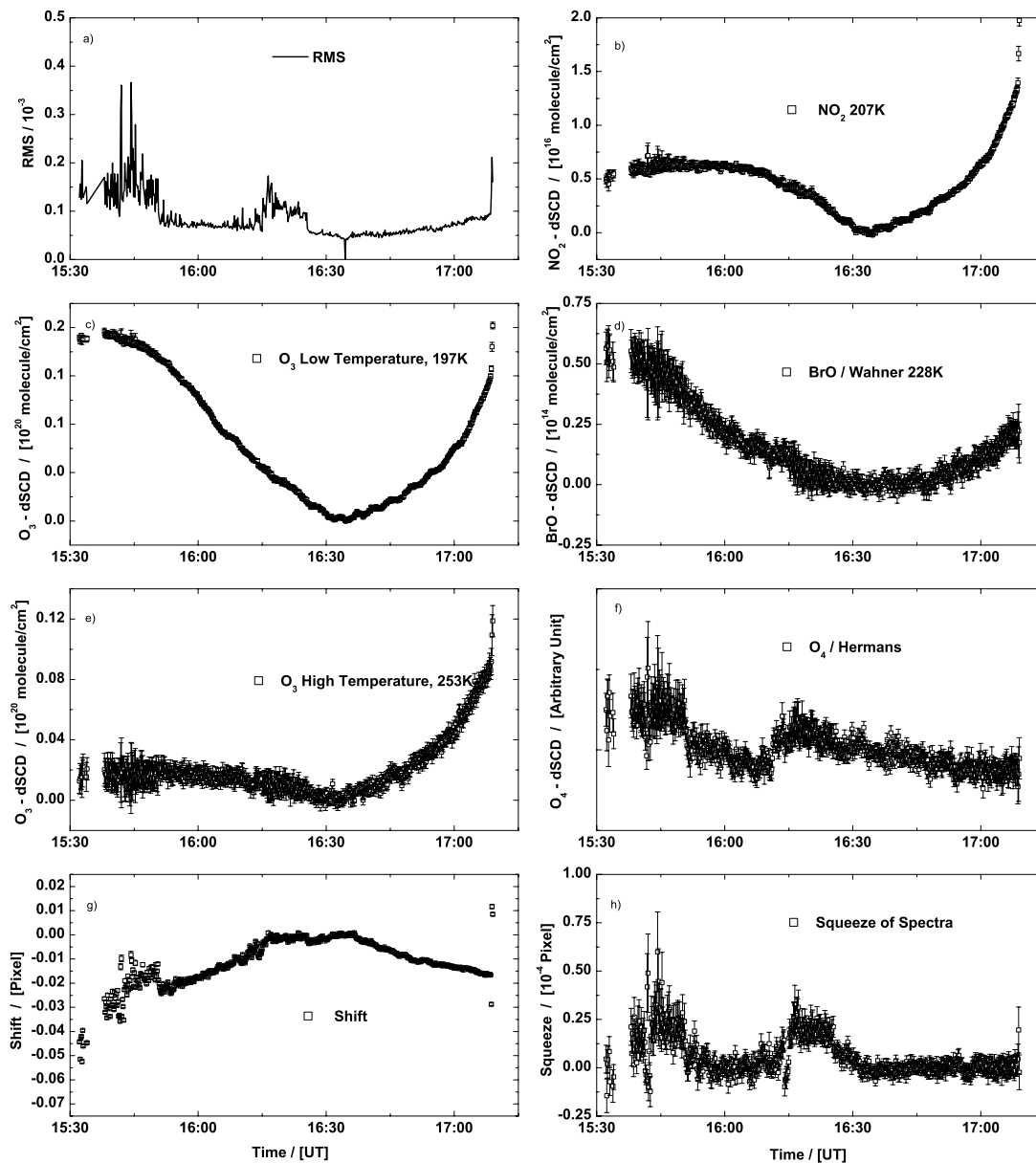


Figure 6.26: Same as Figure 6.3 but for the balloon flight at Aire sur L'Adour on October 9, 2003.

An advantage of the fast ascent was that float altitude was reached at a low solar zenith angle of 80.8° at 16:32 UT. Float measurements were continued until 17:08 UT and $SZA = 87.5^\circ$. The extensive float measurements allowed for a perfect Langley plot (see chapter 9) and provided optimum conditions for the absolute radiometric calibration (see [Gurlit *et al.* 2005] and [Lindner 2005]). For a summary of the observation parameters see Table 6.1.

Due to the low SZA of 81.50° at which the Fraunhofer reference spectrum was recorded, the absorber amount contained in the spectrum is very low. By performing a Langley plot (section 6.1.2) an offset of $(1.6 \pm 0.5) \times 10^{13}$ molecule/cm² of BrO was determined. The Fraunhofer reference spectrum was recorded at 16:34:25 UT (see Table 6.2).

Figure 6.26 shows the development of the slant column densities and important fit parameters for the BrO

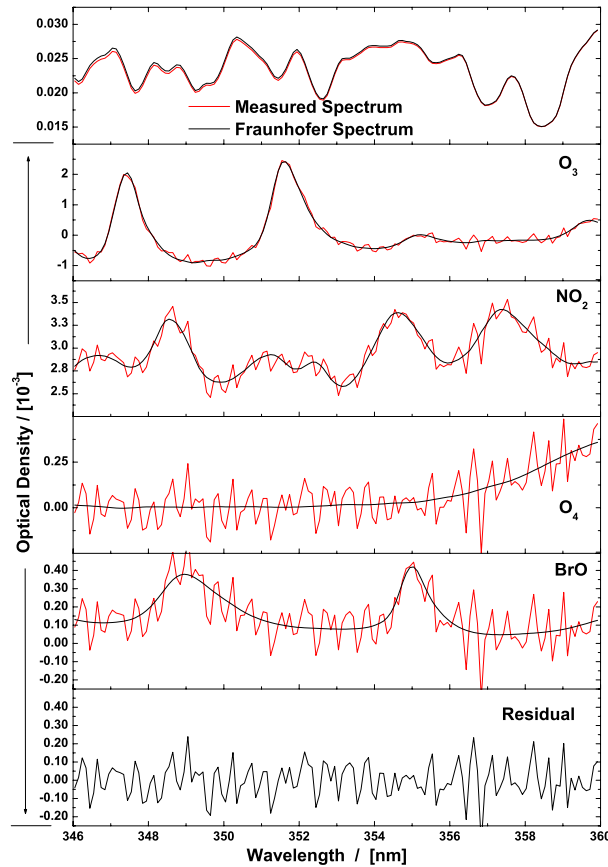


Figure 6.27: Same as Figure 6.2 but for a spectrum recorded during the ascent of the balloon at Aire sur L'Adour on October 9, 2003. The spectrum was recorded at 20.04 km at 73.76° SZA (15:49:57 UT) with 32 scans and a total exposure time of 5.44 seconds.

retrieval in the 346 – 360 nm wavelength range for ascent and float measurements. Laboratory absorption cross-sections of O_3 at $T = 197$ K and $T = 253$ K and NO_2 at $T = 207$ K were used together with literature cross-sections of BrO and O_4 as described in section 6.1.1 (panels b) - f)). In panel a) the resulting root mean square (RMS) of the fit residual is plotted. Panels g) and h) represent the shift and squeeze of the fitted spectra, respectively. During the ascent of the balloon sun-tracker scans were carried out at 15:50:30 to 15:55:10 UT (20.2 – 21.6 km) and again at 16:10:15 to 16:15:10 UT (26.5 – 28.1 km). In between these measurements, the elevation offset was set to a different but constant value. The features of the short measurement gap and the sun-tracker scans can clearly be seen in the fit parameters.

A DOAS fit for a spectrum recorded during the ascent of the balloon is plotted in Figure 6.27. The spectrum was recorded at 20.04 km at 73.76° SZA (15:49:57 UT) with 32 scans and a total exposure time of 5.44 seconds. The upper panel shows the Fraunhofer spectrum (black line) and the measured spectrum (red line). In the panels below the retrieved trace gas absorptions of O_3 (at 197 K), NO_2 (at 207 K), O_4 and BrO are plotted. A 2^{nd} -degree polynomial was included in the fit. The black lines indicate the spectral absorptions and the red line represents the sum of the spectral absorption and the residual of the fit. The lowest panel displays the remaining residual structure which still shows some systematic features but is the lowest for all flights performed so far.

In Figure 6.28 important parameters that are sensitive to small changes in the optical imaging and the quality of the fit are shown. The corresponding elevation and azimuth position offsets of the sun-tracker acquisition mirror for the flight on October 09, 2003 at Aire sur L'Adour are shown in arbitrary units

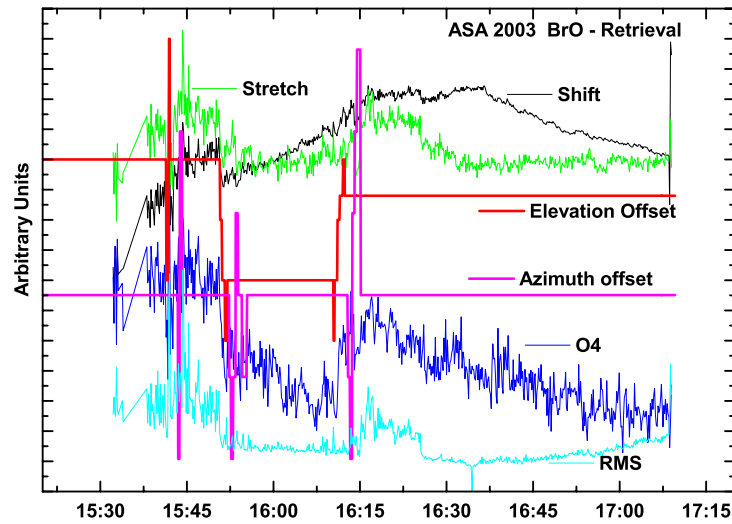


Figure 6.28: Important fit parameters and corresponding elevation and azimuth positions of the sun-tracker acquisition mirror for the flight on October 09, 2003 at Aire sur L'Adour. Shown are elevation and azimuth offsets in arbitrary units as described in section 4.2.2.

as described in section 4.2.2. Changes of the azimuth and elevation position at around 15:50 to 15:55 UT and 16:10 to 16:15 UT result in a discontinuity in the shift and stretch and can also be seen in the O_4 -SCDs. The strong increase in the RMS and stretch before 15:50 UT and from 16:15 to 16:25 UT, at times when the sun tracker offsets were not changed, is due to strong oscillations of the gondola and insufficient stabilisation.

6.3.4 LPMA / DOAS Flight on March 24, 2004 at Kiruna

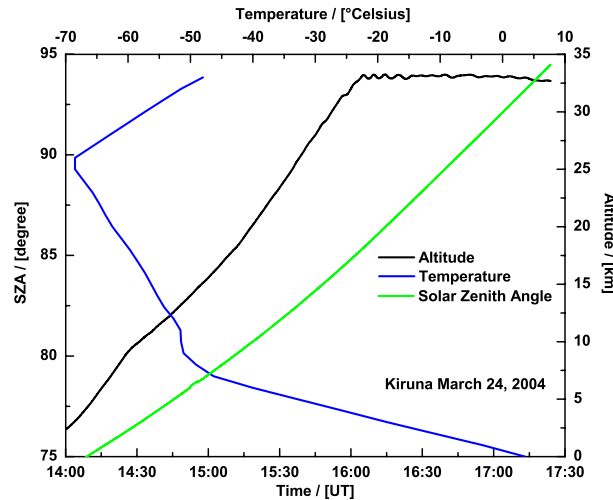


Figure 6.29: Balloon trajectory, temperature and the SZA for UV observations at the position of the balloon for the flight on March 24, 2004 at Kiruna.

The flight was launched on March 24, 2004 at 13:54 UT and $SZA = 74.1^\circ$ at Kiruna (67.9°N , 21.0°E). The altitude profile and the corresponding SZA for UV measurements are shown in Figure 6.29. After 2 h 10 min, the float altitude of ~ 33 km was reached at 16:05 UT and $SZA = 85.6^\circ$. The balloon was cut at 17:50 UT and $SZA = 97.7^\circ$ after ~ 1 h 45 min at float. From the temperature profile, the tropopause height is estimated at ~ 8.9 km. The position of the polar vortex in the northern hemisphere is shown in Figure 6.30 for March 24, 2004 at 00 UT. The 675 K potential temperature level is colour-coded in PVU (Potential Vorticity Units - $10^{-6}\text{Km}^2\text{kg}^{-1}\text{s}^{-1}$). The polar vortex at that time was already disturbed and several filaments had built up. Below 675 K (~ 27.1 km) the potential vorticity over Kiruna was very low, which can be seen in Figure 6.31 - note that the scale for the PVUs changes from the upper to the lower panels. The 400 K, 475 K, 550 K and 675 K levels are plotted. This means that the edge of the vortex only reached out over Scandinavia at higher altitudes in the middle stratosphere. Therefore, measurements performed at the edge of vortex observed both air masses outside and inside the vortex at the same time during balloon ascent. During solar occultation the light rays of the direct sun measurements traversed the vortex edge especially for high solar zenith angles. In Figure 6.31 the trajectory of the balloon is indicated by the thick black line. The thin black lines denote the light rays for occultation measurements, ending at the tangent point. Numbers at the lines indicate the corresponding SZA at balloon position. Although part of the observed air masses were located inside the vortex, no signs of chlorine activation could be observed. The spectra were analysed for absorption features of OClO, which is an indicator of chlorine activation and is discussed in chapter 8. This is in accordance with other observations and the rather high temperatures during that winter.

Only low clouds were present on March 24, 2004 and the gondola could be stabilised quite early during the ascent. Measurements with the DOAS spectrographs started at 3.16 km at 14:04:28 UT and $SZA = 74.58^\circ$. Apart from two small measurement gaps from 4.22 km to 5.71 km (14:08:50 - 14:14:16 UT) and 8.79 km to 9.61 km (14:25:01 - 14:28:38 UT) observations could be performed continuously. The second measurement gap was probably due to strong winds at the tropopause, which cause strong oscillations of the gondola. The mandatory sun-tracker scan, needed to optimise the signal of the LPMA instrument especially for occultation measurements, was performed during the last part of the ascent. Consequently, DOAS UV observations for the ascent between 23.54 km and 28.61 km (15:30:30 and 15:46:52) have to be treated with care. Occultation data is undisturbed and measurements in the UV could be performed from 90.00° to 94.41° SZA (16:45:40 - 17:23:09 UT). For a summary of the observation parameters, see

Table 6.1.

Since float altitude was reached at $SZA = 85.5^\circ$ an extensive Langley plot as shown in Figure 6.5 in section 6.1.2 could be performed. An absorber amount contained in the Fraunhofer reference spectrum of $(2.3 \pm 0.4) \times 10^{13}$ molecule/cm² of BrO was determined. Due to strong oscillations of the gondola during the float part of the flight and resulting large amplitudes of the sun tracker acquisition mirror, two different reference spectra, recorded within one minute, were used in the BrO retrieval for the ascent and the occultation part. Thus the residuals of the occultation-spectra retrieval could be reduced. The Fraunhofer spectrum used for the ascent and occultation were recorded at 16:05:44 UT and $SZA = 85.41^\circ$ and at 16:06:11 and $SZA = 85.46^\circ$, respectively (see Table 6.2).

Figure 6.3 shows the development of the slant column densities and important fit parameters for the BrO retrieval in the 346 – 360 nm wavelength range for ascent and sunset measurements. Laboratory absorption cross-sections of O₃ at T = 197 K and T = 253 K and NO₂ at T = 207 K were used together with literature cross-sections of BrO and O₄ as described in section 6.1.1 (panels b) - f)). In panel a) the resulting root mean square (RMS) of the fit is plotted. Panels g) and h) represent the shift and squeeze of the fitted spectra, respectively. The features of the measurement gaps and the sun-tracker scan can clearly be seen.

A DOAS fit for a spectrum recorded during balloon ascent is plotted in Figure 6.2. The spectrum was recorded at 17.36 km at 79.70° SZA (15:07:53 UT) with 22 scans and a total exposure time of 5.5 seconds. The upper panel shows the Fraunhofer spectrum (black line) and the evaluated spectrum (red line). In the panels below the retrieved trace gas absorptions of O₃ (at 197 K), NO₂ (at 207 K), O₄ and BrO are plotted. A 2nd- degree polynomial was included in the fit. The black lines indicate the spectral absorptions and the red line represents the sum of the spectral absorption and the residual of the fit. The lowest panel displays the remaining residual structure which still shows some systematic features but is very low for this flight. The optical density of BrO is only $0.5 \cdot 10^{-3}$ and clearly found by the fit, indicating the high sensitivity achieved by the DOAS spectrograph.

In Figure 6.32 important parameters that are sensitive to small changes in the optical imaging and the quality of the fit are shown. The corresponding elevation and azimuth position offsets of the sun-tracker acquisition mirror for the flight on March 24, 2004 at Kiruna are shown in arbitrary units as described in section 4.2.2. The sun-tracker scan and adjustments of the mirror position during the occultation part between 17:00 and 17:20 UT can clearly be observed and causes the root mean square of the fit to increase strongly. The increase and oscillations of the RMS between 15:50 and 17:00 UT, at a time when the azimuth and elevation offsets were not modified, are caused by strong oscillations of the gondola.

The effect of the sun-tracker scan and the offset adjustments on the BrO retrieval during occultation is shown in Figure 6.33. The left panel shows a section of the development of BrO-SCD values during the ascent of the balloon and shortly before float. In the right panel corresponding offset adjustments performed during occultation measurements are compared to BrO-SCD values. It can be seen that for small adjustments the effect is within the error bars of the BrO retrieval errors as given by the *WinDOAS* software.

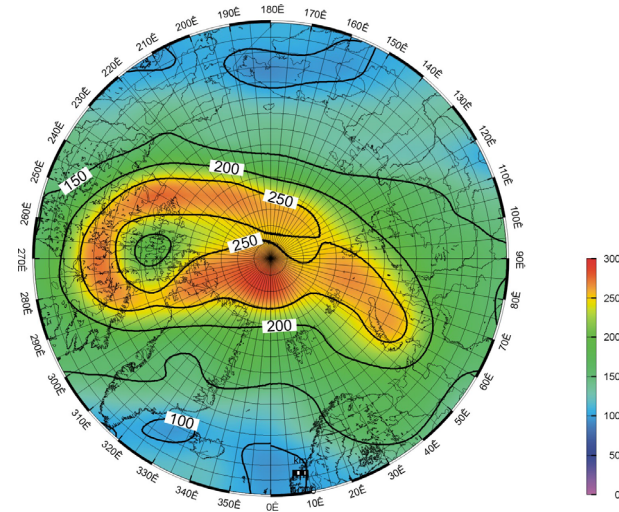


Figure 6.30: Example of the northern hemispheric polar vortex. The 675 K potential temperature level is plotted for March 24, 2004 at 00 UT. The potential vorticity is colour-coded in units of PVU ($10^{-6}\text{Km}^2\text{kg}^{-1}\text{s}^{-1}$).

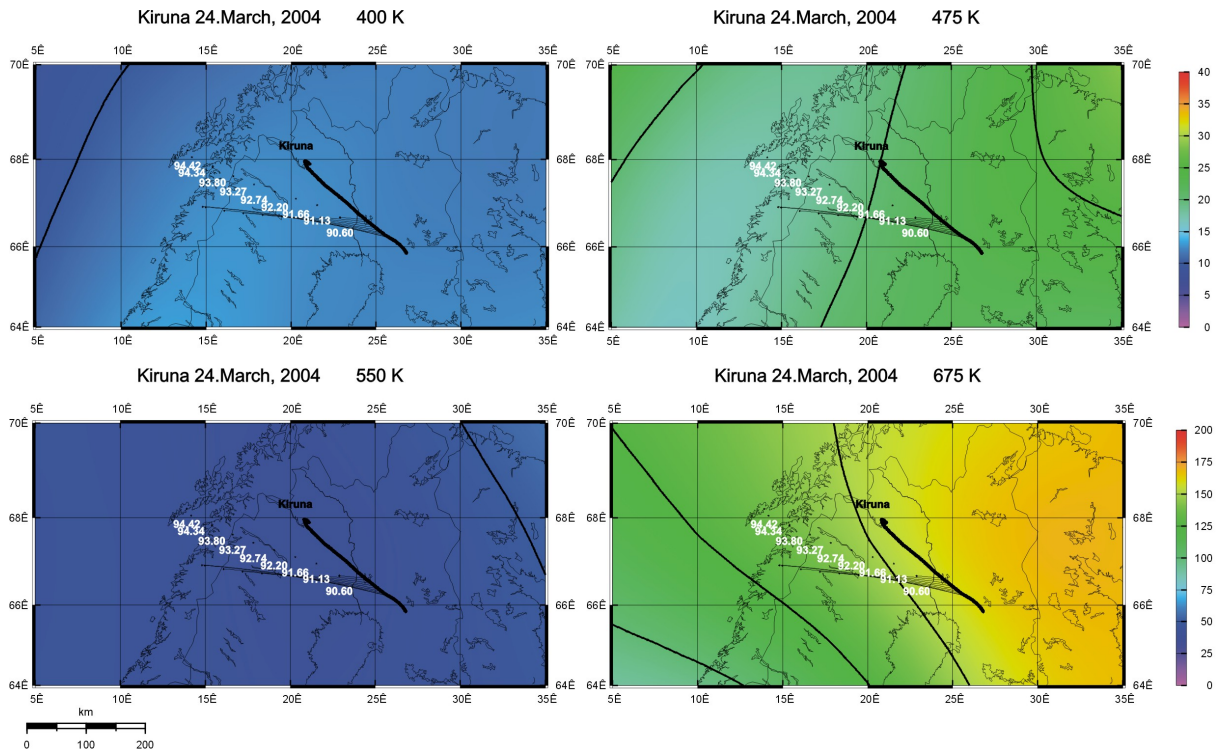


Figure 6.31: Balloon trajectory, observation geometry and potential vorticity of the flight at Kiruna on March 24, 2004. The trajectory is the thick black line. The thin black lines denote the light rays for occultation measurements, ending at the tangent point. Numbers at the lines indicate the SZA. The potential vorticity at March 24, 24 UT, is colour-coded in units of PVU ($10^{-6}\text{Km}^2\text{kg}^{-1}\text{s}^{-1}$) and plotted for the 400 K, 475 K, 550 K and 675 K levels.

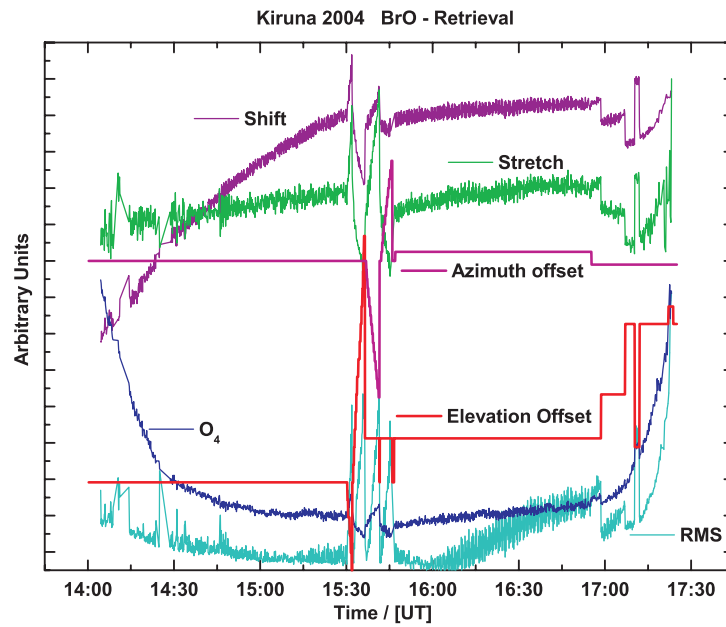


Figure 6.32: Important fit parameters and corresponding elevation and azimuth positions of the sun-tracker acquisition mirror for the flight on March 24, 2004 at Kiruna. Shown are elevation and azimuth offsets in arbitrary units as described in section 4.2.2.

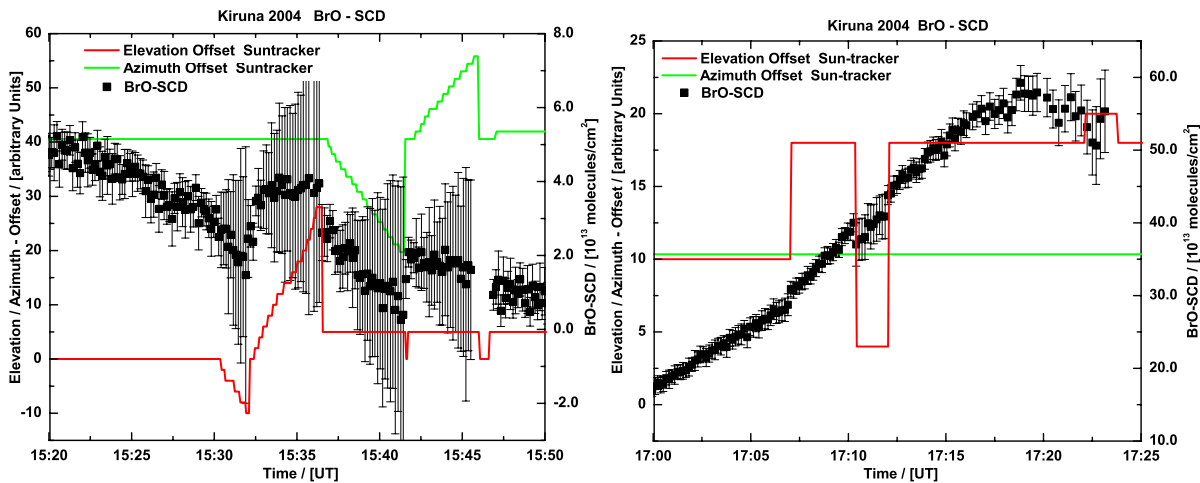


Figure 6.33: Effect of the elevation and azimuth offsets of the acquisition mirror on the BrO-SCD retrieval of the flight on March 24, 2004 at Kiruna. The left panel shows a section of the development of BrO-SCD values during the ascent of the balloon and shortly before float. The sun-tracker scan performed by the LPMA team can clearly be seen. The right panel shows corresponding offset adjustments performed during occultation measurements.

6.3.5 LPMA / DOAS Flight on June 17, 2005 at Teresina

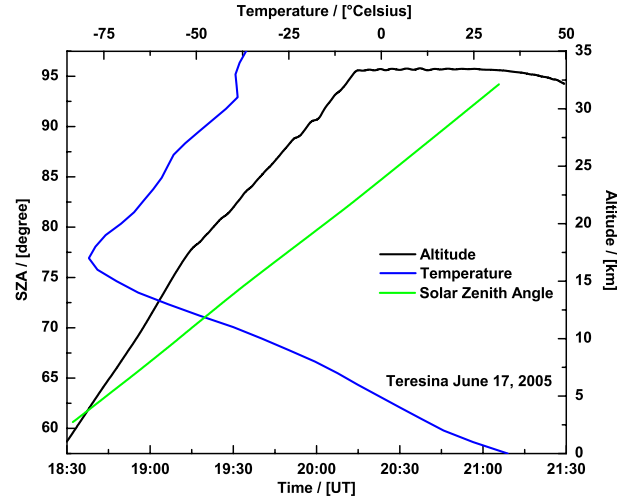


Figure 6.34: Balloon trajectory, temperature and the SZA for UV observations at the position of the balloon for the flight on June 17, 2005 at Teresina.

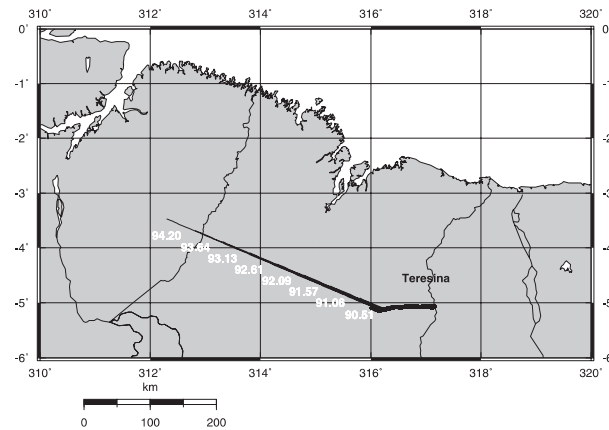


Figure 6.35: Balloon trajectory and observation geometry of the flight on June 17, 2005 at Teresina. The trajectory is the thick black line. The thin black lines denote the light rays for occultation measurements, which end at the tangent point. Numbers at the lines indicate the SZA.

The flight was launched on June 17, 2005 at 18:27 UT and $SZA = 59.8^\circ$ at Teresina, Brazil ($5.1^\circ S$, $42.9^\circ W$). The altitude profile and the corresponding SZA for UV measurements are shown in Figure 6.34. After 1 h 48 min, the float altitude of ~ 33.3 km was reached at 20:15 UT and $SZA = 82.9^\circ$. The balloon stayed at float till long after sunset measurements before it was cut prior to sunrise. From the temperature profile, the tropopause height is estimated at ~ 17.0 km.

In Figure 6.35 the trajectory of the balloon is indicated by the thick black line. The thin black lines denote the light rays for occultation measurements, ending at the tangent point. Tangent points are the areas of main atmospheric absorption. Numbers at the lines indicate the corresponding SZA at the balloon position.

Only low clouds were present on June 17, 2005 over Teresina and the gondola could be stabilised early

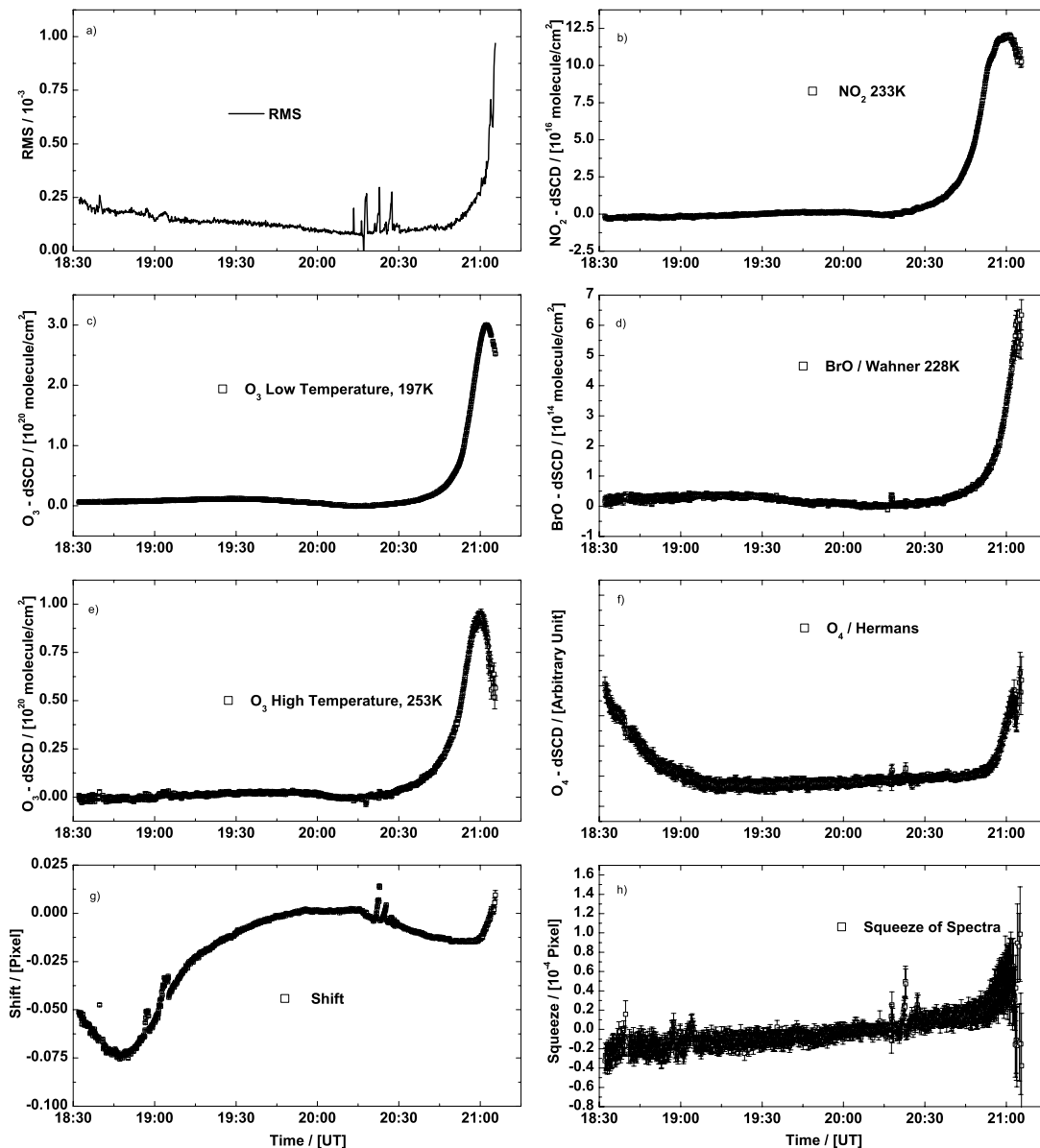


Figure 6.36: Same as Figure 6.3 but for sunset measurements of the balloon flight at Teresina on June 17, 2005. A laboratory absorption cross-sections of NO_2 at $T = 233\text{ K}$ was used here.

during the ascent. Thus measurements with the DOAS spectrographs started at 1.85 km at 18:32:17 UT and $SZA = 60.66^\circ$ and lasted for the ascent up to 33.32 km at 20:16:58 UT and $SZA = 83.22^\circ$. Apart from one small measurement gap from 4.56 km to 4.97 km (18:39:42 - 18:40:52 UT) observations could be performed continuously. After reaching float altitude, the mandatory sun-tracker scan needed to optimise the signal of the LPMA instrument was performed from 20:19:54 to 20:29:17 UT or 83.96° to 86.06° SZA. Since the spectra at or close to the detection limit are not used for the Langley plot basically no spectra were lost due to the sun-tracker scan. Therefore an extensive Langley plot could be performed with the remaining spectra up to $SZA = 90.00^\circ$. An absorber amount contained in the Fraunhofer reference spectrum of $(2.0 \pm 0.5) \times 10^{13}$ molecule/cm² of BrO was determined. The Langley

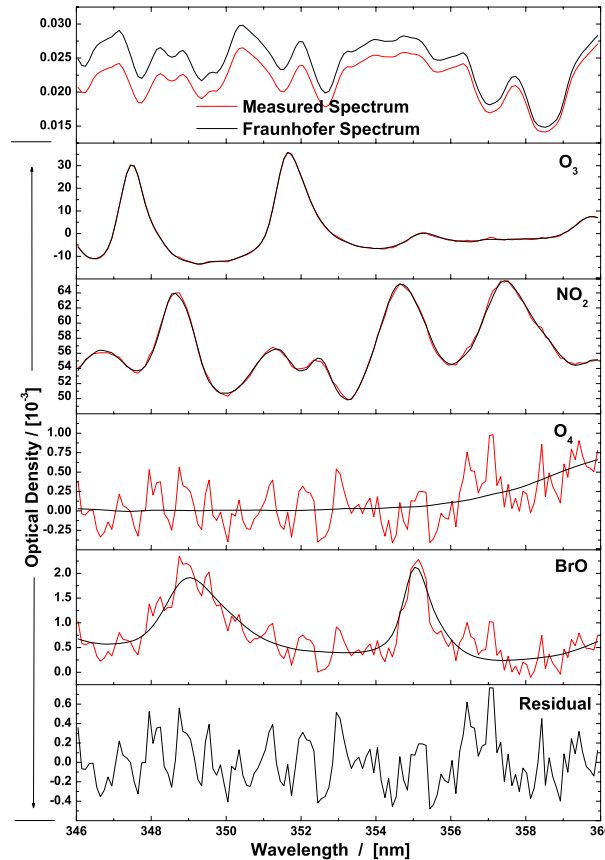


Figure 6.37: Same as Figure 6.2 but for a spectrum recorded during occultation measurements of the balloon at Teresina on June 17, 2005. The spectrum was recorded at 33.46 km at 92.38° SZA (20:57:40 UT) with 8 scans and a total exposure time of 5.0 seconds.

plot is presented in chapter 9.

Occultation data is undisturbed and measurements in the UV could be performed from 90.00° to 94.20° SZA (20:47:06 - 21:05:46 UT). For a summary of the observation parameters see Table 6.1. The Fraunhofer spectrum used for the ascent and occultation was recorded at 20:16:58 UT and $SZA = 83.22^\circ$ (see Table 6.2).

Figure 6.36 shows the development of the slant column densities and important fit parameters for the BrO retrieval in the 346 – 360 nm wavelength range for ascent and sunset measurements. Laboratory absorption cross-sections of O_3 at $T = 197$ K and $T = 253$ K and NO_2 at $T = 207$ K were used together with literature cross-sections of BrO and O_4 as described in section 6.1.1 (panels b) - f)). In panel a) the resulting root mean square (RMS) of the fit is plotted. Panels g) and h) represent the shift and squeeze of the fitted spectra, respectively. The features of the sun-tracker scan can be seen clearly in the RMS and shift of the spectra. The shifts around 19.00 UT are due to strong azimuth oscillations of the gondola and corresponding sun-tracker movements.

A DOAS fit for a spectrum recorded during the ascent of the balloon is plotted in Figure 6.37. The spectrum was recorded during occultation at 33.46 km and 92.38° SZA (20:57:40 UT) with 8 scans and a total exposure time of 5.0 seconds. The upper panel shows the Fraunhofer spectrum (black line) and the measured spectrum (red line). In the panels below the retrieved trace gas absorptions of O_3 (at 197 K), NO_2 (at 207 K), O_4 and BrO are plotted. A 2^{nd} -degree polynomial was included in the fit. The black lines indicate the spectral absorptions and the red line represents the sum of the spectral absorption and

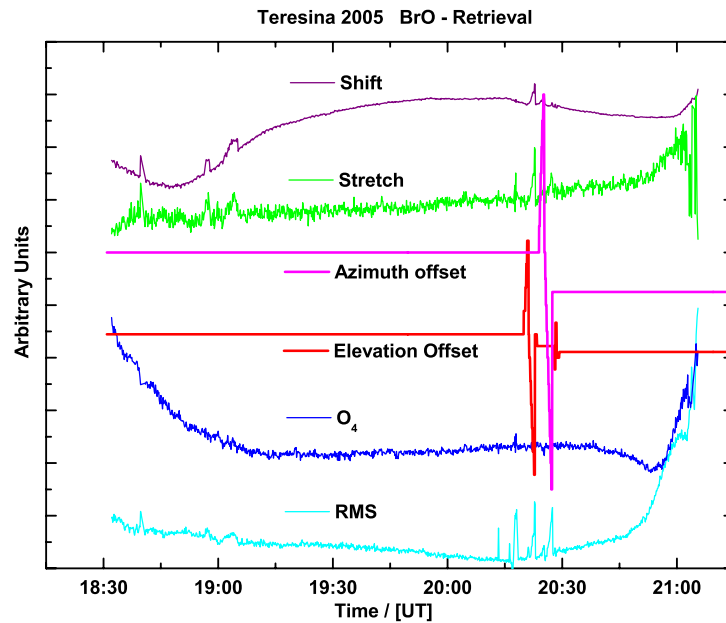


Figure 6.38: Important fit parameters and corresponding elevation and azimuth positions of the sun-tracker acquisition mirror for the flight on June 17, 2005 at Teresina. Shown are elevation and azimuth offsets in arbitrary units as described in section 4.2.2.

the residual of the fit. The lowest panel displays the remaining residual structure which still shows some systematic features.

In Figure 6.38 important parameters that are sensitive to small changes in the optical imaging and the quality of the fit are shown. The corresponding elevation and azimuth position offsets of the sun-tracker acquisition mirror for the flight on June 17, 2005 at Teresina are shown in arbitrary units as described in section 4.2.2. The sun-tracker scan and adjustments of the mirror position during occultation between 20:19 and 20:29 UT can clearly be observed and cause the root mean square of the fit residual to increase significantly. Large RMS values shortly before 20:19 UT are due to azimuth oscillations of the gondola and therefore of the acquisition mirror. After the sun-tracker scan was performed, a small offset signal was adjusted for elevation and azimuth. The offset stayed constant for the remaining part of the flight and did not further influence DOAS measurements.

Chapter 7

Validation of SCIAMACHY BrO Limb Profiles

Since balloon-borne BrO profiling is by nature infrequent with respect to both spatial and temporal coverage, improved instrumentation was required to monitor atmospheric BrO more closely. This shortcoming is only partially overcome by atmospheric BrO observations performed by the Global Ozone Monitoring Experiment (GOME) which has routinely monitored global atmospheric BrO vertical columns since 1996.

The SCIAMACHY (SCanning Imaging Absorption spectroMeter for Atmospheric CHartographY) instrument on the European Envisat (ENVironment SATellite) satellite provides the possibility of profiling BrO from space and receiving a global coverage within 3 days. Envisat was launched into a sun-synchronous low earth orbit on February 28, 2002. SCIAMACHY is a UV / visible / near-IR spectrometer, covering the wavelength range from 220 nm to 2380 nm at a moderate resolution of 0.2 to 1.5 nm (FWHM). It measures either direct sunlight during solar occultation, sunlight scattered by the moon during lunar occultation or sunlight scattered by the Earth's atmosphere in nadir or limb direction (e.g. [Bovensmann 1999]). In limb scattering mode, SCIAMACHY scans the Earth's atmosphere vertically in steps of 3.3 km from the ground to about 100 km tangent height with a vertical field of view (FOV) at the tangent point of ~ 2.8 km and a horizontal FOV of ~ 110 km. A horizontal scan is performed at each tangent height covering 960 km.

In order to exploit their full capacity, new satellite observations as performed by SCIAMACHY need to be validated by means of other established methods. In the case of atmospheric BrO limb profiling, validation is quite a challenging task not only because atmospheric BrO concentrations are low ($< 2 \times 10^7$ molecules/cm³) implying rather low atmospheric BrO absorption in the UV (Optical Densities $< \text{several } 10^{-3}$), but also because BrO is subject to considerable diurnal variation. Validation thus requires either perfect collocation of the validation observation with the satellite profiling (which in practice is not possible, see below), or other methods to account properly for possible temporal or spatial mismatches between both sets of observations.

This study reports on balloon-borne BrO profile measurements using different techniques, performed within the scope of Envisat / SCIAMACHY validation, which were performed for a wide range of geophysical conditions (high, mid and low latitudes during different seasons). The balloon observations include (a) balloon-borne *in situ* resonance fluorescence detection of BrO, (b) balloon-borne solar occultation DOAS measurements of BrO in the UV, and (c) BrO profiling from the solar occultation SAOZ (Système d'Analyse par Observation Zenithale) balloon instrument.

For validation purposes these measurements were coordinated to occur close to Envisat / SCIAMACHY overpasses. However, the large diurnal variation of the BrO radical and, to a lesser extent, presumably small spatial gradients in total stratospheric bromine (and thus BrO) prevent a direct comparison of the

balloon-borne and satellite limb measurements even if a perfect match of both observations i.e., in one altitude range at one time, could be achieved. Moreover, since the different instruments for BrO validation cannot be employed simultaneously and have different sources of random and systematic errors, a direct comparison of these established techniques is virtually impossible.

To overcome all these difficulties, this study uses the following approach: All balloon-borne BrO observations are considered with reference to simulations of the tried and tested 3-D CTM (Chemical Transport Model) SLIMCAT [*Chipperfield 1999; Chipperfield et al. 2005*]. If available, the referencing is achieved by comparing the model data with measured dynamic parameters (such as source gas profiles of N₂O, CH₄, ...) and photochemical parameters (profiles of O₃, NO₂, ...). In a second step, matching forward and backward air mass trajectories between the balloon and satellite observations are calculated [*Lumpe et al. 2003; Reimer and Kaupp 1997; Danilin et al. 2002*]. A 1-D photochemical model is run along the air mass trajectories on different altitude levels. The 1-D model is initialised with output data of the 3-D model and further constrained by measured dynamic and photochemical parameters. The total stratospheric bromine, regularly obtained by the DOAS instrument (see chapter 9), is also constrained in the 3-D and 1-D models. Finally, based on the different observations and dynamic and photochemical calculations, stratospheric BrO profiles adequate for comparison with SCIAMACHY are calculated. For some test cases first retrievals of SCIAMACHY BrO profiles are compared with these validation profiles.

This chapter is organised as follows; section 7.1 briefly describes the techniques used to obtain the BrO profiles from the individual instruments. Methods and tools used to model the photochemical change along trajectories are described in section 7.2. Section 7.3 reports on the individual measurements and comparisons with the SCIAMACHY BrO observations. This section is also describing further constraints of the 3-D model predictions as given by the various observations. These findings are interpreted and discussed in section 7.4 with respect to inherent errors of each measurement technique.

7.1 Balloon-Borne and Satellite BrO Measurements

Since the DOAS measurements, the DOAS BrO evaluation and the profile inversion are already described in chapters 4 and 6, this section will focus on the balloon-borne observations onboard the TRIPLE gondola and from the SAOZ instrument. The last part is dedicated to a short description of the SCIAMACHY BrO limb profiling.

7.1.1 Resonance Fluorescence BrO Measurements

Stratospheric profiles of BrO were measured *in situ* using the well-established chemical-conversion resonance fluorescence technique [*Brune et al. 1989*]. Stratospheric air is sucked through a rectangular duct by means of a Roots pump. The duct consists of an air inlet, an NO injector, one chlorine and two bromine detection modules stacked behind each other. NO is periodically injected into the air stream in order to convert BrO molecules to bromine atoms in a fast chemical reaction. The atoms are detected downstream by means of a resonance fluorescence arrangement working at 131.8 nm and consisting of a vacuum UV emission lamp and photomultiplier in a rectangular configuration. The photomultiplier signal consists of a background signal, due to Rayleigh and chamber scatter, and the Br resonance fluorescence signal when NO is added. From the difference signal between NO on and off periods (10 s each) Br atom concentrations can be derived employing a pressure dependent calibration. Laboratory calibrations are carried out before and after each flight using the fast chemical titration of chlorine atoms by molecular bromine to ensure the accuracy of the measurements [*Brune et al. 1989; Toohey et al. 1990*]. In brief, a known amount of chlorine atoms is titrated by bromine molecules forming an equivalent amount of bromine atoms and BrCl molecules in a very fast and quantitative reaction. The chlorine atom concentration is measured by vacuum UV absorption using the absorption cross section as determined by *Schwab and Anderson [1987]*.

Measured Br atom concentrations are converted into BrO initial concentrations by means of a kinetic

model employing seven relevant reactions generating and consuming Br atoms and measured temperatures and pressures. In this model, reaction rates as recommended by *Sander et al.* [2003] and rates as determined from intercomparisons of the independent Br atom measurements in modules B and C are used. Details are subject to a forthcoming publication. The overall accuracy of the measurements generally is about 35 % for BrO with a detection limit of about 5 pptv within 1 min. integration time in the altitude range between 18 and 30 km. Lower down, measurements suffer from oxygen absorption and at low pressures, starting at around 30 km, wall loss of Br atoms in the flow tube noticeably effects the measurement, explaining a possible low bias.

Within the framework of the SCIAMACHY validation campaigns, the TRIPLE multi-instrument payload performed 3 validation flights. TRIPLE consists of the Jülich ClO / BrO *in situ* instrument described above, the cryogenic whole air sampler of the University of Frankfurt for observation of long-lived tracers and the Jülich Fast *in situ* Stratospheric Hygrometer (FISH). An ECC ozone sonde (electrochemical concentration cell) was onboard for all flights, except on June 9, 2003.

7.1.2 SAOZ BrO Measurements

BrO is measured by solar occultation in the 320 – 400 nm UV spectral range during the afternoon ascent of the balloon at $\text{SZA} < 90^\circ$ and at the beginning of sunset from float altitude up to $92^\circ - 93^\circ$ SZA, when the contribution of scattered light becomes too large for continuing the measurements. In the following only the ascent data is used. The sunlight is collected by a combination of a conical mirror and diffusers within a field of view of 360° azimuth and $+15^\circ$ to -5° elevation.

The spectral resolution of the spectrometer is 0.9 nm with an oversampling of 10. There is no temperature stabilisation. The system is run at ambient temperature, cooling by about 15° C during the flight. The measurements are repeated every 30 s resulting in a vertical sampling of about 200 m during the balloon ascent. A full description of the instrument and the retrieval algorithm can be found in *Pundt et al.* [2002]. The spectral retrieval of BrO slant column densities is carried out with the WINDOAS algorithm [*Van Roozendael and Fayt* 2000] according to the settings described in *Pundt et al.* [2002]. Because of the small BrO SCD at relatively high sun during ascent, the data is smoothed with a triangular filter to increase the S/N ratio.

As a result, the altitude resolution is degraded to 3 km. Associated random errors are those provided by the spectral fit, averaged within the 3 km layer and divided by the square root of the number of data points. The data recorded in presence of clouds is removed using a colour index method.

Profile retrievals are carried out using the onion peeling technique. Random errors are propagated in the retrieval algorithm. Their amplitude increases at decreasing SZA. The impact of photochemical changes during the balloon ascent, and the contribution of scattered light, are ignored. As shown by *Pundt et al.* [2002] this may result in a maximum error of 0.17 pptv and 0.3 to 0.4 pptv respectively. The major systematic error comes from the uncertain estimation of the residual BrO column above float altitude. A constant BrO mixing ratio of 14 ± 2 pptv is generally assumed. The uncertainty arising from this decreases at decreasing altitude and is taken into account in the error bars shown. Systematic errors due to the BrO cross-section's uncertainty and its temperature dependence, estimated at $+5 / -10$ % by *Pundt et al.* [2002], are not included.

7.1.3 SCIAMACHY BrO Profile Retrieval

The Harvard Smithsonian algorithm is described elsewhere [*Sioris et al.* 2005]. The general spectral fitting and inversion equation are presented in *Sioris et al.* [2003]. Thus the method is only summarized here. Limb scan measurements contain two independent dimensions, namely wavelength and tangent height (TH). Therefore, the retrieval problem is divided into two steps: the spectral fitting and the inversion to obtain the vertical distribution. Radiances in the lower stratosphere are normalised with radiances from the upper atmosphere. This removes the Fraunhofer and Ring effect structure quite effectively. Absorption cross-sections and other pseudo-absorbers [*Sioris et al.* 2005] are fitted as basis functions to

the normalised radiances, resulting in observed BrO-SCDs, which are then interpolated onto a standard TH grid. This data analysis procedure is mimicked to obtain modelled BrO-SCDs. The modelling involves radiative transfer (RT) simulations [McLinden *et al.* 2002] to generate radiances that are then spectrally fitted. The vertical profile of BrO in the RT model is updated iteratively until convergence between modelled and measured BrO-SCDs is reached [Sioris *et al.* 2005]. A further convergence criterion has been added: if the agreement between modelled and observed BrO-SCDs at the bottom of the simulated TH range is not within 1 %, this relative difference must not increase monotonically with decreasing TH. This protects the retrieval from finding extreme values at the lower altitude limit. On March 25, 2004, the O₃ profile measured by DOAS in ascent [Butz *et al.* 2005] was used as a forward model input to the SCIAMACHY BrO retrieval since the model [McLinden *et al.* 2002] O₃ profile deviated from the true condition substantially due to dynamic reasons.

7.2 Modelling

To interpret the observations of atmospheric processes measurements must be compared with models. These models are used to verify the agreement between different measurements and the estimation of parameters or species that were not or cannot be measured. One application of models is the calculation of the diurnal variation of chemical species along trajectories of air parcels.

7.2.1 Trajectory Modelling

Balloon-borne measurements are inherently restricted by different constraints, limiting their flexibility in satellite validation. First, the launch window depends not only on the surface weather conditions, but also on stratospheric winds which determine the balloon's trajectory and the match location. Furthermore, the probed air masses of some balloon payloads are influenced directly by astronomical parameters, such as the solar zenith angle for solar occultation measurements (e.g., LPMA / DOAS payload). In practice, all these constraints make it difficult to match the temporal and spatial factors of the balloon measurements directly with the individual satellite measurements. Air mass trajectory matching can partly compensate for these restrictions [Lumpe *et al.* 2003].

Here, air mass trajectory calculations are used for matching the balloon-borne measurements with SCIAMACHY observations. The calculations are courtesy of K. Grunow and are performed at the FU-Berlin. The trajectory model uses the operational analysis and forecasts of the European Centre for Medium Range Weather Forecasts (ECMWF) - or a combination of both - given every 6 hours on a $2.5^\circ \times 2.5^\circ$ latitude / longitude grid. The ECMWF data is interpolated to 25 user-defined isentropic levels extending from the surface up to 1600 K. The internal time step for integrating the air masses' path is 10 minutes and the diabatic and climatological heating rates are based on Newtonian cooling. The results (trajectory points) are stored for each hour [Reimer and Kaupp 1997].

Backward and forward trajectories are started at the balloon measurement locations which depend on the individual measurement technique. In the case of the TRIPLE *in situ* payload, the air mass trajectory end and start points are given by the balloon trajectory. For the LPMA / DOAS and the SAOZ remote-sensing payloads, the start and end points are calculated from knowledge of the balloon flight trajectory and the known observation geometry given by the line-of-sight for each measurement. For post-flight analysis, air mass forward and backward trajectories are calculated for up to 10 days, but for balloon flight planning purposes the time range is limited by the available ECMWF forecasts (analyses are available up to 12 UT of the day before, forecasts for every 6 hours up to 72 hours). The actual geolocations of SCIAMACHY observations are taken from the SCIAMACHY Operational Support Team (SOST) on its website (<http://atmos.af.op.dlr.de/projects/scops/>). Here, the overpass time, the geolocation and detailed measurement specifications (e.g. swath, measurement duration, ground pixel size) can be downloaded for the SCIAMACHY limb and for the SCIAMACHY nadir mode for each Envisat orbit. For the air mass trajectory-based matching technique only the area covered by tangent points (light blue areas in Figure 7.1 - similar plots for all DOAS flights discussed here,

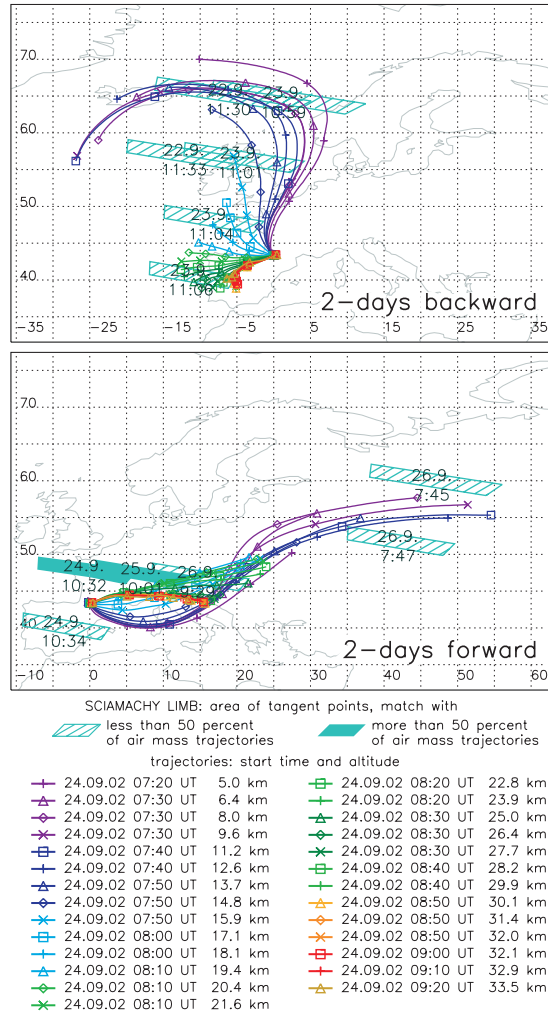


Figure 7.1: Two days backward (upper panel) and forward (lower panel) air mass trajectories for TRIPLE ascent observations at Aire sur l'Adour, France, on September 24, 2002. Envisat / SCIAMACHY orbit numbers matching with the TRIPLE trajectory are 2940, 2954, 2968, 2982, 2995, and 2996. The light blue rectangles represent the area probed by SCIAMACHY limb observations.

can be found at the end of this chapter, see Figure 7.12 to 7.15) of SCIAMACHY limb observation is considered in more detail. This information is used to find satellite measurement points along individual air mass trajectories, for which the spatial and temporal mismatch is as small as possible. The match criterion is chosen based on the experience of the ozone Match experiment [von der Gathen *et al.* 1995]: a time mismatch between the satellite observation and the air mass trajectory started at the balloon observation of $< \pm 1$ hour and an area mismatch of $< \pm 500$ km. If SCIAMACHY observations do not fulfil these criteria, the distance criterion is extended up to 1000 km. In this study only SCIAMACHY limb measurements are considered.

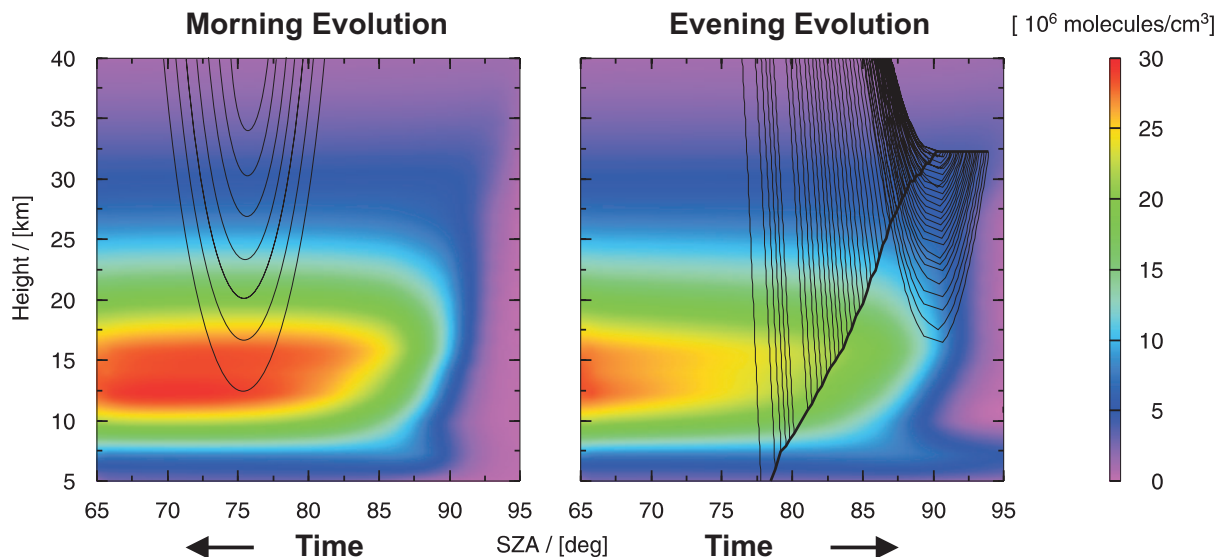


Figure 7.2: Colour-coded model concentration field of BrO as a function of height and SZA, for the DOAS balloon flight on March 23, 2003 at Kiruna (67.9°N, 22.1°E). Left and right panels show the morning and evening evolution of BrO respectively. The black lines in the left panel represent the line-of-sight of a SCIAMACHY limb scan. In the right panel the observation geometry of the DOAS measurements is shown for every twentieth spectrum measured during ascent and every tenth spectrum during solar occultation. The thick black line represents the trajectory of the balloon and the thin black lines indicate the optical path from the Sun to the balloon instrument for measurements during ascent and solar occultation. Note that in the real atmosphere the lines-of-sight are close to being straight lines, but the projection of the Earth's curvature on a straight x -axis causes the lines-of-sight to appear curved in the presentation.

7.2.2 Chemical Modelling

As outlined above, the use of a validated 3-D CTM photochemical model is necessary when different measurements of stratospheric radicals are compared and validated. Figure 7.2 demonstrates why the model has to be used to compare SCIAMACHY BrO limb measurements, left panel, with LPMA / DOAS balloon ascent and occultation observations shown in the right panel. The measured line-of-sight BrO absorption is indicated by the thin black lines in both panels. In addition, the thick black line in the right panel represents the balloon trajectory. Here, the observations are superimposed a photochemical simulation of stratospheric BrO from the SLIMCAT 3-D CTM [Chipperfield 1999] for March 23, 2003. The observation geometry for SAOZ measurements is basically the same as for LPMA / DOAS. For TRIPLE observations the situation is less complicated since measurements are performed *in situ*, but still at varying SZA.

SLIMCAT is a 3-D off-line CTM with detailed treatment of the stratospheric photochemistry. The model temperatures and horizontal winds are specified from analyses and the vertical transport in the stratosphere is diagnosed from radiative heating rates. In the stratosphere the model uses an isentropic coordinate extended down to the surface using hybrid sigma-theta levels [Chipperfield 2005]. The troposphere is assumed to be well-mixed.

The CTM was integrated with a horizontal resolution of $7.5^\circ \times 7.5^\circ$ and 24 levels extending from the surface to about 55 km. The model was forced using ECMWF analyses and the simulation started on January 1, 1977. The model halogen loading was specified from observed tropospheric CH_3Br and halon loadings [WMO 2003]. In addition, an extra 4 pptv bromine was modelled in a tracer to represent

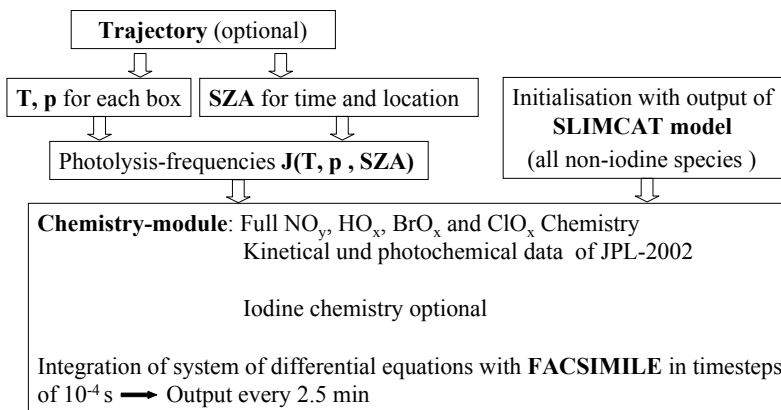


Figure 7.3: Schematic overview of the 1-D photochemical model.

bromine-containing very short-lived species (VSLs) and 1 pptv was assumed to be transported to the stratosphere as Br_Y (see *Chipperfield et al.* [2005] and chapter 9 for more details). Accordingly, the total stratospheric bromine loading around 2000 is approximately 21 pptv. Output was saved at 0 UT every 2 days, interpolated to the location of the balloon flights. A 1-D column model was then used to reconstruct the diurnal cycle for comparison with the observations.

The 1-D Chemical Box Model LABMOS¹ is based on the 0-D box model by *Helmling* [1994]. It has been updated and extended to allow for trajectory calculations by *Erle* [1999], *Fitzenberger* [2000] and *Bösch* [2002]. A schematic overview of the model and its input parameters is given in Figure 7.3. Within the scope of this study the model was updated to JPL-2002 kinetics [*Sander et al.* 2003] and extended to 20 potential temperature (Θ) levels between $\Theta = 323 \text{ K}$ ($\simeq 9 \text{ km}$) and $\Theta = 1520 \text{ K}$ ($\simeq 42 \text{ km}$).

The 1-D model calculates the stratospheric photochemistry on forward and backward air mass trajectories with the aim to find best guess profiles for the satellite observations based on the different validation balloon measurements. The model contains bimolecular and trimolecular gas phase reactions as well as photochemical (see section 3.1.2) and heterogeneous reactions. The heterogeneous reactions used in the model are treated according to the parameters given by *Hanson et al.* [1994] (see also section 2.2.5). A complete list of all reactions included in the model can be found e.g. in *Fitzenberger* [2000]. Aerosol loadings are taken from *Deshler et al.* [2003] as recommended by *Dufour et al.* [2005]. Photolysis rates are interpolated with respect to pressure, temperature, overhead ozone and solar zenith angle (SZA) from a SLIMCAT lookup table where the actinic fluxes are calculated as recommended by *Lary and Pyle* [1991] and validated for J_{NO_2} by *Bösch et al.* [2001].

If available, the 1-D model is initialised at 0 UT with 3-D CTM SLIMCAT output of the same day at the balloon launch site. If output is not available on the day of the balloon flight, a decision is made whether to take output from the day before or the day after the flight by comparing measured O_3 , NO_2 and / or tracers such as CH_4 and N_2O with the model and choosing the output that best matches the measurement.

The model is run with fixed pressure and temperature for each Θ level taken from the meteorological support data of the balloon flight; the SZA time-line is taken from the air mass trajectory calculations. In satellite validation these measures guarantee that the photochemical evolution of the modelled air mass corresponds to the true evolution between initialisation of the model, the satellite measurement and balloon-borne observation. For simplicity a single representative SZA time-line is chosen for all Θ levels. Furthermore, each BrO observation conducted by the remote sensing instruments SCIAMACHY, SAOZ and DOAS is a composite of changing photochemical conditions (due to changing SZA) along the line-of-sight. Arguably gradients in BrO arising from this effect are the smallest for the SCIAMACHY observations since it takes measurements during late morning (around 10:30 LT), i.e. far from sunset or sunrise.

¹LAGrangian MOdel of the Stratosphere

Hence a fixed SZA for SCIAMACHY observations is assumed.

Photochemical-weighting factors are calculated to scale balloon observations to the photochemical conditions of the satellite measurements. In the case of DOAS measurements the scaling is performed prior to profile inversion as described in section 6.2.3, thus compensating photochemical changes during the ascent measurements of the balloon. For TRIPLE and SAOZ measurements, the ratio of the model profile at the SZA of the satellite measurement and the model profile at the SZA of the balloon measurement is calculated, and used to scale the profiles accordingly.

The modelling errors are estimated by sensitivity studies following a similar approach as described in *Bracher et al.* [2005]. Several model runs are performed along a representative air mass trajectory with varying model parameters that are important for the photochemical variation of BrO. These parameters include the NO₂ and O₃ profile ($\pm 30\%$), overhead ozone ($\pm 35\%$), the temperature for each Θ level ($\pm 7\text{K}$), the rate constants of reaction BrO + O₃ and BrO + NO₂ ($\pm 20\%$ and $\pm 15\%$), the photolysis rate of BrO and BrONO₂ ($\pm 15\%$) and the aerosol surface area ($\pm 100\%$). The root-mean-square deviation of the vertical profiles from the standard run gives the estimate of the modelling error and therefore the error of the scaling. Although individual profiles can deviate significantly from a standard run profile at the same SZA (e.g. for varied NO₂ profile or J_{BrONO_2} the difference is around 12 % and 10 % at the concentration maximum respectively), the scaling of profiles is hardly affected since the ratio of two profiles of the same model run is used. In the relevant altitude layer between 10 km and 30 km a scaling error of 5 % was obtained. Whenever photochemically-corrected trace gas profiles are shown, the modelling error is added applying Gaussian error propagation.

7.3 Observations and Further Constraints on the Photochemical Modelling

An overview of balloon flights conducted within the framework of the SCIAMACHY validation is given in Table 7.1. It includes information about the date and location of the soundings, the geophysical condition and the SZA range of the measurements (first 4 columns). The right part of the table provides the relevant information with respect to the ‘best’ matching SCIAMACHY limb observations, as indicated by the calculated forward and backward air mass trajectories. For each balloon flight one ‘best’ match is identified for the backward trajectory and one for the forward trajectory calculations. The orbit number and overpass time, the altitude range in which the match obeys the match criteria, the maximum time delay between SCIAMACHY and balloon measurement and the spatial distance between trajectories and SCIAMACHY measurement are given for each match. For future validation exercises using balloon measurements, it is thus recommended to use these identified pixels in SCIAMACHY profile retrieval exercises.

Figures 7.4 to 7.8 display the key findings of the study using the examples of a TRIPLE flight conducted on September 24, 2002 at Aire sur l’Adour, France, a SAOZ flight on January 31, 2004 at Bauru, Brazil, and three DOAS flights on March 23, 2003 and March 24, 2004 at Kiruna, Sweden, and on October 9, 2003 at Aire sur l’Adour, France. The examples are chosen in order to cover a wide range of different geophysical conditions. Each figure shows the original measured BrO profiles i.e., the photochemically-uncorrected balloon measurement (solid black squares) and, if available, the BrO profile as inferred from matching SCIAMACHY observations (red dots). Both sets of observations show large discrepancies primarily due to (1) inherent errors of the measurements, (2) the different daylight time of the individual observations and thus photochemistry-related changes in stratospheric BrO, or (3) possible spatial gradients in stratospheric bromine, although this factor is less likely. For reasons related to (1) the reader is recommended to refer to the relevant literature for each of the techniques used [*Pundt et al.* 2002; *Brune et al.* 1989; *Ferlemann et al.* 1998; *Sioris et al.* 2005]. Within the scope of this study, reasons related to (2) and (3) are dealt with using the trajectory model, the 1-D photochemical model and the SLIMCAT 3-D CTM model. Before correcting the measured BrO profiles for photochemistry and dynamics, further constraints are discussed, which arise from each observation and that can be used for photochemical modelling.

Table 7.1: Compendium of balloon-borne BrO measurements and Envisat / SCIAMACHY overpasses. BA, BD and SO denote balloon ascent, balloon descent and solar occultation, respectively.

Date Time / UT	Location	Geophys. Cond. SZA range	Instrument Observ. Geom.	Satellite coincidence Orbit, Date, Time / UT	Altitude - range / km	Time - delay / h	Spatial - distance / km
Aug. 12, 02 18:15 - 19:10	Kiruna 67.9°N, 21.1° E	high lat. summer SZA: 85° - 89°	SAOZ BA	2342, 11.08.02, 18:21 2352, 12.08.02, 09:37	18 - 30 5 - 30	-24.8 -9.6	179 - 494 182 - 495
Sept., 24, 02 7:08 - 11:39	Aire sur l'Adour 43.7°N, 0.3° W	mid-lat fall SZA: 44° - 88°	TRIPLE BA / BD	2954, 23.09.02, 11:06 2968, 24.09.02, 10:32	21 - 29 16 - 33	-21.6 -2.5	379 - 491 449 - 499
Oct. 1, 02 16:35 - 17:25	Aire sur l'Adour 43.7° N, 0.3° W	mid lat. fall SZA: 79° - 88°	SAOZ BA	3068, 01.10.02, 10:13 3082, 02.10.02, 09:42	13 - 29 13 - 29	-7.1 +17.0	278 - 487 265 - 493
Feb. 23, 03 20:42 - 21:30	Bauru 22.4° S, 49.0°W	subtropics summer SZA: 76° - 85°	SAOZ BA	5145, 23.02.03, 12:56 5160, 24.02.03, 14:04	16 - 21 24 - 28	-8.2 +16.7	403 - 486 125 - 462
March 6, 03 6:25 - 10:49	Kiruna 67.9° N, 21.1° E	high lat. winter SZA: 72° - 86°	TRIPLE BA / BD	5288, 05.03.03, 12:13 5301, 06.03.03, 10:04	16 - 28 5 - 31	-19.6 +3.7	4 - 481 403 - 499
March 16, 03 15:19 - 16:09	Kiruna 67.9°N, 21.1° E	high lat. spring SZA: 84° - 89°	SAOZ BA	5418, 14.03.03, 14:08 5484, 19.03.03, 04:52	23 - 29 16 - 23	-50.0 +61.2	46 - 473 9 - 452
March 23, 03 14:47 - 17:35	Kiruna 67.9° N, 21.1° E	high lat. spring SZA: 79° - 95°	LPMA / DOAS BA / SO	5545, 23.03.03, 11:07 5558, 24.03.03, 09:01	18 - 28 19 - 29	-5.2 +17.4	268 - 496 10 - 495
March 30, 03 16:01 - 16:53	Kiruna 67.9°N, 21.1° E	high lat. spring SZA: 83° - 88°	SAOZ BA	5645, 30.03.03, 10:49 5658, 31.03.03, 08:37	5 - 29 5 - 23	-6.0 +16.8	88 - 307 47 - 494
June 9, 03 4:57 - 9:52	Kiruna 67.9° N, 21.1° E	high lat. summer SZA: 45° - 70°	TRIPLE BA / BD	6652, 08.06.03, 19:01 6661, 09.06.03, 10:18	5 - 31 5 - 34	-11.6 +5.1	19 - 499 60 - 494
Oct. 9, 03 15:39 - 17:09	Aire sur l'Adour 43.7°N, 0.3° W	mid-lat fall SZA: 66° - 88°	LPMA / DOAS BA	8407, 09.10.03, 09:51 8421, 10.10.03, 09:20	17 - 31 25 - 33	-6.5 +17.2	738 - 988 547 - 977
Jan. 31, 04 20:54 - 21:46	Bauru 22.4° S, 49.0°W	subtropics summer SZA: 76° - 86°	SAOZ BA	10040, 31.01.04, 12:06 10055, 01.02.04, 13:15	25 - 30 15 - 21	-9.7 +16.1	287 - 492 33 - 488
Feb. 5, 04 20:25 - 21:12	Bauru 22.4° S, 49.0°W	subtropics summer SZA: 70° - 80°	SAOZ BA	10112, 05.02.04, 12:51 10127, 06.02.04, 13:59	5 - 21 25 - 29	-8.0 +17.0	229 - 495 179 - 479
March 24, 04 13:55 - 17:35	Kiruna 67.9° N, 21.1° E	high lat. spring SZA: 72° - 95°	LPMA / DOAS BA / SO	10798, 24.03.04, 10:35 10811, 25.03.04, 08:24	12 - 33 20 - 26	-5.4 +17.1	371 - 499 383 - 494
June 17, 05 18:32 - 21:07	Teresina 5.1° S, 42.9°W	tropics winter SZA: 61° - 94°	LPMA / DOAS BA / SO	17240, 17.06.05, 11:53 17255, 18.06.05, 13:02	25 - 30 5 - 33	-8.1 +18.4	382 - 491 6 - 490

7.3.1 Photochemical Modelling and its Constraints

Before addressing photochemical modelling in more detail, 3 different constraints for the modelling are discussed. These constraints are obtained from the balloon soundings performed within the scope of this study - total stratospheric bromine, vertical transport and photochemical constraints.

Total Stratospheric Bromine

For stratospheric sounding of the LPMA / DOAS payload, total stratospheric bromine (Br_Y) can be inferred for altitudes above balloon float altitude. Such a constraint is particularly important because it largely constrains Br_Y in the lower stratosphere (taken here from the tropopause to the balloon float altitude). Stratospheric Br_Y concentrations are known to have levelled-off in recent years and thus spatial gradients (~ 1 pptv across the global stratosphere) in Br_Y due to different age of air masses are expected to be small (for details see [Montzka et al. 2003]). Once total stratospheric Br_Y is known, an accurate constraint is available for stratospheric BrO taking $[\text{BrO}] \leq [\text{Br}_Y]$. BrO can in principle be further constrained, though less accurately, using results from a photochemical model.

Here, observations made on October 9, 2003 at Aire sur l'Adour are used to infer total stratospheric Br_Y from DOAS measurements. For details on total stratospheric Br_Y , see chapter 9. A Langley plot is performed, where the slope of measured BrO absorption is analysed as a function of the calculated total air mass at balloon float altitude (33 km), covering a SZA range between 84.27° and 87.52° (Figure 9.3). For this observation the slope of the least-squares-fitted data results in an average BrO mixing ratio of (14.5 ± 1.5) pptv above 33 km. For this flight, the SLIMCAT calculations show that the $[\text{BrO}] / [\text{Br}_Y]$ ratio is around 0.76 at 33 km, 0.8 at 36 km, 0.76 at 40 km, 0.54 at 45 km, and 0.23 at 50 km. The line-of-sight weighted average is concluded to be 0.72 for these conditions. Combining all uncertainties, the measurement thus indicates $[\text{Br}_Y] = (20.1 \pm 2.8)$ pptv above 33 km at northern mid-latitudes by late

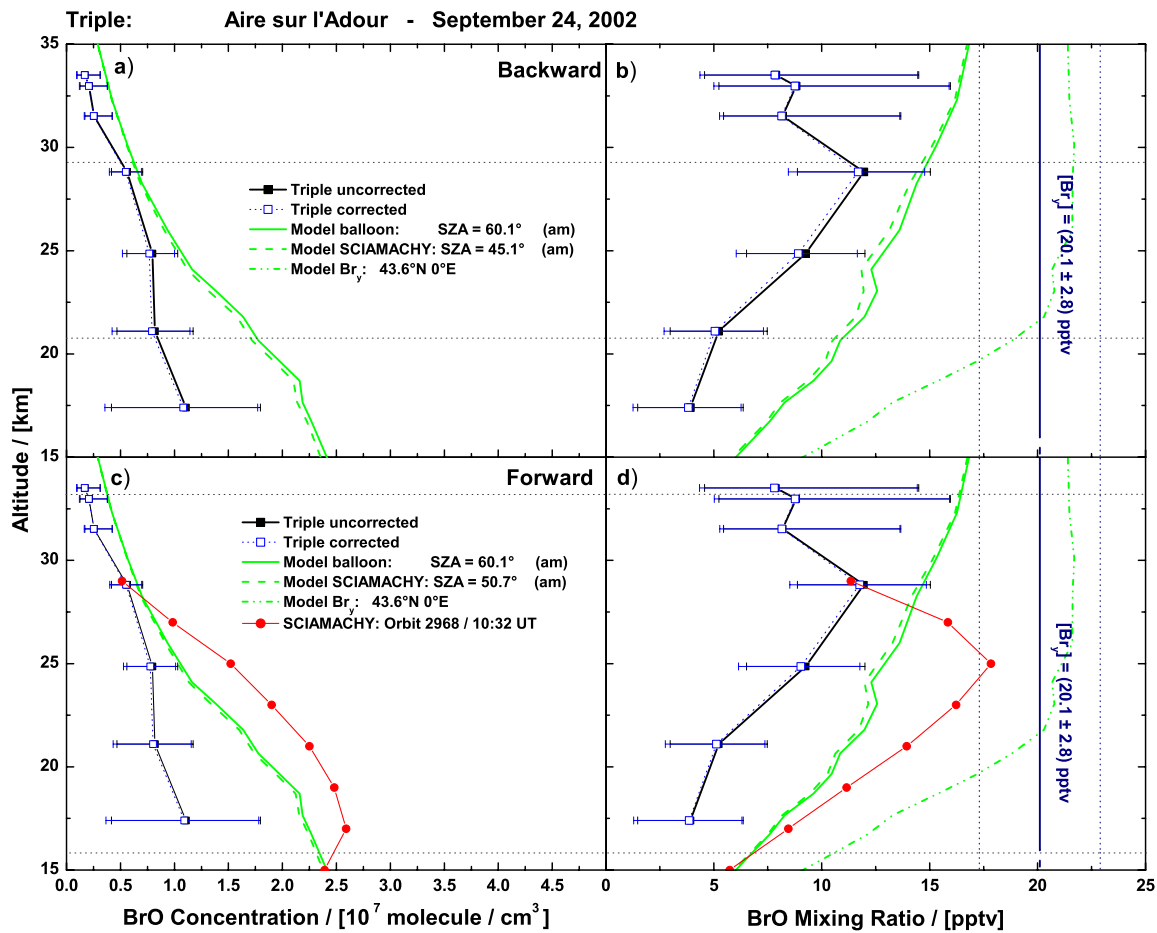


Figure 7.4: Comparison of a BrO profile measured by TRIPLE during balloon ascent on September 24, 2002 at Aire sur l'Adour with model calculations and SCIAMACHY limb retrievals. Black squares represent the photochemically-uncorrected balloon measurement and blue squares the balloon profile photochemically corrected to the SZA of the SCIAMACHY measurement. Corresponding model profiles at the SZA of the balloon and satellite observations are shown as solid and dashed green lines respectively. Total inorganic Br_γ volume mixing ratios as used in the model (green dash-dotted line) and as retrieved by DOAS measurements (vertical dark blue lines - see text for details) are also indicated. SCIAMACHY measurements are shown as red circles and the altitude range for the match (as given in Table 7.1) is indicated as thin dotted horizontal lines. Panels a) and b) show calculations for the 'best' backward match and panel c) and d) for the 'best' forward match. Concentrations and volume mixing ratios are given for each case.

2003 (see chapter 9).

Vertical Transport

The diabatic vertical transport in the stratosphere is also known to be of particular concern in 3-D CTM modelling i.e., for high (Arctic) and low (tropical) latitudes [Chipperfield 1999]. In order to compensate for potential deficits in the vertical transport, the tracers N₂O and CH₄, which are available for TRIPLE

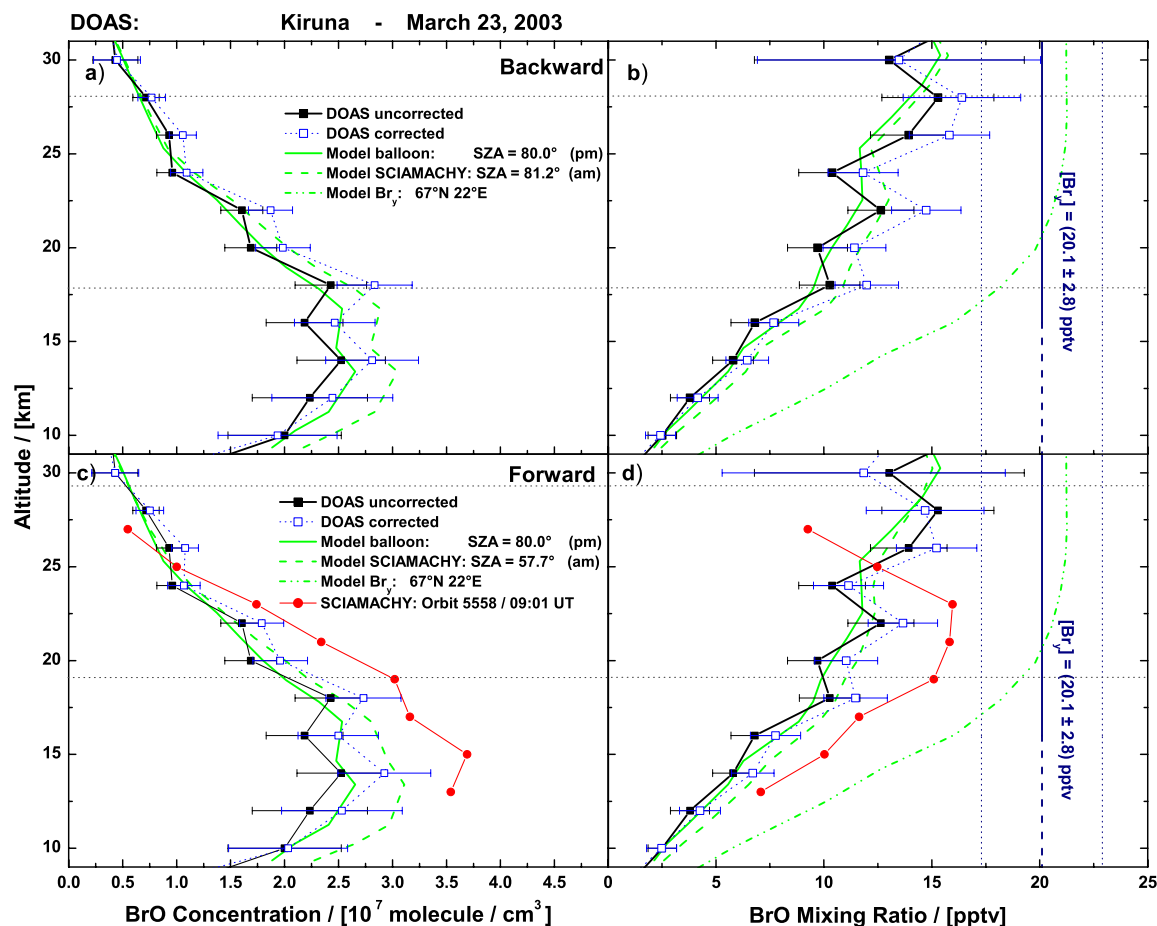


Figure 7.5: Same as Figure 7.4, but for a BrO profile measured by DOAS during balloon ascent on March 23, 2003 at Kiruna.

and LPMA / DOAS flights, are also compared with the 3-D CTM output. Since dynamic tracers are not measured simultaneously for the SAOZ flights, O_3 is used as an indicator for the vertical transport. In particular, the vertical transport is tested for the balloon flights presented in this study, as follows: For the TRIPLE flight on September 24, 2002 it is found that the measured dynamic tracers N_2O and CH_4 agree excellently with the CTM SLIMCAT simulations. Good agreement with SLIMCAT is also found for the LPMA / DOAS flight on March 23, 03 (right panel in Figure 7.9). Unfortunately for the October 9, 2003 and the March 24, 2004 LPMA / DOAS flight no LPMA profiles are available to date, thus measured and modelled tracer profiles cannot be compared. Therefore, the dynamics are verified by the O_3 profile simultaneously recorded with the DOAS instrument, see left panels in Figure 7.10 and Figure 7.11. For the October 9, 2003 flight N_2O SCDs measured by the LPMA instrument are available and compared with modelled values in the right panel of Figure 7.10. Measured values correspond well with the model and thus also indicate no large inconsistencies in the dynamics. The same procedure was performed for the SAOZ flight on January 31, 2004 since no other transport tracers were available. In all three cases the measured O_3 profile is found to correspond well with the model.

The overall good agreement of the model with the tracer data supports the findings of *Feng et al.* [2005] who found that the version of SLIMCAT used here, with the CCM radiation scheme, performed well in this respect. Therefore, large uncertainties in the vertical transport are considered unlikely for the balloon flights discussed here.

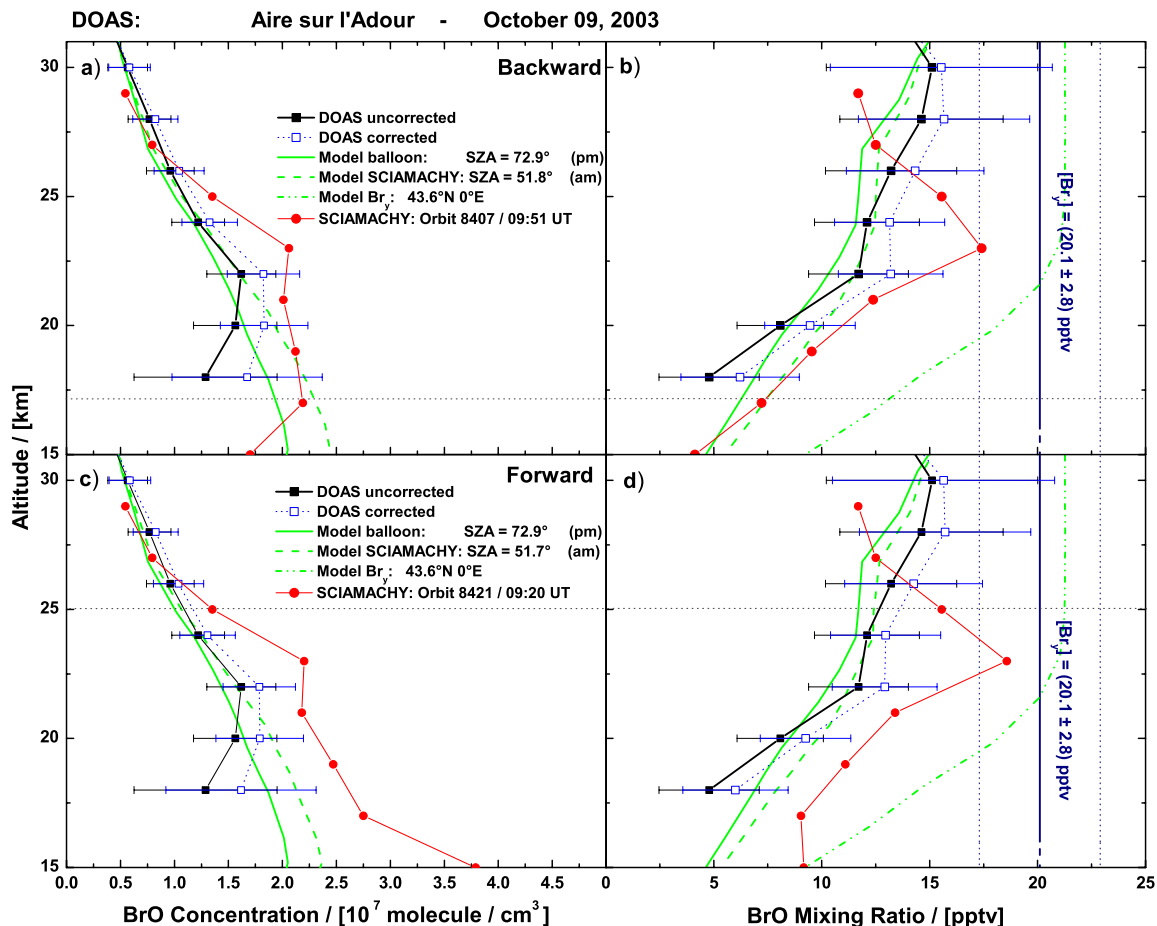


Figure 7.6: Same as Figure 7.4, but for a BrO profile measured by DOAS during balloon ascent on October 9, 2003 at Aire sur l'Adour.

Photochemistry and its Constraints

Potential disagreement between observations and the model also arises from photochemistry-related uncertainties (see e.g. *Canty et al.* [2005]). It is found useful to constrain the 1-D photochemical calculations with the measured abundances of NO_2 and O_3 [*Bracher et al.* 2005]. BrO reacts efficiently with NO_2 to BrONO_2 , with the photolysis of BrONO_2 being the most important back reaction during daytime. Therefore, stratospheric BrO is strongly dependent on NO_2 and an appropriate scaling of the 1-D photochemical modelling may reduce potential errors in BrO comparison studies to a great extent. Fortunately for the SAOZ and DOAS BrO observations such a scaling can easily be performed since NO_2 and BrO profiles are measured simultaneously. For the TRIPLE BrO observation such a scaling of modelled/measured NO_2 is more difficult since the NO_2 is not measured on that payload. Therefore, SCIAMACHY NO_2 observations [*Sioris et al.* 2004] are used, which were validated by balloon measurements by *Butz et al.* [2005].

The SCIAMACHY NO_2 profile for the TRIPLE flight on September 24, 2002 matches the model values between 22 and 33 km but shows up to 50 % smaller concentrations below 22 km. The accuracy of the SCIAMACHY measurements is discussed in *Butz et al.* [2005]. Model values of NO_2 for the SAOZ flight on January 31, 2004 basically agree with the measured profile within the given error bars below 25 km but

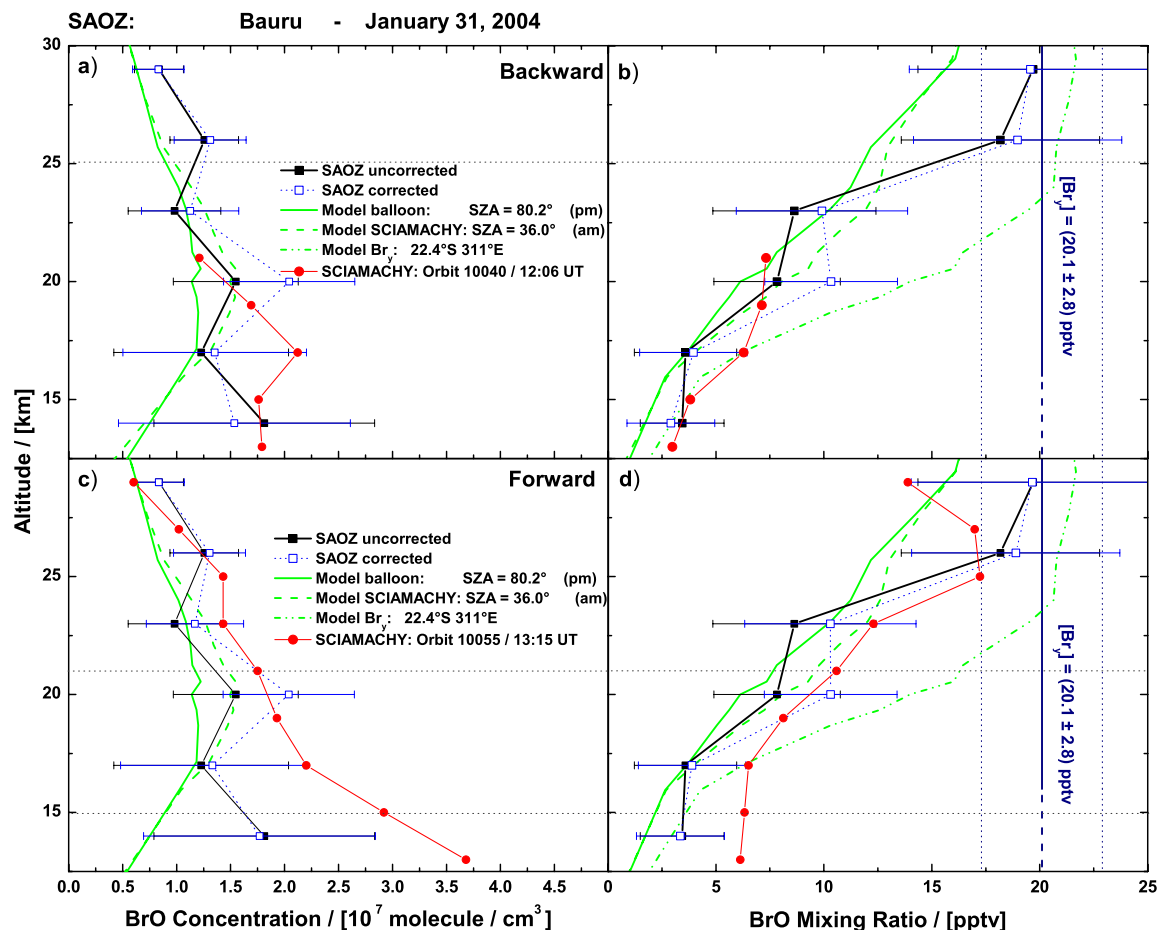


Figure 7.7: Same as Figure 7.4, but for a BrO profile measured by SAOZ during balloon ascent on January 31, 2004 at Bauru.

are systematically lower ($\sim 30\%$ at 20 km). Above 25 km, up to balloon float altitude at around 30 km, the agreement is very good. For the DOAS flight on March 23, 2003 the model NO_2 shows systematically higher values (10% – 40%) above 15 km than indicated by observations (left panel in Figure 7.9). The DOAS NO_2 observations on October 9, 2003 coincide with the model above 27 km and below 20 km within the given errors, but the model profile is up to 40% higher in-between. As shown in the right panel of Figure 7.11, model results for March 24, 2004 underestimate DOAS measurements below 20 km by 10% – 20% and overestimate them above 22 km up to balloon float altitude by up to 20%. Further photochemistry-related uncertainties in the SAOZ and DOAS observations are kept small when only using measurements for $\text{SZA} \leq 88^\circ$, i.e. discarding solar occultation profiles from SAOZ and DOAS.

7.4 Results and Discussion

Panels a) and b) in Figures 7.4 to 7.8 show concentration and volume mixing ratio (VMR) profiles for the ‘best’ backward match and panels c) and d) show corresponding profiles of the ‘best’ forward match. Each panel shows the original measured, photochemically-uncorrected BrO balloon measurement (solid black squares) and the photochemically-corrected BrO profile (open blue squares), which is to be compared with the SCIAMACHY measurement of the corresponding ‘best’ backward or forward match. The orbit

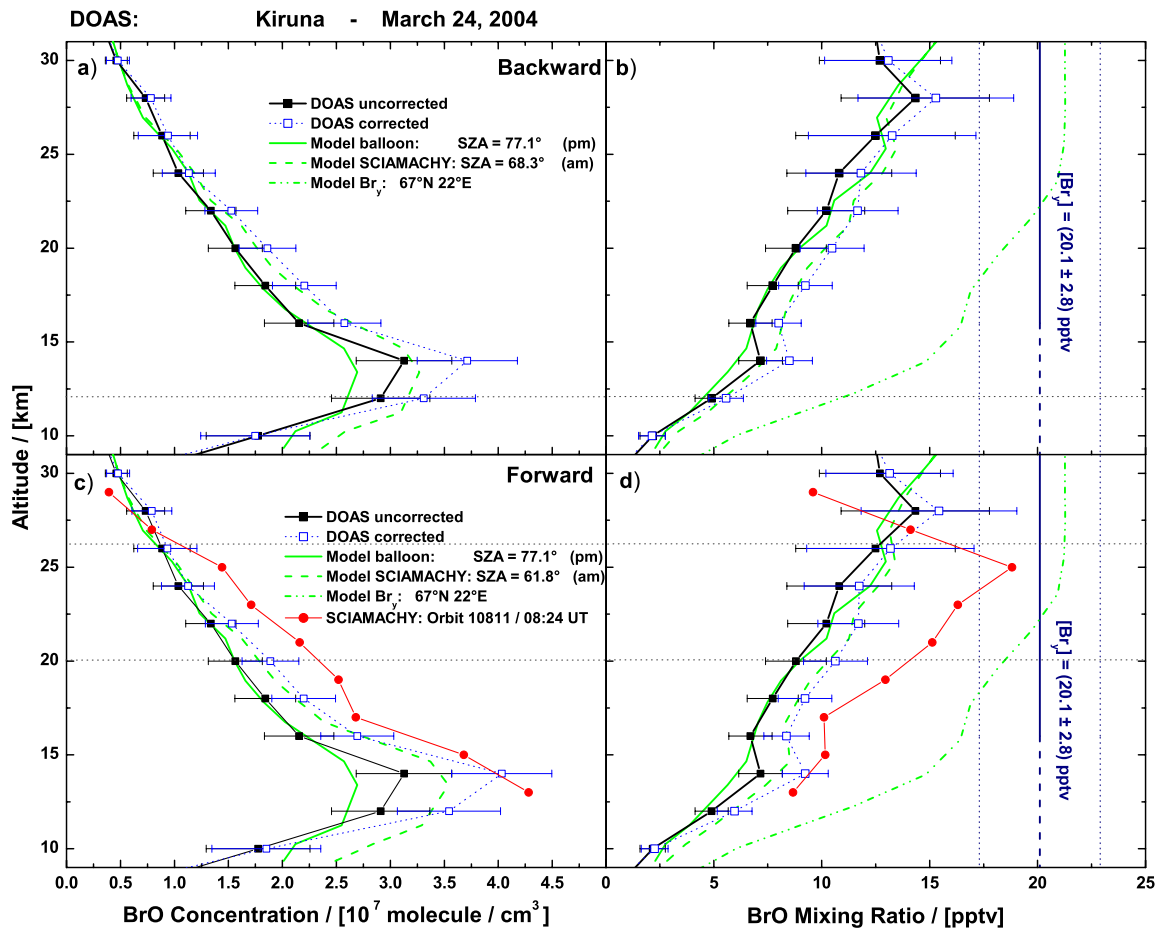


Figure 7.8: Same as Figure 7.4, but for a BrO profile measured by DOAS during balloon ascent on March 24, 2004 at Kiruna.

number and time of each SCIAMACHY match are given in the label of each figure and in Table 7.1. Error bars of the photochemically-corrected profiles include the estimated error for the photochemical scaling as described in section 7.2. Model profiles at the SZA of the balloon and the satellite observation are shown as solid and dashed green lines, respectively. Total inorganic Br_γ volume mixing ratios as used in the model are also indicated as dash-dotted green line. SCIAMACHY measurements are shown as red circles and the altitude range which fulfils the match criteria (as summarized in Table 7.1), is indicated by the thin dotted horizontal lines. In cases where only one horizontal line is plotted (e.g. backward match in Figure 7.8), the match criteria are fulfilled above the indicated altitude, over the entire plotted range. Certain orbits of Level 1 SCIAMACHY data remain unavailable and cannot be presented in this study. Total inorganic Br_γ and its uncertainty, inferred from DOAS BrO as described above, is marked by dark blue vertical lines.

TRIPLE mid-latitude measurements on September 24, 2002 were performed between 55.6° and 67.9° SZA. The value SZA = 60.1° was chosen as a scaling reference for the balloon observation. The SZA of the SCIAMACHY measurement is 45.1° for the backward match and 50.7° for the forward match. Since satellite and balloon measurements were taken in the morning well after sunrise, and the diurnal variation of BrO during the morning is rather small (see Figure 7.2), the scaling over the entire altitude range is < 5 %, for both the backward and forward match. Model results over the entire

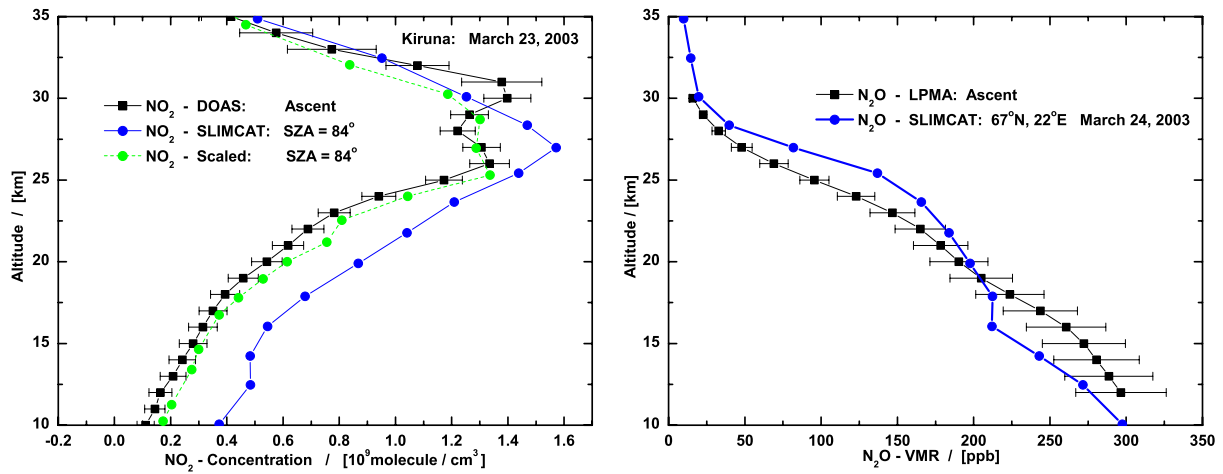


Figure 7.9: NO_2 and N_2O profiles measured by the LPMA / DOAS instruments during balloon ascent at Kiruna on March 23, 2003.

altitude range are much larger than TRIPLE measurements. Comparing the dynamic tracers N_2O and CH_4 between model predictions and TRIPLE measurements, shows good agreement. NO_2 was scaled to match SCIAMACHY observations of the 10:32 UT limb scan of orbit 2968, the same forward match used for BrO comparison. SCIAMACHY NO_2 profiles tend to show lower values below 20 km than balloon validation measurements [Butz *et al.* 2005], possibly causing an overprediction of BrO in the model. However, even if no NO_2 scaling is performed in the model, modelled BrO is much higher than TRIPLE measurements. Thus, apart from unknown instrumental problems, the discrepancy between modelled and measured BrO cannot be explained. Although the time lag for the backward match between the satellite and the balloon measurement is quite short (-2.5 h) and match criteria are fulfilled between 16 and 33 km (see Table 7.1), the corresponding SCIAMACHY profile is too large for observations below 27 km.

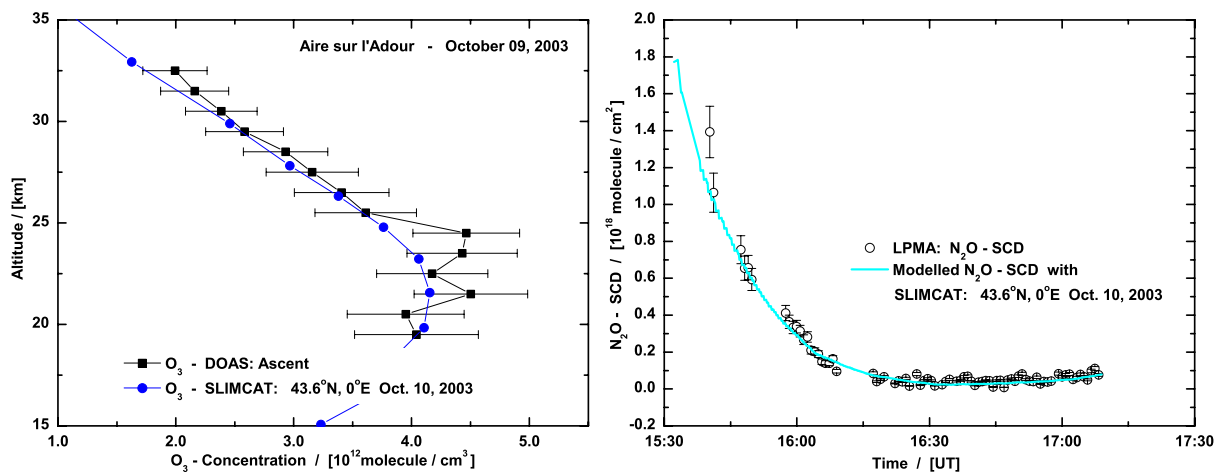


Figure 7.10: O_3 profile and N_2O - SCD values measured by the LPMA / DOAS instruments during balloon ascent at Aire sur l'Adour on October 09, 2003.

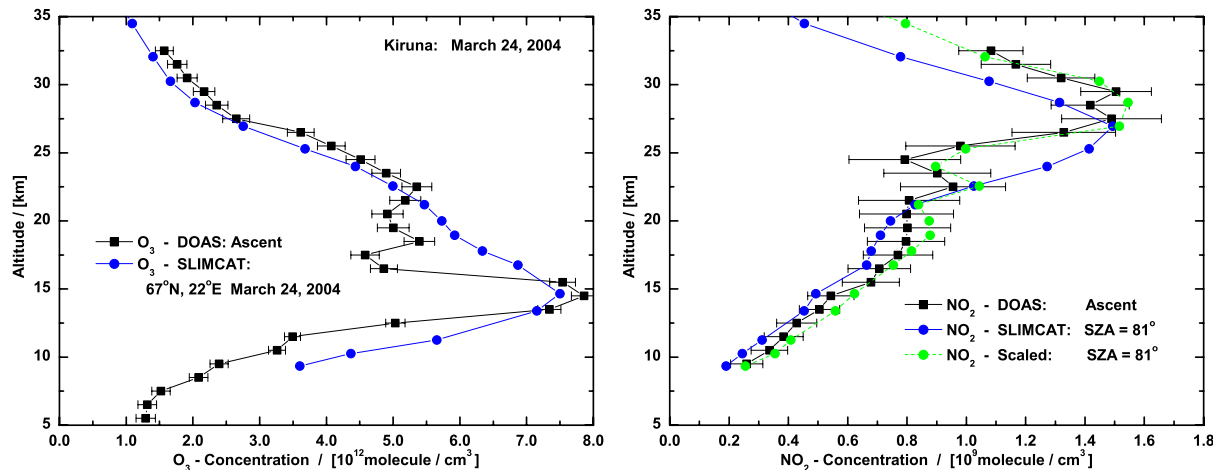


Figure 7.11: O_3 and NO_2 profiles measured by the DOAS instrument during balloon ascent at Kiruna on March 24, 2004.

DOAS high-latitude ascent measurements taken on March 23, 2003 were performed between 77.9° and 88.8° SZA. For comparison the model output is plotted at 80.0° SZA. The photochemically corrected DOAS profile is obtained as described in section 7.2 and by *Butz et al.* [2005]. The SZAs of the SCIAMACHY backward and forward match are 81.2° and 57.7° , respectively. Compared to the TRIPLE flight, the scaling for the backward and forward match is much higher (up to 15%) since DOAS measurements took place during late afternoon, before sunset. The agreement of the dynamic tracers N_2O and CH_4 between model predictions and LPMA measurements is warranted and NO_2 was scaled to DOAS measurements in the 1-D model, as described in section 7.3.1. The overall agreement with the model is very convincing for the photochemically-uncorrected and corrected profiles. The SCIAMACHY profile for the forward match has a time delay of +17.4 hours and match criteria are obeyed from 19 to 29 km. SCIAMACHY values for this profile are in general higher than predicted.

DOAS mid-latitude ascent measurements taken on October 9, 2003 were performed between 71.0° and 81.5° SZA. For comparison purposes, the model output is plotted at 72.9° SZA. Since the SZAs of the SCIAMACHY backward and forward matches are 51.8° and 51.7° , respectively, both scalings are similar. Due to strong oscillations of the gondola, measurements could only begin at ~ 16 km, causing higher uncertainty of the lowest profile point at 18 km. Agreement of the dynamic tracers between model predictions and LPMA measurements could not be assessed, since no LPMA data is available to date. Therefore, dynamics were verified by O_3 measurements, which showed good agreement over the altitude range covered. NO_2 was scaled in the 1-D model as before. DOAS measurements coincide well with the model over the entire range. The SCIAMACHY profile for the backward match, which has a time delay of -6.5 hours and match criteria obeyed above 17 km, is generally in good agreement, although most values tend to be too high. The forward match with a time delay of +17.2 hours lies within the given errors above 25 km, but shows again high values in the lower stratosphere, where match criteria are not fulfilled.

SAOZ subtropical ascent measurements taken on January 31, 2004 before sunset were performed between 76° and 86° SZA and thus a scaling reference for the balloon observation of 80.2° SZA was used. The SZAs of the SCIAMACHY backward and forward match are both 36° . As for the DOAS flight, the scaling for the backward and forward match is significant. The agreement of the dynamics adopted in the model with observations could only be verified by comparing O_3 profiles also measured by the SAOZ instrument indicating that large dynamic uncertainties can be ruled out. Simultaneous measurements of NO_2 allowed it to be scaled in the 1-D model. Agreement with the model for BrO between 17 km and

25 km is convincing, but measurements below and above, are larger and even close to total Br_Y . The comparison with a SCIAMACHY backward match shows agreement with the balloon measurements, although it is outside the matching altitude range. Below 17 km the SCIAMACHY profile tends to have $[\text{BrO}] > [\text{Br}_Y]$. The forward match shows a similar good agreement but again has too high values in the lower stratosphere.

DOAS high-latitude ascent measurements taken on March 24, 2004 were performed between 74.6° and 85.4° SZA. For comparison the model output is plotted at 77.1° SZA. Since the SZAs of the SCIAMACHY backward and forward match are 68.3° and 61.8° , respectively, the scaling is very similar. Agreement of the dynamic tracers N_2O and CH_4 between model predictions and LPMA measurements could not be assessed, since no LPMA data is available to date. Therefore, dynamics could only be verified by O_3 measurements, which showed an overall good agreement over the entire altitude range. NO_2 was scaled in the 1-D model as before. The correspondence with the model is very convincing. The available SCIAMACHY profile for the forward match has a time delay of +17.1 hours and match criteria are obeyed only between 20 and 26 km, where the satellite profile shows 25 to 55 % higher values.

Overall, the agreement of the balloon BrO observations from the 3 instruments with the model is encouraging. The tracer data measured by balloon instruments is found to correspond with the SLIMCAT CTM and therefore large uncertainties in vertical transport can be ruled out. All profiles fall within the constrained total Br_Y and mostly agree with the model within the error range. An exception is the TRIPLE flight, where the source of discrepancy is unclear, since dynamic and photochemical causes could be eliminated. After the scaling of NO_2 in the model, DOAS and SAOZ BrO profiles coincide with the model at almost every altitude within the errors (15 to 30 % for DOAS and 25 to 50 % for SAOZ, depending on altitude and measurement conditions).

For the SCIAMACHY retrievals presented here, no clear trend can be observed, except that the Harvard retrieval mostly shows higher values than expected from the photochemically-corrected balloon validation profiles, especially for lower altitudes, where sensitivity of the satellite instrument decreases. Sources of error might be spatial variations of BrO within the match criteria of 1 hour and 500 km, although this is very unlikely. Smaller discrepancies could be explained outside the matching altitude ranges, where air masses travelled along different trajectories that do not obey the match criteria. But overall the diurnal variation of BrO (without large spatial gradients) should be able to explain most of the scaling factor used to correct the profiles. The larger time delay for forward matches (see Table 7.1), and therefore the increasing uncertainty in the air mass trajectory calculation, could theoretically explain higher discrepancies compared to backward matches, but this is not the case for the present observations.

7.5 Conclusions

Stratospheric BrO abundances measured from 3 different balloon sensors were compared with reference to the 3-D CTM SLIMCAT model output. Model calculations were used to generate a BrO profile validation set for the new Envisat / SCIAMACHY satellite instrument and were compared with first retrieval exercises of SCIAMACHY BrO limb profiling. Since the diurnal variation of BrO and the spatial and temporal difference between the different observations prevent a direct comparison, the observations were considered with reference to outputs from the 3-D CTM. Air mass trajectory calculations were used to identify coincident SCIAMACHY limb measurements. The balloon-borne BrO profiles were photochemically scaled along the trajectories with a 1-D stratospheric chemistry model to match the photochemical conditions of the satellite observations. Model predictions were constrained by simultaneous observations with the balloon instruments, of dynamic and photochemical relevant parameters.

Total $[\text{Br}_Y] = (20.1 \pm 2.8)$ pptv obtained from DOAS BrO observations at mid-latitudes in 2003, served as an upper limit of the comparison. The good agreement of balloon trace gas measurements with the

SLIMCAT model indicates that vertical transport is considered correctly and is not a major source of error. Within the given range of errors of the different measurement techniques, most of the balloon observations agree with model BrO. Initial BrO profiles available from SCIAMACHY agree to $< \pm 50\%$ with the photochemically-corrected balloon observations, with less agreement below 20 km. This should encourage a further improvement of the satellite retrieval.

The presented set of BrO balloon profiles is meant to be representative and, according to the trajectory calculations, the most suitable set of SCIAMACHY BrO validation profiles and is thus recommended for future SCIAMACHY limb BrO retrieval exercises.

The LPMA / DOAS flight at Teresina on June 17, 2005 has not been analysed in detail yet and will be part of a future study. Trajectory calculations, similar to Figure 7.4, for the four DOAS SCIAMACHY validation flights are shown in Figures 7.12 to 7.15 on the following pages.

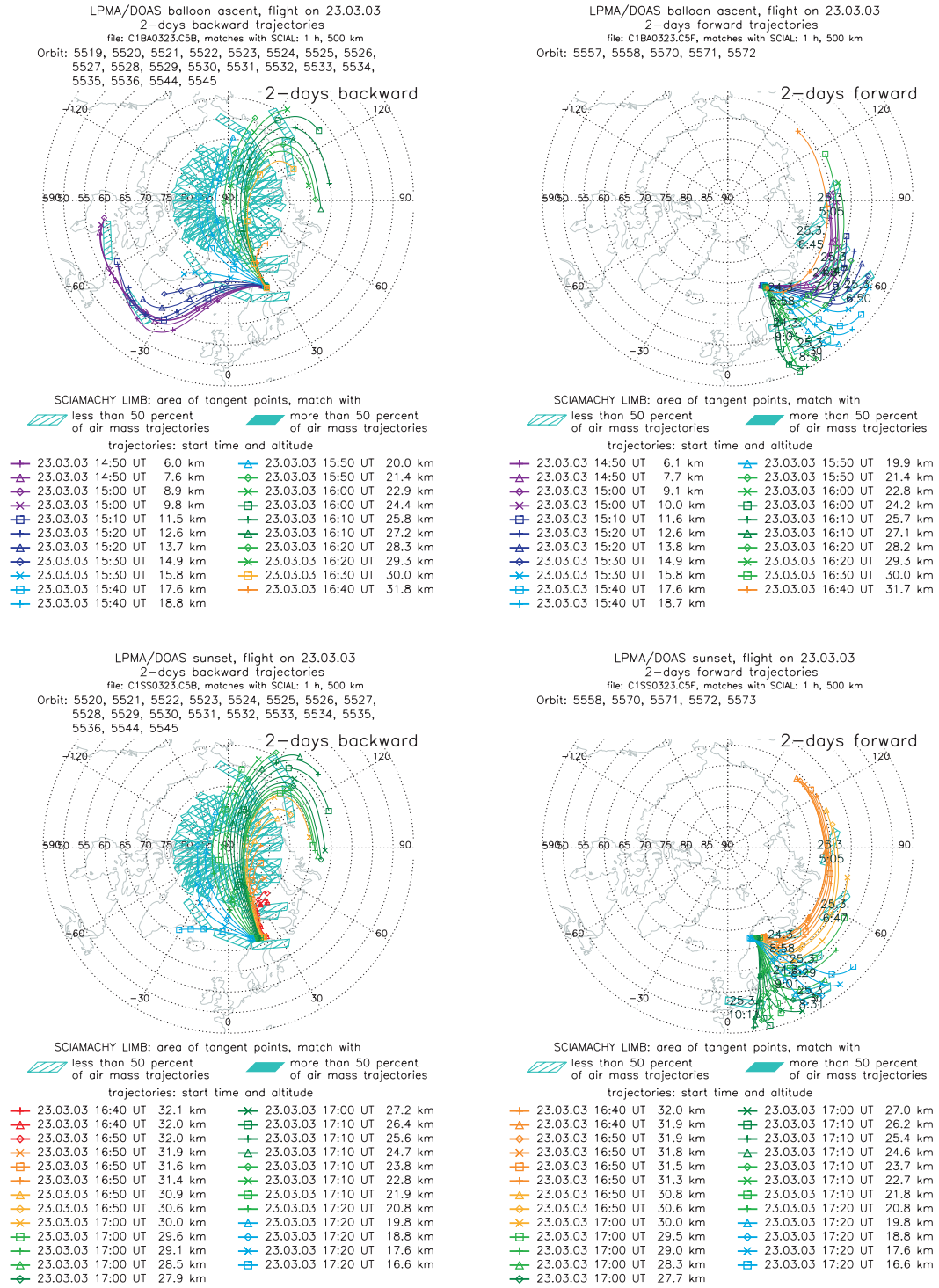


Figure 7.12: Two days backward (left panels) and forward (right panels) air mass trajectories for the ascent (upper panels) and occultation (lower panels) observations for the LPMA/DOAS flight on March 23, 2003 at Kiruna. The considered ENVISAT / SCIAMACHY orbit numbers and trajectory start times and altitudes are given in the individual headers and legends, respectively. The light blue rectangles represent the areas of tangent points, which are probed by the SCIAMACHY limb observations and meet the match criteria (see text for details). Plots by courtesy of FU-Berlin.

LPMA/DOAS balloon ascent, flight on 09.10.03
 2-days backward trajectories
 file: BA031009.C5B, matches with SCIAL: 1 h, 1000 km
 Orbit: 8393, 8394, 8407, 8408

LPMA/DOAS balloon ascent, flight on 09.10.03
 2-days forward trajectories
 file: BA031009.C5F, matches with SCIAL: 1 h, 1000 km
 Orbit: 8421, 8422, 8434, 8435, 8436

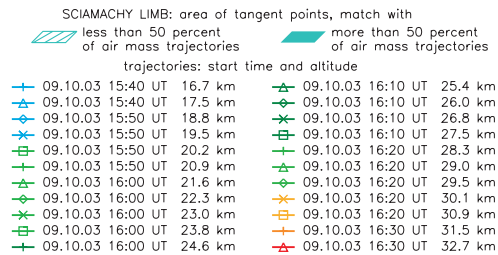
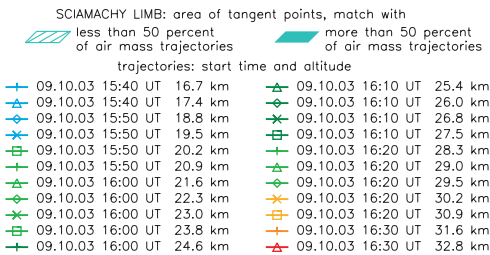
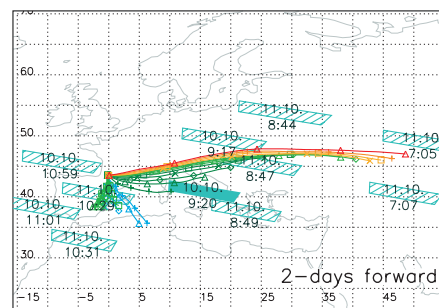
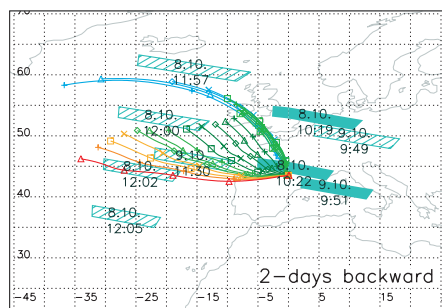
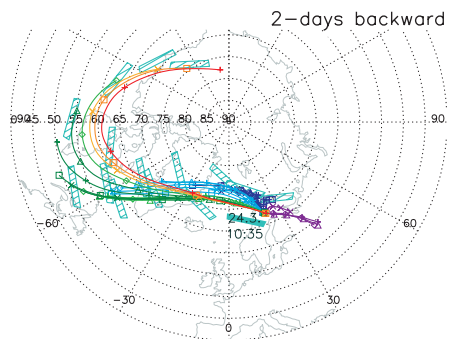


Figure 7.13: Same as Figure 7.12 but for the LPMA/DOAS flight on October 09, 2003 at Aire sur l'Adour and ascent observations only. Plots by courtesy of FU-Berlin.

LPMA/DOAS balloon ascent, flight on 24.03.04
 2-days backward trajectories
 file: BA040324.C5B, matches with SCIAL: 1 h, 500 km
 Orbit: 10772, 10773, 10774, 10775, 10776, 10783, 10784, 10785, 10786, 10787, 10798



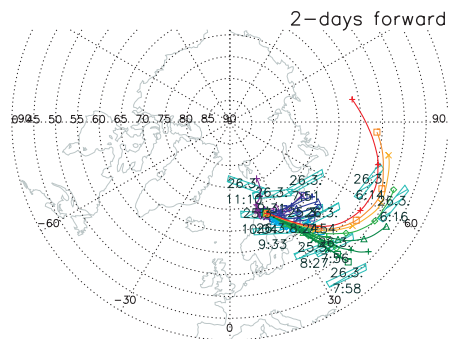
SCIAMACHY LIMB: area of tangent points, match with

	less than 50 percent of air mass trajectories		more than 50 percent of air mass trajectories
--	---	--	---

trajectories: start time and altitude

+	24.03.04 14:10 UT	5.7 km	+	24.03.04 15:10 UT	18.1 km
+	24.03.04 14:20 UT	6.8 km	+	24.03.04 15:20 UT	19.2 km
+	24.03.04 14:30 UT	7.9 km	+	24.03.04 15:30 UT	20.4 km
+	24.03.04 14:40 UT	9.9 km	+	24.03.04 15:40 UT	21.6 km
+	24.03.04 14:50 UT	10.6 km	+	24.03.04 15:50 UT	22.8 km
+	24.03.04 14:40 UT	11.3 km	+	24.03.04 16:00 UT	24.0 km
+	24.03.04 14:40 UT	12.0 km	+	24.03.04 15:40 UT	25.4 km
+	24.03.04 14:50 UT	12.8 km	+	24.03.04 15:40 UT	26.7 km
+	24.03.04 14:50 UT	13.6 km	+	24.03.04 15:40 UT	28.0 km
+	24.03.04 14:50 UT	14.4 km	+	24.03.04 15:50 UT	29.4 km
+	24.03.04 15:00 UT	15.3 km	+	24.03.04 15:50 UT	30.7 km
+	24.03.04 15:00 UT	16.2 km	+	24.03.04 16:00 UT	31.5 km
+	24.03.04 15:10 UT	17.2 km	+	24.03.04 16:00 UT	32.6 km

LPMA/DOAS balloon ascent, flight on 24.03.04
 2-days forward trajectories
 file: BA040324.C5F, matches with SCIAL: 1 h, 500 km
 Orbit: 10811, 10812, 10824, 10825, 10826, 10827



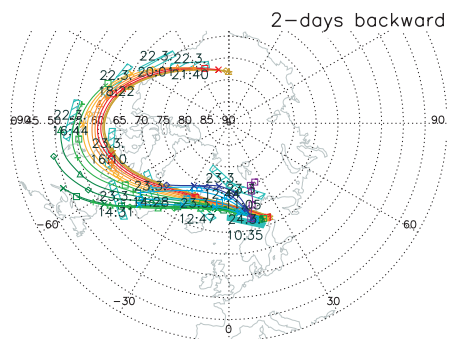
SCIAMACHY LIMB: area of tangent points, match with

	less than 50 percent of air mass trajectories		more than 50 percent of air mass trajectories
--	---	--	---

trajectories: start time and altitude

+	24.03.04 14:10 UT	5.7 km	+	24.03.04 15:10 UT	18.1 km
+	24.03.04 14:20 UT	6.8 km	+	24.03.04 15:20 UT	19.2 km
+	24.03.04 14:30 UT	7.9 km	+	24.03.04 15:30 UT	20.4 km
+	24.03.04 14:40 UT	9.9 km	+	24.03.04 15:40 UT	21.6 km
+	24.03.04 14:50 UT	10.6 km	+	24.03.04 15:50 UT	22.8 km
+	24.03.04 14:40 UT	11.3 km	+	24.03.04 16:00 UT	24.0 km
+	24.03.04 14:40 UT	12.0 km	+	24.03.04 15:40 UT	25.4 km
+	24.03.04 14:50 UT	12.8 km	+	24.03.04 15:40 UT	26.7 km
+	24.03.04 14:50 UT	13.6 km	+	24.03.04 15:40 UT	27.9 km
+	24.03.04 14:50 UT	14.4 km	+	24.03.04 15:50 UT	29.4 km
+	24.03.04 15:00 UT	15.3 km	+	24.03.04 15:50 UT	30.6 km
+	24.03.04 15:00 UT	16.2 km	+	24.03.04 16:00 UT	31.4 km
+	24.03.04 15:10 UT	17.1 km	+	24.03.04 16:00 UT	32.5 km

LPMA/DOAS sunset, flight on 24.03.04
 2-days backward trajectories
 file: SS040324.C5B, matches with SCIAL: 1 h, 500 km
 Orbit: 10773, 10774, 10775, 10776, 10784, 10785, 10786, 10787, 10798



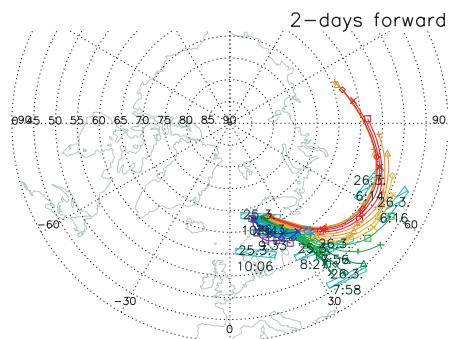
SCIAMACHY LIMB: area of tangent points, match with

	less than 50 percent of air mass trajectories		more than 50 percent of air mass trajectories
--	---	--	---

trajectories: start time and altitude

+	24.03.04 16:50 UT	33.2 km	+	24.03.04 17:10 UT	25.8 km
+	24.03.04 16:50 UT	33.2 km	+	24.03.04 17:10 UT	24.5 km
+	24.03.04 16:50 UT	33.3 km	+	24.03.04 17:10 UT	23.4 km
+	24.03.04 16:50 UT	32.8 km	+	24.03.04 17:10 UT	22.1 km
+	24.03.04 16:50 UT	32.2 km	+	24.03.04 17:20 UT	20.7 km
+	24.03.04 17:00 UT	31.9 km	+	24.03.04 17:20 UT	19.3 km
+	24.03.04 17:00 UT	31.5 km	+	24.03.04 17:20 UT	17.8 km
+	24.03.04 17:00 UT	30.9 km	+	24.03.04 17:20 UT	16.4 km
+	24.03.04 17:00 UT	30.3 km	+	24.03.04 17:20 UT	15.1 km
+	24.03.04 17:00 UT	29.6 km	+	24.03.04 17:20 UT	13.9 km
+	24.03.04 17:00 UT	28.7 km	+	24.03.04 17:30 UT	12.2 km
+	24.03.04 17:10 UT	27.8 km	+	24.03.04 17:30 UT	9.7 km
+	24.03.04 17:10 UT	26.9 km			

LPMA/DOAS sunset, flight on 24.03.04
 2-days forward trajectories
 file: SS040324.C5F, matches with SCIAL: 1 h, 500 km
 Orbit: 10811, 10812, 10824, 10825, 10826



SCIAMACHY LIMB: area of tangent points, match with

	less than 50 percent of air mass trajectories		more than 50 percent of air mass trajectories
--	---	--	---

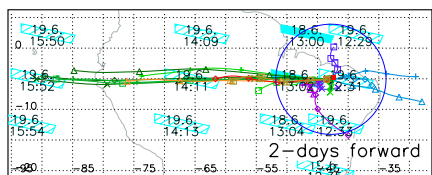
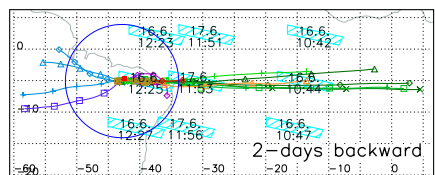
trajectories: start time and altitude

+	24.03.04 16:50 UT	33.1 km	+	24.03.04 17:10 UT	25.7 km
+	24.03.04 16:50 UT	33.0 km	+	24.03.04 17:10 UT	24.5 km
+	24.03.04 16:50 UT	32.7 km	+	24.03.04 17:10 UT	23.4 km
+	24.03.04 16:50 UT	32.2 km	+	24.03.04 17:10 UT	22.1 km
+	24.03.04 16:50 UT	32.2 km	+	24.03.04 17:20 UT	20.7 km
+	24.03.04 17:00 UT	31.8 km	+	24.03.04 17:20 UT	19.3 km
+	24.03.04 17:00 UT	31.4 km	+	24.03.04 17:20 UT	17.8 km
+	24.03.04 17:00 UT	30.9 km	+	24.03.04 17:20 UT	16.4 km
+	24.03.04 17:00 UT	30.2 km	+	24.03.04 17:20 UT	15.1 km
+	24.03.04 17:00 UT	29.5 km	+	24.03.04 17:20 UT	13.9 km
+	24.03.04 17:00 UT	28.6 km	+	24.03.04 17:30 UT	12.2 km
+	24.03.04 17:10 UT	27.7 km	+	24.03.04 17:30 UT	9.7 km
+	24.03.04 17:10 UT	26.8 km			

Figure 7.14: Same as Figure 7.12 but for the LPMA/DOAS flight on March 24, 2004 at Kiruna. Plots by courtesy of FU-Berlin.

LPMA/DOAS balloon ascent, flight on 17.06.05
 2-days backward trajectories
 file: LAPR0617.C5B, matches with SCIAL: 1 h, 1000 km
 Orbit: 17225, 17226, 17240

LPMA/DOAS balloon ascent, flight on 17.06.05
 2-days forward trajectories
 file: LAPR0617.C5F, matches with SCIAL: 1 h, 1000 km
 Orbit: 17255, 17269, 17270, 17271



SCIAMACHY LIMB: area of tangent points, match with

trajectory: start time and altitude	less than 50 percent of air mass trajectories	more than 50 percent of air mass trajectories
17.06.05 18:40 UT 5.2 km	+	+
17.06.05 18:50 UT 7.1 km	+	+
17.06.05 18:50 UT 9.0 km	+	+
17.06.05 19:00 UT 11.0 km	+	+
17.06.05 19:00 UT 13.2 km	+	+
17.06.05 19:10 UT 15.4 km	+	+
17.06.05 19:10 UT 17.4 km	+	+
17.06.05 19:20 UT 18.7 km	+	+
17.06.05 19:20 UT 20.1 km	+	+
17.06.05 19:30 UT 21.3 km	+	+
17.06.05 19:40 UT 22.9 km	+	+
17.06.05 19:40 UT 24.2 km	+	+
17.06.05 19:50 UT 25.7 km	+	+
17.06.05 19:50 UT 27.2 km	+	+
17.06.05 20:00 UT 28.4 km	+	+
17.06.05 20:00 UT 29.5 km	+	+
17.06.05 20:10 UT 31.3 km	+	+
17.06.05 20:10 UT 32.8 km	+	+
17.06.05 20:20 UT 33.4 km	+	+
17.06.05 20:20 UT 33.4 km	+	+

SCIAMACHY LIMB: area of tangent points, match with

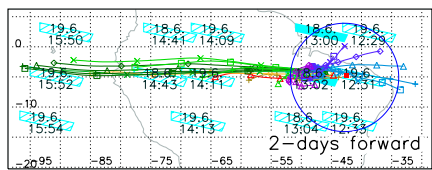
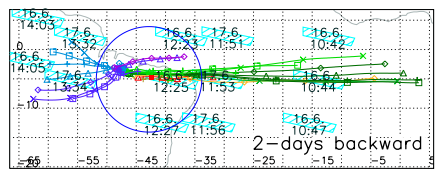
trajectory: start time and altitude	less than 50 percent of air mass trajectories	more than 50 percent of air mass trajectories
17.06.05 18:40 UT 5.2 km	+	+
17.06.05 18:50 UT 7.1 km	+	+
17.06.05 18:50 UT 9.0 km	+	+
17.06.05 19:00 UT 11.0 km	+	+
17.06.05 19:00 UT 13.2 km	+	+
17.06.05 19:10 UT 15.3 km	+	+
17.06.05 19:10 UT 17.4 km	+	+
17.06.05 19:20 UT 18.6 km	+	+
17.06.05 19:20 UT 20.0 km	+	+
17.06.05 19:30 UT 21.2 km	+	+
17.06.05 19:40 UT 22.9 km	+	+
17.06.05 19:40 UT 24.2 km	+	+
17.06.05 19:50 UT 25.6 km	+	+
17.06.05 19:50 UT 27.1 km	+	+
17.06.05 20:00 UT 28.3 km	+	+
17.06.05 20:00 UT 29.4 km	+	+
17.06.05 20:10 UT 31.2 km	+	+
17.06.05 20:10 UT 32.7 km	+	+
17.06.05 20:20 UT 33.3 km	+	+
17.06.05 20:20 UT 33.3 km	+	+

Radius 1000 km around Teresina
 planned SCIA geolocations from SOST
 not all trajectories plotted, trajectories calculated on 20050906, matches on 20050909, FU Berlin

Radius 1000 km around Teresina
 planned SCIA geolocations from SOST
 not all trajectories plotted, trajectories calculated on 20050906, matches on 20050909, FU Berlin

LPMA/DOAS sunset, flight on 17.06.05
 2-days backward trajectories
 file: LSPR0617.C5B, matches with SCIAL: 1 h, 1000 km
 Orbit: 17225, 17226, 17227, 17240, 17241

LPMA/DOAS sunset, flight on 17.06.05
 2-days forward trajectories
 file: LSPR0617.C5F, matches with SCIAL: 1 h, 1000 km
 Orbit: 17255, 17256, 17269, 17270, 17271



SCIAMACHY LIMB: area of tangent points, match with

trajectory: start time and altitude	less than 50 percent of air mass trajectories	more than 50 percent of air mass trajectories
17.06.05 20:50 UT 33.5 km	+	+
17.06.05 20:50 UT 32.5 km	+	+
17.06.05 21:00 UT 30.4 km	+	+
17.06.05 21:00 UT 28.7 km	+	+
17.06.05 21:00 UT 27.0 km	+	+
17.06.05 21:00 UT 26.2 km	+	+
17.06.05 21:00 UT 25.4 km	+	+
17.06.05 21:00 UT 24.5 km	+	+
17.06.05 21:00 UT 23.7 km	+	+
17.06.05 21:00 UT 22.8 km	+	+
17.06.05 21:00 UT 21.9 km	+	+
17.06.05 21:00 UT 20.9 km	+	+
17.06.05 21:00 UT 18.9 km	+	+
17.06.05 21:10 UT 17.8 km	+	+
17.06.05 21:10 UT 16.7 km	+	+
17.06.05 21:10 UT 15.7 km	+	+
17.06.05 21:10 UT 14.7 km	+	+
17.06.05 21:10 UT 13.6 km	+	+
17.06.05 21:10 UT 12.6 km	+	+
17.06.05 21:10 UT 11.6 km	+	+
17.06.05 21:10 UT 10.0 km	+	+
17.06.05 21:10 UT 8.1 km	+	+

SCIAMACHY LIMB: area of tangent points, match with

trajectory: start time and altitude	less than 50 percent of air mass trajectories	more than 50 percent of air mass trajectories
17.06.05 20:50 UT 33.4 km	+	+
17.06.05 20:50 UT 32.5 km	+	+
17.06.05 21:00 UT 30.4 km	+	+
17.06.05 21:00 UT 28.9 km	+	+
17.06.05 21:00 UT 26.1 km	+	+
17.06.05 21:00 UT 25.4 km	+	+
17.06.05 21:00 UT 24.5 km	+	+
17.06.05 21:00 UT 23.7 km	+	+
17.06.05 21:00 UT 22.7 km	+	+
17.06.05 21:00 UT 21.8 km	+	+
17.06.05 21:00 UT 20.8 km	+	+
17.06.05 21:00 UT 18.8 km	+	+
17.06.05 21:10 UT 17.8 km	+	+
17.06.05 21:10 UT 16.7 km	+	+
17.06.05 21:10 UT 14.6 km	+	+
17.06.05 21:10 UT 13.6 km	+	+
17.06.05 21:10 UT 12.6 km	+	+
17.06.05 21:10 UT 11.6 km	+	+
17.06.05 21:10 UT 9.9 km	+	+
17.06.05 21:10 UT 8.1 km	+	+

Radius 1000 km around Teresina
 planned SCIA geolocations from SOST
 not all trajectories plotted, trajectories calculated on 20050906, matches on 20050909, FU Berlin

Radius 1000 km around Teresina
 planned SCIA geolocations from SOST
 not all trajectories plotted, trajectories calculated on 20050906, matches on 20050909, FU Berlin

Figure 7.15: Same as Figure 7.12 but for the LPMA/DOAS flight on June 17, 2005 at Teresina. Plots by courtesy of FU-Berlin.

Chapter 8

Stratospheric OCIO

The bromine and chlorine catalytic ozone depletion cycles are coupled via the reaction of BrO and ClO. The three reaction channels produce OCIO, ClOO and BrCl as described in section 2.2.3. Due to the fast photolysis of BrCl and the impact-induced decay of ClOO to Cl and molecular oxygen, the generation of BrCl and ClOO leads to ozone depletion. As more than 50% of the educts lead to the formation of OCIO at stratospheric temperatures, this species is well suited to investigate this catalytic ozone depletion cycle. Still, the relationship between OCIO and ClO amounts is not linear, as it is limited by BrO for highly activated conditions [Sessler *et al.* 1995; Canty *et al.* 2005].

The only OCIO evaluation of DOAS balloon measurements has been presented by *Fitzenberger* [2000]. Four balloon flights were analysed to determine how much OCIO was present in the stratosphere. Three flights were performed at high latitudes during winter, where OCIO was expected to be formed and one at mid latitudes during late fall/beginning of winter. In all cases significant amounts of OCIO were found. For the flight at Kiruna on February 14, 1997 low OCIO values were expected since the flight took place at the edge of the activated polar vortex, with occultation measurements pointing outside the vortex. For details on the flights and the balloon trajectory relative to the polar vortex, see *Fitzenberger* [2000] and *Bösch* [2002]. The second flight at Kiruna during winter took place on February 10, 1999. Balloon ascent was again at the edge of the vortex, but occultation measurements pointed inside the vortex. Some chlorine activation was observed during winter 1998/1999, but in general temperatures were too high for PSC formation. The third high-latitude winter flight at Kiruna was performed on February 18, 2000. It was one of the coldest winters in the lower stratosphere in the last decades with a strong polar vortex and high chlorine activation. The LPMA/DOAS balloon flight was well inside the vortex, but with occultation measurements pointing toward the edge.

The mid-latitude flight at Leon on November 23, 1996 took place well outside the vortex, although the boundary of one vortex fragment was close to northern Spain. From general knowledge of stratospheric chemistry, no formation of detectable amounts of OCIO would be expected. High values retrieved by *Fitzenberger* [2000] with up to 10 pptv of OCIO are rather puzzling and cannot be explained by model and trajectory calculations. Furthermore, OCIO DOAS retrievals by *Fitzenberger* [2000] for the Kiruna winter flights showed much higher values than can be explained by comparison with model calculations. Balloon ascent measurements in particular, with significant OCIO SCD values for Kiruna 1999 and Kiruna 2000 observations, showed up to 10 times higher values than model calculations.

In this study a reevaluation of OCIO for the 4 flights is presented. The first part of this chapter emphasises the difficulties of the DOAS OCIO evaluation and gives an error estimate. Sections 8.2; 8.3 and 8.4 present case studies for OCIO observations at Kiruna on February 14, 1997, February 10, 1999 and February 18, 2000. Observations are compared with model results and new findings for photochemical parameters.

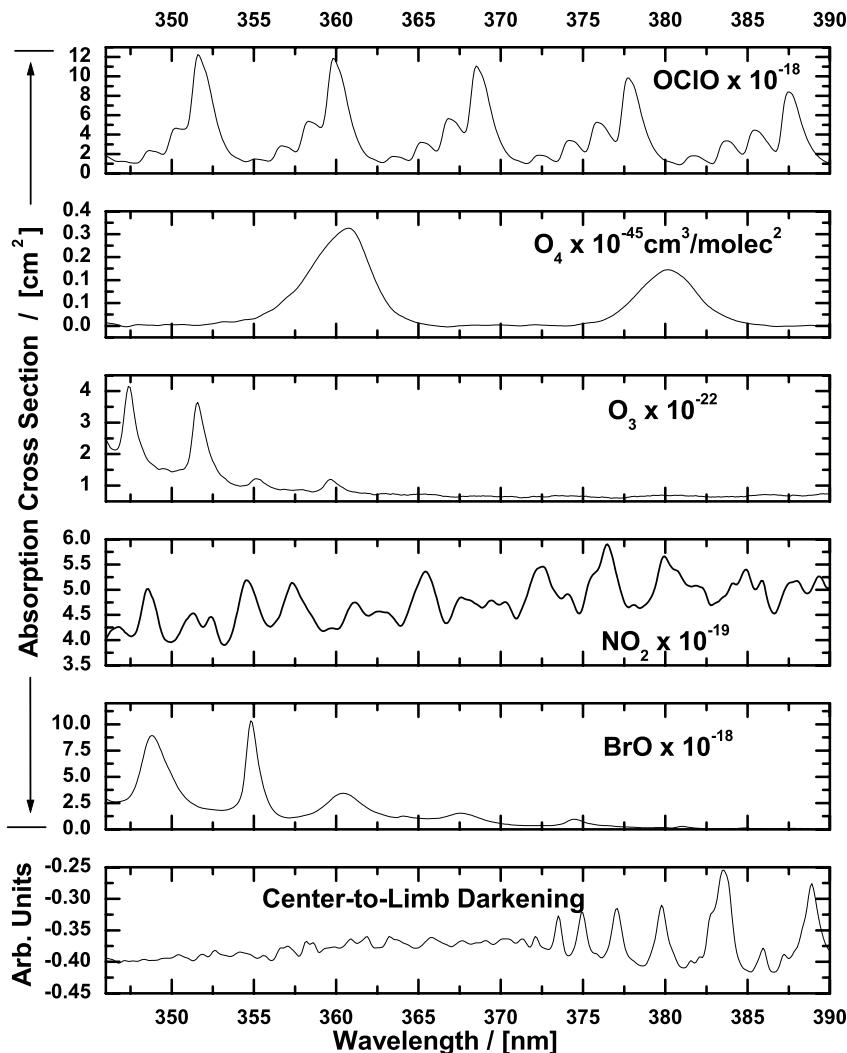


Figure 8.1: Absorption cross-sections in the UV OCIO retrieval range (346 – 390 nm) at the resolution of the spectrograph. Top to bottom: OCIO [Kromminga et al. 2003], O₄ [Hermans 2002] (collisional pair absorption cross-section), Ozone [Voigt et al. 2001], NO₂ [Voigt et al. 2002], BrO [Wahner et al. 1988] and center to limb darkening correction (section 3.4.1) obtained according to Bösch [2002].

8.1 OCIO Evaluation

The DOAS technique make it possible to retrieve the UV OCIO absorption signatures of the vibrational and rotational absorption bands of the $\tilde{A}^2A_2 \leftarrow \tilde{X}^2B_1$ electronic transition. Reference spectra used for the OCIO DOAS evaluation were obtained in the same way as reference spectra used for the BrO evaluation described in section 6.1.1. Laboratory references of NO₂ (at T= 203 K) and O₃ (at T= 197 K and T= 253 K) were calibrated, with respect to wavelength and absolute value, with the NO₂ and O₃ high resolution cross-sections given by Voigt et al. [2002] and Voigt et al. [2001]. I_0 corrections were performed as described in section 6.1.1. The O₄ laboratory spectrum of Hermans [2002], the BrO absolute cross-section measured by Wahner et al. [1988] at T= 228 K and the OCIO absolute cross-section at T= 213 K from Kromminga et al. [2003] were included in the fit. Unfortunately OCIO was only measured during flights before 2001. Therefore, reference spectra recorded with the

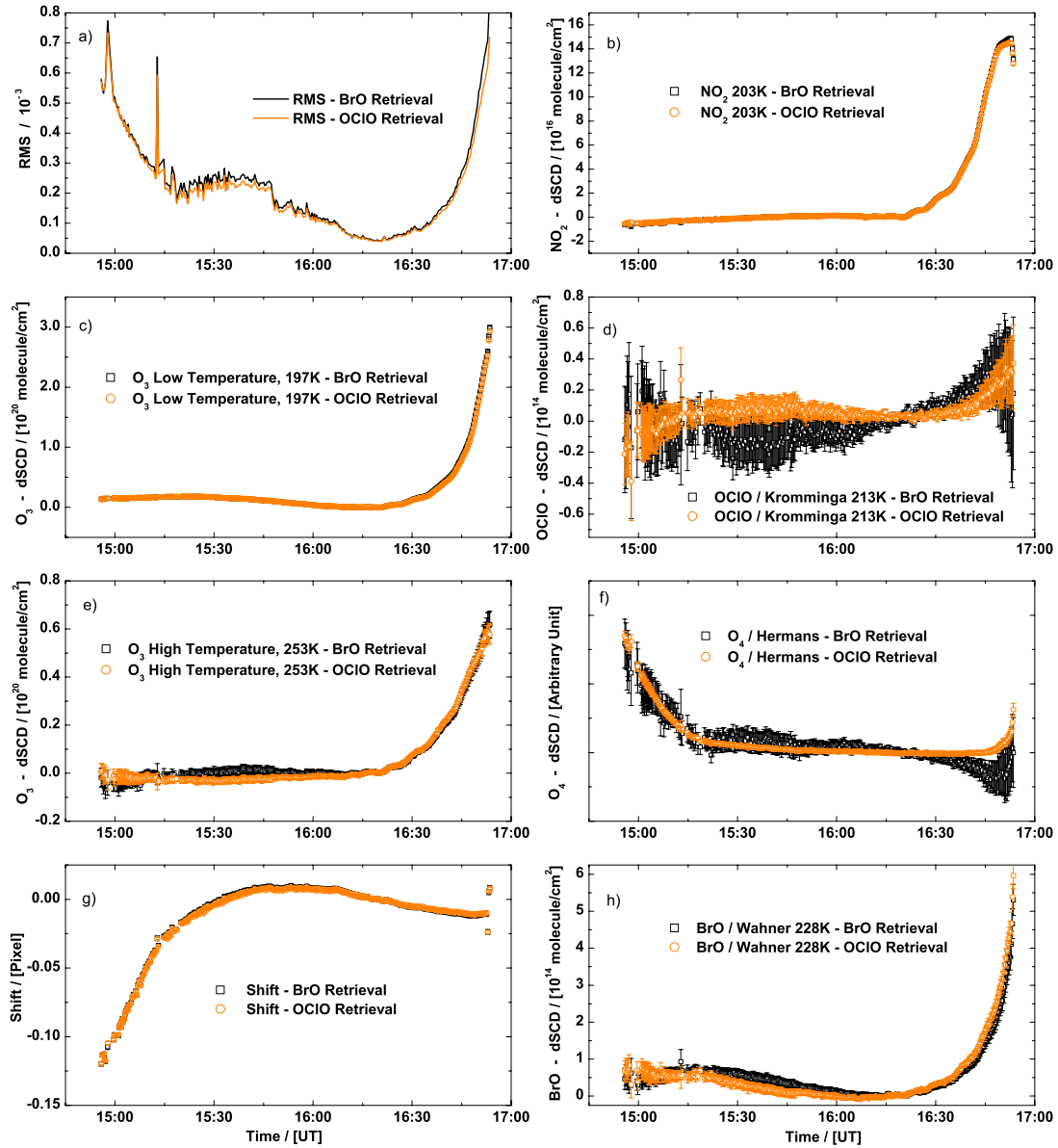


Figure 8.2: Development of the slant column densities and important fit parameters for the OCIO retrieval in the 346 – 372 nm wavelength range (orange) and for the BrO retrieval in the 346 – 360 nm wavelength range (black) for the ascent and sunset measurements of the balloon flight at Leon on November 23, 1996. Laboratory absorption cross-sections of O_3 at $T=197\text{K}$ and $T=253\text{K}$ and NO_2 at $T=203\text{K}$ were used together with literature cross-sections of OCIO, BrO and O_4 as described in the text (panels b) - f)). In panel a) the resulting root mean square (RMS) of the fit is plotted. Panels g) and h) represent the shift and squeeze of the fitted spectra, respectively.

balloon spectrograph in the laboratory after 2001, as described in chapter 5, could not be used. For future flights it will be especially interesting to compare UV absorptions with OCIO signatures recorded with the Vis spectrograph between 400 nm and 430 nm. This was the primary motivation behind

changing the wavelength range covered by the Vis spectrograph to smaller wavelengths (see section 4.1.2).

Most suited for OCIO evaluation is a subwindow of the wavelength interval between 346 nm and 390 nm, covered by the UV spectrograph, as indicated in Figure 8.1. Below 346 nm the O_3 absorption is too strong and above 390 nm large Fraunhofer absorption lines make a DOAS retrieval impossible. It was discovered that one of the most crucial factors in the evaluation of OCIO is the correct choice of subwindow. Subwindows covering only one absorption band of OCIO can be ruled out since the subset of pixels available for the DOAS fit is not sufficient for the high number of parameters to be fitted. *Fitzenberger* [2000] used different wavelength ranges (345 – 370 nm, 362 – 382 nm, 362 – 380 nm, 346 – 365 nm, 362 – 390 nm and 346 – 368 nm) for analysing OCIO for 4 balloon flights. The most common wavelength range used by other groups is the 362–390 nm (± 2 nm) interval (see e.g. *Wagner et al.* [2001]). The advantage of analysing wavelengths larger than 362 nm is that the O_3 absorption does not have to be considered in the fit. For direct sun measurements, a center-to-limb-darkening correction has to be included for $\lambda > 372$ nm [*Bösch* 2002] (see Figure 8.1).

Although the BrO cross-section has only small absorption signatures at around 368 nm and 374 nm it shows strong anti-correlation with the OCIO cross-section. Therefore, different results are obtained by including or excluding BrO in the DOAS fit in the 362 – 390 nm range. If included in the fit the BrO SCD values are too high compared to the standard BrO retrieval in the 346 – 360 nm range, thus generating lower OCIO values. If BrO is not included in the fit, the obtained OCIO values are overestimated. If no other sources of error were present, true OCIO values would lie between the two retrieval values, resulting in an additional SCD error of $\sim 15\%$ above the detection limit (generally around $(2 - 4) \times 10^{13}$ molecules/cm²).

Testing different retrieval ranges also showed that higher systematic residual structures are obtained in

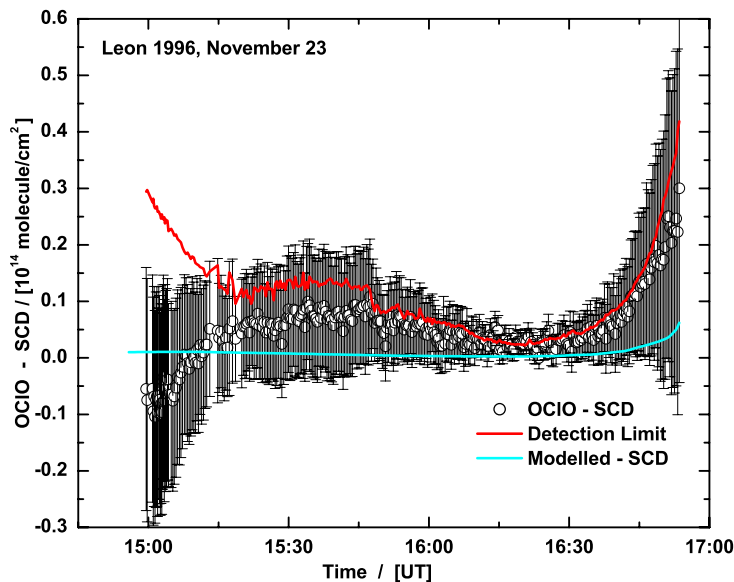


Figure 8.3: Development of the OCIO SCD values for the balloon flight at Leon on November 23, 1996. The detection limit and modelled SCDs as described in the text are plotted in red and blue respectively for comparison.

the 362 – 390 nm interval. This is mainly due to stronger Fraunhofer absorption features for $\lambda > 370$ nm but might also be due to small unknown absorptions of other trace gases. In the 346 – 365 nm and 346 – 385 nm windows strong anti-correlations of OCIO with O_4 are observed. Accurate fitting of O_4 is essential to obtain realistic OCIO values and a shift of 0.1 nm has to be applied to the O_4 spectrum of

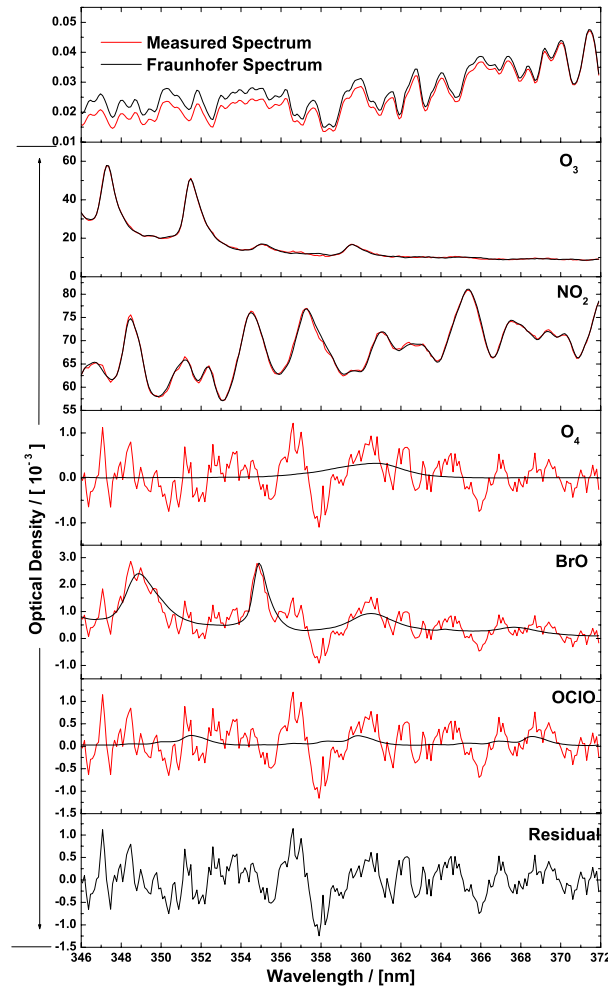


Figure 8.4: OCIO DOAS evaluation in the 346 – 372 nm wavelength range for a spectrum recorded during occultation measurements of the balloon flight at Leon on November 23, 1996. The spectrum was recorded at 30.76 km at 92.05° SZA (16:48:53 UT) with 16 scans and a total exposure time of 14.87 seconds. The upper panel shows the Fraunhofer spectrum (black line) and the measured spectrum (red line). In the panels below the retrieved trace gas absorptions of O_3 (at 197 K), NO_2 (at 203 K), O_4 , BrO and OCIO as described in the text are plotted. A 5^{th} - degree polynomial was included in the fit. The black lines indicate the spectral absorptions and the red line represents the sum of the spectral absorption and the residual of the fit. The lowest panel displays the remaining residual structure.

Hermans [2002]. In addition the 346 – 385 nm interval covers almost 400 pixels, which makes accurate DOAS retrieval difficult. Furthermore, OCIO shows a larger correlation with NO_2 than in other OCIO retrieval windows.

Anti-correlations of OCIO with BrO are also present between 357 and 385 nm and from 362 to 385 nm, where the later interval generally showed wider scatter of OCIO SCD values than the other intervals. Best results are obtained from 346 to 372 nm. Here correlations of OCIO with BrO and O_4 are minimal although the choice of the degree of the polynomial, which is used to approximate broad-band components, is still crucial. Naturally the polynomial highly correlates with the relatively broad-banded O_4 and thus influences OCIO values. Comparing the development of O_4 SCDs from the Vis spectrograph with values

obtained from the OCIO evaluation in the 346 – 372 nm range for different balloon flights showed that a 5th- degree polynomial should be used in the DOAS fit rather than a 4th- degree polynomial. Figures 8.2, 8.6, 8.12 and 8.23 show the development of the slant column densities and important fit parameters for OCIO retrieval in the 346 – 372 nm wavelength range (orange) and for BrO retrieval in the 346 – 360 nm wavelength range (black) for the 4 flights analysed for OCIO absorptions. Panel h) of each figure shows the corresponding BrO SCDs, which agree within the given error bars of the OCIO and BrO retrieval, for all four flights. Therefore, strong correlations of BrO and OCIO can be ruled out in the 346 – 372 nm interval, demonstrating the accuracy of the OCIO evaluation.

The OCIO re-evaluation in the 346–372 nm interval shows systematically lower values compared to results obtained by *Fitzenberger* [2000]. Especially in the case of the mid-latitude flight at Leon, on November 23, 1996, OCIO values are even below the detection limit (see Figure 8.3), whereas *Fitzenberger* [2000] received SCD values up to 3.7×10^{14} molecule/cm², i.e. ~ 10 times as high.

In contrast to BrO, the amount of OCIO absorption present in the Fraunhofer spectrum is negligible, and no Langley-plot needs to be performed (see section 6.1.2). Thus, differential SCDs obtained by the DOAS evaluation of the spectra as shown in the Figures, are considered total SCDs. The detection limit (section 3.4) as plotted in Figure 8.3 is twice the error given by the *WinDOAS* evaluation software.

Figure 8.4 shows a typical DOAS retrieval for a spectrum recorded at 92.05° for the Leon 1996 balloon flight. The optical density of OCIO is significantly lower than the remaining residual structures. The large systematic residual feature at 356 – 358 nm is due to temperature effects in the NO₂ cross-section and therefore incorrect removal of NO₂ absorptions. The high SCD values found by *Fitzenberger* [2000] could not be reproduced in the 346 – 372 nm interval, nor in any other wavelength range. For reasons explained above (e.g. O₄ correlations) different retrieval ranges can lead to higher values, but can still not reproduce the retrieval of *Fitzenberger* [2000]. A possible explanation is the incorrect wavelength alignment of O₄, O₃ or NO₂. In principle, the effect of incomplete removal of absorptions and resulting larger residual structures, can also be observed in this study. This is mainly the case for occultation measurements, where residual structures rise with increasing SZA. Thus, for a small absorber like OCIO the DOAS fit misinterprets residual structures as OCIO absorptions, resulting in increasing SCDs for increasing SZA during occultation. This effect can be observed for every DOAS balloon flight, also for measurements where OCIO is definitely not present in significant amounts. Higher SCD values for occultation measurements compared to modelled SCDs, as shown in Figure 8.3 for Leon 1996 (occultation starting at 16:38 UT), can therefore be explained. However, within the given errors of the *WinDOAS* evaluation these values are still in accordance with model results and cannot explain the 10 times higher values obtained by *Fitzenberger* [2000].

Modelled SCDs plotted in Figure 8.3 are obtained as described in section 6.1.2. The Br_y content in the model was adjusted to DOAS BrO observations as described in chapter 9 and ClO quantities were compared to TRIPLE balloon measurements as reported by *Vogel et al.* [2005]. For a short description of the TRIPLE payload, see chapter 7. TRIPLE observations were performed outside the vortex at Leon on November 14, 1996. The ClO profile correspond well with values obtained with the SLIMCAT CTM model. During daylight about 150 pptv and 200 pptv were measured at $\Theta = 600$ K and $\Theta = 800$ K respectively. *Vogel et al.* [2005] also found an overall good agreement between photochemical box model calculations and measurements, and deduced that no substantial uncertainties exist in midlatitude chlorine chemistry in the stratosphere. Since ClO used in the model study presented here corresponds well with TRIPLE measurements, and BrO is consistent with DOAS measurements, the modelled SCD values in Figure 8.3 are expected to be accurate.

Inaccuracies due to the degree of polynomial used and the high residual structures in the fitting procedure, allow a total fitting error of 1.5 times the DOAS fit error to be defined. Another 10% SCD error is taken into account for the OCIO cross-section and temperature uncertainties and is added to the total fitting error, applying Gaussian error propagation. Whenever model comparisons are shown in this chapter, SCD errors are plotted with corresponding error bars. Within these errors, modelled and retrieved OCIO SCDs for the Leon 1996 flight correspond well with one another (Figure 8.3).

Model results presented here are obtained using the same model described in chapter 7, the only difference being that the model is used in stacked mode, rather than calculating photochemistry along trajectories.

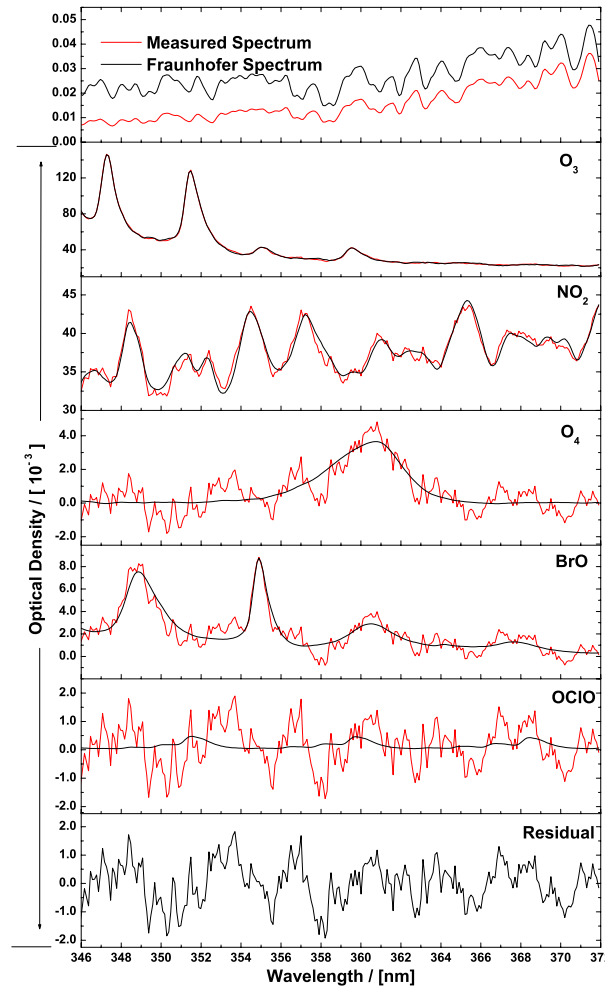


Figure 8.5: Same as Figure 8.4 but for a spectrum recorded during occultation measurements of the balloon flight at Kiruna on February 14, 1997. The spectrum was recorded at 29.79 km at 93.39° SZA (14:44:29 UT) with 3 scans and a total exposure time of 9.18 seconds.

LPMA data and DOAS NO₂ and O₃ profiles given in this chapter are courtesy of A. Butz. Part of the work can be found in *Butz et al.* [2005]. Important flight parameters for UV observations for the balloon flights presented in the following sections, can be obtained from Table 6.1 and 6.1.

8.2 The LPMA / DOAS Measurements at Kiruna on February 14, 1997

Figure 8.6 shows fit results of the BrO and OCIO retrieval for the flight at Kiruna on February 14, 1997. Panel d) displays OCIO values from the 346 – 372 nm retrieval range. OCIO values are very low and, as indicated in Figure 8.7, are hardly above the detection limit. In Figure 8.5 a typical OCIO fit in the 346 – 372 nm wavelength range is shown for a spectrum recorded at 93.39° SZA (14:44 UT). The optical density of OCIO is much smaller than the remaining residual structure of the fit. Fit parameters and development of SCDs for the DOAS OCIO evaluation are shown in Figure 8.6. Although no sensitivity

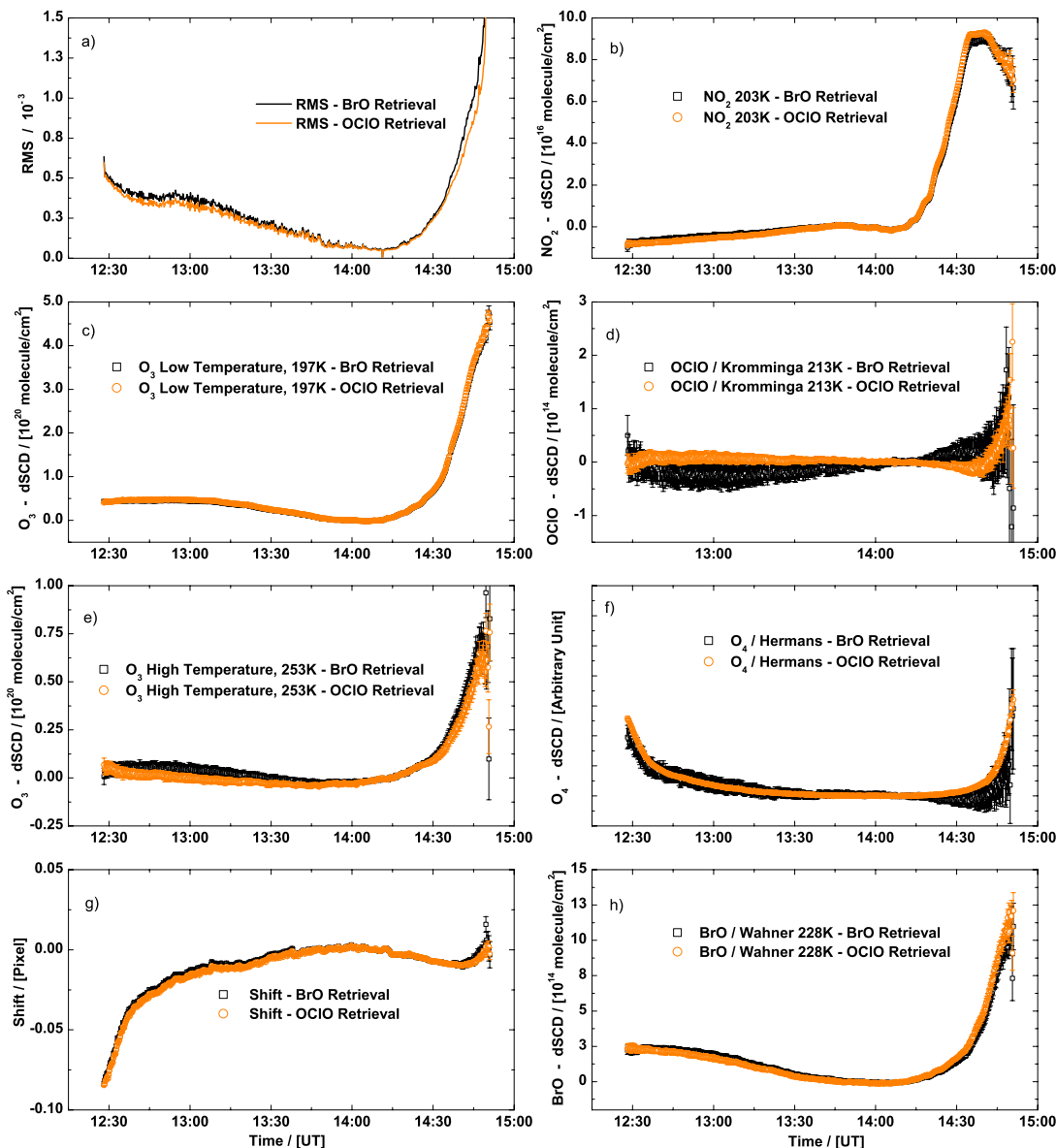


Figure 8.6: Same as Figure 8.2 but for the balloon flight at Kiruna on February 14, 1997.

studies are possible with values mainly below the detection limit, a standard model comparison was performed.

A comparison of tracers has shown, that the dynamics are modelled correctly by SLIMCAT. N_2O (shown in Figure 8.8) and CH_4 volume mixing ratio profiles, recorded by the LPMA instrument, show reasonable agreement overall, but also indicate that air masses inside and outside the vortex were probed during occultation measurements. Since the SLIMCAT model output is an average value taken from 4 grid points adjacent to the Kiruna station, it is clear that small features at the boundary of the vortex cannot be represented correctly.

LPMA measurements of the reservoir HCl (right panel in Figure 8.8) also indicate that some chlorine activated inside vortex air was observed during occultation measurements at around 20 km. Overall the model has lower HCl values above 15 km, but agreement should be sufficient for a rough model

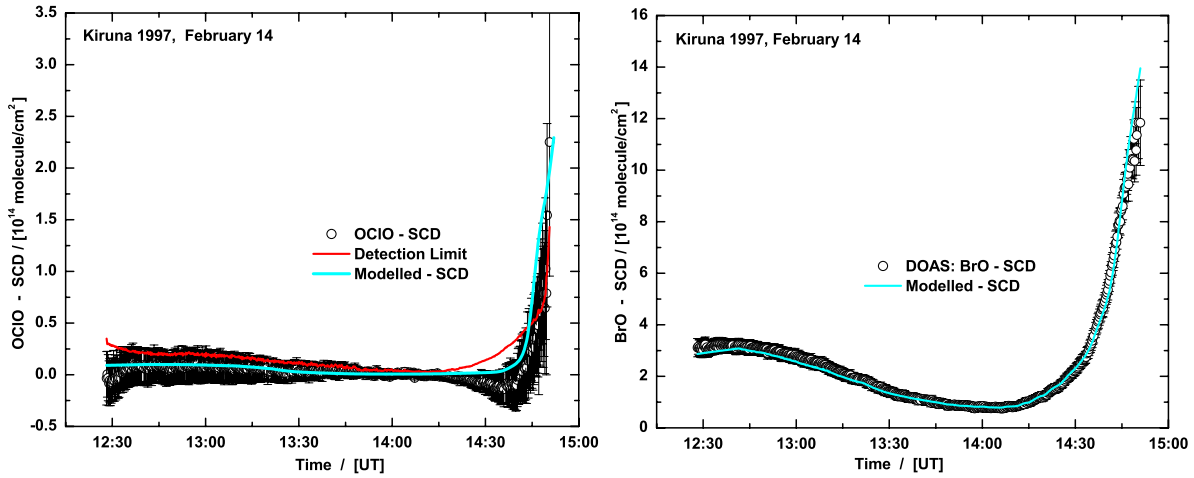


Figure 8.7: Development of OCIO and BrO SCD values for the balloon flight at Kiruna on February 14, 1997. Modelled SCDs as described in the text are plotted in blue for comparison. The detection limit for OCIO is shown in red.

comparison. Unfortunately the chlorine reservoir species ClONO_2 was not measured by LPMA during this flight. Otherwise simultaneous measurements of HCl and ClONO_2 could be used to derive ClO_x ($= \text{Cl} + \text{ClO} + 2 \times \text{Cl}_2\text{O}_2 + \text{OCIO}$) for modelling.

Since the formation of OCIO mainly depends on the amount of BrO, it is essential to check and, if necessary, adjust values in the model. For the Kiruna 1997 balloon flight a total Br_Y of ~ 18 pptv can be inferred from BrO measurements as explained in chapter 9. In Figure 8.7 the measured and modelled BrO SCDs are plotted and show good agreement. The same holds true for the BrO profile, which is not shown here. In order to obtain correct BrO values in the model, it is also necessary to adjust the amount of NO_2 used in the model, as described in chapter 7. O_3 and NO_2 concentration profiles are compared in Figure 8.9 and show very good agreement with SLIMCAT output. Therefore, NO_2 does not need to be scaled in the 1D-model.

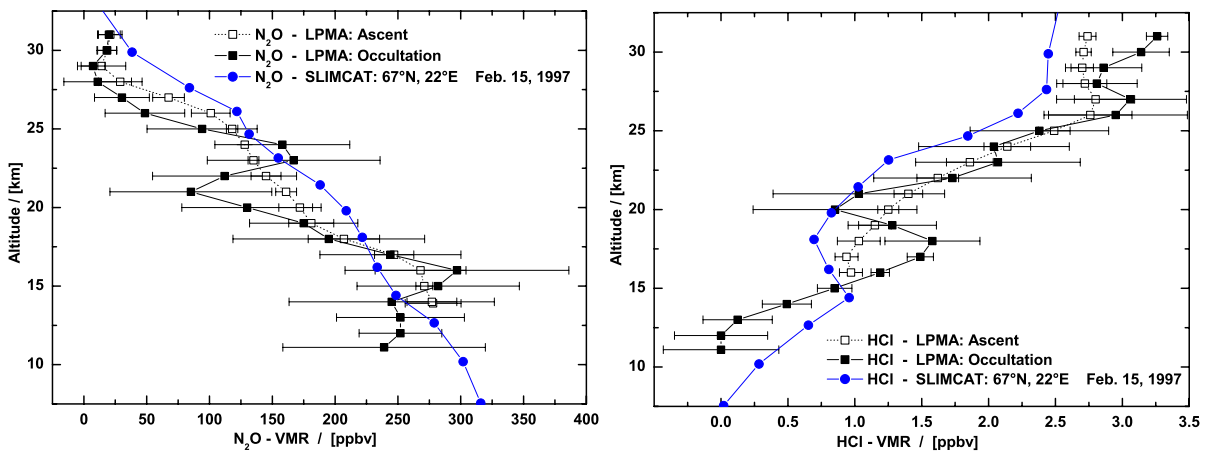


Figure 8.8: N_2O and HCl volume mixing ratio profiles as measured by the LPMA-FTIR, compared to SLIMCAT model output, for the balloon flight at Kiruna on February 14, 1997. Ascent and occultation profiles are shown.

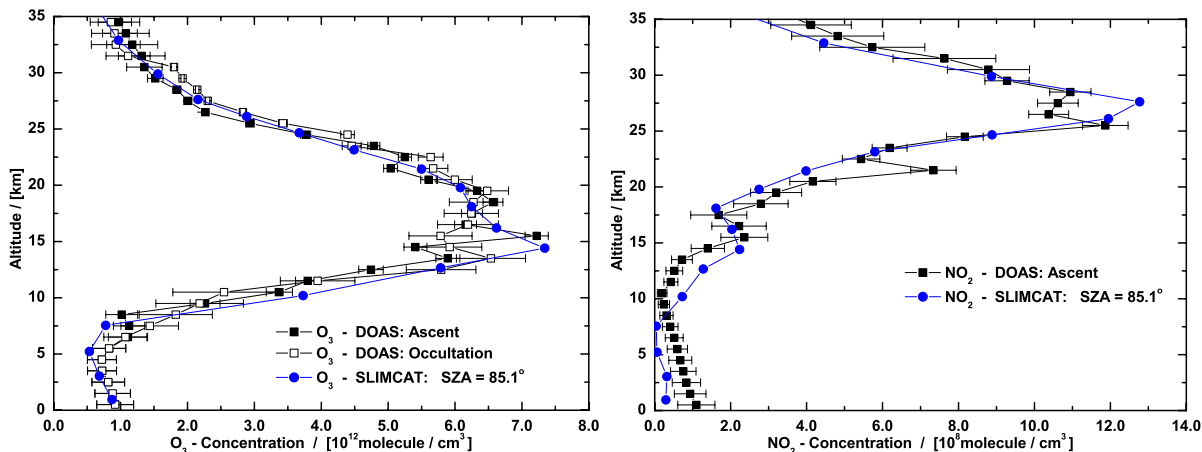


Figure 8.9: O_3 and NO_2 concentrations measured with the DOAS Vis spectrograph in comparison to SLIMCAT model output at $SAZ = 85.1^\circ$, for the balloon flight at Kiruna on February 14, 1997. O_3 ascent and occultation profiles are shown.

Concentration fields of BrO and OCIO are plotted in Figure 8.10. The only significant amounts of OCIO are formed between 15 to 20 km for $SAZ > 92^\circ$, which is in accordance with modelled OCIO SCDs in Figure 8.7. Agreement with measured values is given within errors, where negative measured values at the beginning of occultation are due to correlations and residual structures in the DOAS fit. Furthermore, it can be observed that modelled OCIO values increase faster during occultation, which can be explained by higher chlorine activation in the model, as indicated by lower HCl abundances.

OCIO values close to or slightly over the detection limit mean that the Kiruna 1997 observations are not well suited to a stringent test of photochemistry, but on the other hand they do not indicate any major inconsistencies.

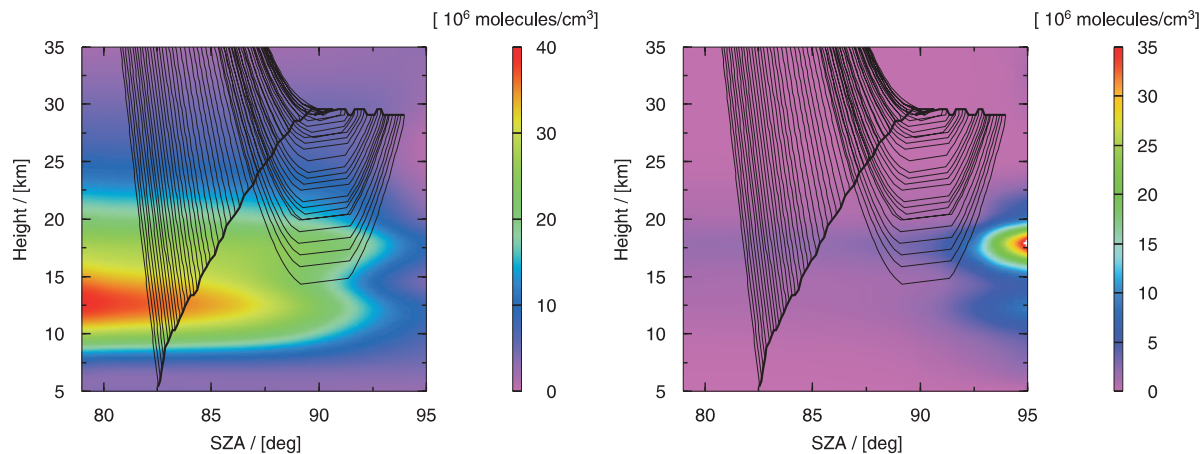


Figure 8.10: Colour-coded model concentration fields of BrO (left) and OCIO (right) from SLIMCAT output at Kiruna ($67^\circ N$, $22^\circ E$) on February 14, 1997. The observation geometry is superimposed (see e.g. Figure 6.6 for explanation).

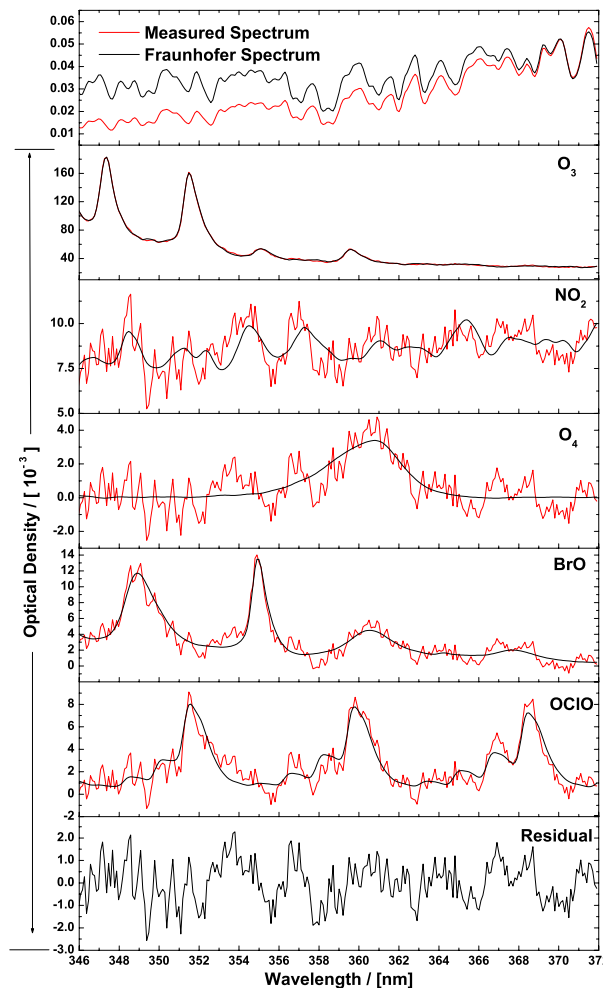


Figure 8.11: Same as Figure 8.4 but for a spectrum recorded during occultation measurements of the balloon flight at Kiruna on February 10, 1999. The spectrum was recorded at 28.32 km at 93.25° SZA (14:37:17 UT), with 1 scan and a total exposure time of 15.0 seconds.

8.3 The LPMA / DOAS Measurements at Kiruna on February 10, 1999

The OCIO DOAS fit of spectra recorded at Kiruna on February 10, 1999, shows clear signs of OCIO absorption (Figure 8.11). Panel d) in Figure 8.12 shows the development of OCIO SCDs. OCIO values obtained in the BrO retrieval range (346–360 nm) scatter around zero for ascent and float measurements, but correspond well during occultation, where high values are observed. O₄ SCDs in the OCIO retrieval range also correspond well with measurements obtained using the Vis spectrograph. The left panel of Figure 8.13 shows the detection limit; OCIO occultation values are clearly above the limit. As for Kiruna 1997, measurements took place at the edge of the vortex, pointing inside the vortex during occultation. Temperatures of the probed air masses were moderately low with a minimum of 193 K between 20 and 25 km altitude. This winter only had short periods and small areas in which temperatures were low enough to allow the existence of NAT PSC particles. It was a dynamically active winter with a disturbed and relatively weak vortex. Large amounts of PSC particles leading to enhanced chlorine activation could

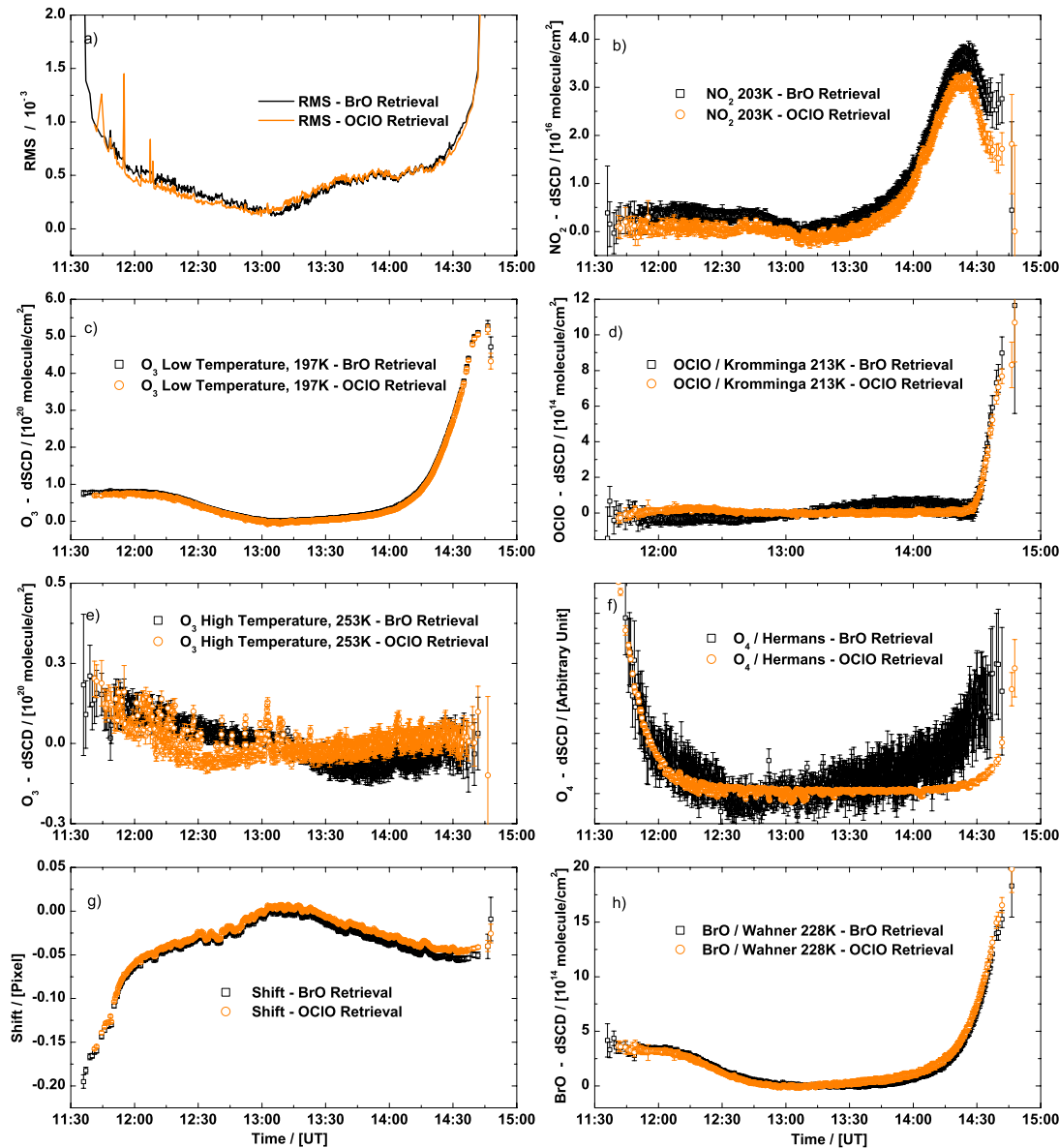


Figure 8.12: Same as Figure 8.2 but for the balloon flight at Kiruna on February 10, 1999.

not build up. Two warmings with complete breakdowns of the vortex occurred at the beginning of December and March. The vortex re-established in April and the final breakdown occurred at the end of May [EC-Report 2001b].

No significant ozone depletion (less than 5%) was observed during this winter at northern latitudes (see also Figure 2.15). Nevertheless, some chlorine and bromine activations were observed and are also predicted by models. Backward air mass trajectories indicate that the observed air masses were of polar origin and were not exposed to much sunlight during the last few days before the measurement [Fitzenberger 2000]. Since temperatures were generally too high for PSC formation, heterogeneous chemistry on background aerosols is important.

Dynamics and history of the probed air masses are accounted for by the SLIMCAT 3-D CTM. Modelled OCIO SCDs, as shown in Figure 8.13, which were calculated from the SLIMCAT concentration field,

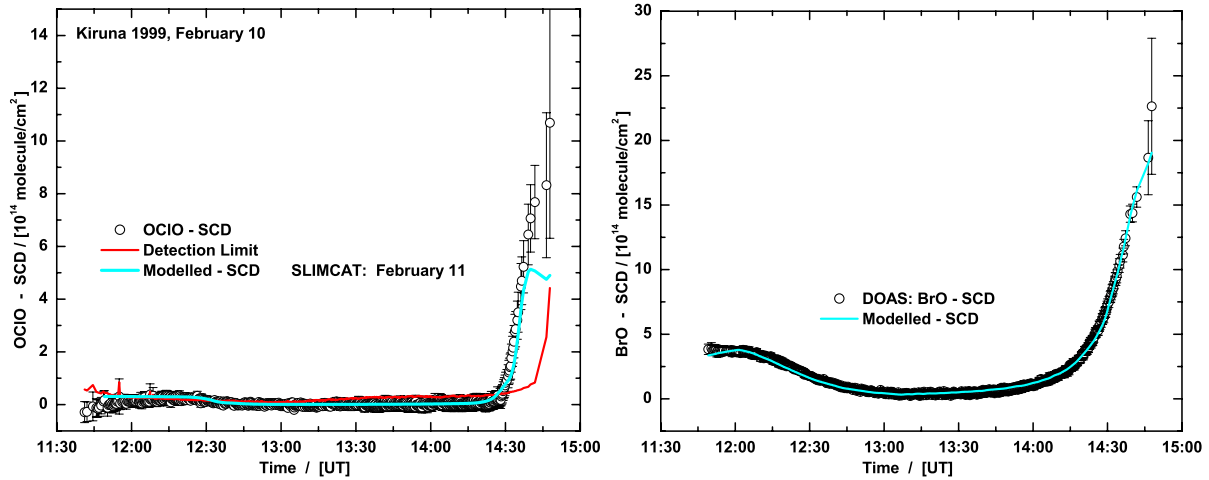


Figure 8.13: Development of OCIO and BrO SCD values for the balloon flight at Kiruna on February 10, 1999. Modelled SCDs as described in the text are plotted in blue for comparison. The detection limit for OCIO is shown in red.

correspond well with measurements without scaling, except during late occultation. The following section verifies the validity of SLIMCAT model output and compares this output with measurements. Further constraints and scalings are performed using 1-D model calculations.

A total Br_Y of ~ 19.5 pptv can be inferred from BrO measurements as explained in chapter 9 (see right panel in Figure 8.13). Comparing SLIMCAT output data of dynamic tracers with LPMA measurements of N_2O (Figure 8.15) and CH_4 indicates reasonable agreement. It can be observed that below 20 km, more inside vortex air masses were probed during occultation observations than during ascent measurements, and that the model corresponds more to outside vortex conditions above 20 km. This can partly be explained by the fact that the model is an average of four grid points around the Kiruna station. The O_3 profiles (not shown here) derived from DOAS ascent and occultation measurements [Butz *et al.* 2005; Bösch 2002], also indicate that inside vortex air was probed during occultation. This can be seen by up to 20% lower O_3 values during occultation, between 10 and 20 km, compared to ascent observations.

The SLIMCAT NO_2 profile has an unrealistically high value at 20.6 km (blue shaded stripe in the upper right panel of Figure 8.14) that can also be observed indirectly in the ClONO_2 profile in Figure 8.15. Since simple scaling of NO_2 could not remove this feature, the height segment was omitted and values interpolated from the two adjacent height segments. Overall, DOAS observations and modelled NO_2 indicate a denoxified stratosphere below 21 km.

LPMA measurements of HCl and ClONO_2 allow available ClO_X to be derived. Since Cl_Y was not measured at the same time it had to be determined with the help of TRIPLE measurements performed at Kiruna on February 6, 1999. The cryogenic whole air sampler of the University of Frankfurt installed on the TRIPLE gondola measures all relevant long-lived tracers. Therefore a $\text{N}_2\text{O} - \text{Cl}_Y$ correlation can be derived [Engel *et al.* 1999], allowing Cl_Y to be inferred for the LPMA / DOAS measurements 5 days later (see also Figure 2.9). The calculated ClO_X ($= \text{Cl}_Y - \text{HCl} - \text{ClONO}_2$) is plotted in Figure 8.16 and compared to ClO_X of the SLIMCAT model. The low ClO_X value at 23 km and the high value at 26 km inferred from the measurements are due to ClONO_2 values as shown in Figure 8.15. In the relevant altitude range between 15 and 22 km the modelled and measured values correspond well, except at around 18 km, where the modelled ClO_X is much lower. Therefore modelled ClO_X values were scaled to observations at this altitude level, although the scaling has no major influence on the overall OCIO observations, since OCIO values mainly depend on the amount of BrO.

When adjustments in the 1-D model are performed as described - i.e. scaling of NO_2 , O_3 , Br_Y and ClO_X

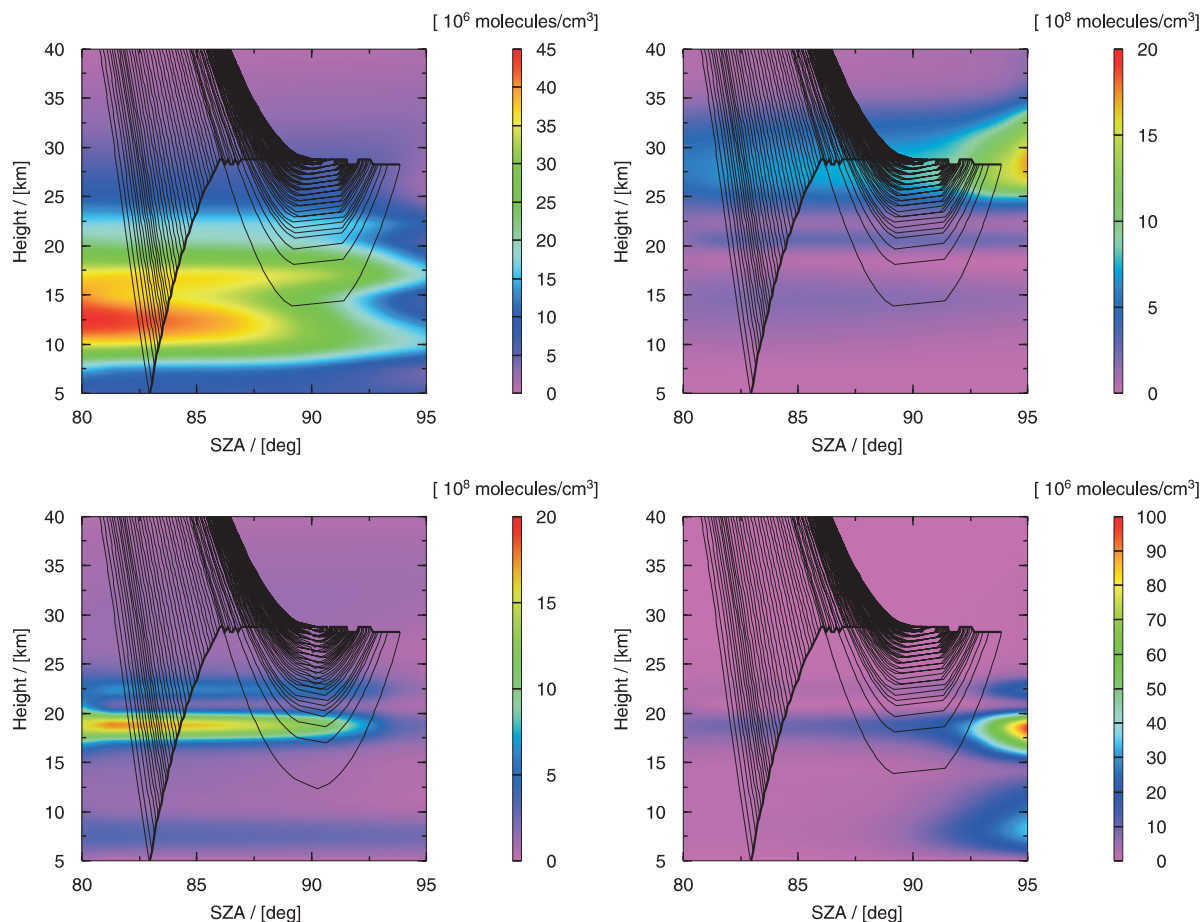


Figure 8.14: Colour-coded model concentration fields of BrO (upper left panel), NO_2 (upper right panel), ClO (lower left panel) and OCIO (lower right panel) from SLIMCAT output at Kiruna (67°N , 22°E) on February 10, 1999. The observation geometry is superimposed (see e.g. Figure 6.6 for explanation).

(at one altitude), and one height segment is omitted from the SLIMCAT output - the resulting modelled OCIO SCDs correspond excellently with occultation measurements. In Figure 8.17 the ascent and occultation measurements are magnified. SLIMCAT results are shown for purposes of comparison, as in Figure 8.13, in light blue. The green line labeled ‘standard run’ is the resulting SCD development from the 1-D model. It was discovered that scaling NO_2 is responsible for most of the differences between SLIMCAT and the 1-D model results. Ascent measurements are not expected to correspond as well, since measurements were taken at the edge of the vortex and ClONO_2 , and therefore ClO_x , cannot be inferred from ascent observations. A correlation plot of measured and modelled OCIO SCDs for this ‘standard model run’ is shown in Figure 8.18. Occultation values for SZAs $> 92^\circ$ are highlighted in blue. The large scatter of low values is mainly due to float spectra, which scatter around zero. The good agreement for occultation values above the detection limit ($> \sim 4 \times 10^{13} \text{ molecule/cm}^2$) is convincing.

Two model runs were carried out, where the chlorine and bromine load were changed to 70% of the actual value (dashed red and magenta lines in Figure 8.17). Although the uncertainty in Br_Y and Cl_Y are less than 10%, the test shows the response of the model and that the relationship between OCIO and ClO amounts is not linear, but limited by BrO. In another model simulation, the reaction rate of BrO with NO_2 was increased by 50%, approximately reflecting uncertainties at stratospheric temperatures as given

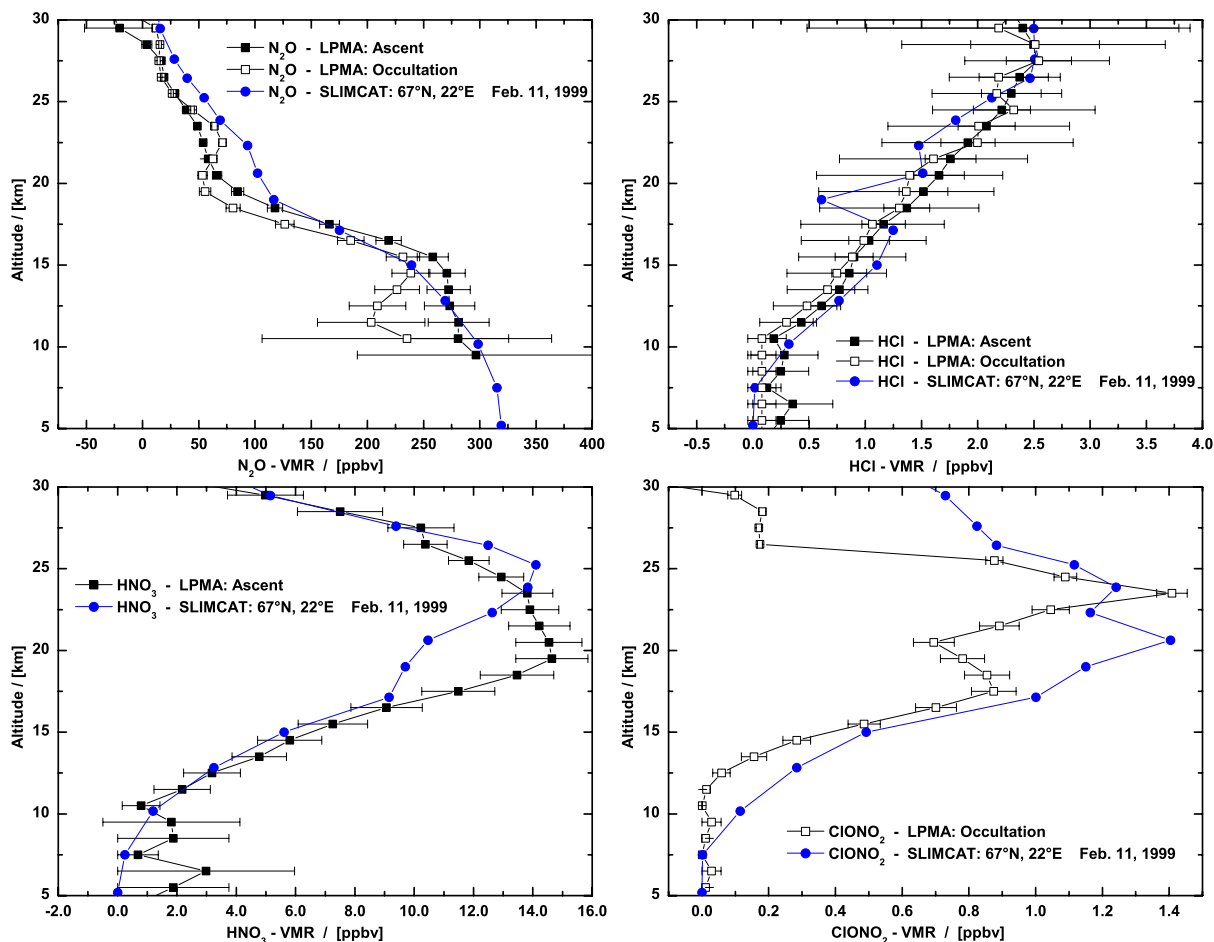


Figure 8.15: N_2O , HCl, HNO_3 and $ClONO_2$ volume mixing ratio profiles as measured by the LPMA-FTIR, compared to SLIMCAT model output (February 11, 1999), for the balloon flight at Kiruna on February 10, 1999. Ascent and occultation profiles are shown.

by Sander *et al.* [2003]. The effect on OCIO values is small, leading to a decrease of OCIO abundances due to the fact that less BrO is available (blue line in Figure 8.17).

The latest findings of Canty *et al.* [2005] (see also Figure 2.13) were investigated in a separate model run, plotted as grey line in Figure 8.17. Using an isentropic trajectory model constrained by observed profiles of ClO_x and DOAS BrO measurements, Canty *et al.* [2005] show that a nighttime profile of OCIO [Rivière *et al.* 2003] in the Arctic vortex during the winter of 2000 is overestimated (see section 8.4). Calculated abundances of nighttime OCIO are shown to be sensitive to the abundance of BrO_x ($BrO + BrCl$), to details of the air parcel history during the most recent sunrise / sunset transitions, and the BrCl yield from the reaction $BrO + ClO$. The discrepancy between measured and modelled nighttime OCIO suggests that production of OCIO occurs more slowly than implied by standard photochemistry. If the yield of BrCl from the reaction of $BrO + ClO$ is increased from 7% (JPL 2002 value) to 11% (near the upper limit of the uncertainty), good agreement is found between measured and modelled nighttime OCIO. The impact is found to be considerably smaller on OCIO observations obtained during twilight ($90 \leq SZA \leq 92$), when photolytic processes are still active. By increasing the BrCl yield to 11% in this study, the model tends to underestimate measured values, which on the other hand, are slightly overestimated by the standard run.

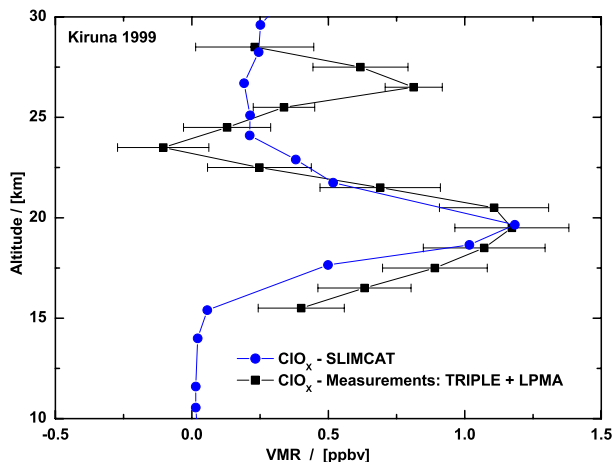


Figure 8.16: Comparison of ClO_x from a SLIMCAT model simulation (blue) for 67°N , 22°E on February 11, 1999, with ClO_x inferred from TRIPLE and LPMA / DOAS balloon measurements (black) as described in the text.

von Hobe et al. [2005] discuss a re-evaluation of the $\text{ClO} / \text{Cl}_2\text{O}_2$ equilibrium constant based on stratospheric in-situ observations. Their measurements suggest that the thermal equilibrium between the dimer formation and dissociation is shifted significantly towards the monomer compared to the current JPL-2002 recommendations. A fit of the JPL format for equilibrium constants yields $k_{eq} = 4.06 \times 10^{-23} \exp(6201/T)$ compared to the JPL-2002 value of $k_{eq} = 1.27 \times 10^{-27} \exp(8744/T)$. The yellow line in Figure 8.17 gives the results of a model run performed with values suggested by *von Hobe et al.* [2005]. As expected, modelled OCIO values are larger and close to the upper error limits, due to more available ClO .

A combined model run (dark green line) using the findings of *Canty et al.* [2005] and *von Hobe et al.* [2005] gives equally good results as the standard run using JPL-2002 kinetics. Since there are too many uncertainties in the modelling, scaling and the DOAS OCIO evaluation and since basically all model runs (apart from the unrealistic ones with altered Br_Y and Cl_Y) match within the

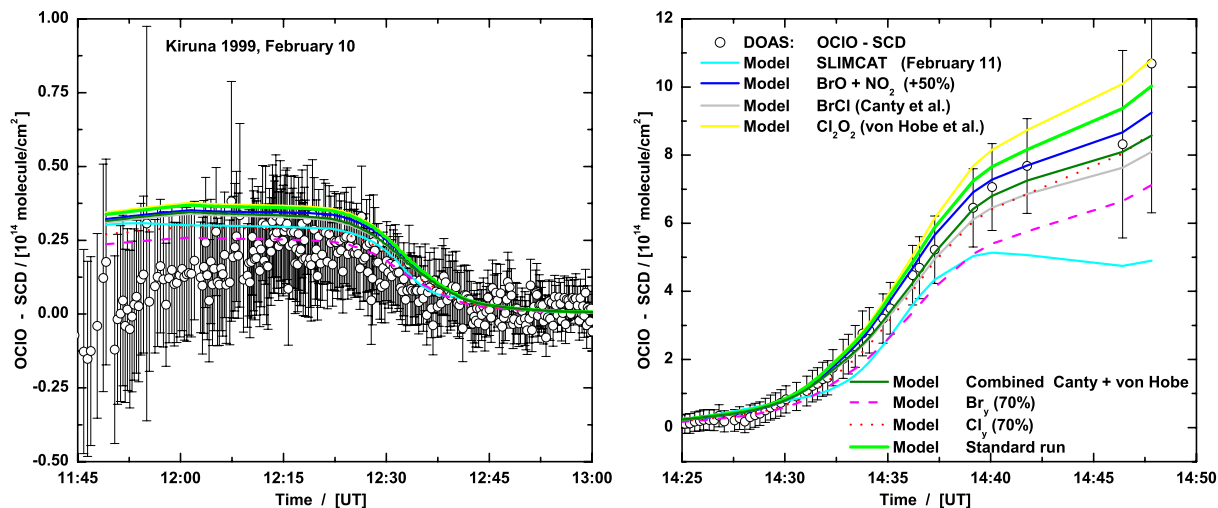


Figure 8.17: Development of OCIO SCD values for the balloon flight at Kiruna on February 10, 1999, compared to different model studies as described in the text.

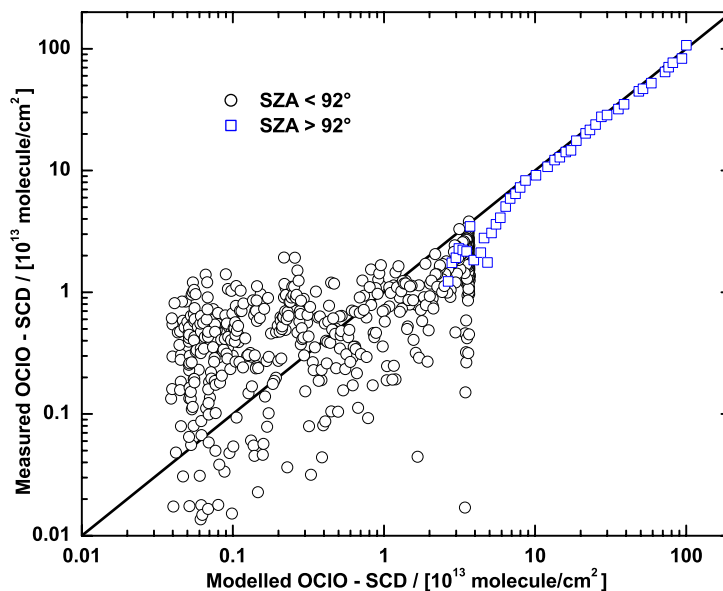


Figure 8.18: Comparison of measured and modelled OCIO SCDs for the balloon flight at Kiruna on February 10, 1999. Modelled values are taken from the standard model run.

stated error range, a final conclusion cannot be drawn.

This study does not infer OCIO profiles from DOAS measurements, since no new information would be gained from doing so. Retrieval of OCIO profiles from occultation measurements also proves to be impossible without photochemical scaling since photochemical change during twilight is too strong.

Figure 8.19 shows the evolution of almost all bromine species involved in the inorganic bromine chemistry at the 453 K potential temperature level. Br and Br₂ are missing, but are much less abundant at low altitudes than the other bromine species. BrO only appears when photochemistry sets in, while BrONO₂ is converted to HOBr and subsequently to BrCl during the polar night. HOBr produces BrO and OH in the morning. Especially during sunset, BrO reacts with ClO to generate OCIO, ClOO and BrCl. This increase of BrCl can be seen clearly. Some chlorine monoxide is converted to OCIO, until BrO is removed and mainly converted to BrCl, and consequently is no longer available as a reaction partner. Since BrCl is photolysed very rapidly, BrO appears when air masses are sunlit. Therefore, BrONO₂ forms again when BrO reacts with NO₂. In general it can also be observed that the more sunlight that reaches the air masses, the more important HOBr and BrONO₂ become as nighttime reservoirs. At the beginning of the night, BrONO₂ is a more important reservoir than HOBr, while in the morning most of the bromine nitrate has been converted heterogeneously to HOBr. Since HOBr is photolysed faster than BrONO₂ it leads to the morning / evening asymmetry observed in BrO concentrations. For the polar winter conditions shown here, this asymmetry is not as pronounced as at lower latitudes.

The chlorine chemistry is shown in the left panel of Figure 8.19 for the 453 K potential temperature level. ClO, Cl₂O₂, OCIO and BrCl are the photochemically most active chlorine species and vary in relation to one another from day to night, while the other chlorine species do not vary significantly. OCIO is nearly constant during the night at around 80 pptv. OCIO values at initialisation are higher than modelled values at sunset (-8 hours before endpoint) due to the scaling of NO₂ and the history of the air masses contained in the SLIMCAT output, which is used for initialisation at 0 UT (here -24 hours before endpoint of the calculation). This means that a new equilibrium value results. Due to the fast photolysis of OCIO, daytime values are rather low and a rapid build-up of significant amounts is only observed for SZAs > 92° as can be seen in Figure 8.14.

Nitrogen species are shown in Figure 8.20. The active NO_x species NO and NO₂ only appear during the sunlit phases. The reaction of HNO₃ with OH is also triggered by sunlight, producing NO₃. During polar

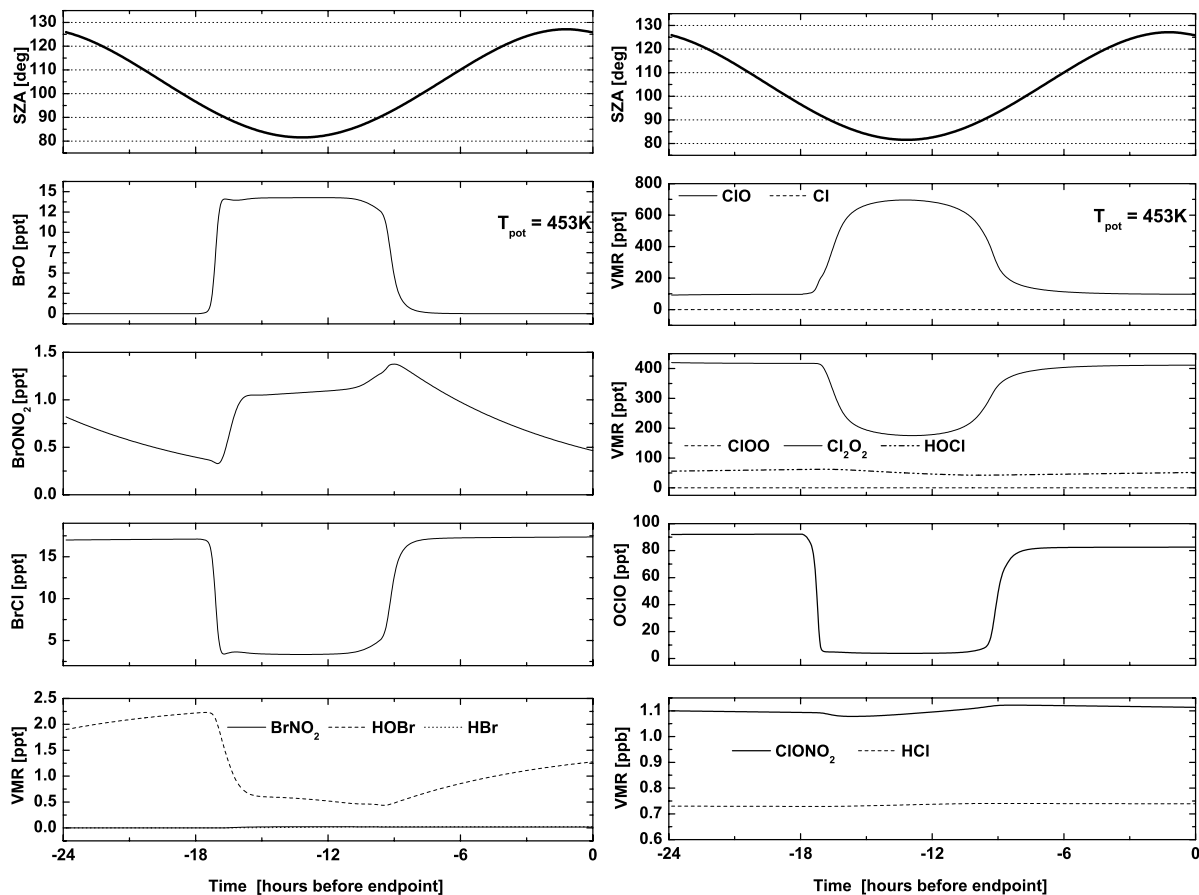


Figure 8.19: Evolution of bromine and chlorine species on the 453 K potential temperature isentropic level for a one-day stacked model simulation starting at 0 UT on February 10, 1999. The model is initialised with SLIMCAT output at 67°N, 22°E.

night, NO_3 is consumed by the reaction with NO_2 , forming N_2O_5 .

The left panel of Figure 8.20 shows the evolution of the oxygen species. O_3 decreases slightly during daylight at a rate of ~ 20 ppbv/day. At night O_3 mixing ratios remain constant. In Figure 8.21 the ozone depletion rate is given in ppbv per day for the relevant altitude range between 10 and 25 km. As expected, the peak value of ozone depletion (~ 20 ppbv per day) is observed at around 18 km, where chlorine activation is highest. Ozone loss from the SLIMCAT model is shown for comparison. The increase of ozone loss above 25 km is due to the NO_x cycle.

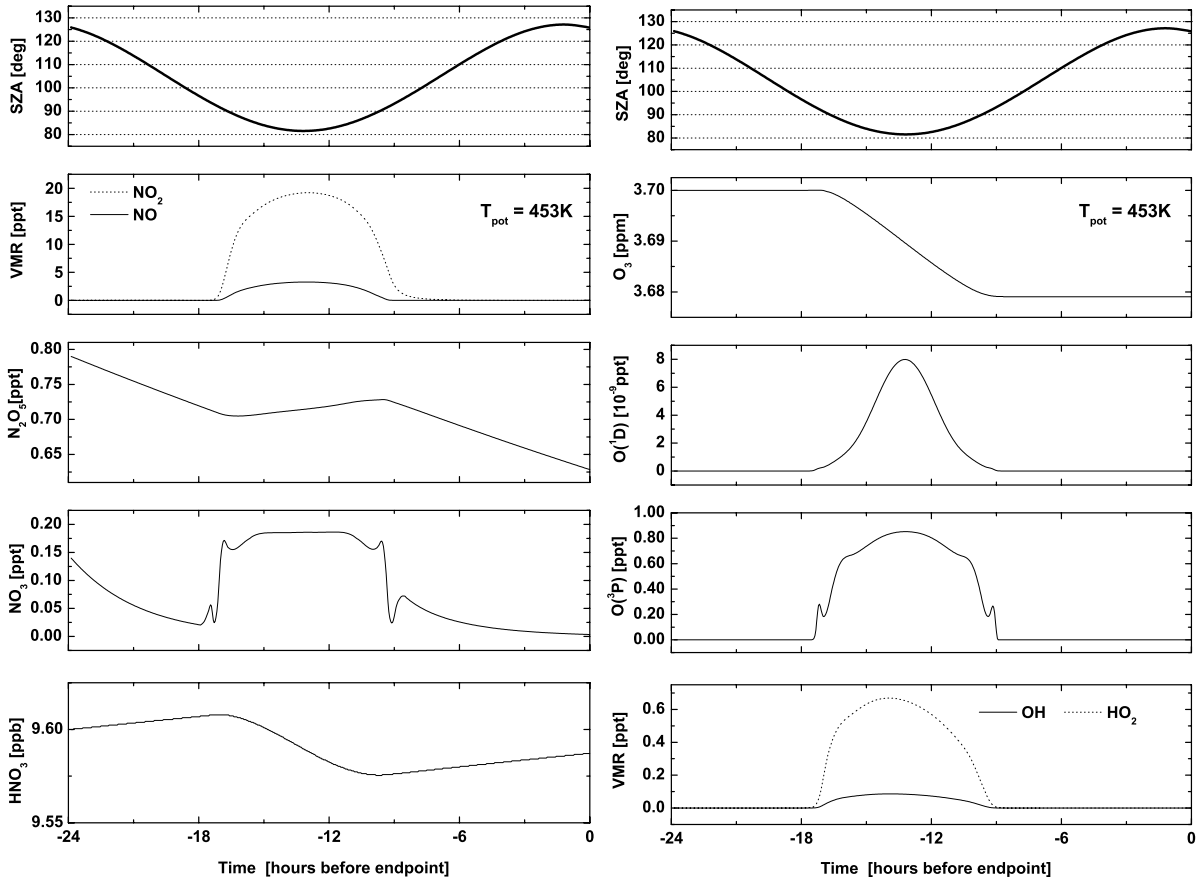


Figure 8.20: Evolution of nitrogen and oxygen species on the 453 K potential temperature isentropic level for a one-day stacked model simulation starting at 0 UT on February 10, 1999. The model is initialised with SLIMCAT output at 67°N, 22°E.

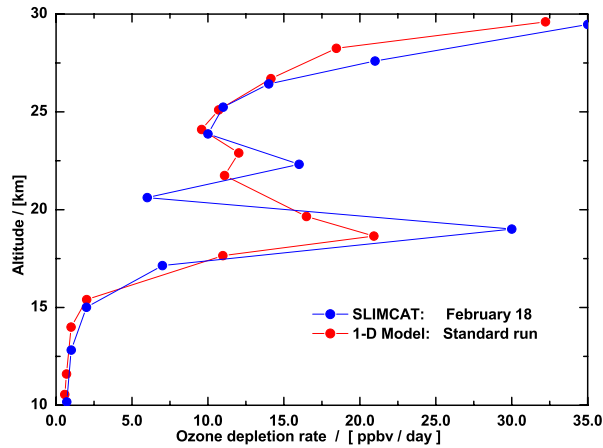


Figure 8.21: Ozone depletion rate as a function of altitude in ppbv per day at Kiruna on February 10, 1999.

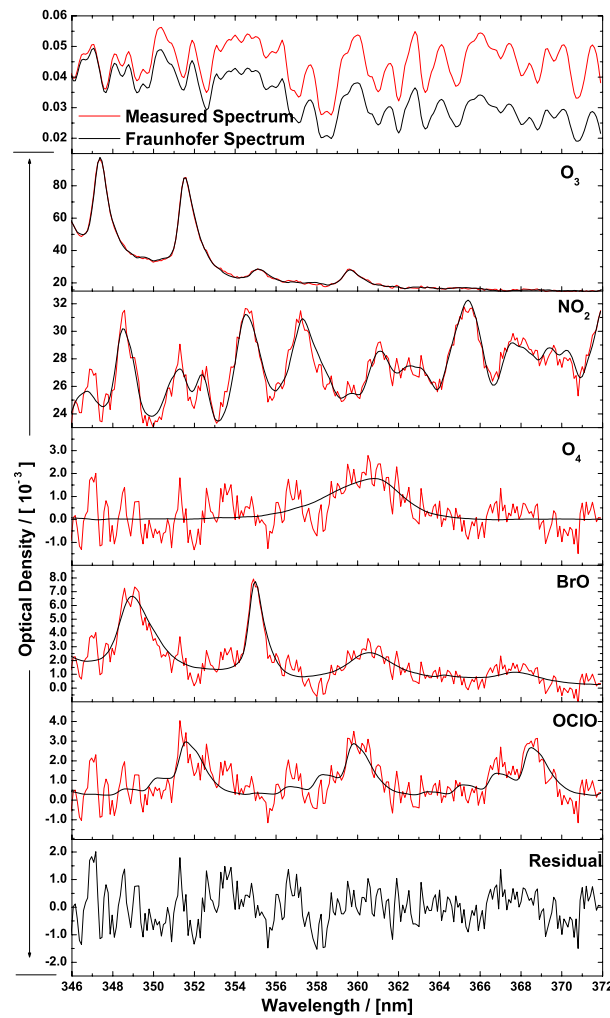


Figure 8.22: Same as Figure 8.4 but for a spectrum recorded during occultation measurements of the balloon flight at Kiruna on February 18, 2000. The spectrum was recorded at 30.02 km at 93.15° SZA (14:54:22 UT) with 1 scan and a total exposure time of 65.0 seconds.

8.4 The LPMA / DOAS Measurements at Kiruna on February 18, 2000

During the arctic winter of 1999/2000 a strong and highly-activated polar vortex formed and denoxification and denitrification occurred. It was one of the coldest winters in the lower stratosphere since 1964/65. The polar region cooled rapidly in the first half of November, with the polar vortex becoming stronger throughout the stratosphere. Temperatures fell below the PSC threshold in the middle stratosphere by mid-November and in the lower stratosphere by end of the month. During the first half of December the vortex intensified and was cold and mostly undisturbed during the second half. The center of the strong vortex lay between Scandinavia and the Pole with minimum temperatures around and below 188 K. Throughout January, the vortex was cold and strong and the minimum temperatures were low enough for PSC formation. In February, an upper stratospheric warming affected the lower stratospheric circulation. However, during the first week of February minimum temperatures temporarily reached the PSC

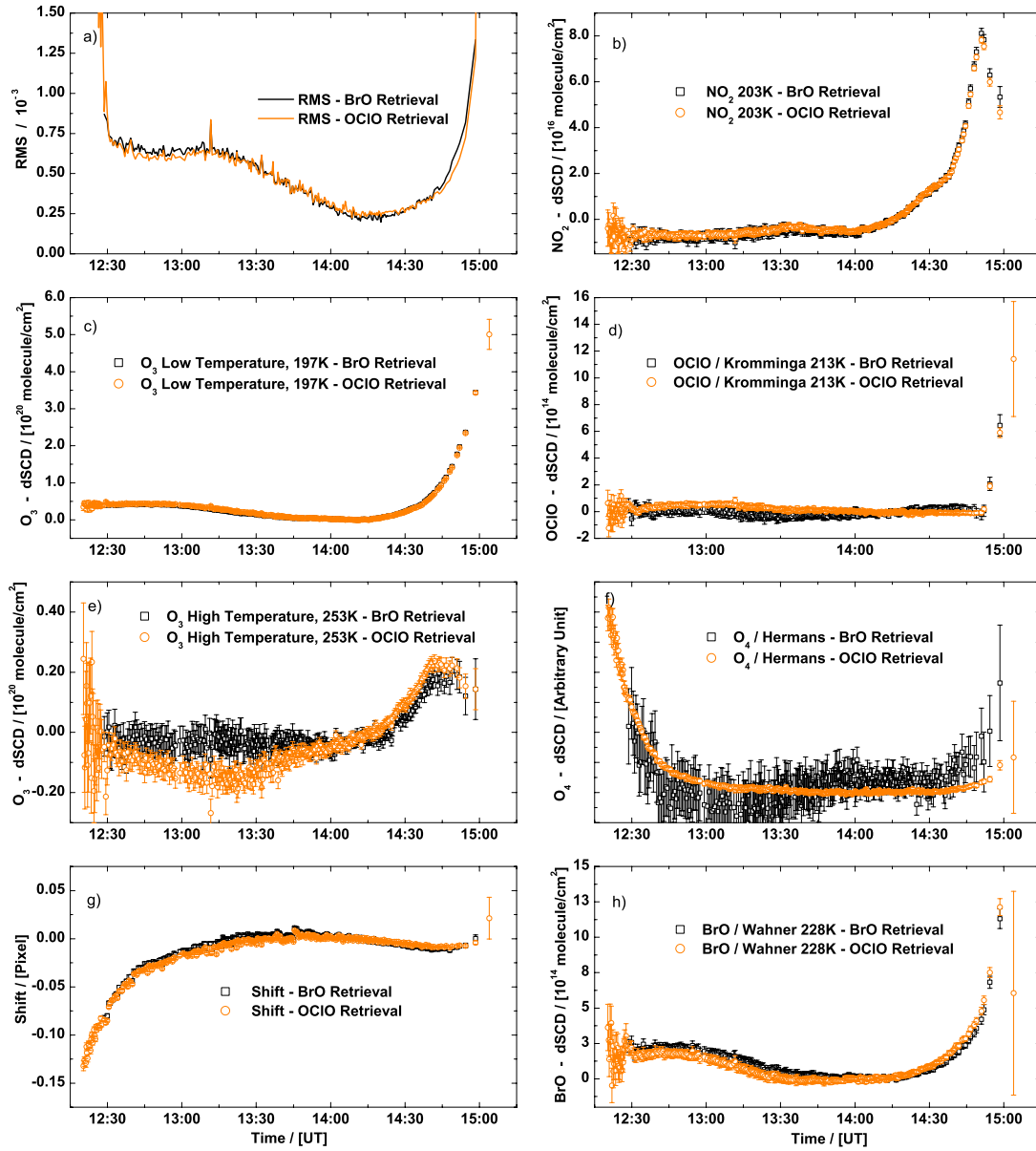


Figure 8.23: Same as Figure 8.2 but for the balloon flight at Kiruna on February 18, 2000.

type 2 threshold. The stratosphere above Europe was warm, with Scandinavia outside the polar vortex except for a few days around February 18. During March, minimum temperatures were continuously below the PSC threshold in the lower stratosphere. In mid-March, the temperatures rose above the PSC threshold. The vortex split and the two parts drifted to Canada and Eastern Europe [Naujokat *et al.* 2000; EORCU 2000]. PSCs were observed extensively in the vortex, with two main periods from mid-December to early February and from late February to mid-March. The vortex was strongly activated and extensively denitrified to a degree only previously observed in Antarctica [Santee *et al.* 2000]. Accordingly, a large local ozone loss of more than 70 % was observed in the altitude range of 18 – 20 km. Most of the ozone loss occurred in March, but losses in January and February were also significant. The total column of ozone loss was about 20 – 25 % [EORCU 2000].

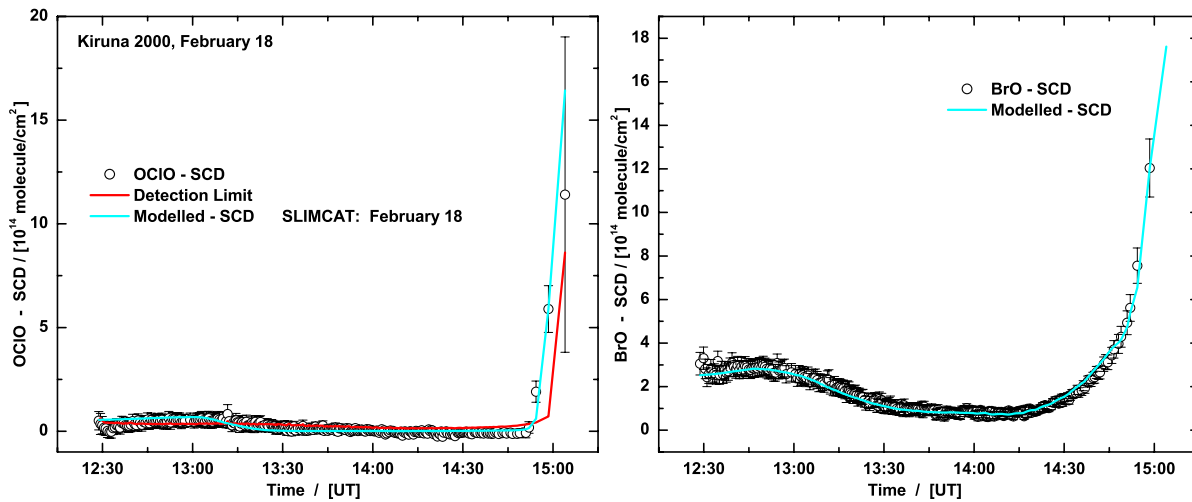


Figure 8.24: Development of OCIO and BrO SCD values for the balloon flight at Kiruna on February 18, 2000. Modelled SCDs as described in the text are plotted for comparison in blue. Additionally the detection limit for OCIO is shown in red.

DOAS balloon measurements took place inside the vortex during ascent and occultation, although observations during occultation pointed towards and were close to the vortex edge. Due to the use of the optical preanalyzer (see e.g. section 4.1.2) and a change in its filtering function during the flight, the number of recorded spectra and the signal-to-noise ratio in the DOAS evaluation is comparatively low [Fitzenberger 2000]. Figure 8.22 shows the evaluation of one of the 4 occultation spectra for which OCIO absorptions were observed. The development of OCIO SCDs and other fit parameters is found in Figure 8.23. The root mean square of the residual in panel a) indicates the poor data quality compared to other flights.

Modelled and measured OCIO and BrO SCDs are shown in Figure 8.24 together with the OCIO detection limit. Modelled OCIO SCDs are calculated from SLIMCAT output data and already correspond well with observations. Modelled BrO SCDs are obtained from a 1-D model run with a scaled total Br_Y of ~ 20.5 pptv (see chapter 9).

The DOAS NO_2 profile coincides with the SLIMCAT NO_2 profile and only needs significant scaling above 25 km, where SLIMCAT model values are about 50 % higher. Both profiles have low NO_2 levels up to ~ 20 km where they increase rapidly, with SLIMCAT values already starting to rise at 18 km, indicating a mismatch in the dynamics. Between 15 and 22 km the values of the SLIMCAT O_3 profile are about 10 % higher and are scaled accordingly. Unfortunately the quality of LPMA data is also rather poor for this balloon flight and only N_2O and HCl profiles can be retrieved from ascent measurements as given in Figure 8.26. While the HCl profile corresponds well with SLIMCAT, the N_2O profile deviates significantly and indicates a stronger descent of air masses in the model between 15 and 20 km. This can partly be explained again by the SLIMCAT model output, which covers a large area and therefore different conditions.

Figure 8.25 shows SLIMCAT model concentration fields of BrO, NO_2 , OCIO and ClO. Compared to the previous winter, much higher concentrations of ClO and therefore OCIO exist, and chlorine activation is present over a broader altitude range (see Figure 8.14 for comparison). Since no ClONO_2 profile is available as for the Kiruna 1999 flight, ClO_X cannot be calculated with the help of TRIPLE measurements (N_2O - Cl_Y correlation) performed at the end of January at Kiruna. Therefore, 1-D model calculations only include scaling of Br_Y , NO_2 and O_3 . The results of this ‘standard run’ are displayed in Figures 8.27 and 8.28. The mismatch in dynamics between model and observations can be seen in the ascent measurements, where modelled values decrease earlier. From the occultation values it can be seen that

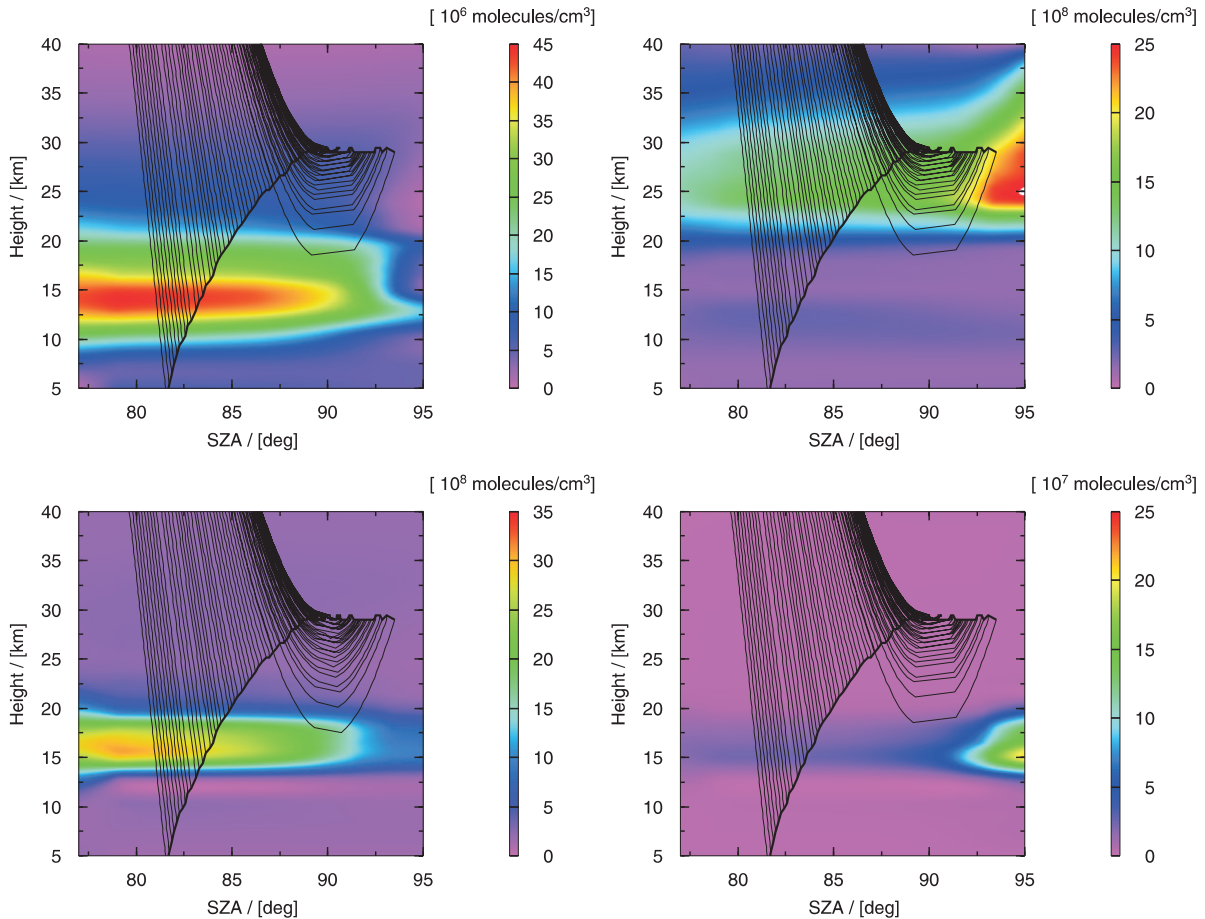


Figure 8.25: Colour-coded model concentration fields of BrO (upper left panel), NO₂ (upper right panel), ClO (lower left panel) and OCIO (lower right panel) from SLIMCAT output at Kiruna (67°N, 22°E) on February 18, 2000. The observation geometry is superimposed (see e.g. Figure 6.6 for explanation).

only 4 spectra show significant OCIO absorptions. The first of these spectra was recorded at 14:52 UT at 92.9° SZA and a tangent height of ~ 21 km. This is in accordance with the values shown in Figure 8.25, where basically zero OCIO concentration is present above ~ 20 km. The abrupt bends in the modelled data are due to the altitude levels included in the model. As the tangent height decreases it eventually crosses the boundary to a lower altitude level which is then included in model calculations. This also causes the mismatch of the data point at 14:54 UT.

As for the Kiruna 1999 model simulations, a model run was performed with the BrCl yield according to *Canty et al.* [2005]. A second model run used the ClO / Cl₂O₂ equilibrium constant as recommended by *von Hobe et al.* [2005]. The combined run with recommendations according to *Canty et al.* [2005] and *von Hobe et al.* [2005] is also compared to the standard run in Figure 8.27.

In Figure 8.29 nighttime profiles of the different model runs (SZA = 100°) are compared to the SALOMON nighttime OCIO observations reported by *Rivière et al.* [2003] and used by *Canty et al.* [2005] (see Figure 2.13). SALOMON lunar occultation measurements were performed between ~ 50 and ~ 150 hPa at Kiruna on January 23, 2000. The flight took place inside the vortex, but close to the edge (Figure 1 in *Rivière et al.* [2004]). Twilight profiles at SZA = 90°, when OCIO builds up rapidly from negligible daytime abundances to nighttime values, are also shown. As expected the OCIO values obtained from the

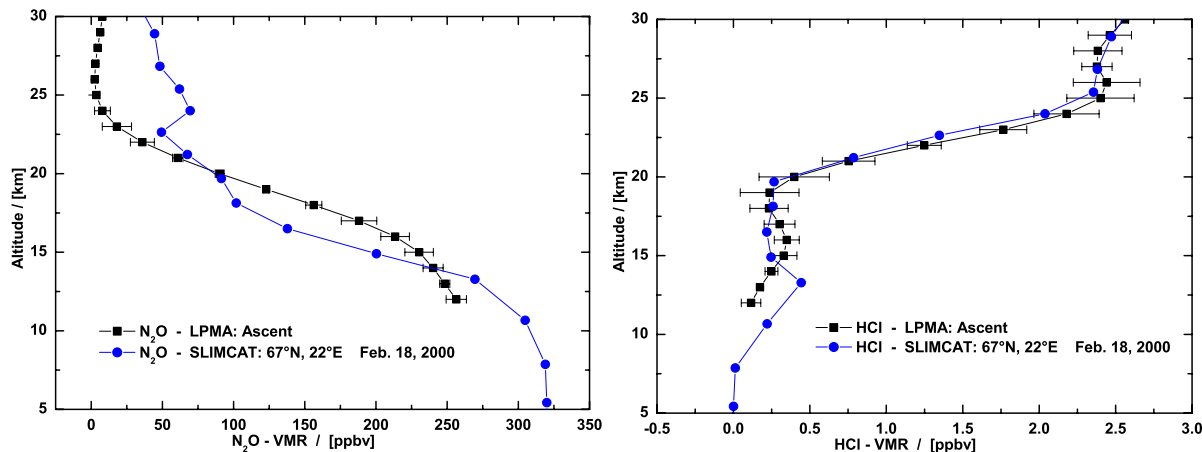


Figure 8.26: N_2O , and HCl volume mixing ratio profiles as measured by the LPMA-FTIR, compared to SLIMCAT model output (February 18, 2000), for the balloon flight at Kiruna on February 18, 2000.

model run with changed ClO / Cl_2O_2 equilibrium constant [von Hobe et al. 2005], are highest at twilight, as more ClO is available. Nighttime abundances are almost the same as for the standard run, although values are slightly smaller since build-up of $BrCl$ is faster (see also Figure 4 in Canty et al. [2005]). The modelled profile with changed $BrCl$ yield corresponds well with SALOMON observations. The same holds true for the nighttime profile of the combined model run, in which values are also determined by the rapid build-up of $BrCl$.

Due to the uncertainties of the modelling and scaling, and particularly as the dynamic tracers do not match well between the model and observations (Figure 8.27), it is not possible to decide which model run matches best and gives the most realistic results from DOAS results alone. If the SALOMON measurements are correct and correspond to the conditions of the DOAS observations, they can be used as an additional constraint for the model simulation, therefore confirming results from Canty et al. [2005]

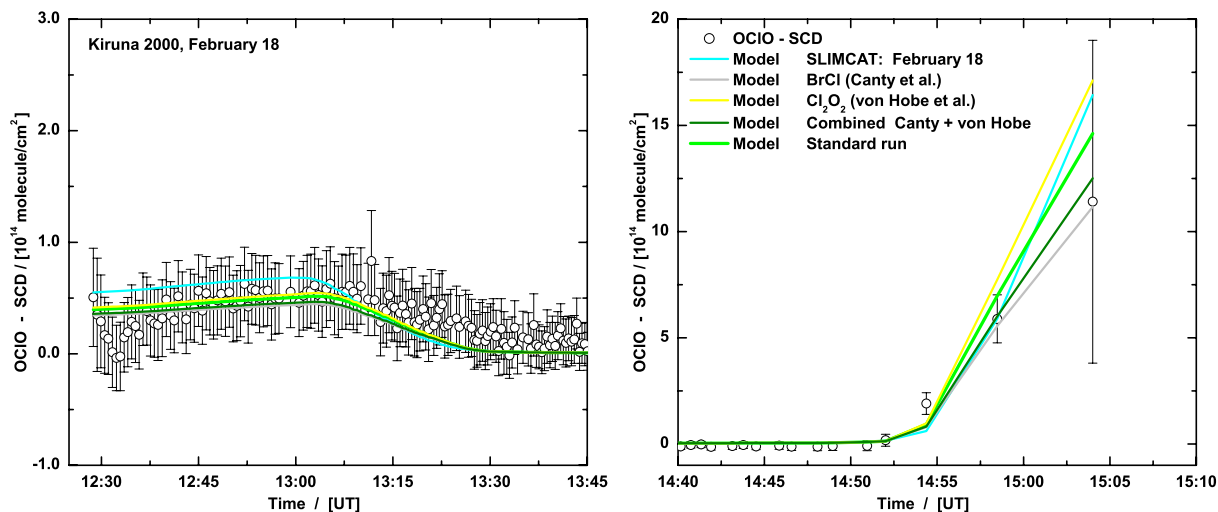


Figure 8.27: Development of OCIO SCD values for the balloon flight at Kiruna on February 18, 2000, compared to different model studies as described in the text.

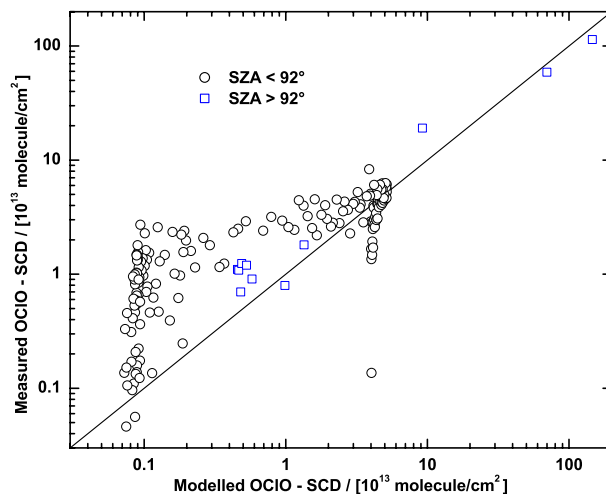


Figure 8.28: Comparison of measured and modelled OCIO SCDs for the balloon flight at Kiruna on February 18, 2000. Modelled values are according to the standard model run.

and possibly those from *von Hobe et al.* [2005].

It has to be mentioned that SALOMON measurements took place 1) in a filament of the vortex located over Scandinavia, i.e. with occultation measurements possibly observing inside and outside vortex air masses at the same time, 2) 4 weeks before DOAS measurements, i.e. possibly under different conditions of chlorine activation and subsidence of air masses and 3) SALOMON simultaneously observed high values of NO_2 reported by *Rivière et al.* [2003] which are difficult to understand with known chemistry and do not correspond to the denoxified conditions of DOAS observations. High amounts of NO_2 coinciding with increased OCIO have been reported by *Rivière et al.* [2003] and *Rivière et al.* [2004] for three SALOMON flights and in all cases could not be explained with known chemistry. This might indicate a systematic instrumental or retrieval error.

In Figure 8.30 the ozone depletion rate is given in ppbv per day for the relevant altitude range between

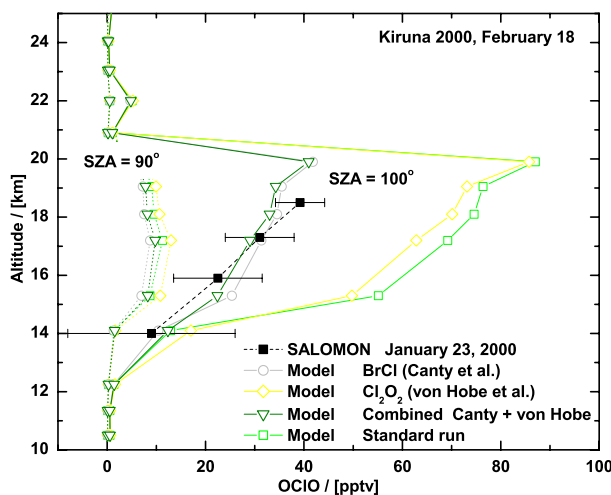


Figure 8.29: A nighttime OCIO profile recorded with the SALOMON instrument [*Rivière et al.* 2003] at Kiruna on January 23, 2000, compared to modelled profiles.

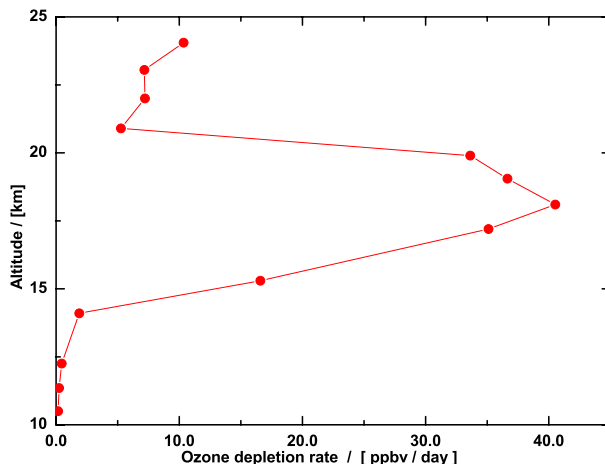


Figure 8.30: Ozone depletion rate as a function of altitude in ppbv per day at Kiruna on February 18, 2000.

10 and 25 km. As expected, the peak value of ozone depletion is observed at ~ 18 km, where chlorine activation is highest. These values are in good agreement with the study of *Frieler et al.* [2005], reporting values of ~ 4 ppbv ozone loss per sunlit hours at the 450 K level (~ 18 km) for the Arctic during this time. With approximately 7.5 hours of $\text{SZA} < 90^\circ$ at Kiruna on February 18, 2000, an ozone depletion rate of ~ 30 ppbv / day is obtained from these values, which is in accordance with the 30 to 40 ppbv / day reported here.

8.5 Conclusions

A re-evaluation of DOAS OCIO observations has largely removed previous discrepancies between measurements and model simulations reported by *Fitzenberger* [2000]. This also solved the problem of OCIO observations outside the vortex at mid-latitudes at Leon, Spain, in 1996. Three case studies for Arctic winter flights performed at Kiruna, show that the agreement between model simulations and the known chemistry and DOAS observations is in general very good and that no major uncertainties and inconsistencies exist. A detailed model study for Kiruna 1999 measurements used ClO_X values derived from a measured $\text{N}_2\text{O} - \text{Cl}_Y$ correlation [*Engel et al.* 1999], and HCl and ClONO_2 values from LPMA observations. The model study allowed to test photochemistry and to derive altitude dependent ozone loss rates of up to $\sim (20)$ ppbv / day at 18 km. Recent findings on photochemistry from *Canty et al.* [2005] and *von Hobe et al.* [2005] do not contradict DOAS measurements but further constraints are needed to prove their validity.

For the Kiruna 1999 and Kiruna 2000 flights, ClO abundances should be verified in a future study with TRIPLE measurements performed during the same time. The ozone depletion rate of $\sim (30 - 40)$ ppbv / day for Kiruna 2000 observations at around the 450 K level, correspond well with values reported by *Frieler et al.* [2005]. Future DOAS balloon flights well inside the activated Arctic vortex, with improved performance of the instrument, possible OCIO measurements using the mini-DOAS instrument [*Weidner et al.* 2005] and simultaneous LPMA measurements, would be very useful for further studies on stratospheric chemistry, since discrepancies still exist between the observations and models.

Chapter 9

Total Stratospheric Bromine

Stratospheric bromine is the second most important halogen known to destroy stratospheric ozone. At present its contribution to the total stratospheric ozone loss is estimated at about 25% [WMO 2003]. There has recently been great improvement in understanding the stratospheric budget and chemistry of bromine (e.g. [Schauffler *et al.* 1998; Wamsley *et al.* 1998; Harder *et al.* 2000]). However, a major issue that is still unresolved is the impact of VSL (very short-lived, i.e. with a lifetime of less than half a year [WMO 2003]) organic bromine species on the photochemistry of the upper troposphere and lower stratosphere (UTLS), where they are converted to reactive forms of bromine [Dvortsov *et al.* 1999] and the amount of inorganic bromine influx from the troposphere into the stratosphere [Ko *et al.* 1997] (see also Figure 2.7). In-situ mass spectrometric analyses of aerosols at the tropopause suggest that ~ 1 pptv of Br is tied to aerosols [Murphy and Thompson 2000]. Tropospheric inorganic bromine (Br_Y) may add to the organic bromine (Br_Y^{org}) input into the stratosphere if transported through the tropopause.

From the mid-1900s to 1995, bromine from halons and methyl bromide more than doubled in the atmosphere [Fraser *et al.* 1999; Butler *et al.* 1999; WMO 2003]. Together with the increase of chlorine abundances, the increase of stratospheric bromine has led to the depletion of stratospheric ozone. While chlorine from long-lived gases has decreased in the lower atmosphere since around 1994 [Montzka *et al.* 1996], there is still concern about the increase of bromine, especially since bromine is about 50 times more efficient than chlorine in destroying stratospheric ozone [WMO 2003].

The first part of this chapter presents an estimate of total stratospheric bromine inferred from DOAS BrO measurements over about a 10 year period. Implications for the UTLS region and correlations with simultaneously measured tracers are discussed in the second and third part.

9.1 Stratospheric Bromine Trend

Accurate knowledge of the amount of bromine entering the stratosphere from bromine-containing organic source gases is required to evaluate bromine-catalyzed losses of stratospheric ozone and inorganic bromine partitioning in the stratosphere. The primary source gases of stratospheric bromine are methyl bromide (CH_3Br), Halon-1211 (CBrClF_2), Halon-1301 (CBrF_3) and Halon-2402 ($\text{C}_2\text{Br}_2\text{F}_4$) (see also section 2.2.3). Methyl bromide has both natural and anthropogenic sources. Figure 9.1 shows the historical trend and the strength of individual sources of CH_3Br . The primary use of industrially produced CH_3Br is for fumigation, but it is also produced by burning leaded gas and biomass. Oceans are the main natural source and are also one of the primary sinks. Other sinks are reactions with OH, photolysis in the stratosphere and uptake by soils and aquatic bacteria [e.g. Schauffler *et al.* 1998 and WMO 2003]. Reeves [2003] pointed out that the current understanding of the present-day atmospheric budget of CH_3Br is incomplete, with sinks far out-weighting sources by about 30%. According to Reeves [2003] an

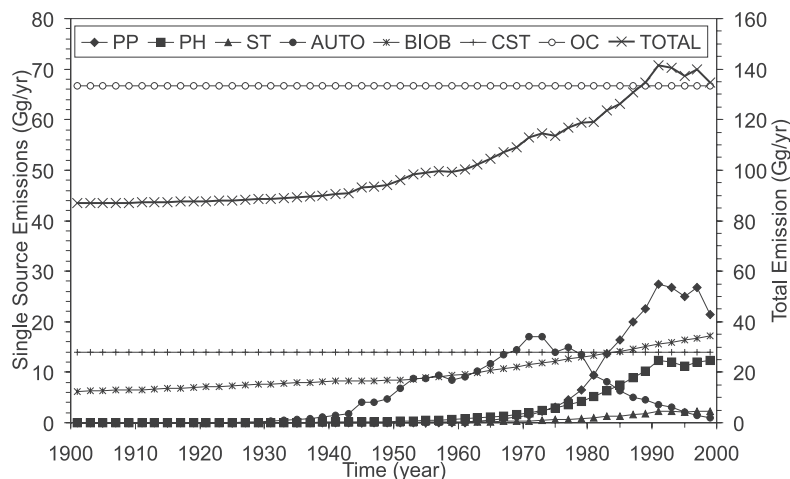


Figure 9.1: Historical trends assigned to the strengths of individual sources of CH_3Br . The sources are designated as PP, preplanting fumigation; PH, post harvesting fumigation; ST, structural fumigation; AUTO, automobiles; BIOB, biomass burning; CST, coastal salt marshes; OC, ocean emission. The trend in total emissions from all these sources is plotted against the right hand axis. Adopted from Reeves [2003].

additional source or sources are required, which must have existed prior to industrial use of CH_3Br , if the current estimates of the known sources and lifetime of CH_3Br are correct (see also Table 1-9 of WMO [2003]). The most recent estimate of the global lifetime of CH_3Br is 0.7 (0.4 - 1.1) years [WMO 2003].

Mixing ratios of CH_3Br in the southern hemisphere have increased by about 3 pptv since 1900 and peaked at around 9 pptv at the end of the 20th century. Saltzman *et al.* [2004] inferred a mean CH_3Br mixing ratio of 5.8 pptv from an Antarctic ice core for mean gas dates from 1671 to 1942. These results are consistent with estimates of the impact of anthropogenic activity (fumigation, combustion and biomass burning). The use of methyl bromide as a fumigant in developed countries was scheduled to begin decreasing after 1998. The Montreal Protocol and its amendments (Figure 2.11) specifies that

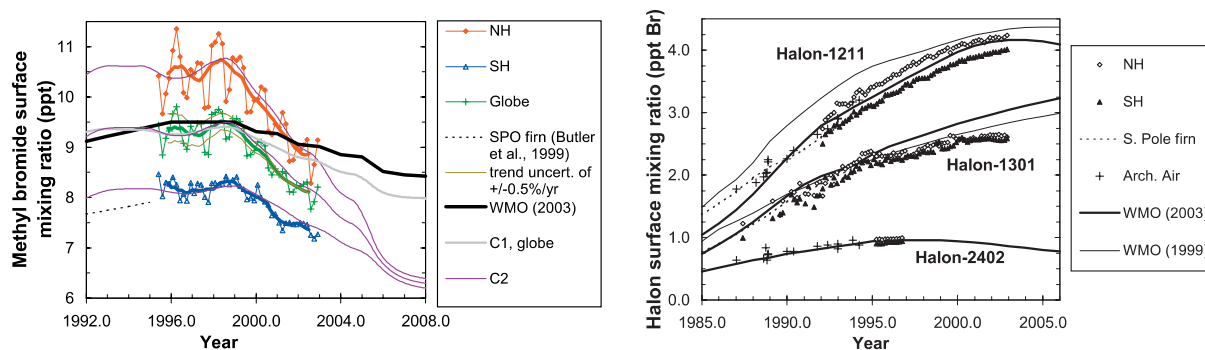


Figure 9.2: **Left panel:** Bimonthly hemispheric and global mixing ratios of methyl bromide measured at the Earth's surface (coloured points; coloured thick lines are 12-month running means). Results are compared to a WMO global mean scenario and box-model calculations (C_1). **Right panel:** Measured hemispheric mixing ratios of the most abundant halons at Earth's surface as ppt Br, compared to results from WMO scenarios. Adopted from Montzka *et al.* [2003].

production of CH_3Br in developed countries should have been reduced from the 1991 levels by 25% in 1999 and by 50% in 2001 [WMO 2003]. Montzka *et al.* [2003] reported that global mean mixing ratios of methyl bromide at the Earth's surface began to decline steadily after 1998 (Figure 9.2) and that the decrease is larger than anticipated. Since atmospheric releases from industrial production represent only a fraction of the total releases of CH_3Br , uncertainty in the magnitude of this fraction limits the ability to describe how CH_3Br mixing ratios will respond to production limits in the revised and amended Montreal Protocol. A substantial fraction of the sources and sinks arise from biological processes, which might be affected significantly by future changes in the climate (e.g. by an increase in temperature). Because of the limited understanding of these processes, it cannot be predicted whether such changes would enhance or reduce mixing ratios of CH_3Br in the future [WMO 2003].

Sources of halons are exclusively anthropogenic and have been used primarily as fire extinguishants since the 1960s. Measurements of H-1211, H-1301, H-2402 and H-1202 in atmospheric air samples collected since 1978 have shown that concentrations of all 4 of these halons have increased substantially during the latter part of the 20th century [Fraser *et al.* 1999; Montzka *et al.* 2003] (see Figure 9.2). Further measurements of H-1211 and H-1301 in air trapped in firn snow have demonstrated that natural sources of these compounds to the atmosphere are minimal or non-existent [Butler *et al.* 1999] and that atmospheric concentrations were zero up to about 1970. The four halons made up 7.7 pptv of organic bromine in 2000 [Montzka *et al.* 2003]. The production and consumption of the halons have been regulated under the Montreal protocol and its amendments, in such a way that production and consumption in developed countries should have ceased in 1994 and should have been frozen in developing countries in 2002 at 1995 - 1997 levels and should be phased out by 2010. Despite these regulations the concentrations of all four halons have increased since 1994, but at a decreasing rate (Figure 9.2). This growth is due to banked halon, defined as material that is contained in inventories and installed equipment. Thus, future mixing ratios are tied to the rate of emissions from these halon banks in addition to the magnitude of future production in developing countries [WMO 2003]. It should be noted that H-1202 is not covered by the Montreal Protocol or its amendments, since most of its production is not deliberate. Although this halon has been used by the military in a few minor applications, it is mostly produced from over-bromination during the production of H-1211 [WMO 2003].

9.1.1 Br_Y Inferred from Stratospheric DOAS BrO Measurements

Inorganic stratospheric bromine (Br_Y) can be inferred by two methods from stratospheric DOAS BrO measurements. One method uses DOAS observations performed at balloon float for SZAs < 90°. As described in section 6.1.2, a Langley plot is performed where the slope of measured BrO absorption is analysed as a function of the calculated total air mass at balloon float altitude (see Figure 9.3). The slope of the least-squares-fitted data results in an average BrO mixing ratio above balloon float. So far, the amount of spectra recorded during balloon float has been sufficient to perform such an accurate Langley plot for 5 balloon flights. The date, place, SZA ranges and the resulting BrO mixing ratios are indicated in the individual panels of Figure 9.3. Table 9.1 summarises the results of all Langley plots for all 13 DOAS balloon flights and indicates the float altitude. As mentioned in section 6.1.2, such a Langley plot only gives the volume mixing ratio above float altitude for a constant BrO mixing ratio, which for BrO is generally only the case between about 30 to 40 km (see for example BrO profile in Figure 9.5). Therefore, balloon flights with float altitudes of around 38 to 39 km (5 in total - Gap 1997, Leon 1998, Kiruna 1998, Gap 1999 and Kiruna 2001) cannot be used for such an analysis. Kiruna 1997, Kiruna 2000 and Kiruna 2003 measurements cannot be used since sufficient data is not available.

The errors of the method are due to uncertainties (a) in the total air mass ($\pm 2\%$) checked by independent temperature and pressure measurements aboard the LPMA / DOAS payload using two independent ray-tracing codes, (b) the spectral retrieval of BrO ($\pm 5\%$), (c) the absorption cross-section of BrO ($\pm 8\%$), and (d) the changing $[\text{BrO}] / [\text{Br}_Y]$ ratio above balloon float altitude.

This ratio can be obtained by considering the bromine chemistry above balloon float altitude during the

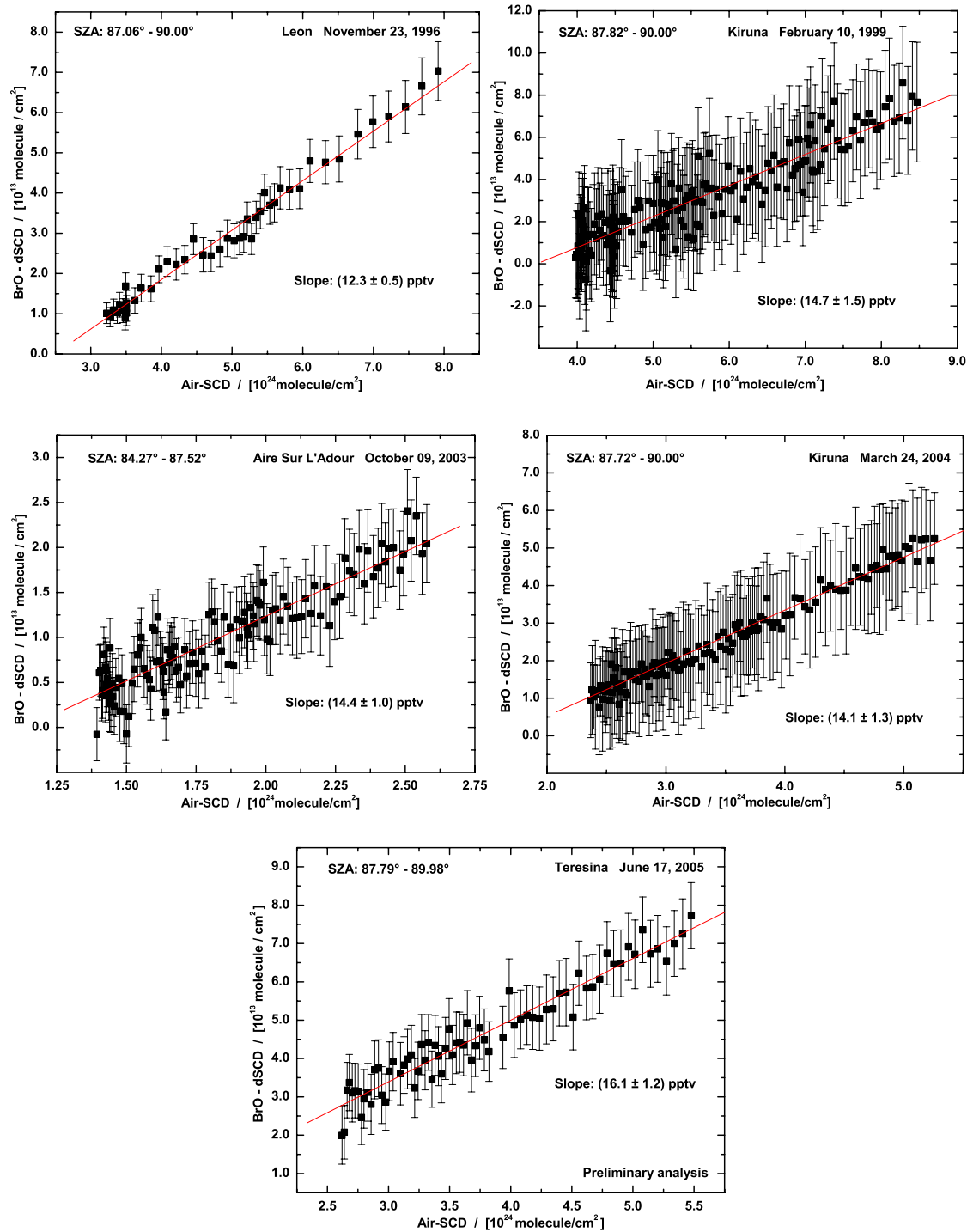


Figure 9.3: Measured BrO absorption as a function of the calculated total air mass observed for the indicated SZA ranges at balloon float altitude (29 to 33 km for the shown cases). The slope of the least-square-fitted data results in the average BrO mixing ratios above float altitude indicated in each plot.

Table 9.1: Inferred BrO volume mixing ratio above float altitude for all 13 DOAS flights. Mixing ratios, given in pptv, are obtained by performing a Langley plot. BV denotes Brunt - Väisälä oscillation.

Date Place	BrO Mixing Ratio above Float / pptv		Float Altitude / km
	Sunset	Sunrise	
Nov. 23, 1996 Leon	All-data: 12.3 ± 0.4 Last 2 BV: 12.3 ± 0.5		31
Feb. 14, 1997 Kiruna			30
June 20, 1997 Gap		All-data: 14.7 ± 0.8 Last 1 BV: 14.5 ± 3.6 Last 2 BV: 16.0 ± 1.0	39
March 19, 1998 Leon	All-data: 11.6 ± 2.4 Last 2 BV: 11.5 ± 3.6		38
Aug.19/20, 1998 Kiruna	All-data: 17.4 ± 2.3 Last 2 BV: 20.8 ± 6.5 Last 3 BV: 20.6 ± 4.5 Last 4 BV: 21.3 ± 2.8	All-data: 15.2 ± 1.8 Last 2 BV: 13.9 ± 3.5	39
Feb. 10, 1999 Kiruna	All-data: 11.1 ± 0.7 Last 3 BV: 15.2 ± 1.9 Last 4 BV: 14.7 ± 1.5		29
June 25, 1999 Gap		All-data: 19.3 ± 1.5 Last 2 BV: 16.6 ± 2.1 Last 3 BV: 19.1 ± 1.6	39
Feb. 18, 2000 Kiruna	All-data: 13.0 ± 3.4		30
Aug.20/21, 2001 Kiruna	All-data: 14.6 ± 6.7 Last 4 BV: 9.7 ± 9.4	All-data: 19.2 ± 6.2	39
March 23, 2003 Kiruna	All-data: 13.5 ± 2.7		33
Oct. 9, 2003 Aire sur l'Adour	All-data: 11.4 ± 0.3 Last 2 BV: 14.7 ± 1.5 Last 3 BV: 14.4 ± 1.0		33
March 24, 2004 Kiruna	All-data: 12.6 ± 0.5 Last 2 BV: 15.6 ± 2.2 Last 3 BV: 14.6 ± 1.6 Last 4 BV: 14.1 ± 1.3 Last 5 BV: 14.1 ± 1.0		33
June 17, 2005 Teresina	All-data: 17.5 ± 0.6 Last 1 BV: 17.4 ± 3.0 Last 2 BV: 16.1 ± 1.2 Last 3 BV: 17.5 ± 0.8		33

day. In the sunlit upper stratosphere, the most important bromine reactions ($\geq 90\%$ - e.g. SLIMCAT) are



Inaccuracies in this simple photochemical scheme are due to the BrO cross-section, the quantum yield for BrO photo-dissociation (reaction 9.1), the rate coefficient $k_{\text{Br}+\text{O}_3}$ for reaction 9.2 and the ozone

Table 9.2: $[BrO] / [Br_Y]$ ratio for the balloon flights shown in Figure 9.3

Height / [km]	Leon 1996	Kiruna 1999	Aire sur l'Adour 2003	Kiruna 2004	Teresina 2005
31	0.65	0.72			
33	0.72	0.75	0.76	0.77	0.78
36	0.79	0.78	0.80	0.81	0.80
40	0.76	0.64	0.76	0.74	0.77
45	0.52	0.37	0.54	0.47	0.60
50	0.22	0.20	0.23	0.20	0.32
Weighted Average	0.69	0.74	0.72	0.69	0.75
$Br_Y / [pptv]$	17.8	19.9	20.1	20.4	21.5

concentration. For example, for the Aire sur l'Adour flight in 2003 the SLIMCAT model calculations show that the $[BrO] / [Br_Y]$ ratio is around 0.76 at 33 km, 0.8 at 36 km, 0.76 at 40 km, 0.54 at 45 km and 0.23 at 50 km. The line-of-sight weighted average is concluded to be 0.72 for these conditions, with the largest uncertainty coming from the uncertainty in k_{Br+O_3} , which is $\pm 20\%$ according to Sander *et al.* [2003]. Combining all uncertainties, the measurement indicates $[Br_Y] = (20.1 \pm 2.8)$ pptv above 33 km at northern mid-latitudes by late 2003. Br_Y for the other flights shown in Figure 9.3 can be derived similarly. The results are summarised in Table 9.2.

Another method to infer Br_Y from DOAS measurements is to compare measured and modelled SCD values. Such a comparison is described in detail in section 6.1.2. An example for the balloon flight at Kiruna on March 24, 2004 is shown in Figure 9.4 for occultation measurements. Ascent measurements are not considered since the partitioning in the lower stratosphere (LS) might not be modelled correctly.

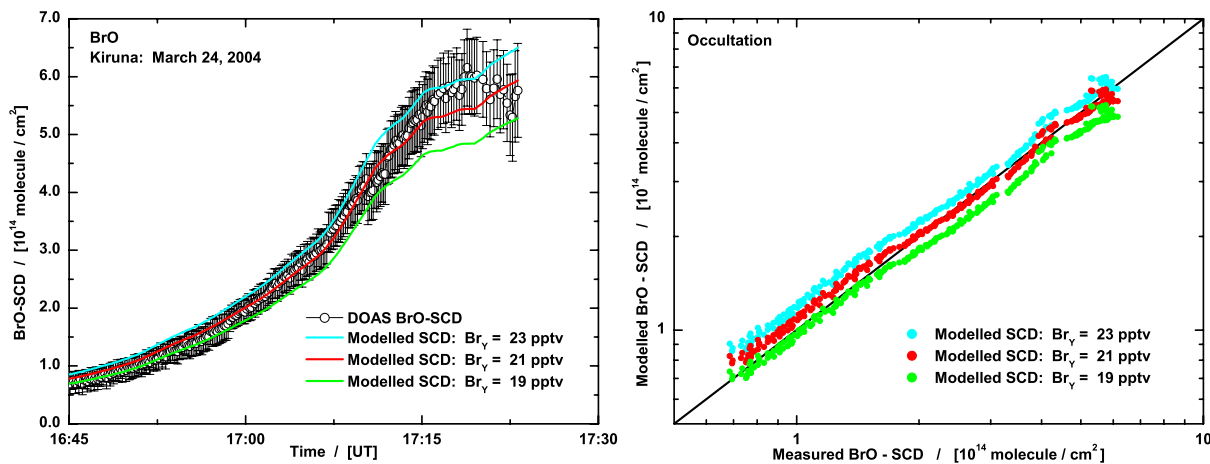


Figure 9.4: Comparison of measured and modelled BrO SCD values for occultation measurements during the balloon flight at Kiruna on March 24, 2004. The left panel shows a direct comparison of the development of the measured SCD values with 3 model scenarios with different total Br_Y loading. In the right panel the corresponding correlation plots are shown.

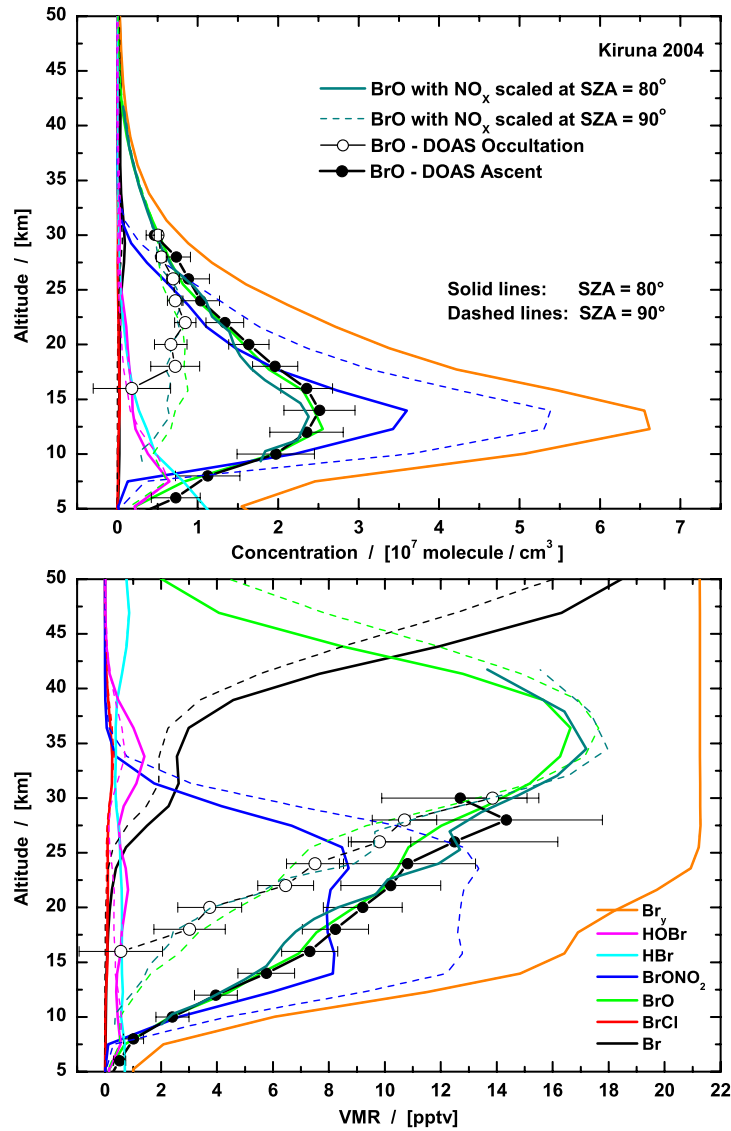


Figure 9.5: Modelled concentration and volume mixing ratio profiles for all important bromine species for a SZA of 80° (solid) and 90° (dashed) at Kiruna on March 24, 2004. DOAS ascent and occultation profiles are shown for comparison. Note that the legends are valid for both panels.

This is due to the fact that the inorganic bromine, i.e. the release of bromine from the organic precursors is still subject to research (dealt with in the next section) and that incorrect modelling of the dynamics causes incorrect concentrations and therefore SCD values in the LS. Both sources of error can be avoided if measurements are only considered for probed air masses above the altitude where all Br_Y^{org} has been converted to Br_Y . For the Kiruna 2004 measurements this is the case above 24 km as shown in Figure 9.5. NO_2 and O_3 are scaled in the model calculations as described in chapter 7. Three model runs with different Br_Y are compared with DOAS measurements in Figure 9.4. The right panel shows a correlation plot of the modelled versus the measured BrO - SCDs. Values after 17:15 UT should be disregarded since the tangent height of observations is lower than 22 km, meaning that incorrect modelling of Br_Y might play an important role. It is deduced here that Br_Y was around 21 pptv for these conditions. Such a

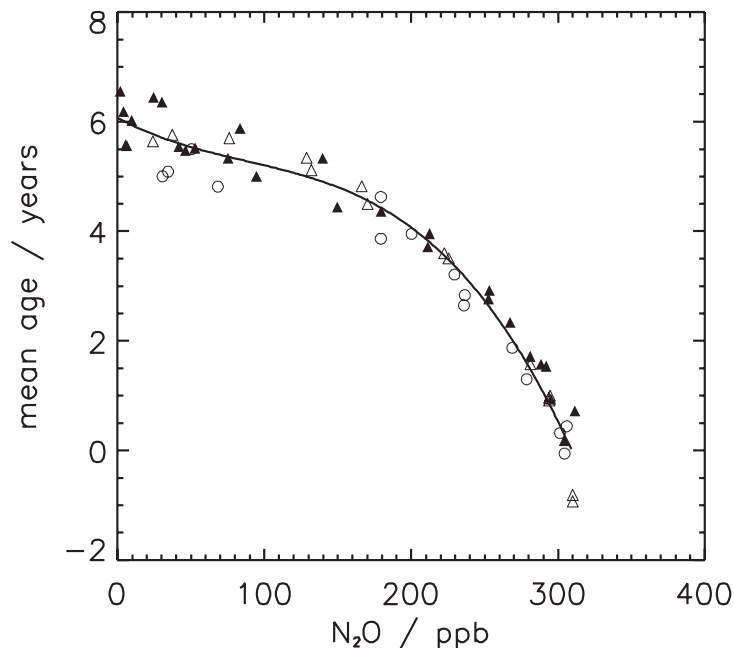


Figure 9.6: Correlation between N_2O and mean age as determined by Engel et al. [2002].

comparison was performed for all DOAS BrO measurements (not shown here) in order to infer Br_Y for each balloon flight.

In Figure 9.5 all important inorganic bromine species are shown for an SZA of 80° (solid lines) and 90° (dashed lines), corresponding to ascent and occultation observations respectively. The retrieved BrO profiles for DOAS ascent and occultation measurements are shown for comparison. BrO from the SLIMCAT model is shown in green and BrO from a model run with NO_x scaled to DOAS observations is shown as light blue lines to demonstrate the effect that the scaling of NO_x has in this case. Modelled and measured profiles match perfectly. The rapid increase of $BrONO_2$ at dusk is also nicely demonstrated. Furthermore, it can be seen that above float altitude, the bromine chemistry is dominated by Br and BrO.

Combining all the available information inferred from DOAS BrO measurements and other publications, it is possible to reconstruct a recent history of the stratospheric bromine inventory. The basic idea of this reconstruction is to put together the inferred stratospheric bromine and the air age information from simultaneous measurements of N_2O - using the knowledge of the temporal trend of this species in the troposphere. Since the source gases of stratospheric bromine are emitted at the surface of the Earth, a given tropospheric evolution can only be observed in the stratosphere with a temporal delay. During transport into and within the stratosphere, air masses are further mixed. The mean effect of transport and mixing can be characterised by the concept of age of air, see e.g. Hall and Plumb [1994]. Species with no appreciable sources or sinks in the stratosphere whose tropospheric mixing ratios also increase linearly can be used to determine the mean age of air in stratospheric air parcels. A conservative tracer can be used to evaluate the mean age of an air parcel by comparing the measured mixing ratio in the stratospheric parcel to a value in a time series of tropospheric mixing ratios of e.g. CO_2 , CFC-115 or SF_6 [Wamsley et al. 1998]. Figure 9.6 shows the correlation between N_2O and the mean age of air as determined by Engel et al. [2002], based on a combination of CO_2 and SF_6 observations. LPMA measurements of N_2O as shown, for example, in Figure 7.9, are used to infer the age of the air masses probed around float altitude. The error of the correlation is given as ± 1 year, due to the error in the N_2O - age of air correlation and the error of LPMA measurements. For the Kiruna 2004 measurements, N_2O was taken from SLIMCAT, and for the Teresina 2005 measurements N_2O was taken from preliminary

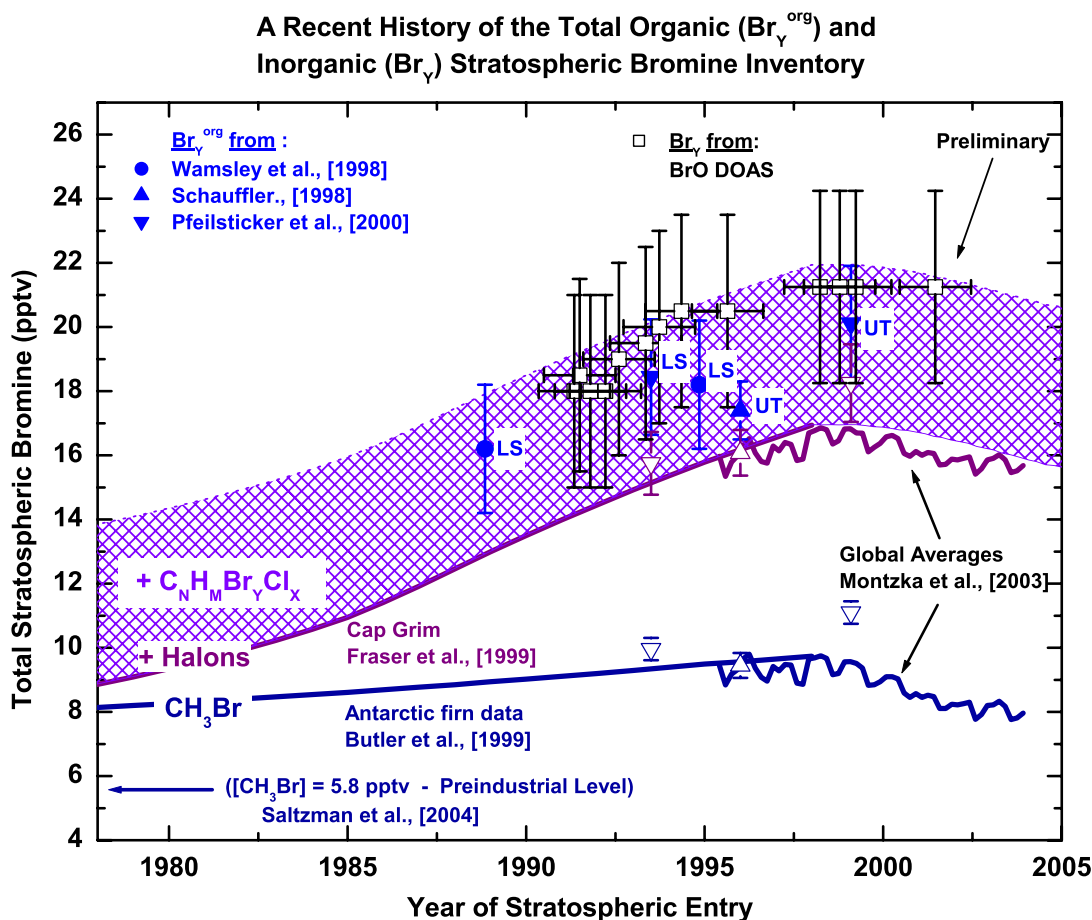


Figure 9.7: Measured trends for bromine in the troposphere (lines) and stratosphere (points): global tropospheric bromine from methyl bromide as measured in ambient air and firn air (dark blue line) [Butler et al. 1999; Montzka et al. 2003]; global tropospheric bromine from the sum of methyl bromide plus halons as measured in ambient air, archived air and firn air (purple line) [Fraser et al. 1999; Butler et al. 1999; Montzka et al. 2003]; tropospheric bromine from VSL organic bromine compounds, or transport of bromine bearing inorganic gases or bromine containing aerosols across the tropopause (blue shaded area) [WMO 2003; Murphy and Thompson 2000; Salawitch et al. 2005]; total organic bromine from source gas as measured in whole air samples (blue symbols) [Wamsley et al. 1998; Schauffler et al. 1998; Pfeilsticker et al. 2000]; total inorganic bromine derived from stratospheric measurements of BrO and photochemical modelling that accounts for BrO / Br_Y partitioning (open black squares). The years indicated on the abscissa are sampling times for tropospheric data. For stratospheric DOAS data, the date corresponds to the time when that air was last in the troposphere, i.e. sampling date minus mean stratospheric age from simultaneous N_2O measurements.

TRIPLE measurements (courtesy of A. Engel from the University of Frankfurt) performed a week after the LPMA / DOAS balloon flight.

In Figure 9.7 the past measured trend in Br_Y^{org} determined from ambient air, archived air and firn air samples and Br_Y from balloon-borne DOAS measurements is displayed. As described at the beginning of this chapter, measurements of the long-lived precursors, CH_3Br and halons, peaked around 1998 and since then have declined [Montzka et al. 2003]. DOAS measurements follow this trend but show an

additional offset. The role of short-lived bromine source gases (labelled as $C_N H_M Br_Y Cl_X$ in Figure 9.7) is still subject to research and DOAS measurements indicate 3.5 to 5 pptv of these species, or tropospheric inorganic bromine, are transported into the stratosphere. The error of the Br_Y inferred from DOAS is estimated at ± 3 pptv due to uncertainties in the BrO absorption cross-section and its temperature dependence ($\sim 10\%$, see also section 6.2), the amount of BrO contained in the Fraunhofer reference spectrum and 1 to 1.5 pptv for modelling errors and uncertainties in the SCD comparison. Since the conditions are similar for all flights, the same error is used for all of them.

Total organic bromine from source gases measured in whole air samples in the UT and LS [Wamsley *et al.* 1998; Schauffler *et al.* 1998; Pfeilsticker *et al.* 2000] shows also higher values than halons and CH_3Br alone can explain. Schauffler *et al.* [1998] observed an average 6% contribution from dibromomethane and 0.8% from bromochloromethane in the tropical UT. During their measurements they also occasionally observed significant amounts of bromoform and dibromochloromethane (see e.g. Table 9.3 for the chemical formula). In the study of Pfeilsticker *et al.* [2000] significant amounts of VSL organic bromine species (20.0 ± 0.7 pptv) are also reported for measurements at the UT. The $Br_Y = (21.5 \pm 3.0)$ pptv inferred from DOAS BrO measurements [Pfeilsticker *et al.* 2000] was re-analysed here and a new value of $Br_Y = (19.5 \pm 3.0)$ pptv was obtained.

By comparing DOAS measurements with model simulations using varied bromine precursors, the composition of the additional 3.5 to 5 pptv of Br_Y^{org} , needed to explain DOAS measurements can be constrained. This issue is discussed in the next section.

The time range covered by DOAS balloon-borne measurements is rather short compared to the organic high-precision measurements of CH_3Br and the halons. It also has to be taken into account that the organic measurements are in-situ measurements and the inorganic method relies on remote sensing measurements. The agreement is still very convincing, but more measurements are needed to investigate the influx of VSL organic bromine species and a possible transport of tropospheric inorganic bromine into the stratosphere in more detail. Research is needed in particular in the tropics since they are likely to be the main global source regions of this input. Another important issue in the future will be to monitor the impact of the agreements made in the Montreal protocol and its amendments. DOAS measurements indicate a levelling of Br_Y in the stratosphere but within uncertainties it is not possible to predict if Br_Y will decline or even increase in future. The contribution of VSL organic bromine compounds might be highly variable, depending on how quickly they are transported from the Earth's surface to the stratosphere. A change in future climate, e.g. an increase in oceanic temperatures and therefore an increased release of natural organic bromine precursors, might cause Br_Y to increase in the stratosphere despite any agreements on anthropogenic releases of Br_Y^{org} . Analyses of whole air samples taken at the north-eastern coast of Brazil in mangrove woods [Schwärzle 2005] showed CH_2Br_2 mixing ratios between 0.5 and 2.2 pptv, and $CHBr_3$ mixing ratios ranging from 12 to 24 pptv. If such high mixing ratios of VSL bromine species are ubiquitous at the coast and the ocean, and if they are rapidly transported from the planetary boundary layer into the tropical stratosphere by convection, then they can contribute significantly to stratospheric bromine.

9.2 Contribution of Very Short-Lived Organic Bromine Species

There has long been speculation regarding the role of decomposition products of VSL chlorine and bromine species in the UTLS (upper troposphere - lower stratosphere), where the role of VSL chlorine-containing compounds has received less attention than bromine counterparts. As shown in the previous section, DOAS observations suggest up to 5 pptv of additional organic bromine source gases in addition to the known amount caused by halons and CH_3Br . There has been much discussion suggesting that this excess bromine partly resides in the troposphere, due to an ubiquitous background level of 1 to 2 pptv of BrO (e.g. Ko *et al.* [1997]; Pfeilsticker *et al.* [2000]). Volcanoes have also been identified as a source of tropospheric BrO by Bobrowski *et al.* [2003] with local mixing ratios as high as 1 ppb. Excess bromine has important implications for photochemistry of tropospheric and / or stratospheric O_3 depending on where it resides.

Table 9.3: Lifetime and median volume mixing ratio of the most important organic bromine species in the tropical upper troposphere (not indicated for halons and methyl bromide - see Figure 9.2). Values according to WMO [2003] and references therein.

Common Name	Chemical Formula	Lifetime / [years]	Median VMR / [pptv] in Tropical UT (8 to 12 km)
Halon - 1301	CBrF ₃	65	*
Halon - 1211	CBrClF ₂	16	See Figures
Halon - 1202	CBr ₂ F ₂	2.9	9.1 and 9.2
Halon - 2402	CBrF ₂ CBrF ₂	20	for their trend
Methyl bromide	CH ₃ Br	0.7	*
Dibromomethane	CH ₂ Br ₂	0.33	0.81 - 0.9
Bromofrom	CHBr ₃	0.07	0.3 - 0.54
Dibromochloromethane	CHBr ₂ Cl	0.19	0.04 - 0.1
Bromodichloromethane	CHBrCl ₂	0.21	0.08 - 0.14

Observations of VSL bromocarbons in the boundary layer are in the 0.02 to 5 pptv range WMO [2003]. Most of these substances have higher concentrations in the marine boundary layer in regions with high ocean productivity. Dibromomethane with a lifetime of approximately 4 months is reasonably well mixed throughout the troposphere (see also Table 9.3). Blake *et al.* [2001] report mixing ratios of 0.8 to 1.2 pptv in the tropics at 12 km altitude and Schauffler *et al.* [1998] of 0.3 to 0.7 pptv at 15 to 19 km. Bromoform (see also Table 9.3) is mainly emitted from marine sources. 0.7 to 1.9 pptv were measured over the Pacific and reported by Blake *et al.* [2001]. Recently Quack *et al.* [2004] showed in their study that CHBr₃ has a source throughout the tropical open ocean. Oceanic bromoform is the major source of organic bromine in the atmosphere and may contribute to reactive bromine in the UTLS (e.g. Dvortsov *et al.* [1999]). With its relatively short atmospheric lifetime of 2 to 4 weeks and its spatial and temporal variability in production and sea-to-air flux, CHBr₃ has a strongly varying atmospheric distribution. Atmospheric mixing ratios range from 0.5 to 27.2 pptv (comparable to levels reported by Schwärzle [2005] - see above) with elevated levels (2.4 to 4.4 pptv) at the equator [Quack *et al.* 2004]. Their findings indicate the possibility that changes in climate and surface winds could contribute to the variability of the supply of bromine to the tropical LS. Carpenter *et al.* [2005] report on observations of CHBr₃ performed at Mace Head, Ireland. They observed a maximum of CHBr₃ from spring until autumn and a winter minimum, with mixing ratios of 5.3 ± 1.0 pptv and 1.8 ± 0.8 pptv respectively. The emission sources are mainly macroalgae, but they also found evidence for a small terrestrial flux from peatland ecosystems, which has not previously been accounted for as a CHBr₃ source.

Other VSL organic bromine species such as CHBrCl₂ and CHBr₂Cl (see Table 9.3) are also thought to have mainly marine sources and to have similar distributions to CHBr₃. Schauffler *et al.* [1998] reported mixing ratios in the tropics at 10 km of 0.1 to 0.15 pptv for CHBrCl₂ and 0.05 to 0.2 pptv for CHBr₂Cl, and at 15 km values below 0.03 pptv for CHBrCl₂ and below 0.02 pptv for CHBr₂Cl. A variety of other VSL organic bromine source gases exists that might also contribute to Br_Y in the stratosphere. For more details see, for example, WMO [2003].

One important issue in the study of halogen source gases is to track the life cycle of a source gas to evaluate how its emission affects the inorganic halogen budget of the stratosphere [WMO 2003]. Like other halogen source gases, the VSL bromine source gases are mainly emitted at the surface. Two pathways are distinguished for delivering the products to the stratosphere (see also Figure 2.7). One is the source gas injection pathway (SGI - [WMO 2003]), where the source gas is transported directly to the stratosphere and reacts there to release the halogen atoms. The other possibility is the product gas

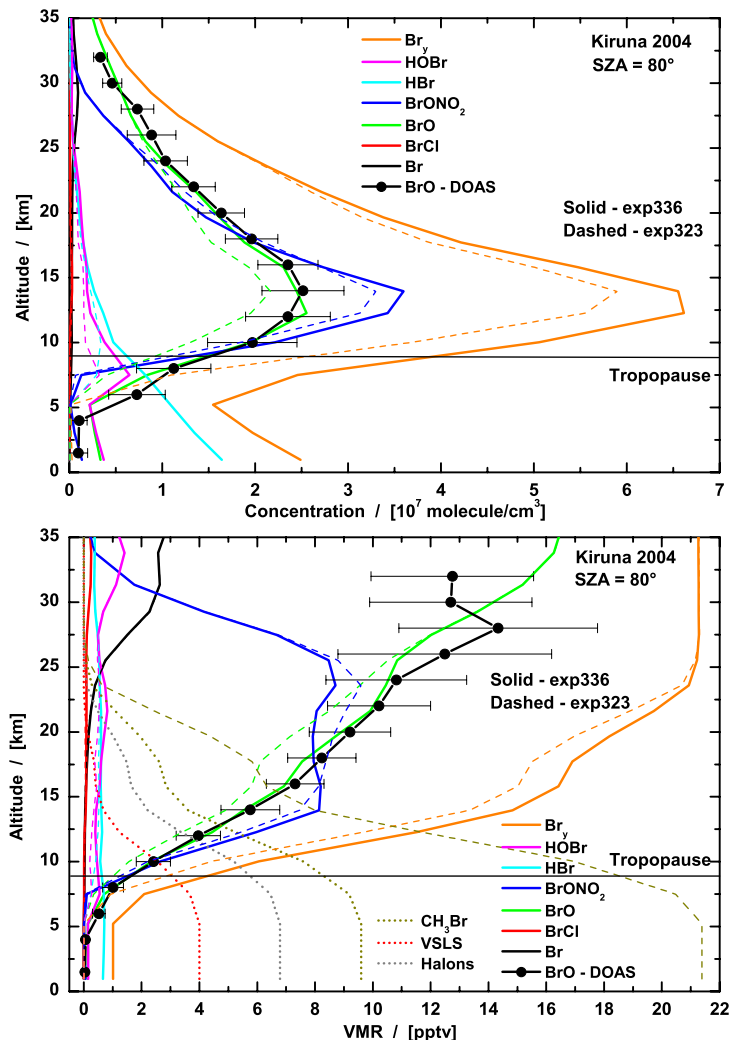


Figure 9.8: Modelled concentration and volume mixing ratio profiles for all important bromine species for $\text{SZA} = 80^\circ$ at Kiruna on March 24, 2004. Two SLIMCAT model runs are compared: with contributions to bromine source gases from methyl bromide, halons and very short-lived substances (experiment 336 - solid lines / CH_3Br , halons and VSLs themselves are shown as dotted lines); with contribution to bromine source gases from methyl bromide only (experiment 323 - dashed lines). DOAS ascent profiles are shown for comparison.

injection pathway (PGI) involving the transport to the stratosphere of intermediate or final products produced in the troposphere. The efficiencies of both pathways depends on the removal rate of a source gas, by chemical (reaction with OH) or physical processes (UV photodissociation) in the troposphere as compared to the transport rate from the ground to the stratosphere [WMO 2003].

Vertical transport times from the surface to the UT are shortest in the tropics. There the transition from the troposphere to the stratosphere takes place in the TTL (tropical tropopause layer - see also Figure 2.7). Transport from the surface to the UT and TTL occurs mainly through convection. The transition from air with typical tropospheric composition to air with typical stratospheric composition, does not occur abruptly across the tropical tropopause. Air parcels rise slowly into the stratosphere, driven by Brewer-Dobson circulation. To a small extent deep convection prepenetrates deep into the TTL and a small

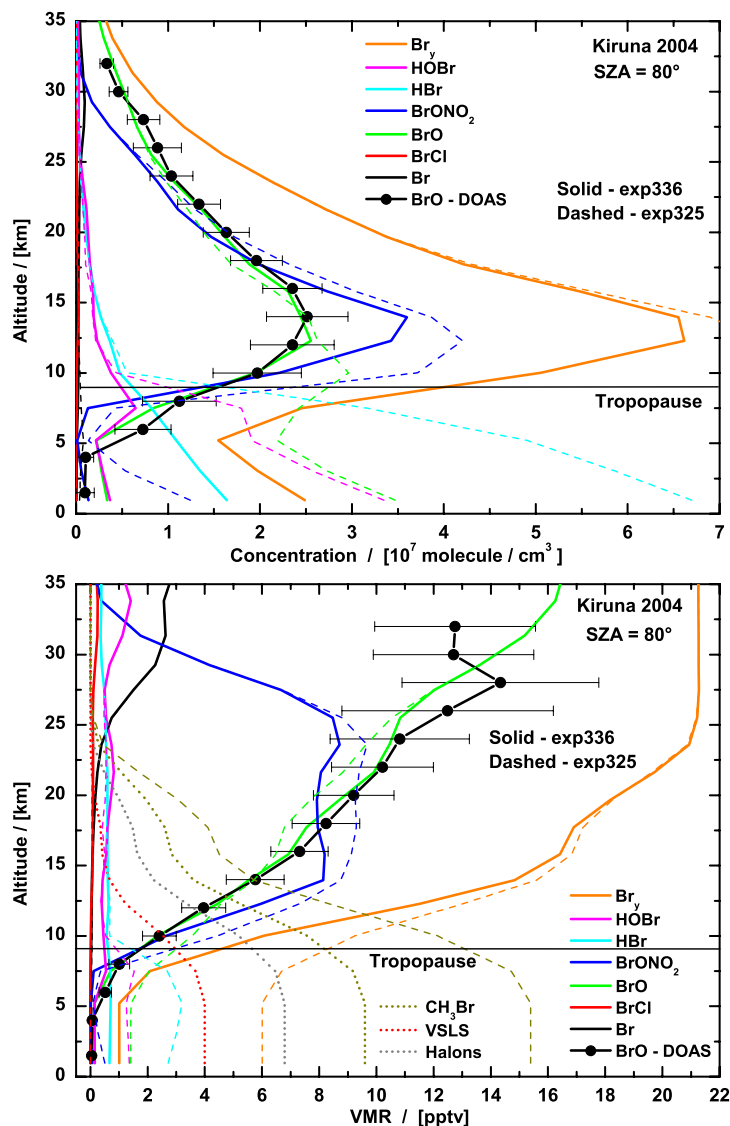


Figure 9.9: Modelled concentration and volume mixing ratio profiles for all important bromine species for SZA = 80° at Kiruna on March 24, 2004. Two SLIMCAT model runs are compared: with contributions to bromine source gases from methyl bromide, halons and very short-lived substances (experiment 336 - solid lines / CH₃Br, halons and VSLs themselves are shown as dotted lines); with contributions to bromine source gases from methyl bromide and 6 pptv of bromine bearing inorganic gases transported across the tropopause (experiment 325 - dashed lines). DOAS ascent profiles are shown for comparison.

fraction of surface air might be injected directly into the stratosphere (see e.g. Gettelman *et al.* [2004, Corti *et al.* [2005]). Air exchange across the extratropical tropopause is accomplished by processes over a large range of temporal and spatial scales. The net mass exchange is controlled by global-scale processes as part of the Brewer-Dobson circulation, e.g. Holton *et al.* [1995]. Nevertheless, synoptic-scale frontal systems and to a lesser extent midlatitude deep convection can bring constituents from the boundary layer to the UT. These processes may thus also transport VSL substances, their degradation products and inorganic halogen into the lower stratosphere [WMO 2003]. However, it has to be noted that the

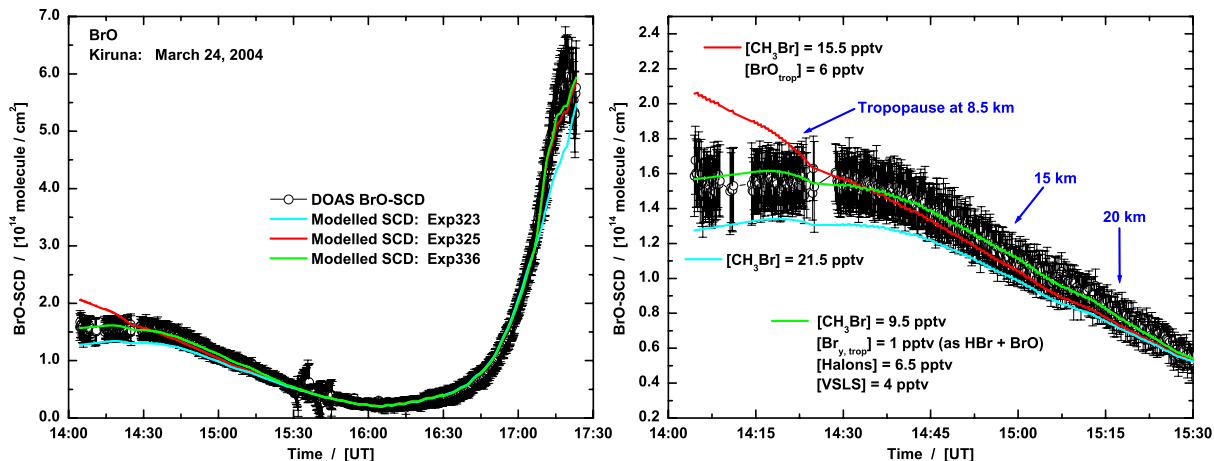


Figure 9.10: Development of modelled and measured BrO SCDs for the balloon flight at Kiruna on March 24, 2004. The three model runs use different organic bromine source gases as indicated in the legend, but all have $Br_Y = 21.5$ pptv. The right panel is a zoom into ascent measurements.

precise mechanisms of the cross-tropopause transport and their consequences for VSL substances are still controversial and subject to ongoing research.

For most DOAS flights, measurements were started early enough during ascent to make observations in the troposphere and especially in the UTLS region. In the past, comparisons of DOAS observations with SLIMCAT model data [e.g. Harder *et al.* 1998; Fitzenberger 2000] always showed some discrepancies in the LS around the concentration maximum. The overall shape of the profile and concentrations above the concentration maximum were modelled well, but DOAS measurements were consistently higher at the concentration maximum. Up to experiment 323 (internal numbering of M. Chipperfield denoting different SLIMCAT model runs - in short exp323), the bromine loading was

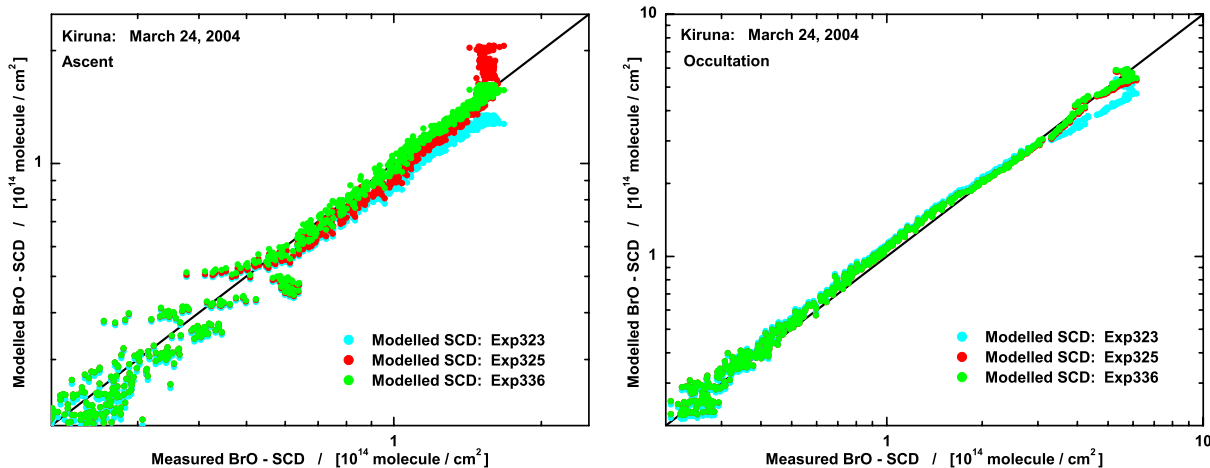


Figure 9.11: Correlation plots for measured versus modelled BrO SCDs for the Kiruna 2004 balloon flight. The 3 model runs described in Figure 9.10 and in the text are compared. The left and right panels show ascent and occultation measurements respectively.

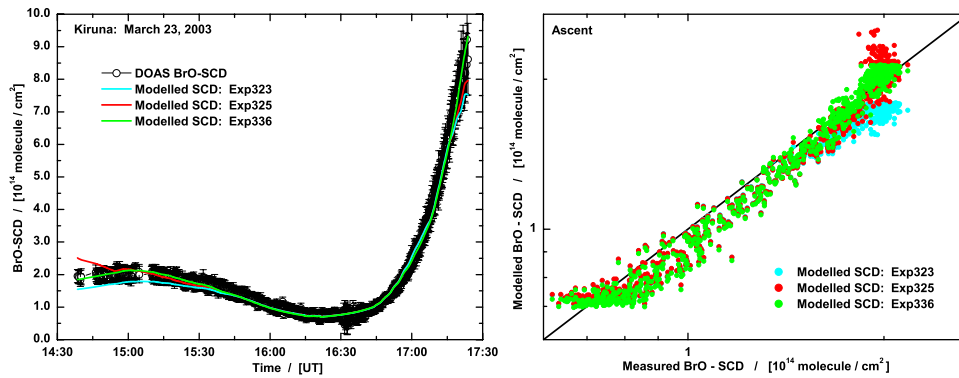


Figure 9.12: Similar to Figures 9.10 and 9.11 but for the balloon flight at Kiruna on March 23, 2003. Right panel shows ascent measurements only.

modelled as CH_3Br only, i.e. the known trend of CH_3Br and the halons was treated as one source gas - methyl bromide. Total Br_Y had been adjusted though to reflect the total stratospheric bromine loading observed by DOAS balloon soundings and was approximately 21 pptv around 2000.

In order to get a more realistic representation of the bromine source gases and their release in the LS, it was decided to specify the bromine loading from observed tropospheric CH_3Br and halon loadings [WMO 2003]. To reflect the additional 3.5 to 5 pptv observed by DOAS, an extra 4 pptv of bromine was modelled in a tracer to represent bromine-containing, very short-lived species (modelled as CH_2Br_2) and 1 pptv was assumed to be transported to the stratosphere as Br_Y (exp336 - see Chipperfield *et al.* [2005]). In order to investigate if a large influx of BrO (and consequently other inorganic bromine species) could be responsible for a higher Br_Y in the lower stratosphere, another model run (exp325) was performed, in which the bromine loading was specified as CH_3Br (= 15.5 pptv) and tropospheric BrO (= 6 pptv).

Figures 9.8 and 9.9 show a comparison of the DOAS BrO profile inferred from balloon ascent observations at Kiruna on March 24, 2004 with SLIMCAT model output at an SZA of 80° . Concentrations and volume mixing ratios of all important bromine species are plotted for exp336 and exp323 in Figure 9.8 and for exp336 and exp325 in Figure 9.9. Since the troposphere is not treated in the LABMOS 1-D model used by the DOAS balloon group, SLIMCAT output is shown directly, i.e. no scaling of NO_2 was performed here, but was verified to have little effect. Only volume mixing ratios of the source gases are shown. It can be seen nicely how the source gases are converted to inorganic bromine in the lower

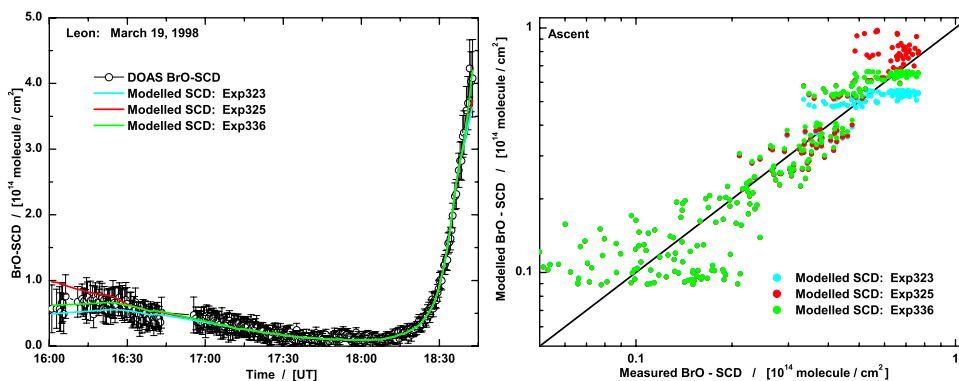


Figure 9.13: Similar to Figures 9.10 and 9.11 but for the balloon flight at Leon on March 19, 1998. Right panel shows ascent measurements only.

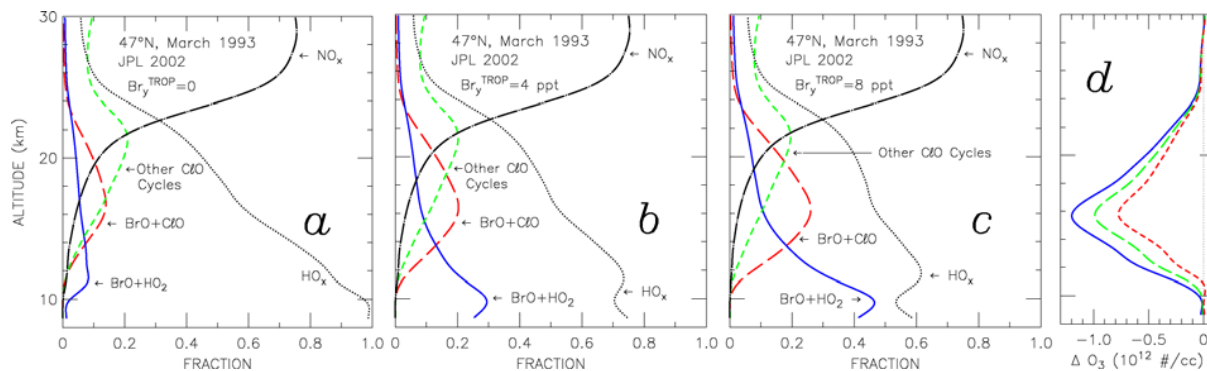


Figure 9.14: Figure 5 of the study by Salawitch *et al.* [2005]. Fraction of odd oxygen loss by various catalytic cycles within the AER model at 47° N, March 1993, for model runs with $\text{Br}_Y^{\text{TROP}}$ (Br_Y near the tropopause) of 0, 4 and 8 pptv (panels a-c, as indicated). Panel d shows the difference between the ozone profile at 47° N, March 1993 and the profile at 47° N, March 1980 for runs with $\text{Br}_Y^{\text{TROP}}$ of 0 (red short dashed), 4 (green dashed) and 8 (solid blue) pptv.

stratosphere and slowly build up total reactive bromine. BrO concentrations of exp323 show too low values around the maximum, which is matched perfectly by exp336.

With the tropopause around 9 km on that day, one can see that both model and measurements indicate ~ 1 pptv of inorganic bromine in the upper troposphere (around 8 km). It has to be noted though that the DOAS profile point at 6 km is not too reliable, due to measurement gaps during ascent (see section 6.3.4). A Br_Y of 3 to 4 pptv is found right above the tropopause (10 to 11 km). Overall it can be said that the release of Br_Y from the source gases is rather rapid - an observation confirmed by other DOAS balloon flights, which are not all presented in this study.

When 6 pptv of BrO is injected directly into the troposphere (exp325), other inorganic species are formed and an equilibrium builds up in which most of the 6 pptv of inorganic bromine resides as HBr (~ 3 pptv) and equal amounts of HOBr and BrO (~ 1.5 pptv). In Figure 9.9 the maximum BrO concentration is matched quite well by modelled BrO from exp325, but amounts of BrO below the concentration maximum are largely overestimated. Even half the amount of BrO (here ~ 0.75 pptv) in the troposphere (below 8 km) would still be too high. In general, DOAS BrO observations 2 km or further below the tropopause are compatible with 0 pptv and do not indicate BrO values larger than 0.5 pptv. Schofield *et al.* [2004] found an upper limit of 0.9 pptv for ubiquitous tropospheric BrO at 80° from their ground measurements at 45°S. From the high variability of the measurements Schofield *et al.* [2004] inferred a mean value of 0.2 pptv for a well mixed troposphere.

Figure 9.10 shows a direct comparison of the measured BrO SCD values with model results from exp323, exp325 and exp336. Exp336 matches perfectly with observations whereas exp325 has too high values for measurements containing tropospheric absorptions. Exp323 is systematically too low up to ~ 20 km. Correlation plots of the different model runs with measured BrO SCDs are presented separately in Figure 9.11 for ascent and occultation observations. Figures 9.12 and 9.13 show two further examples from a high and a mid-latitude flight at Kiruna and Leon.

The implications for ozone loss due to increased Br_Y in the UTLS, based on DOAS observations are currently being investigated by Chipperfield *et al.* [2005]. Salawitch *et al.* [2005] showed how additional Br_Y (without clearly identifying the sources) near the tropopause affects ozone depletion over the past 25 years. They found better agreement between measured and modelled ozone trends as also suggested by WMO [2003]. The model is run using the WMO *Ab* scenario for time evolution of Br_Y , Cl_Y , aerosols etc. with Br_Y then increased by either 4 or 8 pptv [Salawitch *et al.* 2005]. Figure 9.14 gives an overview of the model photochemistry and ozone loss by catalytic cycles at 47° N in March

1993 [Salawitch *et al.* 2005]. Increasing additional Br_Y at the tropopause from 0 pptv to 4 and 8 pptv shows that increased ozone loss is associated with a greater catalytic loss caused by the BrO+ClO cycle. Furthermore, for non-zero additional Br_Y at the tropopause, ozone loss below about 14 km is not purely dominated by HO_X photochemistry anymore, since the BrO+HO₂ cycle becomes more significant [Salawitch *et al.* 2005].

It should be noted that throughout this study, SLIMCAT model results are taken from exp336 unless stated otherwise.

9.2.1 First Tropical BrO Profile

A tropical BrO balloon profile has been measured for the first time. Details of the flight are given in section 6.3.5. Since satellite instruments are not sensitive to the upper troposphere - lower stratosphere, or even the troposphere (see chapter 7), this DOAS BrO profile presents the first accurate measurement up to the mid stratosphere in the tropics. Due to the low BrO SCD values observed for these measurements, the BrO SCDs were filtered with a Gaussian filter 1 km in width before profile inversion. Figure 9.15 shows a model comparison (similar to Figure 9.5) for the BrO ascent (corresponding to a SZA of $\sim 74^\circ$) and occultation ($\sim 90^\circ$) profiles measured at Teresina, Brazil, on June 17, 2005 (preliminary analysis). The ascent profile matches perfectly with the model results from SLIMCAT (exp336). This demonstrates again the validity of the implementation of VSL compounds into SLIMCAT. Around 1 to 3 pptv BrO are observed at the thermal tropopause at ~ 17 km and both the modelled and the measured profile demonstrate the rapid release of inorganic bromine from its source gases. The fact that the occultation profiles do not correspond, is rather strange and currently unexplained (also seen in a direct SCD comparison - not shown here). BrO profiles from a constrained model run with scaled NO₂ are included in Figure 9.15 for comparison. It can be seen that scaling of NO₂ only has a small effect on the BrO profile and does not explain the observed discrepancy. It can be speculated whether the HO_X chemistry and therefore HOBr plays a more important role than at mid or high-latitudes. Further results, e.g. from other balloon observations or satellite instruments performed around the same time are needed to make a more specific assessment.

9.3 Correlation between Tracers and Br_Y

The LPMA / DOAS balloon payload offers the unique possibility of measuring tracers (N₂O and CH₄ from LPMA) and Br_Y derived from DOAS BrO simultaneously - see section 9.1. The correlation of Br_Y with tracers is especially important for the modelling community, since such correlations are used to model the influx into the stratosphere and the release of Br_Y from the source gases. Wamsley *et al.* [1998] were the first to derive such a correlation for CFC-11 (CCl₃F) and Br_Y. They combined measurements of H-1211 and mean age estimates from SF₆ (similar to Figure 9.6) both measured in the stratosphere up to 20 km, with simultaneous measurements of CFC-11, measurements of brominated compounds in stratospheric whole air samples and records of tropospheric organic bromine mixing ratios. From these measurements they calculated the mixing ratio of total bromine in the lower stratosphere and its partitioning between organic and inorganic compounds [Wamsley *et al.* 1998].

Figures 9.16 to 9.22 show the correlations of BrO and inferred Br_Y, with N₂O and CH₄ for 7 LPMA / DOAS balloon flights. A 1 pptv error was estimated for the BrO to Br_Y scaling. Except for the Gap 1999 observations, ascent measurements were used for BrO. BrO SCD values were filtered with a Gaussian filter 1 km in width before profile inversion in order to avoid oscillations in the profile and to obtain a smooth correlation. Correlations as modelled by SLIMCAT from exp323 (when available) and exp336 (see section 9.2) are included for comparison. When available, Br_Y inferred from a Langley plot is also indicated (section 9.1). The Br_Y - N₂O correlation given by Wamsley *et al.* [1998] is also plotted. Wamsley *et al.* [1998] do not give the correlation of Br_Y - N₂O directly but of Br_Y - CFC-11 together with a correlation of N₂O to CFC-11 for the tropics ($-20^\circ < \text{latitude} < 20^\circ$ - here used for Teresina 2005

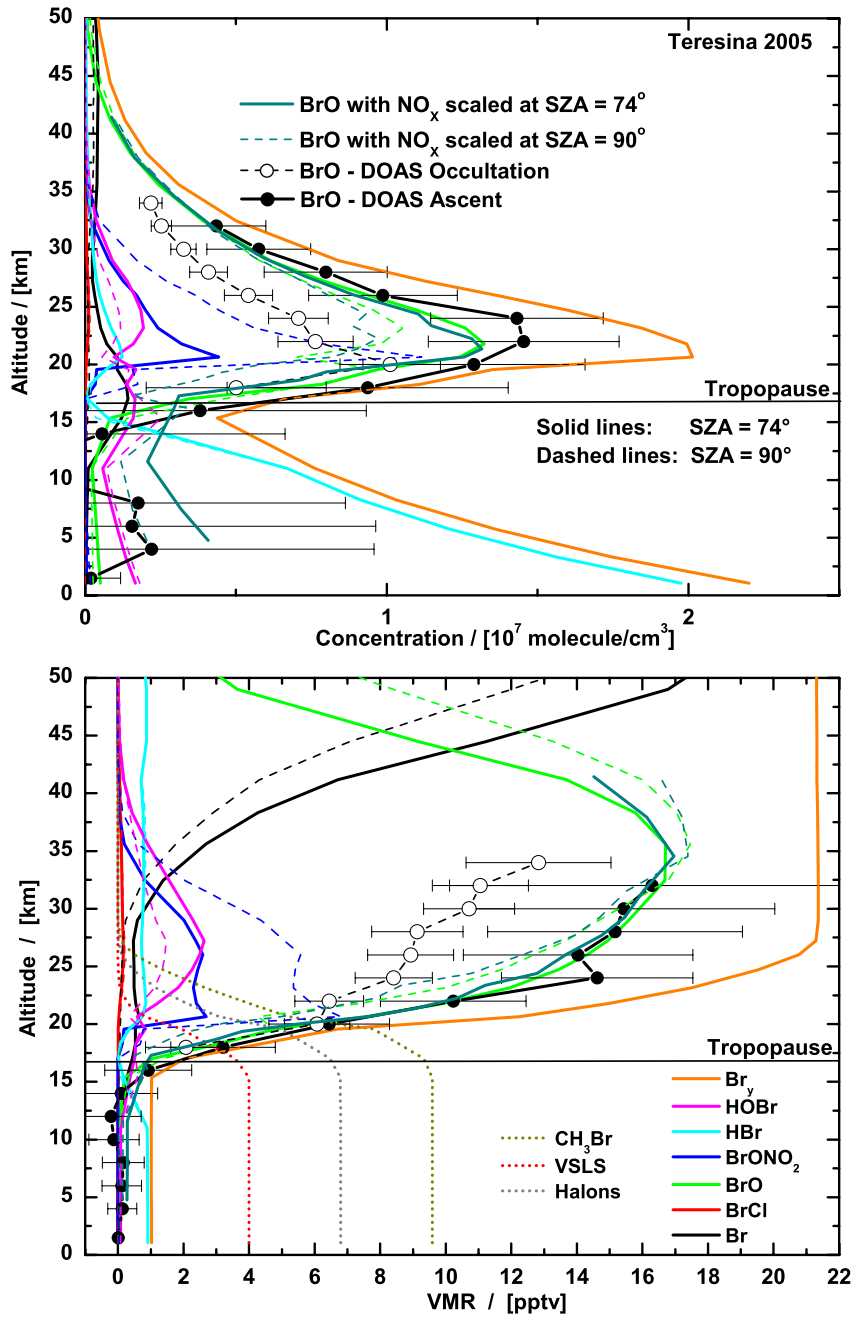


Figure 9.15: Modelled concentration and volume mixing ratio profiles for all important bromine species for a SZA of 74° (solid) and 90° (dashed) at Teresina on June 17, 2005. DOAS ascent and occultation profiles are shown for comparison.

presented in Figure 9.22) and extratropics (latitude $> 20^\circ$ or latitude $< -20^\circ$). The tropical correlation is valid for N_2O mixing ratios between 225 and 310 ppbv and the extratropical correlation is valid for N_2O mixing ratios between 130 and 310 ppbv. The measurements used by *Wamsley et al.* [1998] were performed in fall 1994. Unfortunately CFC-11 is scaled in SLIMCAT, i.e. it also accounts for other or-

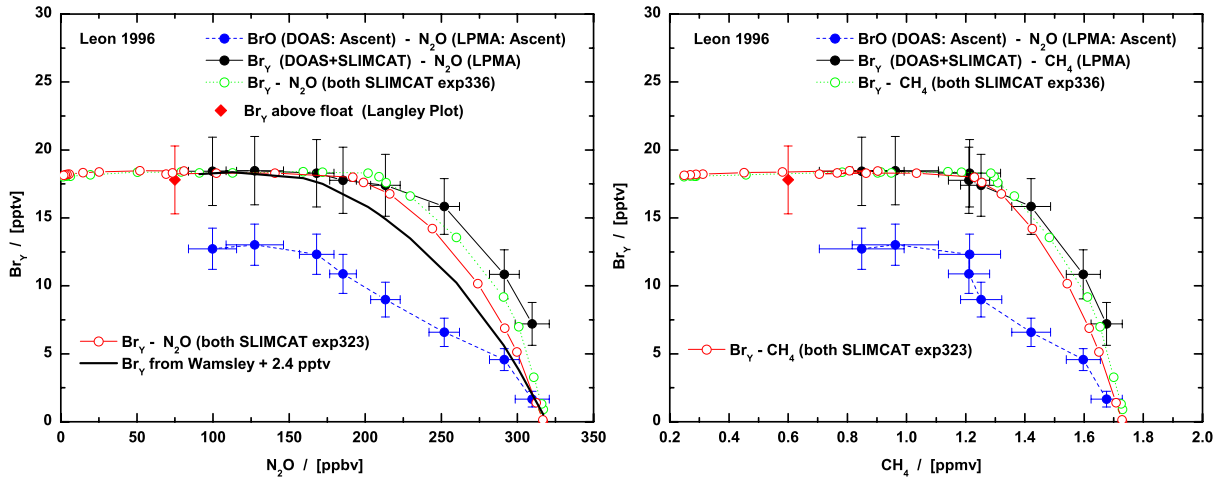


Figure 9.16: Correlation between Br_Y derived from DOAS BrO measurements and N_2O and CH_4 from LPMA observations in the stratosphere for the Leon 1996 balloon flight. The correlation of BrO with N_2O and CH_4 is shown in blue and results purely from simultaneous measurements performed during the balloon ascent. The black curve represents the correlations of Br_Y derived from BrO measurements and modelling, with N_2O and CH_4 . For comparison, correlations are shown with Br_Y , N_2O and CH_4 taken from the SLIMCAT exp336 and exp323 model runs, and the $Br_Y - N_2O$ correlation according to Wamsley *et al.* [1998] (thick black line). The red square marks total Br_Y above float as derived by the Langley plot described in section 9.1.

ganic chlorine species and is not used as the CFC-11 tracer alone, thus not reflecting the real atmospheric trend in CFC-11. All three species Br_Y , N_2O and CH_4 are not constant over time but show a trend in the atmosphere (see e.g. Figure 9.7). A constant offset of inorganic bromine was added in each case as indicated in the legend to account for the difference in Br_Y between Wamsley *et al.* [1998] measurements and DOAS observations. For Gap 1999 and Kiruna 1997 only DOAS and LPMA data and correlations from exp336 are shown as a detailed analysis is difficult in both cases. During Gap 1999, only occultation measurements were performed, requiring a strong scaling from BrO to Br_Y , i.e. relying too much on

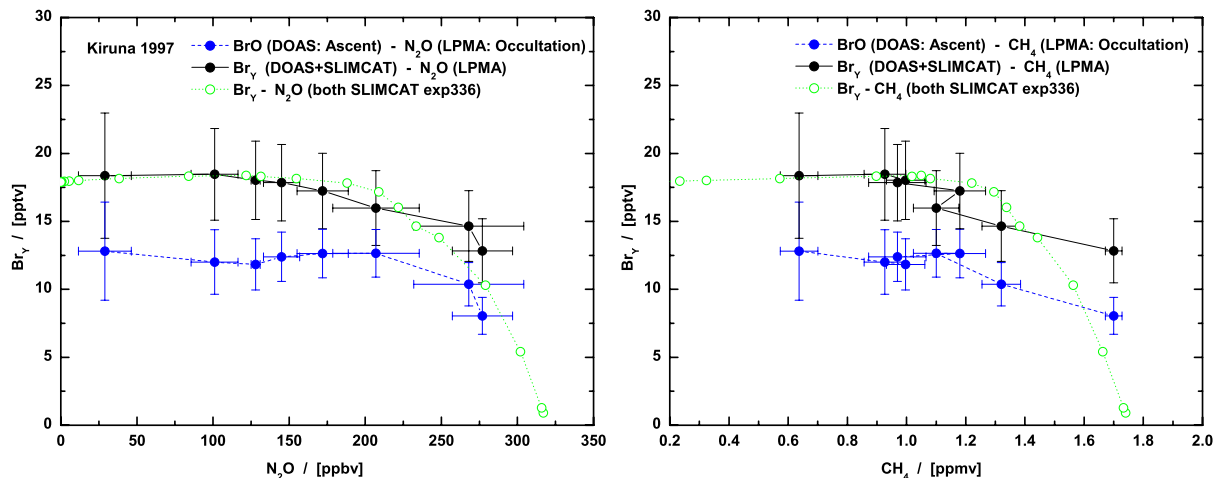


Figure 9.17: Same as Figure 9.16 but for the balloon flight at Kiruna in February 1997.

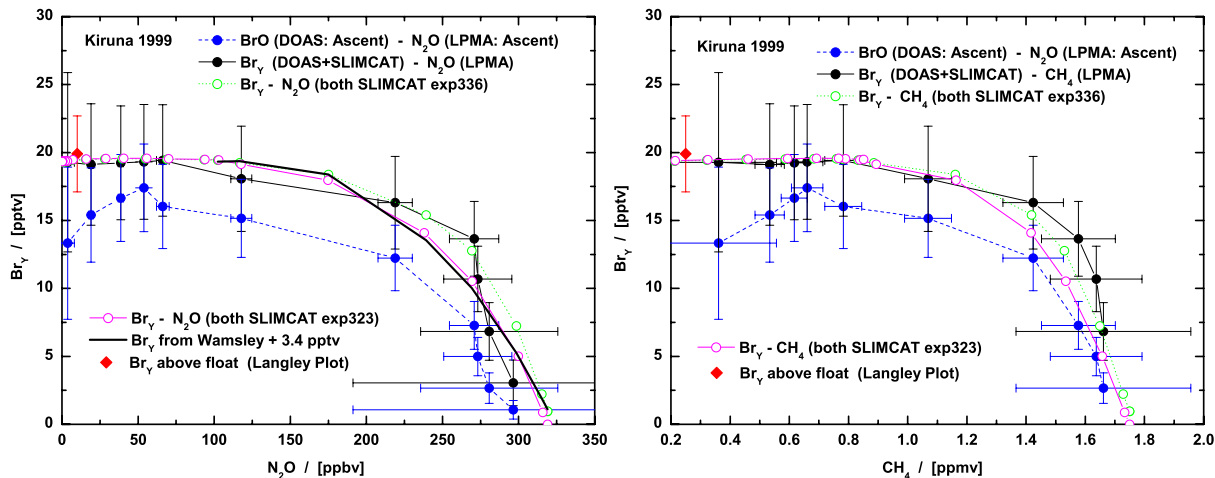


Figure 9.18: Same as Figure 9.16 but for the balloon flight at Kiruna in February 1999.

model simulations. Furthermore, occultation measurements do not reach down to the low Br_Y values. Kiruna 1997 measurements took place at the vortex edge, making the dynamical situation difficult (see section 8.2).

Atmospheric methane (CH_4) is a greenhouse gas whose radiative properties and atmospheric chemistry affect both climate and stratospheric ozone. Measurements of CH_4 in air extracted from polar ice indicate that its abundance during the last 420,000 years of the preindustrial era varied between 350 ppbv and 700 ppbv [WMO 2003]. In 2000 CH_4 was estimated to around 1780 ppbv. Systematic measurements of CH_4 show that its global abundance at the Earth's surface continues to increase with an average growth rate of 7.9 ± 0.1 ppbv / year from 1984 to 2000 [WMO 2003].

The atmospheric abundance of N_2O , which is the major source of ozone-depleting nitrogen oxides (see section 2.2.2), has been increasing steadily for decades. Its averaged global mixing ratio at the beginning of 2001 was 315 to 317 ppbv with an averaged rate of increase of ~ 0.75 ppbv / year [WMO 2003].

The shape of the correlations is due to the decrease of N_2O and CH_4 with increasing altitude, caused by loss or sink processes (reaction with OH and photolysis) and the increase of Br_Y with altitude, caused

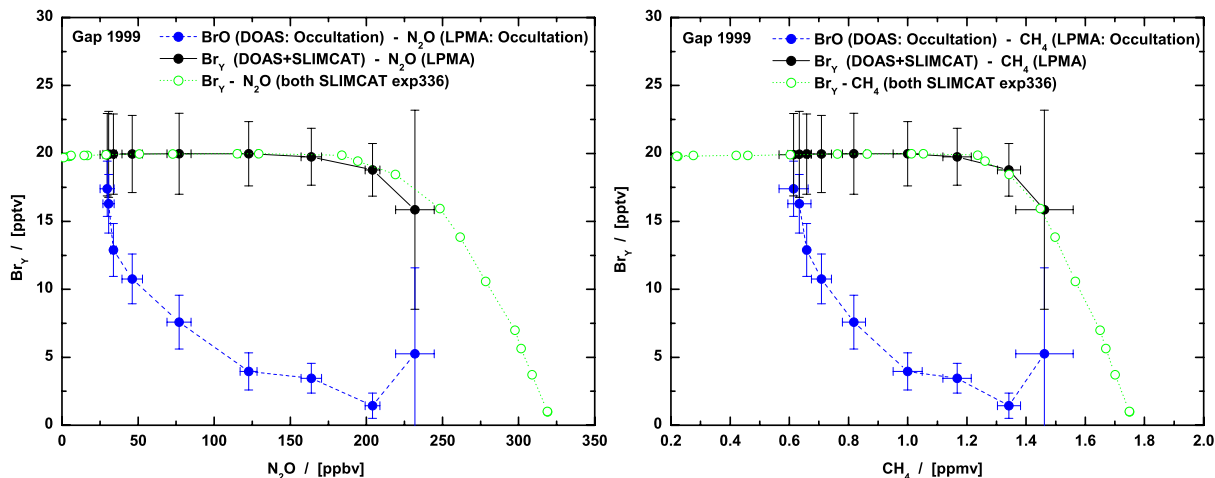


Figure 9.19: Same as Figure 9.16 but for the balloon flight at Gap in June 1999 and occultation measurements.

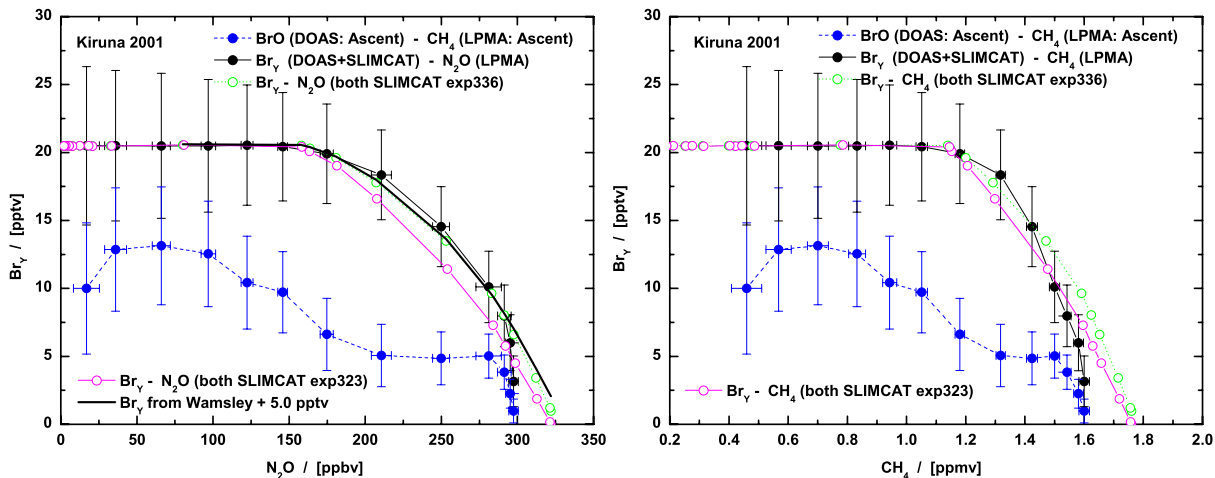


Figure 9.20: Same as Figure 9.16 but for the balloon flight at Kiruna in March 2001.

by its release from the organic source gases (see section 9.2). Once organic bromine has been converted into inorganic forms, as shown for example in Figure 9.15, Br_Y remains constant, as can be observed in Figures 9.16 to 9.22. As expected, exp336 shows a steeper increase of Br_Y with decreasing N_2O or CH_4 . When scaled (i.e. by adding the indicated offset), the *Wamsley et al.* [1998] correlation matches well the correlations derived from high latitude LPMA / DOAS observations. For mid latitudes (Leon 1996) and for the tropics (Teresina 2005), the *Wamsley et al.* [1998] correlation is too flat and does not model the rapid increase of Br_Y with decreasing N_2O . Although it must be mentioned that for Leon 1996 measurements, SLIMCAT does not model the dynamic situation well and further comparisons are necessary. Unfortunately N_2O and CH_4 LPMA data for the Teresina 2005 and the Kiruna 2004 (not shown here) flights are not available at present, but once they are will make an important contribution. For Teresina 2005, TRIPLE N_2O (courtesy of A. Engel) measurements from a balloon flight at Teresina on June 25 (one week after LPMA / DOAS) are available and used for this preliminary analysis. Kiruna 2001 LPMA / DOAS observations were used to derive an updated correlation, as compared to *Wamsley et al.* [1998], for high latitudes. Equations 9.4 and 9.5 give the $Br_Y - N_2O$ and $Br_Y - CH_4$ cor-

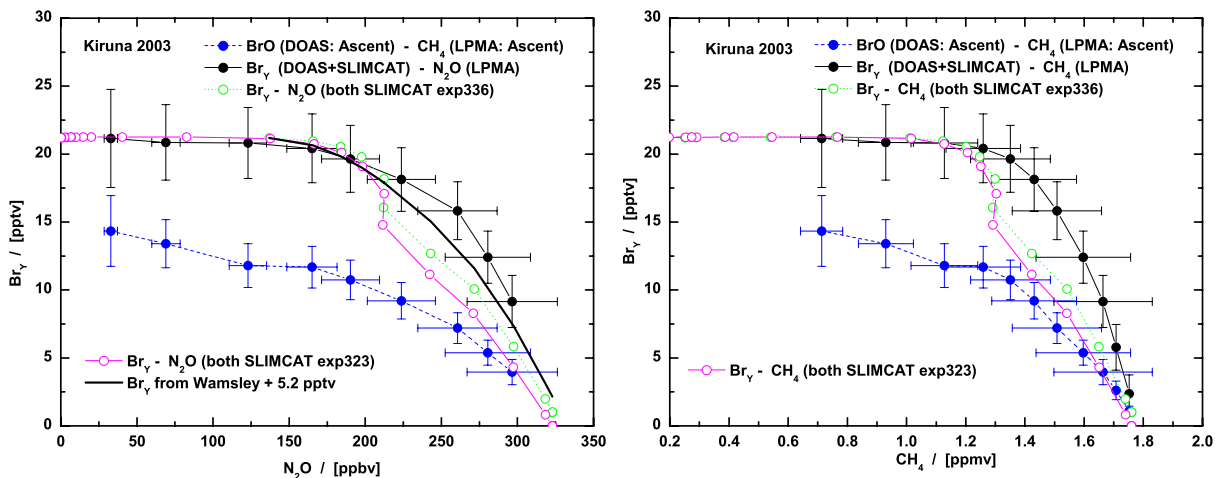


Figure 9.21: Same as Figure 9.16 but for the balloon flight at Kiruna in March 2003.

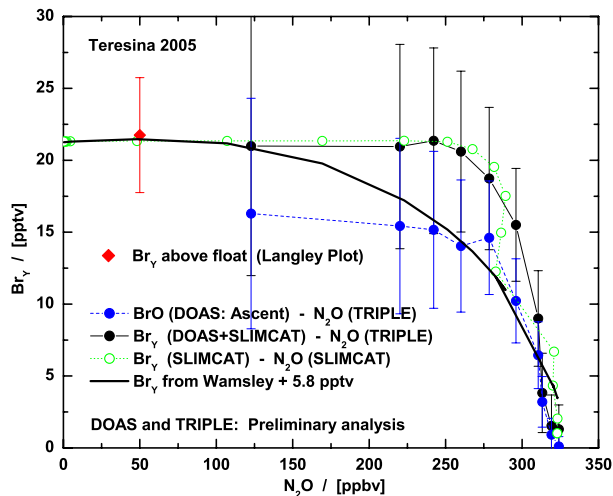


Figure 9.22: Same as Figure 9.16 but for the balloon flight at Teresina on June 17, 2005 and for N_2O only. N_2O measurements (courtesy of A. Engel) were taken during a TRIPLE balloon flight on June 25.

relations ($[Br_Y]$ in pptv, $[N_2O]$ in ppbv and $[CH_4]$ in ppmv) for this time (August 21, 2001) for observed air masses at float altitude as old as 6 years (see also section 9.1).

$$[Br_Y] = 18.376 + 0.1212 \cdot [N_2O] - 0.0018 \cdot [N_2O]^2 + 9.664 \cdot 10^{-6} \cdot [N_2O]^3 - 1.892 \cdot 10^{-8} \cdot [N_2O]^4 \quad (9.3)$$

$$[Br_Y] = 11.6403 + 54.0874 \cdot [CH_4] - 118.8673 \cdot [CH_4]^2 + 111.3144 \cdot [CH_4]^3 - 37.5787 \cdot [CH_4]^4 \quad (9.4)$$

The $Br_Y - N_2O$ correlation is valid from 25 to 310 ppbv and the $Br_Y - CH_4$ correlation from 0.4 to 1.7 ppmv.

Once LPMA data from Kiruna 2004 and Teresina 2005 is available, when additional LPMA data has been reanalysed (Kiruna 1998, Leon 1998) and new model simulations (e.g. for Leon 1996) are made available, correlations can also be derived for mid latitudes and the tropics, and the correlations presented here can be confirmed.

9.4 Summary

DOAS BrO balloon measurements in combination with model simulations allow to infer total inorganic stratospheric bromine. Combining the information from all 13 DOAS flights a recent history of the total inorganic stratospheric bromine inventory can be constructed. Stratospheric Br_Y peaked around 1998 at 21 ± 3 pptv and since then shows constant levels (see Figure 9.7). Compared to the known trend of organic source gases (halons and CH_3Br), Br_Y inferred from DOAS observations is consistently 3.5 to 5 pptv higher. This discrepancy can be explained by a contribution of short-lived bromine source gases to total Br_Y^{org} as shown by comparisons with different SLIMCAT model runs. DOAS measurements in the tropics, where most of the influx of the source gases is believed to take place, are also in good agreement with model simulations regarding the total Br_Y and its precursors.

Non-zero amounts of Br_Y are observed around the tropopause. Above the tropopause Br_Y increases

rapidly in agreement with recent SLIMCAT model simulations which include contributions of VLSL. BrO measurements in the troposphere, 2 km or further below the tropopause, are compatible with 0 pptv and do not indicate BrO values larger than 0.5 pptv, which is in agreement with findings of *Schofield et al.* [2004].

Similar to the study of *Wamsley et al.* [1998] correlations between tracers (N_2O and CH_4) and Br_γ were derived from LPMA / DOAS measurements and SLIMCAT model output. An updated correlation, as compared to *Wamsley et al.* [1998], is given for high latitude summer. When a detailed analysis of the tropical LPMA / DOAS observations is available similar correlations can also be derived for the tropics.

Chapter 10

Conclusion

Absorption spectra, recorded with the UV DOAS spectrograph during thirteen LPMA / DOAS balloon flights since 1996, were analysed for BrO and OCIO signatures. The last five balloon flights were conducted within the scope of this study at high- and mid latitudes and in the tropics. Previous flights were re-analysed.

- Repairs and minor changes were performed on the DOAS spectrograph to ensure an optimum performance of the instrument - section 4.1.2.
- The accuracy of the DOAS retrieval was improved compared to previous flights by recording a new set of absorption reference spectra in the laboratory - chapter 5. This is essential for the retrieval of small absorbers like BrO and OCIO and also needs to be performed in future, after completing modifications on the optical setup of the spectrograph.
- During initial tests for the absolute calibration (results not presented here but can be found, for example in *Gurlit et al.* [2005]) and a first data evaluation, some instrumental effects were observed - section 4.2. One is the correlation of the imaging in the UV with the pointing of the sun-tracker. This effect is not fully understood yet and needs to be monitored and investigated, and if possible, prevented in future.
- The BrO absorption cross-section and its temperature dependence, which are currently the major sources of error in the DOAS evaluation ($\sim 10\%$), need to be characterised more precisely.
- In order to increase the sensitivity in the UV, especially during occultation measurements, telescopes with larger light entrance should be considered. To avoid saturation of the photodiodes during ascent, a filter wheel could be installed, which would allow the illumination to be modified. Higher sensitivity in the UV would also allow for the possibility of performing nighttime lunar occultation measurements, which would be especially interesting for detecting OCIO inside the polar vortex.

BrO and OCIO observations were interpreted with the help of the SLIMCAT [*Chipperfield and Pyle 1998*] 3-D chemical transport model and 1-D photochemical model simulations, which were further constrained by LPMA / DOAS observations of other species.

- DOAS BrO profiles (and profiles from the TRIPLE and SAOZ balloon instruments) were used to validate BrO limb profiles from the SCIAMACHY instrument on the European Envisat satellite. Photochemical change was calculated along air mass trajectories to match the balloon with the satellite observations. Thus, a set of BrO balloon profiles was produced, which is meant to be representative and, according to the trajectory calculations, the most suitable set of SCIAMACHY BrO validation profiles and is thus recommended for future SCIAMACHY limb BrO retrieval exercises - chapter 7.

- OCIO observations inside and at the edge of the vortex, recorded during 3 winter flights at Kiruna, were re-analysed and existing discrepancies between measurements and model simulations were removed. Model comparisons with the known chemistry are able to reproduce DOAS OCIO twilight measurements generally very well. Recent findings on photochemistry from *Canty et al.* [2005] and *von Hobe et al.* [2005] do not contradict DOAS measurements but further constraints are needed to prove their validity - chapter 8.
- For two of these flights, altitude-dependent ozone loss rates of $\sim (30 - 40)$ ppbv / day for Kiruna 2000 and of $\sim (20)$ ppbv / day for Kiruna 1999 observations at around the 450 K level were inferred by a detailed model study.
- In future more accurate OCIO measurements inside the vortex are required to further investigate the photochemistry - mainly the pathways of the BrO plus ClO reaction [*Canty et al.* 2005].
- Total inorganic stratospheric bromine was inferred for all DOAS flights and a recent history of the total organic and inorganic stratospheric bromine inventory was constructed. Br_Y from DOAS is consistently 3.5 to 5 pptv higher than the known trend in halons and CH₃Br can account for - section 9.1.
- Comparisons of DOAS measurements with different SLIMCAT model runs show that additional short-lived bromine source gases can account for the observed discrepancy in total organic and inorganic bromine - section 9.1.
- Total inorganic bromine in the stratosphere peaked at around 1998 at 21 ± 3 pptv and since then shows constant levels - Figure 9.7.
- In future more BrO DOAS observations are needed to monitor whether reduction in anthropogenic organic bromine precursors (covered by the Montreal protocol and its amendments) reaches the stratosphere and with what time delay. It is also possible that an increase of natural VSL bromine substances (e.g. due to an increase in ocean surface temperature) causes further increase of bromine in the stratosphere.
- DOAS observations indicate non-zero amounts of inorganic bromine around the tropopause, with a rapid increase above, in agreement with recent SLIMCAT model simulations.
- Recent DOAS measurements in the tropics, where most of the influx of the source gases is believed to take place, are in good agreement with model simulations regarding the total Br_Y and its precursors - section 9.2.1. However, more measurements are needed for a detailed understanding of chemical processes in the tropical TTL and LMS.
- A detailed analysis of the tropical LPMA / DOAS observations (including tracers such as N₂O and CH₄) in combination with whole air sample measurements performed at the same time by TRIPLE, will give more insight into the rather unexplored conditions of the photochemistry in the tropics. Of special interest are the UTLS and the amount of short-lived precursors observed there.
- Measurements of BrONO₂ (and other inorganic bromine species besides BrO) in the stratosphere are needed to rule out uncertainties in the understanding of bromine photochemistry, especially for the reaction of BrO with NO₂.
- Although tremendous progress has been made during the last 20 years in the understanding of ozone chemistry, there are still discrepancies and uncertainties that prevent to model past ozone losses correctly or to predict the future of stratospheric ozone [*WMO* 2003]. This is especially important since ozone is also a greenhouse gas and relevant to the climate.

Publications

Parts of this work have been published in:

- Dorf, M., H. Bösch, A. Butz, C. Camy-Peyret, M. Chipperfield, A. Engel, F. Goutail, K. Grunow, F. Hendrick, S. Hrechanyy, B. Naujokat, J.-P. Pommereau, M. van Roozendael, C. Sioris and F. Stroh and F. Weidner and K. Pfeilsticker, Balloon-borne stratospheric BrO measurements: Intercomparison with ENVISAT/SCIAMACHY BrO limb profiles, *submitted to Atmos. Chem. Phys. Discuss.*, 2005

Contributions have been made to the following articles:

- Canty, T., E.D. Rivière, R.J. Salawitch, G. Berthet, J.-B. Renard, K. Pfeilsticker, M. Dorf, A. Butz, H. Bösch, R.M. Stimpfle, D.M. Wilmouth, E.C. Richard, D.W. Fahey, P.J. Popp, M.R. Schoeberl, L.R. Lait and T.P. Bui, Nighttime OClO in the winter Arctic vortex, *J. Geophys. Res.*, **110**, D01301, 2005.
- Weidner, F., H. Bösch, H. Bovensmann, J.P. Burrows, A. Butz, C. Camy-Peyret, M. Dorf, K. Gerilowski, W. Gurlit, U. Platt, C. von Friedeburg, T. Wagner, and K. Pfeilsticker, Balloon-borne Limb profiling of UV/vis skylight radiances, O₃, NO₂ and BrO: technical set-up and validation of the method, *Atmos. Chem. Phys.*, **5**, 1409-1422, 2005.
- Gurlit, W., H. Bösch, H. Bovensmann, J.P. Burrows, A. Butz, C. Camy-Peyret, M. Dorf, K. Gerilowski, A. Lindner, S. Noel, U. Platt, F. Weidner, and K. Pfeilsticker, The UV-A and visible solar irradiance spectrum: Inter-comparison of absolutely calibrated, spectrally medium resolved solar irradiance spectra and from balloon- and satellite-borne measurements, *Atmos. Chem. Phys.*, **5**, 1879-1890, 2005.
- Butz, A., H. Bösch, C. Camy-Peyret, M. Chipperfield, M. Dorf, G. Dufour, K. Grunow, P. Jeseck, S. Kühl, S. Payan, I. Pepin, J. Pukite, A. Rozanov, C. von Savigny, C. Sioris, T. Wagner, F. Weidner and K. Pfeilsticker, Inter-comparison of Stratospheric O₃ and NO₂ abundances retrieved from balloon borne direct sun observations and Envisat/SCIAMACHY limb measurements, *Atmos. Chem. Phys. Discuss.*, 2005
- Sioris, C.E., L.J. Kovalenko, C.A. McLinden, R.J. Salawitch, M. Van Roozendael, F. Goutail, M. Dorf, K. Pfeilsticker, K. Chance, C. von Savigny, X. Liu, T.P. Kurosu, J.-P. Pommereau, H. Bösch and J. Frerick, Latitudinal and vertical distribution of bromine monoxide and inorganic bromine in the lower stratosphere from SCIAMACHY limb scatter measurements, *in preparation*, 2005
- Frieler, K., M. Rex, R.J. Salawitch, T. Canty, M. Streibel, R.M. Stimpfle, K. Pfeilsticker, M. Dorf, D.K. Weisenstein, S. Godin-Beekmann and P. von der Gathen, Towards a better quantitative understanding of polar stratospheric ozone loss, *submitted to Geophys. Res. Lett.*, 2005

List of Figures

2.1	Vertical structure of the Earth's atmosphere	5
2.2	Schematic diagram showing the structure of, and transport within, the stratosphere.	7
2.3	Formation of the geostrophic wind	9
2.4	Example of the northern hemnspheric polar vortex.	11
2.5	The O ₃ loss rates due to catalytic cycles	15
2.6	The NO _Y family	16
2.7	Chemical and dynamical processes affecting VSL substances	18
2.8	Primary source gases of chlorine and bromine for the stratosphere	20
2.9	Reactive chlorine gas observations from space	21
2.10	Mean tropospheric organic Br from flask measurements	21
2.11	Effect of the Montreal Protocol	22
2.12	Stratospheric bromine chemistry	23
2.13	BrCl yield according to Canty et al.	24
2.14	Simplified scheme of the NAT formation	26
2.15	Ozone loss rates at 475 K	28
2.16	Reactive uptake coefficients of the key stratospheric heterogeneous processes	29
3.1	Extraterrestrial and sea level solar spectrum	34
3.2	Illustration of the DOAS principle	36
3.3	Temperature dependence of the differential BrO cross section	41
4.1	LPMA/DOAS balloon gondola	46
4.2	Absorption cross sections in the UV wavelength range	47
4.3	Absorption cross sections in the visible wavelength range	48
4.4	Schematic drawing of the DOAS instrument	49
4.5	Spectral shift depending on the temperature of the spectrograph	50
4.6	Nonlinearity of the dark current for the UV spectrograph	51
4.7	Test of the detector's linearity response	52
4.8	Illustration of the single-board computer MC68332 timing problem	53
4.9	Dependence of the average intensity on the sun-tracker position	54
4.10	BrO retrieval for different positions of the sun-tracker acquisition mirror	55
4.11	Field of view of the UV telescope	55
4.12	Residual structures for different elevation offset positions of the sun-tracker	56
5.1	High resolution O ₃ cross section convolved with different instrument slit functions	58
5.2	Sketch of the flow tube	59
5.3	Sketch of the measurement setup for taking reference spectra	60
5.4	O ₃ laboratory absorption cross section	61
5.5	Br ₂ absorption cross section	61
5.6	BrO laboratory absorption cross section	62

5.7	HONO laboratory absorption cross section	63
5.8	N ₂ O ₄ absorption cross section	64
5.9	NO ₂ laboratory absorption cross section	64
5.10	OClo laboratory absorption cross section	65
5.11	BrO-retrieval with convolved and laboratory cross sections	66
6.1	Correlation coefficients for the BrO evaluation	70
6.2	BrO DOAS evaluation for a spectrum recorded during ascent at Kiruna, 2004	71
6.3	Development of the slant column densities for the 2004 Kiruna balloon flight	72
6.4	BrO SCD retrieval for different BrO cross-sections	73
6.5	Langley plot	74
6.6	Colour-coded model concentration field of BrO at Kiruna (67°N, 22°E) on March 24, 2004	75
6.7	BrO SCD development for the 2000 Kiruna balloon flight	75
6.8	Observation geometry	77
6.9	Example of a BrO profile inversion for Kiruna 2003 ascent measurements	80
6.10	BrO and NO ₂ photochemical evening evolution	81
6.11	Example of a BrO profile inversion for Kiruna 2003 occultation measurements	82
6.12	Balloon trajectory, temperature and the SZA for Kiruna 2001	85
6.13	Balloon trajectory and observation geometry of the flight at Kiruna in August, 2001	85
6.14	Development of the SCDs and important fit parameters for August 21, Kiruna 2001	86
6.15	Development of the SCDs and important fit parameters for August 22, Kiruna 2001	87
6.16	BrO DOAS evaluation for a spectrum recorded during ascent in Kiruna on August 21, 2001	88
6.17	Important parameters and position of the sun-tracker acquisition mirror for Kiruna 2001	89
6.18	Balloon trajectory, temperature and the SZA for Kiruna 2003.	90
6.19	Example of the northern hemnspheric polar vortex.	90
6.20	Balloon trajectory, observation geometry and potential vorticity for Kiruna 2003	91
6.21	Development of the SCDs and important fit parameters for Kiruna 2003	92
6.22	BrO DOAS evaluation for a spectrum recorded during ascent at Kiruna, 2003	93
6.23	Important parameters and position of the sun-tracker acquisition mirror for Kiruna 2003	94
6.24	Balloon trajectory, temperature and the SZA for Aire 2003	95
6.25	Balloon trajectory of the flight on October 09, 2003 at Aire sur l'Adour	95
6.26	Development of the SCDs and important fit parameters for Aire 2003	96
6.27	BrO DOAS evaluation for a spectrum recorded during ascent at Aire sur L'Adour, 2003	97
6.28	Important parameters and position of the sun-tracker acquisition mirror for Aire 2003	98
6.29	Balloon trajectory, temperature and the SZA for Kiruna 2004	99
6.30	Example of the northern hemnspheric polar vortex.	101
6.31	Balloon trajectory, observation geometry and potential vorticity for Kiruna 2004	101
6.32	Important parameters and position of the sun-tracker acquisition mirror for Kiruna 2004	102
6.33	Effect of elevation and azimuth offsets of acquisition mirror on the BrO-SCD retrieval	102
6.34	Balloon trajectory, temperature and the SZA for Teresina 2005	103
6.35	Balloon trajectory and observation geometry for Teresina 2005	103
6.36	Development of the SCDs and important fit parameters for Teresina 2005	104
6.37	BrO DOAS evaluation for a spectrum recorded during occultation at Teresina, 2005	105
6.38	Important parameters and position of the sun-tracker acquisition mirror for Teresina 2005	106
7.1	Backward and forward air mass trajectories for TRIPLE ascent observations at Aire	111
7.2	Colour-coded model concentration field of BrO as a function of height and SZA	112
7.3	Schematic overview of the photochemical model	113
7.4	Comparison of a BrO profile measured by TRIPLE on September 24, 2002 with model.	116
7.5	Comparison of a BrO profile measured by DOAS on March 23, 2003 with model.	117
7.6	Comparison of a BrO profile measured by DOAS on October 9, 2003 with model.	118
7.7	Comparison of a BrO profile measured by SAOZ on January 31, 2004 with model.	119

7.8	Comparison of a BrO profile measured by DOAS on March 24, 2004 with model.	120
7.9	NO ₂ and N ₂ O profiles measured at Kiruna on March 23, 2003	121
7.10	O ₃ profile and N ₂ O - SCD values measured at Aire sur l'Adour on October 09, 2003 . . .	121
7.11	O ₃ and NO ₂ profiles measured at Kiruna on March 24, 2004	122
7.12	Air mass trajectories for the LPMA/DOAS flight on March 23, 2003 at Kiruna	125
7.13	Air mass trajectories for the LPMA/DOAS flight on October 09, 2003 at Aire sur l'Adour	126
7.14	Air mass trajectories for the LPMA/DOAS flight on March 24, 2004 at Kiruna	127
7.15	Air mass trajectories for the LPMA/DOAS flight on June 17, 2005 at Teresina	128
8.1	Absorption cross-sections in the UV OCIO retrieval range (346 – 390 nm)	130
8.2	Development of the SCDs and important fit parameters for Leon 1996	131
8.3	Development of the OCIO SCD values for the balloon flight at Leon, 1996	132
8.4	OCIO DOAS evaluation for a spectrum recorded during occultation at Leon, 1996	133
8.5	OCIO DOAS evaluation for a spectrum recorded during occultation at Kiruna, 1997 . . .	135
8.6	Development of the SCDs and important fit parameters for Kiruna, 1997	136
8.7	Development of OCIO and BrO SCD values for Kiruna, 1997	137
8.8	N ₂ O and HCl volume mixing ratio profiles for Kiruna 1997	137
8.9	O ₃ and NO ₂ concentrations for Kiruna 1997	138
8.10	Colour-coded model concentration fields of BrO and OCIO at Kiruna on February 14, 1997	138
8.11	OCIO DOAS evaluation for a spectrum recorded during occultation at Kiruna, 1999 . . .	139
8.12	Development of the SCDs and important fit parameters for Kiruna, 1999	140
8.13	Development of OCIO and BrO SCD values for Kiruna, 1999	141
8.14	Model concentration fields of BrO, NO ₂ , ClO and OCIO at Kiruna on February 10, 1999 .	142
8.15	N ₂ O, HCl, HNO ₃ and ClONO ₂ volume mixing ratio profiles for Kiruna, 1999	143
8.16	Comparison of ClO _x for Kiruna 1999	144
8.17	Development of OCIO SCD values compared to different model studies for Kiruna 1999 .	144
8.18	Comparison of measured and modelled OCIO SCDs for Kiruna 1999.	145
8.19	Evolution of bromine and chlorine species for Kiruna 1999	146
8.20	Evolution of nitrogen and oxygen species for Kiruna 1999	147
8.21	Ozone depletion rate as a function of altitude at Kiruna on February 10, 1999.	147
8.22	OCIO DOAS evaluation for a spectrum recorded during occultation at Kiruna, 2000 . . .	148
8.23	Development of the SCDs and important fit parameters for Kiruna 2000	149
8.24	Development of OCIO and BrO SCD values for Kiruna 2000	150
8.25	Model concentration fields of BrO, NO ₂ , ClO and OCIO at Kiruna on February 18, 2000 .	151
8.26	N ₂ O, and HCl volume mixing ratio profiles for Kiruna 2000	152
8.27	Development of OCIO SCD values for Kiruna 2000	152
8.28	Comparison of measured and modelled OCIO SCDs for Kiruna 2000	153
8.29	Comparison of OCIO profiles for Kiruna 2000	153
8.30	Ozone depletion rate as a function of altitude at Kiruna on February 18, 2000	154
9.1	Historical trends assigned to the strengths of individual sources of CH ₃ Br	156
9.2	Measured hemispheric mixing ratios of methyl bromide and the most abundant halons . .	156
9.3	Measured BrO absorption as a function of the calculated total air mass	158
9.4	Comparison of measured and modelled BrO SCD values for Kiruna, 2004	160
9.5	Modelled concentration and VMR profiles for bromine species at Kiruna, 2004	161
9.6	Correlation between N ₂ O and mean age	162
9.7	Measured trends for bromine in the troposphere and stratosphere	163
9.8	Modelled concentration and volume mixing ratio profiles for SLIMCAT exp336 and exp323	166
9.9	Modelled concentration and volume mixing ratio profiles for SLIMCAT exp336 and exp325	167
9.10	Development of modelled and measured BrO SCDs for 3 different model runs	168
9.11	Correlation plots for measured versus modelled BrO SCDs for Kiruna 2004	168
9.12	Development and correlation plots for measured and modelled BrO SCDs for Kiruna 2003	169

9.13	Development and correlation plots for measured and modelled BrO SCDs for Leon 1998	169
9.14	Fraction of odd oxygen loss by various catalytic cycles within the AER model	170
9.15	Modelled concentration and VMR profiles for bromine species at Teresina, 2005	172
9.16	Correlation of Br _Y with N ₂ O and CH ₄ for the Leon 1996 balloon flight	173
9.17	Correlation of Br _Y with N ₂ O and CH ₄ for the Kiruna 1997 balloon flight	173
9.18	Correlation of Br _Y with N ₂ O and CH ₄ for the Kiruna 1999 balloon flight	174
9.19	Correlation of Br _Y with N ₂ O and CH ₄ for the Gap 1999 balloon flight	174
9.20	Correlation of Br _Y with N ₂ O and CH ₄ for the Kiruna 2001 balloon flight	175
9.21	Correlation of Br _Y with N ₂ O and CH ₄ for the Kiruna 2003 balloon flight	175
9.22	Correlation of Br _Y with N ₂ O for the Teresina 2005 balloon flight	176

List of Tables

2.1	Atmospheric lifetimes, emissions and ODP of halogen source gases	20
2.2	PSC classification with respect to their optical properties	26
5.1	Overview of laboratory reference spectra: Vis-Channel	58
5.2	Overview of laboratory reference spectra: UV-Channel	59
6.1	Summary of all 13 successful flights performed to the end of 2005	83
6.2	Summary of important parameters used for the evaluation of the 13 DOAS flights	84
7.1	Compendium of balloon-borne BrO measurements and Envisat / SCIAMACHY overpasses	115
9.1	Inferred BrO volume mixing ratio above float altitude for all 13 DOAS flights	159
9.2	BrO / Br _Y ratio for the balloon flights shown in Figure 9.3	160
9.3	Lifetime and VMR of the most important organic bromine species in the tropical UT	165

References

- Albritton, D. L., A. L. Schmeltekopf, and R. Zare (1976). An introduction to the least-square fitting of spectroscopic data. In R. Narahari and M. W. Weldon (Eds.), *Molecular Spectroscopy: Modern Research*. Academic, Orlando, Florida.
- Aliwell, S., M. Van Roozendaal, P. Johnston, A. Richter, T. Wagner, D. Arlander, J. Burrows, D. Fish, R. Jones, K. Tornkvist, J.-C. Lambert, K. Pfeilsticker, and I. Pundt (2002, January). Analysis for BrO in zenith-sky spectra: An intercomparison exercise for analysis improvement. *J. Geophys. Res.*, Vol. 107, No. D14.
- Andrews, D. G., J. R. Holton, and C. B. Leovy (1987). Middle atmosphere dynamics. *Academic Press, Orlando*.
- Avallone, L. M., D. W. Toohey, S. M. Schauffler, L. E. H. W. H. Pollock, and E. L. Atlas (1993). In-situ measurements of ClO at mid-latitudes: Is there an effect from Mt. Pinatubo. *Geophys. Res. Lett.*, Vol. 20, 2519–2522.
- Bates, D. R. and M. Nicolet (1950). Atmospheric hydrogen. *Pap. Astron. Soc. Pacific*, Vol. 62.
- Bauer, N. (1997). Charakterisierung des DOAS-Ballon-Spektrographen zur Bestimmung stratosphaerischer Spurenstoffe. *Master thesis, Institut für Umweltphysik, Universität Heidelberg*.
- Blake, N. J., D. R. Blake, I. J. Simpson, J. P. Lopez, N. A. C. Johnston, A. L. Swanson, A. S. Katzenstein, S. Meinardi, B. C. Sive, J. J. Colman, E. Atlas, F. Flocke, S. A. Vay, M. A. Avery, and F. S. Rowland (2001). Large-scale latitudinal and vertical distributions of NMHCs and selected halocarbons in the troposphere over the Pacific Ocean during the March-April 1999 Pacific Exploratory Mission (PEM-Tropics B). *J. Geophys. Res.*, Vol. 106, 32627–32644.
- Bobrowski, N., G. Hönninger, B. Galle, and U. Platt (2003). Detection of bromine monoxide in a volcanic plume. *Nature*, Vol. 423, 273–276.
- Bösch, H. (2002). *Studies of Stratospheric Nitrogen and Iodine Chemistry with Balloon Borne DOAS Measurements*. Dissertation, Institut für Umweltphysik, Universität Heidelberg.
- Bösch, H., C. Camy-Peyret, M. P. Chipperfield, R. Fitzenberger, H. Harder, U. Platt, and K. Pfeilsticker (2003). Upper limits of stratospheric IO and OIO inferred from center-to-limb-darkening-corrected balloon-borne solar occultation visible spectra: Implications for total gaseous iodine and stratospheric ozone. *J. Geophys. Res.*, Vol. 108, No. D15, 4455.
- Bösch, H., C. Camy-Peyret, M. P. Chipperfield, R. Fitzenberger, H. Harder, C. Schiller, M. Schneider, T. Trautmann, and K. Pfeilsticker (2001). Comparison of measured and modeled stratospheric UV/visible actinic fluxes at large solar zenith angles. *Geophys. Res. Lett.*, Vol. 28, No. 7, 1179–1182.
- Bovensmann, H. (1999). SCIAMACHY: Mission Objectives and Measurement Modes. *J. Atmos. Sci.*, Vol. 56, 127–150.
- Bracher, A., B.-M. Sinnhuber, A. Rozanov, and J. P. Burrows (2005). Using a photochemical model for the validation of NO₂ satellite measurements at different solar zenith angles. *Atmos. Chem. Phys.*, Vol. 5, No. SRef-ID: 1680-7324/acp/2005-5-393, 393–408.
- Bransden, B. and C. Joachain (1983). *Physics of atoms and molecules*. Essex CM20 2 JE, England: Longman Group Limited.

- Brasseur, G. and C. Granier (1992). Mount Pinatubo aerosols, chlorofluorocarbons, and ozone depletion. *Science*, No. 257, 1239–1242.
- Brasseur, G. and S. Solomon (1986). *Aeronomy of the middle atmosphere*. Dordrecht, Boston, Lancaster, Tokyo: D. Reidel Publ.
- Brewer, A. W. (1949). Evidence for a world circulation provided by the measurement of helium and water vapor distribution in the stratosphere. *Q. J. R. Meteorol. Soc.*, Vol. 75, 351–363.
- Browell, E. V., C. F. Butler, S. Ismail, P. A. Robinette, A. F. Carter, N. S. Higdson, O. B. Toon, M. R. Schoeberl, and A. F. Tuck (1990). Airborne lidar observations in the wintertime arctic stratosphere: Polar stratospheric clouds. *Geophys. Res. Lett.*, Vol. 17, 385–388.
- Brune, W. H., J. G. Anderson, and K. R. Chan (1989). In situ observations of BrO over Antarctica: ER-2 aircraft results from 54°S to 72°S latitude. *J. Geophys. Res.*, Vol. 94, 16,649 – 16,663.
- Burkholder, J. B. and R. K. Talukdar (1994). Temperature dependence of the ozone absorption spectrum over the wavelength range 410 to 760 nm. *Geophys. Res. Lett.*, Vol. 21, No. 7, 581–584.
- Burrows, J. P., A. Dehn, B. Deters, S. Himmelmann, A. Richter, S. Voigt, and J. Orphal (1999). Atmospheric remote-sensing reference data from GOME: temperature-dependent absorption cross section of ozone in the 231 - 794 nm range. *J. Quant. Spectroscopy and Rad. Transfer*, Vol. 61, 509–517.
- Bussemer, M. (1993). Der Ring-Effekt: Ursachen und Einfluß auf die spektroskopische Messung stratosphärischer Spurenstoffe. *Master thesis, Institut für Umweltphysik, Universität Heidelberg.*
- Butler, J. H., M. Battle, M. Bender, S. A. Montzka, A. D. Clarke, E. Saltzman, C. Sucher, J. Severinghaus, and J. W. Elkins (1999). A twentieth century record of atmospheric halocarbons in polar firn air. *Nature*, Vol. 399, 749–755.
- Butz, A., H. Bösch, C. Camy-Peyret, M. P. Chipperfield, M. Dorf, G. Dufour, K. Grunow, P. Jeseck, S. Köhl, S. Payan, I. Pepin, J. Pukite, A. Rozanov, C. von Savigny, C. Sioris, T. Wagner, F. Weidner, and K. Pfeilsticker (2005). Inter-comparison of Stratospheric O₃ and NO₂ abundances retrieved from balloon-borne direct sun observations and Envisat/SCIAMACHY limb measurements. *Atmos. Chem. Phys. Discuss.*,
- Camy-Peyret, C., P. Jeseck, T. Hawat, G. Durr, G. Berubeé, L. Rochette, and D. Huguenin (1995). The LPMA balloon borne FTIR spectrometer for remote sensing of the atmospheric constituents. In *12th ESA Symposium on Rocket and Balloon Programmes and Related Research*.
- Camy-Peyret, C., P. Jeseck, S. Payan, T. Hawat, G. Durr, and J.-M. Flaud (1995). Comparison of CH₄ and N₂O profiles at high and mid-latitudes using the LPMA balloon borne Fourier Transform instrument. In *Air Pollution Research Report, Polar Stratospheric Ozone Symposium, Schliersee*.
- Camy-Peyret, C. Payan, S., P. Jeseck, Y. Té, T. Hawat, K. Pfeilsticker, H. Harder, R. Fitzenberger, and H. Bösch (1999). Recent results obtained with the LPMA and DOAS balloon-borne instruments during the ILAS, SABINE and THESEO campaigns. In *14th ESA Symposium on Rocket and Balloon Programmes and Related Research*.
- Cantrell, C., J. Davidson, M. A.H., S. R.E., and J. Calvert (1990). Temperature-dependent formaldehyde cross sections in the near-ultraviolet spectral region. *J. Phys. Chem.*, Vol. 94, 3902–3908.
- Canty, T., E. D. Rivière, R. J. Salawitch, G. Berthet, J.-B. Renard, K. Pfeilsticker, M. Dorf, A. Butz, H. Bösch, R. M. Stimpfle, D. M. Wilmouth, E. C. Richard, D. W. Fahey, P. J. Popp, M. R. Schoeberl, L. R. Lait, and T. P. Bui (2005). Nighttime OClO in the winter Arctic vortex. *J. Geophys. Res.*, Vol. 110, No. D01301.
- Carlotti, M. (1988). Global fit approach to the analysis of limb-scanning atmospheric measurements. *Appl. Opt.*, Vol. 27, 3250–3254.
- Carpenter, L. J., D. Wevill, S. O’Doherty, G. Spain, and P. Simmonds (2005). Atmospheric bromoform at Mace Head, Ireland: Evidence for a peatland source. *Atmos. Chem. Phys. Discuss.*, Vol. 5, 5935–5955.
- Carslaw, K. S., J. T. Peter, T. Bacmeister, and S. D. Eckermann (1999). Widespread solid particle formation by mountain waves in the Arctic stratosphere. *J. Geophys. Res.*, Vol. 104, 1827–1836.

- Carslaw, K. S., M. Wirth, A. Tsias, B. P. Luo, A. Dörnbrack, M. Leutbecher, H. Volkert, W. Renger, J. T. Bacmeister, E. Reimer, and T. Peter (1998). Increased stratospheric ozone depletion due to mountain-induced atmospheric waves. *Nature*, Vol. 391, 675–678.
- Chapman, S. (1930). On ozone and atomic oxygen in the upper atmosphere. *Phil. Mag.*, Vol. 10.
- Chipperfield, M. P. (1999). Multiannual simulations with a three-dimensional chemical transport model. *J. Geophys. Res.*, Vol. 104, No. D1, 1781–1805.
- Chipperfield, M. P. (2005). New Version of the TOMCAT/SLIMCAT Off-Line Chemical Transport Model: Intercomparison of Stratospheric Tracer Experiments. *Q. J. Roy. Meteorol. Soc.*, (submitted).
- Chipperfield, M. P., W. Feng, M. Dorf, and K. Pfeilsticker (2005). Mid-latitude Ozone Changes: Studies with a 3-D CTM Forced by ERA-40 Analyses. pp. (in preparation for ACP).
- Chipperfield, M. P., W. Feng, and M. Rex (2005). Arctic ozone loss and climate sensitivity: Updated three-dimensional model study. *Geophys. Res. Lett.*, Vol. 32, No. doi:10.1029/2005GL022674, L11813.
- Chipperfield, M. P. and J. A. Pyle (1998). Model sensitivity studies of arctic ozone depletion. *J. Geophys. Res.*, Vol. 103, No. D21, 28389–28403.
- Coffey, M. T., W. G. Mankin, and A. Goldman (1981). Simultaneous spectroscopic determination of the latitudinal, seasonal and diurnal variability of stratospheric N_2O , NO , NO_2 and HNO_3 . *J. Geophys. Res.*, Vol. 86, 7331–7341.
- Cordero, E. C. and S. R. Kawa (2001). Ozone and tracer transport variations in the summer northern hemisphere stratosphere. *J. Geophys. Res.*, Vol. 106, No. D11, 12227–12239.
- Corti, T., B. P. Luo, T. Peter, H. Vömel, and Q. Fu (2005). Mean radiative energy balance and vertical mass fluxes in the equatorial upper troposphere and lower stratosphere. *Geophys. Res. Lett.*, Vol. 32, 6802–+.
- Cox, R., D. Sheppard, and M. Stevens (1982). Absorption coefficients and kinetics of the BrO radical using molecular modulation. *J. Photochem.*, Vol. 19, 189–207.
- Cox, R. A., W. J. Bloss, and R. L. Jones (1999). OIO and the atmospheric cycle of iodine. *Geophys. Res. Lett.*, Vol. 26, No. 13, 1857–1860.
- Crutzen, P. J. (1970). The influence of nitrogen oxides on the atmospheric ozone content. *Quart. J. Met. Soc.*, Vol. 96.
- Crutzen, P. J. and F. Arnold (1986). Nitric acid cloud formation in the cold Antarctic stratosphere: a major cause for the springtime ozone hole. *Nature*, Vol. 324, 651–655.
- Danilin, M. Y., M. K. W. Ko, L. Froidevaux, M. L. Santee, L. V. Lyjak, R. M. Bevilacqua, J. M. Zawodny, Y. Sasano, H. Irie, Y. Kondo, J. M. Russell, C. J. Scott, and W. G. Read (2002). Trajectory hunting as an effective technique to validate multiplatform measurements: Analysis of the MLS, HALOE, SAGE-II, ILAS, and POAM-II data in October–November 1996. *J. Geophys. Res.*, Vol. 107 (D20), No. 4420, doi:10.1029/2001JD002012.
- David, C., S. Bekki, S. Godin, G. Mégie, and M. P. Chipperfield (1998). Polar stratospheric clouds climatology over Dumont d’Urville between 1989 and 1993 and the influence of volcanic aerosols on their formation. *J. Geophys. Res.*, Vol. 103, 22163–22180.
- DeMore, W. B., S. P. Sander, D. M. Golden, R. F. Hampson, M. J. Kurylo, C. J. Howard, A. R. Ravishankara, C. E. Kolb, and M. J. Molina (1997). Chemical kinetics and photochemical data for use in stratospheric modeling. *Technical Report, NASA/JPL Publication*, , No. 97-4.
- Deshler, T., M. Hervig, D. Hofmann, J. Rosen, and J. Liley (2003). Thirty years of in situ stratospheric aerosol size distribution measurements from Laramie, Wyoming (41°N), using balloon-borne instruments. *J. Geophys. Res.*, Vol. 108, No. D5.
- Dobson, G. M. B. (1956). Origin and distribution of the polyatomic molecules in the atmosphere. *Proc. R. Soc. London A*, Vol. 236, 187–193.

- Dufour, G., S. Payan, F. Lefèvre, G. Berthet, M. Eremenko, A. Butz, P. Jeseck, Y. Te, K. Pfeilsticker, and C. Camy-Peyret (2005). 4D comparison method to study NO_y partitioning in summer polar stratosphere. Influence of aerosol burden. *Atmos. Chem. Phys.*, Vol. 5, 919–926.
- Dvortsov, V., M. A. Geller, S. Solomon, S. M. Schauffler, E. L. Atlas, and D. R. Blake (1999). Rethinking reactive halogen budget in the midlatitude stratosphere. *Geophys. Res. Lett.*, Vol. 26, No. 12, 1699–1702.
- EC-Report (2001a). European Research in the stratosphere 1996-2000. Scientific Assessment of the European Commission.
- EC-Report (2001b). European Research in the stratosphere 1996-2000, Advances in our understanding of the ozone layer during THESEO. Scientific Assessment of the European Commission Community Research, ISBN 92-894-1398-0.
- Engel, A., U. Schmitt, W. B. Sturges, S. Penkett, K. Pfeilsticker, U. Platt, F. Stroh, C. Schiller, R. Müller, D. McKenna, J. Ovarlez, C. Camy-Peyret, M. Pirre, and J. B. Renard (1999). Final Report: HALOMAX-Mid and high latitude stratospheric distribution of long and short lived halogen species during the maximum of the chlorine loading. *CEC-Contract*, Vol. ENV4-CT97-0524.
- Engel, A., M. Strunk, M. Müller, H.-P. Haase, C. Poss, I. Levin, and U. Schmidt (2002, June). Temporal development of total chlorine in the high-latitude stratosphere based on reference distributions of mean age derived from CO_2 and SF_6 . *J. Geophys. Res.*, Vol. 107.
- EORCU (2000). The northern hemisphere stratosphere in the winter and spring of 1999/2000. *Preliminary report*.
- Erle, F. (1999). Untersuchungen zur Halogenaktivierung der winterlichen Stratosphäre anhand flugzeuggestützter spektroskopischer Messungen. *Ph. D. thesis, Institut für Umweltphysik, Universität Heidelberg*.
- Fahey, D. W., R. S. Gao, K. S. Carslaw, J. Kettleborough, P. J. Popp, M. J. Northway, J. C. Holece, S. C. Ciciora, R. J. McLaughlin, T. L. Thompson, R. H. Winkler, D. G. Baumgardner, B. Gandrun, P. O. Wennberg, S. Dhaniyala, K. McKinney, T. Peter, R. J. Salawitch, T. P. Bui, J. W. Elkins, C. R. Webster, E. L. Atlas, H. Jost, J. C. Wilson, R. L. Herman, A. Kleinböhl, and M. von König (2000). The detection of large HNO_3 - containing particles in the winter Arctic stratosphere. *Science*, Vol. 291.
- Fahey, D. W., S. R. Kawa, E. L. Woodbridge, P. Tin, J. C. Wilson, H. H. Jonasson, J. E. Dye, D. Baumgardner, S. Borrmann, D. W. Toohey, L. M. Avalone, M. H. Proffitt, J. Margitan, M. Loewenstein, J. R. Podolske, R. J. Salawitch, S. C. Wofsy, M. K. W. Ko, D. E. Anderson, M. R. Schoeberl, and K. R. Chan (1993). In situ measurements constraining the role of sulphate aerosols in midlatitude ozone depletion. *Nature*, , No. 363, 509–514.
- Farman, J. C., B. G. Gardiner, and J. D. Shanklin (1985). Large losses of total ozone in Antarctica reveal seasonal ClO_x/NO_x interaction. *Nature*, Vol. 315, 207–210.
- Feng, W., M. Chipperfield, S. Davies, B. Sen, G. Toon, J. Blavier, C. Webster, C. Volk, A. Ulanovsky, F. Ravagnani, P. von der Gathen, H. Jost, E. Richard, and H. Claude (2005). Three-dimensional model study of the Arctic ozone loss in 2002/03 and comparison with 1999/2000 and 2003/04. *Atmos. Chem. Phys.*, Vol. 5, 139–152.
- Ferlemann, F. (1998). Ballongestützte Messung stratosphärischer Spurenstoffe mit differentieller optischer Absorptionsspektroskopie. *Ph. D. thesis, Institut für Umweltphysik, Universität Heidelberg*.
- Ferlemann, F., N. Bauer, R. Fitzenberger, H. Harder, H. Osterkamp, D. Perner, U. Platt, M. Scheider, P. Vradelis, and K. Pfeilsticker (2000). Differential optical absorption spectroscopy instrument for stratospheric balloon-borne trace gas studies. *Appl. Opt.*, Vol. 39, 2377–2386.
- Ferlemann, F., C. Camy-Peyret, R. Fitzenberger, H. Harder, T. Hawat, H. Osterkamp, M. Schneider, D. Perner, U. Platt, P. Vradelis, and K. Pfeilsticker (1998). Stratospheric BrO profiles measured at different latitudes

- and seasons: Instrument description, spectral analysis and profile retrieval. *Geophys. Res. Lett.*, Vol. 25, No. 20, 3847–3850.
- Feynman, R. B., R. B. Leighton, and M. Sand (1965). *The Feynman lectures on physics*. Reading, Palo Alto, London: Addison-Wesley Publishing Company Inc.
- Finlayson-Pitts, B. J. and J. J. N. Pitts (1986). *Atmospheric chemistry : fundamentals and experimental techniques*. New York: Wiley and Sons.
- Fish, D., R. Jones, and K. Strong (1995). Mid-latitude observations of the diurnal variation of stratospheric BrO. *J. Geophys. Res.*, Vol. 100, 18,863–18,871.
- Fish, D. J. and R. L. Jones (1995). Rotational Raman scattering and the Ring effect in zenith-sky spectra. *Geophys. Res. Lett.*, Vol. 22, No. 7, 811–814.
- Fitzenberger, R. (2000). Investigation of the stratospheric inorganic bromine budget for 1996-2000: Balloon-borne measurements and model comparison. *Ph. D. thesis, Institut für Umweltphysik, Universität Heidelberg.*
- Fitzenberger, R., H. Bösch, C. Camy-Peyret, M. Chpperfield, H. Harder, U. Platt, J. Pyle, T. Wagner, and K. Pfeilsticker (2000). First profile measurement of tropospheric BrO. *Geophys. Res. Lett.*, Vol. 27, 2921–2924.
- Fleischmann, O. C., M. Hartmann, J. Orphal, and J. P. Burrows (2001). FT measurements of the BrO absorption cross section. *University of Bremen, Institute of remote sensing.*, in preparation.
- Fraser, P. J., D. E. Oram, C. E. Reeves, and S. A. Penkett (1999). Southern hemisphere halon trends (1987-1998) and global halon emissions. *J. Geophys. Res.*,
- Frieler, K., M. Rex, R. Salawitch, T. Canty, M. Streibel, R. Stimpfle, K. Pfeilsticker, M. Dorf, D. Weisenstein, S. Godin-Beekmann, and P. von der Gathen (2005). Towards a better quantitative understanding of polar stratospheric ozone loss. *Geophys. Res. Lett.*, (submitted).
- Funk, O. (2000). Photon pathlengths distributions for cloudy skies - Oxygen A-band measurements and radiative transfer model calculations. *Ph. D. thesis, Institut für Umweltphysik, Universität Heidelberg.*
- Gottelman, A., P. M. D. F. Forster, M. Fujiwara, Q. Fu, H. Vömel, L. K. Gohar, C. Johanson, and M. Ammerman (2004). Radiation balance of the tropical tropopause layer. *J. Geophys. Res. (Atmosphere)*, Vol. 109, 7103–+.
- Gilles, M. K., A. A. Turnipseed, J. B. Burkholder, A. R. Ravishankara, and S. Solomon (1997). Kinetics of the IO radical. 2. reaction of IO with BrO. *J. Phys. Chem. A*, Vol. 101, 5526–5534.
- Gomer, T., F. Brauers, F. Heintz, J. Stutz, and U. Platt (1995). MFC, User Manual, Version 1.98. *Institut für Umweltphysik, Universität Heidelberg.*
- Goody, R. M. and Y. L. Yung (1989). Atmospheric radiation. *Oxford University Press, New York, Oxford.*
- Grainger, J. F. and J. Ring (1962). Anomalous Fraunhofer line profiles. *Nature*, Vol. 193, No. 762.
- Greenblatt, G. D., J. J. Orlando, J. B. Burkholder, and A. R. Ravishankara (1990). Absorption measurements of oxygen between 330 and 1140 nm. *J. Geophys. Res.*, Vol. 95, No. D11, 18577–18582.
- Gurlit, W., H. Bösch, H. Bovensmann, J. Burrows, A. Butz, C. Camy-Peyret, M. Dorf, K. Gerilowski, A. Lindner, S. Noel, U. Platt, F. Weidner, and K. Pfeilsticker (2005). The UV-A and visible solar irradiance spectrum: Inter-comparison of absolutely calibrated, spectrally medium resolved solar irradiance spectra from balloon- and satellite-borne measurements. *Atmos. Chem. Phys.*, Vol. 5, 1879–1890.
- Hall, B., J. H. Butler, A. D. Clarke, G. S. Dutton, J. W. Elkins, D. F. Hurst, D. B. King, E. S. Kline, J. Lind, L. Lock, D. Mondeel, F. L. Moore, S. A. Montzka, J. D. Nance, E. A. Ray, P. A. Romashkin, and T. M. Thompson (2002). Halocarbons and other atmospheric trace species, in *Climate Monitoring and Diagnostics Laboratory: Summary Report No. 26, 2000-2001*. Boulder, Colorado, pp. 106–135. NOAA/Climate Monitoring and Diagnostics Laboratory. edited by D.B. King and R.C. Schnell.

- Hall, T. M. and R. A. Plumb (1994, January). Age as a diagnostic of stratospheric transport. *J. Geophys. Res.*, Vol. 99, 1059–1070.
- Hansen, D. R. and K. Mauersberger (1988). The vapour pressure of HNO₃-H₂O solutions. *J. Phys. Chem.*, Vol. 92, 6167–6170.
- Hanson, D. R., A. R. Ravishankara, and S. Solomon (1994). Heterogeneous reactions in sulfuric acid aerosols: A framework for model calculations. *J. Geophys. Res.*, , No. 99, 3615–3629.
- Harder, H. (1999). Messung und Modellierung stratosphärischer Spurenstoffprofile zur Abschätzung des anorganischen Gesamt-Brom-Budgets. *Ph. D. thesis, Institut für Umweltphysik, Universität Heidelberg.*
- Harder, H., H. Bösch, C. Camy-Peyret, M. Chpperfield, R. Fitzenberger, S. Payan, D. Perner, U. Platt, B.-M. Sinnhuber, and K. Pfeilsticker (2000). Comparison of measured and modeled Stratospheric BrO: implications for the total amount of stratospheric bromine. *Geophys. Res. Lett.*, Vol. 27, No. 22, 3695–3698.
- Harder, H., C. Camy-Peyret, F. Ferlemann, R. Fitzenberger, T. Hawat, H. Osterkamp, M. Schneider, D. Perner, U. Platt, P. Vradelis, and K. Pfeilsticker (1998). Stratospheric BrO profiles measured at different latitudes and seasons: atmospheric observations. *Geophys. Res. Lett.*, Vol. 25, No. 20, 3843–3846.
- Harder, J. W., J. W. Brault, P. V. Johnston, and G. H. Mount (1997). Temperature dependent NO₂ cross sections at high spectral resolution. *J. Geophys. Res.*, Vol. 102, No. D3, 3861–3879.
- Harwood, M. H., J. B. Burkholder, M. Hunter, R. W. Fox, and A. R. Ravishankara (1997). Absorption cross sections and self-reaction kinetics of the IO radical. *J. Phys. Chem. A*, Vol. 101, 853–863.
- Harwood, M. H. and R. Jones (1994). Temperature dependent ultraviolet-visible absorption cross sections of NO₂ and N₂O₄: low temperature measurements of the equilibrium constant for 2 NO₂ \longleftrightarrow N₂O₄. *J. Geophys. Res.*, Vol. 99, No. D11, 22955–22964.
- Hausmann, M., U. Brandenburger, T. Brauers, and H. P. Dorn (1999). Simple Monte Carlo methods to estimate the spectral evaluation error in differential-optical-absorption-spectroscopy. *Appl. Opt.*, Vol. 38, No. 3, 462–475.
- Hawat, T., C. Camy-Peyret, P. Jeseck, and R. Torguet (1995). Description and performance of a balloon-borne heliostat for solar absorption measurements. In *12th ESA Symposium on Rocket and Balloon Programmes and Related Research*.
- Helmling, M. (1994). *Modellierungen von photochemischen Prozessen entlang von Luftmassentrajektorien im arktischen Frühjahr*. Master's thesis, Institut für Umweltphysik, Universität Heidelberg.
- Hermans (2002). priv. com. for details see: <http://www.oma.be/BIRA-IASB/Scientific/Topics/lower/LaboBase/acvd/O4Info.html>.
- Hoffmann, D. J., S. J. Oltmans, J. M. Harris, B. J. Johnson, and J. A. Lathrop (1997). Ten years of ozonesonde measurements at the south pole: implications for recovery of springtime Antarctic ozone. *J. Geophys. Res.*, Vol. 102, 8931–8943.
- Holton, J. R., P. H. Haynes, M. E. McIntyre, A. R. Douglass, R. B. Rood, and L. Pfister (1995). Stratosphere-troposphere exchange. *Reviews of Geophysics*, Vol. 33, 403–439.
- Hönninger, G. (1999). Referenzspektren reaktiver Halogenverbindungen für DOAS Messungen. *Master thesis, Institut für Umweltphysik, Universität Heidelberg.*
- Huppert, R. (2000). Theoretische und experimentelle Untersuchungen zum solaren I₀-Effekt. *Master thesis, Institut für Umweltphysik, Universität Heidelberg.*
- Johnston, H. S. (1971). Reduction of stratospheric ozone by nitrogen oxide catalysts from supersonic transport exhaust. *Science*, Vol. 173.
- Johnston, P. V. (1997). Making UV/vis cross sections, reference Fraunhofer and synthetic spectra. unpublished.
- Junge, C. E. (1961). Vertical profiles of condensation nuclei in the stratosphere. *J. Meteorol*, Vol. 18, 501–509.

- Keim, E. R., M. Loewenstein, J. R. Podolske, D. W. Fahey, R. S. Gao, E. L. Woodbridge, R. C. Wamsley, S. G. Donnelly, L. A. DelNegro, C. D. Nevison, S. Solomon, K. H. Rosenlof, C. J. Scott, M. K. W. Ko, D. Weisenstein, and K. R. Chan (1997). Measurements of the NO_y - N_2O correlation in the lower stratosphere: latitudinal and seasonal changes and model comparison. *J. Geophys. Res.*, Vol. 102, No. D11, 13193–13212.
- Kirmse, B., A. Delon, and R. Jost (1997). NO_2 absorption cross section and its temperature dependence. *J. Geophys. Res.*, Vol. 102, No. D13, 16089–16098.
- Ko, M., N. Sze, C. Scott, and D. Weissenstein (1997). On the relation between chlorine/bromine loading and short-lived tropospheric source gases. *J. Geophys. Res.*,.
- Kondo, Y., U. Schmidt, T. Sugita, P. Amedieu, M. Koike, H. Ziereis, and Y. Iwasaka (1994). Total reactive nitrogen, N_2O , and ozone in the winter Arctic stratosphere. *Geophys. Res. Lett.*, Vol. 21, No. 13, 1247–1250.
- Kondo, Y., U. Schmidt, T. Sugita, A. Engel, M. Koike, P. Amedieu, M. R. Gunson, and J. Rodriguez (1996). NO_y correlation with N_2O and CH_4 in the midlatitude stratosphere. *Geophys. Res. Lett.*, Vol. 23, No. 17, 2369–2372.
- Kromminga, H. S., J. Orphal, P. Spietz, S. Voigt, and J. P. Burrows (2003). New measurements of OCIO absorption cross sections in the 325 - 435 nm and their temperature dependence between 213 - 293 K. *J. Photochem. Photobiol. A*, Vol. 157, 149–160.
- Kurucz, R. L., I. Furenlid, J. Brault, and L. Testerman (1984). Solar flux atlas from 296 to 1300 nm. National Solar Observatory, Sunspot, New Mexico, U.S.A.
- Labitzke, K. (1999). Die Stratosphäre. Phänomene, Geschichte, Relevanz. *Springer-Verlag, Berlin, Heidelberg, New York*, , No. ISBN 3-540-65000-8.
- Labitzke, K. and H. van Loon (1988). Associations between the 11-year solar cycle, the QBO and the atmosphere. I - The troposphere and stratosphere in the Northern Hemisphere in winter. *J. of Atmosph. and Terr. Phys.*, Vol. 50, 197–206.
- Lary, D. J. (1996). Gas phase atmospheric bromine chemistry. *J. Geophys. Res.*, Vol. 101, 1505–1516.
- Lary, D. J., M. P. Chipperfield, R. Toumi, and T. Lenton (1996). Heterogeneous atmospheric bromine chemistry. *J. Geophys. Res.*, Vol. 101, 1489–1504.
- Lary, D. J. and J. A. Pyle (1991). Diffuse radiation, twilight and photochemistry. *J. Atmos. Chem.*, 373–392.
- Lindner, A. (2005). Ballongestützte Messungen der extraterrestrischen spektralen solaren Irradianz. *Master thesis, Institut für Umweltphysik, Universität Heidelberg*.
- Loewenstein, M., J. R. Podolske, D. W. Fahey, E. L. Woodbridge, P. Tin, A. Weaver, P. A. Newman, S. E. Strahan, S. R. Kawa, M. R. Schoeberl, and L. R. Lait (1993). New observations of the $\text{NO}_y/\text{N}_2\text{O}$ correlation in the lower stratosphere. *Science*, Vol. 283.
- Lübken, F.-J., K.-H. Fricke, and M. Langer (1996). Noctilucent clouds and the thermal structure near the Arctic mesopause in summer. *J. Geophys. Res.*, Vol. 101, 9489–9508.
- Lumpe, J. D., M. Fromm, K. Hopperl, R. M. Bevilacqua, C. E. Randall, E. V. Browell, W. B. Grant, T. McGee, J. Burris, L. Twigg, E. C. Richard, G. C. Toon, J. J. Margitan, B. Sen, H. Boesch, R. Fitzenberger, K. Pfeilsticker, F. Goutail, and J.-P. Pommereau (2003). Comparison of POAM III ozone measurements with correlative aircraft and balloon data during SOLVE. *J. Geophys. Res.*, Vol. 108, No. D5.
- McCormick, M. P., H. M. Steele, P. Hamill, W. P. Chu, and T. J. Swisler (1982). Polar stratospheric cloud sightings by SAM II. *J. Atmos. Sci.*, Vol. 39, 1387–1397.
- McElroy, M. B., R. J. Salawitch, S. C. Wofsy, and J. A. Logan (1986). Reductions of Antarctic ozone due to synergetic interactions of chlorine and bromine. *Nature*, Vol. 321, 759–762.
- McLinden, C. A., J. C. McConnell, E. Griffioen, and C. T. McElroy (2002). A vector radiative transfer model for the Odin/OSIRIS project. *Can. J. Phys.*, Vol. 80, 375–393.

- Michelson, H. A., G. L. Manney, M. R. Gunson, and R. Zander (1998). Correlations of stratospheric abundances of NO_y , O_3 , N_2O and CH_4 derived from ATMOS measurements. *J. Geophys. Res.*, Vol. 103, No. D21, 28347–28359.
- Milankovitch, M. (1920). Théorie mathématique des phénomènes thermique produit par la radiation solaire. *Gauthier-Villars, Paris*.
- Mohamed-Tahrin, N., A. South, D. Newnham, and R. Jones (2001, May). A new accurate wavelength calibration for the ozone absorption cross section in the near-UV spectral region, and its effect on the retrieval of BrO from measurements of zenith-scattered sunlight. *J. Geophys. Res.*, Vol. 106, No. D9, 9897–9907.
- Molina, L. T. and M. J. Molina (1987). Production of Cl_2O_2 from the self-reaction of the ClO radical. *J. Phys. Chem.*, Vol. 91, 433–436.
- Molina, M. J. and F. S. Rowland (1974). Stratospheric sink for chlororflourmethanes: chlorine atom-catalysed destruction of ozone. *Nature*, Vol. 249, 810–812.
- Montzka, S., J. Butler, B. Hall, D. Mondell, and J. Elkins (2003). A decline in tropospheric organic bromine. *Geophys. Res. Lett.*, Vol. 30, No. 15, 1826–1829.
- Montzka, S. A., J. H. Butler, R. C. Myers, T. M. Thompson, T. H. Swanson, A. D. Clarke, L. T. Lock, and J. W. Elkins (1996). Decline in the tropospheric abundance of halogen from halocarbons: Implications for stratospheric ozone depletion. *Science*, Vol. 272, 1318–1322.
- Mozurkewich, M. and J. Calvert (1988). Reaction probability of N_2O_5 on aqueous aerosols. *J. Geophys. Res.*, , No. 93, 15,889–15,896.
- Murphy, D. M. and D. S. Thompson (2000). Halogen ions and NO^+ in the mass spectra of aerosols in the upper troposphere and lower stratosphere. *Geophys. Res. Lett.*, Vol. 27, 3217–3220.
- MyIntyre, M. and T. Palmer (1983). Breaking planetary waves in the stratosphere. *Nature*, Vol. 305, 593–600.
- Nash, E. R., P. A. Newman, J. E. Rosenfield, and M. R. Schoeberl (1996). An objective determination of the polar vortex using Ertel’s potential vorticity. *J. Geophys. Res.*, Vol. 101, No. D5, 9471–9478.
- Nash, T. (1976). Nitrous acid in the atmosphere and laboratory experiments on its photolysis. *Tellus XXVI*, Vol. 1-2.
- Naujokat, B., K. Labitzke, R. Lenschow, and R.-C. Wohlfart (2000). The stratospheric winter 1999/2000. *Beilage zur Berliner Wetterkarte*.
- Nicolet, M. (1984). On the molecular scattering in the terrestrial atmosphere: An empirical formula for its calculation in the homosphere. *Planet. Space Sci.*, Vol. 32, 1467–1486.
- NOAA-S/T76-1562 (1976). *US Standard Atmosphere*. NOAA-S/T76-1562. Supplement Document, US Printing Documents, Washington DC.
- Noxon, J. F. (1979). Stratospheric NO_2 : global behaviour. *J. Geophys. Res.*, Vol. 84.
- Orlando, J., J. Burkholder, A. Bopegedera, and C. Howard (1982). Absorption coefficients and kinetics of the BrO radical using molecular modulation. *J. Photochem.*, Vol. 19, 189–207.
- Orphal, J. (2003). A critical review of the absorption cross-sections of O_3 and NO_2 in the ultraviolet and visible. *J. Photochem. Photobiol. A*, Vol. 157, 185–209.
- Osterkamp, H. (1997). Messung von atmosphärischen O_4 -Profilen. *Master thesis, Institut für Umweltphysik, Universität Heidelberg*.
- Pawson, S., B. Naujokat, and K. Labitzke (1995). On the polar stratospheric cloud formation potential of the northern hemisphere. *J. Geophys. Res.*, Vol. 100, 23215–23225.
- Payan, S., C. Camy-Peyret, P. Jeseck, T. Hawat, G. Durry, and F. Lefèvre (1998). First direct simultaneous HCl and ClONO_2 profile measurements in the arctic vortex. *Geophys. Res. Lett.*, Vol. 25, No. 14, 2663–2666.
- Payan, S., C. Camy-Peyret, P. Jeseck, T. Hawat, M. Pirre, J.-B. Renard, C. Robert, F. Lefèvre, H. Kanzawa, and Y. Sasano (1999). Diurnal and nocturnal distribution of stratospheric NO_2 from solar and stellar

- occultation measurements in the arctic vortex: comparison with models and ILAS satellite measurements. *J. Geophys. Res.*, Vol. 104, No. D17, 21585–21593.
- Penndorf, R. (1957). Tables of the refractive index for standard air and the Rayleigh scattering coefficient for the spectral region between 0.2 and 200 μ and their application to atmospheric optics. *J. Opt. Soc. Am.*, Vol. 47, No. 2, 176–182.
- Pfeilsticker, K., H. Bösch, C. Camy-Peyret, R. Fitzenberger, H. Harder, and H. Osterkamp (2000). First atmospheric profile measurements of the atmospheric UV/vis O₄ absorption bands strength: Implications for the spectroscopy and the formation enthalpy of the O₂–O₂ dimer. *Geophys. Res. Lett.*,
- Pfeilsticker, K., F. Erle, and U. Platt (1999). Observation of the stratospheric NO₂ latitudinal distribution in the northern winter hemisphere. *J. Atmos. Chem.*, Vol. 32, 101–120.
- Pfeilsticker, K., W. T. Sturges, H. Bösch, C. Camy-Peyret, M. P. Chipperfield, A. Engel, R. Fitzenberger, M. Müller, S. Payan, and B.-M. Sinnhuber (2000). Lower stratospheric organic and inorganic bromine budget for the Arctic winter 1998/99. *Geophys. Res. Lett.*, Vol. 27, No. 20, 3305–3308.
- Platt, U. (1994). Differential optical absorption spectroscopy (DOAS). In M. Sigrist, W. (Ed.), *Air Monitoring by Spectroscopic Techniques*, Volume 127, pp. 27–84. John Wiley & Sons, Inc.
- Platt, U., D. Perner, and H. Pätz (1979). Simultaneous measurement of atmospheric CH₂O, O₃ and NO₂ by differential optical absorption. *J. Geophys. Res.*, Vol. 84, 6329–6335.
- Portmann, R. W., S. S. Brown, T. Gierczak, R. K. Talukdar, J. B. Burkholder, and A. R. Ravishankara (1999). Role of nitrogen oxides in the stratosphere: a reevaluation based on laboratory studies. *Geophys. Res. Lett.*, Vol. 26, No. 15, 2387–2390.
- Press, W. H., B. P. Flannery, S. A. Teukolsky, and W. T. Vetterling (1986). Numerical recipes: the art of scientific computing. *Cambridge, University Press*,
- Prinn, R., R. Weiss, P. Fraser, P. Simmonds, D. Cunnold, F. Alyea, S. O’Doherty, P. Salameh, B. Miller, J. Huang, R. Wang, D. Hartley, C. Harth, L. Steele, G. Sturrock, P. Midgley, and A. McCulloch (2000). A history of chemically and radiatively important gases in air deduced from ALE/GAGE/AGAGE. *J. Geophys. Res.*, Vol. 105, No. D14, 17751–17792.
- Pundt, I., J.-P. Pommereau, M. Chipperfield, M. V. Roozendael, and F. Goutail (2002). Climatology of the stratospheric BrO vertical distribution by balloon-borne UV-visible spectrometry. *J. Geophys. Res.*, Vol. 107, No. D24, doi: 10.1029/2002JD002230.
- Pundt, I., J.-P. Pommereau, C. Phillips, and E. Latelin (1998). Upper limit of iodine oxide in the stratosphere. *J. Atmos. Chem.*, Vol. 30, 173–185.
- Quack, B., E. Atlas, G. Petrick, V. Stroud, S. Schauffler, and D. Wallace (2004). Oceanic bromoform sources for the tropical atmosphere. *Geophys. Res. Lett.*, Vol. 32, L23S05.
- Reeves, C. (2003). Atmospheric budget implications of the temporal and spatial trends in methyl bromide concentration. *J. Geophys. Res.*, Vol. 108.
- Reimer, E. and H. Kaupp (1997). Source identification of odour compounds using trajectories. *Proc. ECO-INFORMA 97*, Vol. Eco-Infoma Press, Bayreuth, 572577.
- Rivière, E., M. Pirre, G. Berthet, J.-B. Renard, and F. Lefèvre (2004). Investigating the Halogen Chemistry From High-Latitude Nighttime Stratospheric Measurements of OCIO and NO₂. *J. Atmosph. Chem.*, Vol. 48, 261–282.
- Rivière, E., M. Pirre, G. Berthet, J.-B. Renard, F. Taupin, N. Huret, M. Chartier, B. Knudsen, and F. Lefèvre (2003). On the interaction between nitrogen and halogen species in the Arctic polar vortex during THESEO and THESEO 2000. *J. Geophys. Res.*, Vol. 108, No. D5.
- Rivière, E. D., N. Huret, F. G. Taupin, J.-B. Renard, M. Pirre, S. D. Eckermann, N. Larsen, T. Deshler, F. Lefèvre, S. Payan, and C. Camy-Peyret (2000). Role of lee waves in the formation of solid polar stratospheric clouds: case studies from February 1997. *J. Geophys. Res.*, Vol. 105, No. D5, 6845–6853.

- Rodgers, C. (2000). *Inverse methods for atmospheric sounding*. Singapore, New Jersey, London, Hongkong: World Scientific.
- Roedel, W. (1992). Physik unserer Umwelt : Die Atmosphäre. *Springer-Verlag, Berlin, Heidelberg, New York*.
- Roscoe, H. K., D. J. Fish, and R. L. Jones (1996). Interpolation errors in the UV-visible spectroscopy for stratospheric sensing: implications for sensitivity, spectral resolution, and spectral range. *Appl. Opt.*, Vol. 35, 427–432.
- Rosenlof, K. H. (1999). Estimates of the seasonal cycle of mass transport and ozone transport at high northern latitudes. *J. Geophys. Res.*, Vol. 104, No. D21, 26511–26523.
- Rothman, L., A. Barbe, D. Benner, L. Brown, C. Camy-Peyret, M. Carleer, K. Chance, C. Clerbaux, V. Dana, V. Devi, A. Fayt, J.-M. Flaud, R. Gamache, A. Goldman, D. Jacquemart, K. Jucks, W. Lafferty, J.-Y. Mandin, S. Massie, V. Nemtchinov, D. Newnham, A. Perrin, C. Rinsland, J. Schroeder, K. Smith, M. Smith, K. Tang, R. Toth, J. Vander Auwera, P. Varanasi, and K. Yoshino (2003). The HITRAN Molecular Spectroscopic Database: Edition of 2000 Including Updates through. *J. Quant. Spec. and Rad. Transf.*, Vol. 82, 1–4.
- Rothman, L. S., C. P. Rinsland, A. Goldman, S. T. Massie, D. P. Edwards, J.-M. Flaud, A. Perrin, C. Camy-Peyret, V. Dana, J.-Y. Mandin, J. Schroeder, A. McCann, R. R. Gamache, R. B. Wattson, K. Yoshino, K. V. Chance, K. W. Jucks, L. R. Brown, V. Nemtchinov, and P. Varanasi (1996). The HITRAN molecular spectroscopic data database and HAWKS (HITRAN atmospheric workstation): 1996 edition. *J. Quant. Spectroscopy and Rad. Transfer*, Vol. 60, 665–710.
- Salawitch, R. J., D. K. Weisenstein, L. J. Kovalenko, C. E. Sioris, P. O. Wennberg, K. Chance, M. K. W. Ko, and C. A. McLinden (2005). Sensitivity of ozone to bromine in the lower stratosphere. *Geophys. Res. Lett.*, Vol. 32, No. L05811.
- Saltzman, E., M. Aydin, W. J. D. Bruyn, D. B. King, and S. Yvon-Lewis (2004). Methyl bromide in preindustrial air: Measurements from an Antarctic ice core. *J. Geophys. Res.*, Vol. 109, No. D05301, doi:10.1029.
- Sander, S., R. R. Friedl, D. M. Golden, M. J. Kurylo, R. E. Huie, V. L. Orkin, A. R. Ravishankara, C. E. Kolb, M. J. Molina, G. K. Moortgart, and B. J. Finlayson-Pitts (2003). Chemical kinetics and photochemical data for use in atmospheric studies. *Technical Report, NASA/JPL Publication*, , No. 02-25.
- Sander, S. P. (1986). Temperature dependence of the NO₃ absorption spectrum. *J. Phys. Chem.*, Vol. 90, 4135–4142.
- Sanders, R. (1996). Improved analysis of atmospheric spectra by including the temperature dependence of NO₂. *J. Geophys. Res.*, Vol. 101, No. D15, 20945–20952.
- Santee, M. L., G. L. Manney, N. J. Livesey, and J. W. Waters (2000). UARS microwave limb sounder observations of denitrification and ozone loss in the 2000 Arctic late winter. *Geophys. Res. Lett.*, Vol. 27, No. 19, 3213–3216.
- Schauffler, S. M., E. L. Atlas, F. Flocke, R. A. Lueb, V. Stroud, and W. Travnicek (1998). Measurement of bromine-containing organic compounds at the tropical tropopause. *Geophys. Res. Lett.*, Vol. 25, No. 3, 317–320.
- Schlager, H. and F. Arnold (1990). Measurements of stratospheric gaseous nitric acid in the winter Arctic vortex using a novel rocket-borne mass spectrometric method. *Geophys. Res. Lett.*, Vol. 17, 433–436.
- Schoeberl, M., L. Lait, P. Newman, and J. Rosenfield (1992). The structure of the polar vortex. *J. Geophys. Res.*, Vol. 97, 7859–7882.
- Schofield, R., K. Kreher, B. J. Connor, P. V. Johnston, A. Thomas, D. Shooter, M. P. Chipperfield, C. D. Rodgers, and G. H. Mount (2004). Retrieved tropospheric and stratospheric BrO columns over Lauder, New Zealand. *J. Geophys. Res. (Atmosphere)*, Vol. 109, D14304.
- Schulte, M. (1996). DAMF V1.22 direct light airmass factors. *Internal paper, Institut für Umweltp Physik, Universität Heidelberg*.

- Schwab, J. J. and J. G. Anderson (1987). Oscillator Strengths of Cl(I) in the Vacuum Ultraviolet: The 2D - 2P Transitions. *J. Quant. Spectrosc. Radiat. Transfer*, Vol. 27, 445 – 457.
- Schwärzle, J. (2005). *Spektroskopische Messungen von Halogenoxiden in der marinen atmosphärischen Grenzschicht in Alcantara / Brasilien*. Staatsexamensarbeit, Institut für Umweltphysik, Universität Heidelberg.
- Seery, D. and D. Britton (1964). The continuous absorption spectra of chlorine, bromine, bromine chloride, iodine chloride, and iodine bromide. *J. Phys. Chem.*, Vol. 68, 2264–2266.
- Sessler, J., M. Chipperfield, J.Pyle, and R. Toumi (1995). Stratospheric OClO measurements as a poor quantitative indicator of chlorine activation. *Geophys.Res.Lett.*, Vol. 22, 687–690.
- Shindell, D. T., S. Wong, and D. Rind (1997). Interannual Variability of the Antarctic Ozone Hole in a GCM. Part I: The Influence of Tropospheric Wave Variability. *J. Atmos. Sci.*, Vol. 54, 2308–2319.
- Sioris, C., C. Haley, C. McLinden, C. von Savigny, I. McDade, J. McConnell, W. Evans, N. Lloyd, E. L. K. Chance, T. Kurosu, D. Murtagh, U. Frisk, K. Pfeilsticker, H. Bösch, F. Weidner, K. Strong, J. Stegman, and G. Megie (2003). Stratospheric profiles of nitrogen dioxide observed by OSIRIS on the Odin satellite. *J. Geophys. Res.*, Vol. 108, 4215.
- Sioris, C., L. Kovalenko, C. McLinden, R. Salawitch, M. V. Roozendael, F. Goutail, M. Dorf, K. Pfeilsticker, K. Chance, C. von Savigny, X. Liu, T. Kurosu, J.-P. Pommereau, H. Bösch, and J. Frerick (2005). Latitudinal and vertical distribution of bromine monoxide and inorganic bromine in the lower stratosphere from SCIAMACHY limb scatter measurements. *submitted to J. Geophys. Res.*.
- Sioris, C. E., T. Kurosu, R. Martin, and K. Chance (2004). Stratospheric and tropospheric NO₂ observed by SCIAMACHY: first results. *Adv. Space Res.*, Vol. 34, 780–785.
- Slusser, J. R., D. J. Fish, E. K. Strong, R. L. Jones, H. K. Roscoe, and A. Sarkissian (1997). Five years of NO₂ vertical column measurements at Faraday(65°S): Evidence for the hydrolysis of BrONO₂ on Pinatubo aerosols. *J.Geophys.Res.*, , No. 102, 12,987–12,993.
- Solomon, S. (1999). Stratospheric ozone depletion: a review of concepts and history. *Rev. Geophys.*, Vol. 37, 275–316.
- Solomon, S., R. R. Garcia, and A. R. Ravishankara (1994). On the role of iodine in ozone depletion. *J. Geophys. Res.*, Vol. 99, No. D10, 20491–20499.
- Solomon, S., R. R. Garcia, F. S. Rowland, and D. J. Wuebbles (1986). On the depletion of Antarctic ozone. *Nature*, Vol. 321, 755–758.
- Solomon, S., G. H. Mount, R. W. Sander, and A. L. Schmeltpopf (1987). Visible spectroscopy at McMurdo station, Antarctica, 2, Observation of OClO. *J. Geophys. Res.*, Vol. 92, 8329–8338.
- Solomon, S., R. W. Portman, R. R. Garcia, W. Randel, F. Wu, R. Nagatani, J. Gleason, L. Thomason, L. R. Poole, and M. P. McCormick (1998). Ozone depletion at midlatitudes: coupling of volcanic aerosols and temperature variability to anthropogenic chlorine. *Geophys. Res. Lett.*, Vol. 25, 1871–1874.
- Solomon, S., R. W. Portmann, R. R. Garcia, L. W. Thomason, L. R. Poole, and M. P. McCormick (1996). The role of aerosol variations in anthropogenic ozone depletion at northern midlatitudes. *J.Geophys.Res.*, , No. 101, 6713–6727.
- Solomon, S., A. L. Schmeltpopf, and R. W. Sanders (1987). On the interpretation of zenith sky absorption measurements. *J. Geophys. Res.*, Vol. 92, No. D7, 8311–8319.
- Steinogger, M. (1999). *Die Sonne als veränderlicher Stern*. Vorlesungsskript 98/99, Institut für Geophysik, Astrophysik und Meteorologie, Universität Graz.
- Sturges, W. T., H. P. McIntire, S. A. Penkett, J. Chappellaz, J.-M. Barnolo, R. Mulvaney, E. Atlas, and V. Stroud (2001). Methyl bromide, other brominated methanes and methyl iodide in polar firn air. *J. Geophys. Res.*, Vol. 106, No. D2, 1595–1606.
- Stutz, J. (1991). *Charakterisierung von Photodiodenzeilen zur Messung stratosphärischer Spurenstoffe*. Diploma thesis, Institut für Umweltphysik, Universität Heidelberg.

- Stutz, J. (1996). Messung der Konzentration troposphärischer Spurenstoffe mittels Differentieller- Optischer-Absorptionsspektroskopie: Eine neue Generation von Geräten und Algorithmen. *Ph. D. thesis, Institut für Umweltphysik, Universität Heidelberg.*
- Stutz, J., E. Kim, U. Platt, P. Bruno, C. Perrino, and A. Febo (2000). UV-visible absorption cross-sections of nitrous acid. *J. Geophys. Res.*, Vol. 105, 14,585–14,592.
- Stutz, J. and U. Platt (1996). Numerical analysis and error estimation of Differential Optical Absorption Spectroscopy measurements with least square fits. *Appl. Opt.*, Vol. 30, No. 30, 6041–6053.
- Sze, N. D., M. K. W. Ko, D. K. Weisenstein, J. M. Rodriguez, R. S. Stolarski, and M. R. Schoeberl (1989). Antarctic ozone hole: Possible implications for ozone trends in the southern hemisphere. *J. Geophys. Res.*, , No. 94, 11,521–11,528.
- Tao, X. and A. Tuck (1994). On the distribution of cold air near the vortex edge in the lower stratosphere. *J. Geophys. Res.*, Vol. 99, 3431–3450.
- Thuillier, G., M. Herse, P. Simon, D. Labs, H. Mandel, and D. Gillotay (1997). Observation of the UV solar irradiance between 200 and 350 nm during the ATLAS-1 mission by the SOLSPEC spectrometer. *Sol. Phys.*, Vol. 171, 283–302.
- Thuillier, G., M. Herse, P. Simon, D. Labs, H. Mandel, D. Gillotay, and T. Foujols (1998). The visible solar spectral irradiance from 350 nm to 850 nm as measured by the SOLSPEC spectrometer during the ATLAS-1 mission. *Sol. Phys.*, Vol. 177, 41–61.
- Tie, X.-X. and G. Brasseur (1996). The importance of heterogeneous bromine chemistry in the lower stratosphere. *Geophys. Res. Lett.*, , No. 23, 2505–2508.
- Tolbert, M. A., M. J. Rossi, and D. M. Golden (1988). Antarctic ozone depletion chemistry: Reactions of N_2O_5 with H_2O and HCl on ice surfaces. *Science*, , No. 240, 1018–1021.
- Toohey, D. W., J. G. Anderson, W. H. Brune, and K. R. Chan (1990). In situ measurements of BrO in the Arctic stratosphere. *Geophys. Res. Lett.*, Vol. 17, No. 513.
- Toon, O. B., P. Hamill, R. P. Turco, and J. Pinto (1986). Condensation of HNO_3 and HCl in the winter polar stratosphere. *Geophys. Res. Lett.*, Vol. 13, 1284–1287.
- Toumi, R., S. Bekki, and R. Cox (1993). A model study of ATMOS observations and the heterogenous loss of N_2O_5 by the sulphate aerosol layer. *J. Atmos. Chem.*, Vol. 16, 135–144.
- Trick, S. (2000). Das Bildungspotential salpetriger Säure(HONO) an städtischen Oberflächen. *Staatsexamensarbeit, Institut für Umweltphysik, Universität Heidelberg.*
- Tsias, A. Wirth, M., K. S. Carslaw, J. Biele, H. Mehrstens, J. Reichelt, C. Wedekind, V. Weiss, W. Renger, R. Neuber, U. von Zahn, B. Stein, and T. Peter (1999). Aircraft lidar observations of enhanced type 1a polar stratospheric clouds during APE-POLECAT. *J. Geophys. Res.*,.
- Van De Hulst, H. C. (1957). Light scattering by small particles. *Dover Publ., New York.*
- Van Roozendael, M. and C. Fayt (2000). WinDOAS 2.1. Software user manual. *Belgium Institute for Space Aeronomie (BIRA/IASB).*
- Van Roozendael, M., T. Wagner, A. Richter, I. Pundt, D. Arlander, J. Burrows, M. P. Chipperfield, C. Fayt, P. Johnston, J. Lambert, K. Kreher, K. Pfeilsticker, U. Platt, J. P. Pommereau, B. Sinnhuber, K. Tornkvist, and F. Wittrock (2002). Intercomparison of BrO Measurements from ERS-2 GOME, Ground-based and balloon platforms. *Adv. Space. Res.*, Vol. 29, No. 22, 1161 – 1666.
- Vogel, B., A. E. R. Müller and, J.-U. Groöf, D. Toohey, T. Woyke, and F. Stroh (2005). Midlatitude ClO during the maximum atmospheric chlorine burden: in situ balloon measurements and model simulations. *Atmos. Chem. Phys.*, Vol. 5, 1623–1638.
- Voigt, C., J. Schreiner, A. Kohlmann, P. Zink, K. Mauersberger, N. Larsen, T. Deshler, C. Kröger, J. Rosen, A. Adriani, F. Ciario, G. Di Donfrancesco, M. Viterbini, J. Ovarlez, H. Ovarlez, D. C., and A. Dörnbrack (2000). Nitric Acid Trihydrate (NAT) in polar stratospheric clouds. *Science*, Vol. 290, 1756–1758.

- Voigt, S., J. Orphal, K. Bogumil, and J. P. Burrows (2001). The temperature dependence (203–293 K) of the absorption cross section of O₃ in the 230–850 nm region measured by Fourier-transform spectroscopy. *J. Photochem. Photobiol. A*, Vol. 143, 1–9.
- Voigt, S., J. Orphal, and J. P. Burrows (2002). The Temperature- and Pressure-Dependence of the Absorption Cross-section of NO₂ in the 250–800 nm Region measured by Fourier-Transform Spectroscopy). *J. Photochem. Photobiol. A*, Vol. 149, 1–7.
- von der Gathen, P., M. Rex, N. Harris, D. Lucic, B. Knudsen, G. Braathen, H. D. Backer, R. Fabian, H. Fast, M. Gil, E. Kyr, I. Mikkelsen, M. Rummukainen, J. Sthelin, and C. Varotsos (1995). Observational evidence for chemical ozone depletion over the Arctic in winter 1991–92. *Nature*, Vol. 375, 131–134.
- von Hobe, M., J.-U. Groöß, R. Müller, S. Hrechanyy, U. Winkler, and F. Stroh (2005). A re-evaluation of the ClO / Cl₂O₂ equilibrium constant based on stratospheric in-situ observations. *Atmos. Chem. Phys.*, Vol. 5, 693–702.
- von König, M. (1996). Aufbau einer bis zu -90° C kühlbaren Meßzelle und Aufnahme von Absorptionsspektren von Halogenoxiden und Ozon. *Master thesis, Institut für Umweltphysik, Universität Heidelberg.*
- Vradelis, P. (1998). Verbesserung der Ballon-DOAS-Messungen durch Streulichtunterdrückung und numerische Untersuchung des Auswerteprozesses. *Master thesis, Institut für Umweltphysik, Universität Heidelberg.*
- Wagner, T., C. Leue, K. Pfeilticker, and U. Platt (2001). Monitoring of the stratospheric chlorine activation by Global Ozone Monitoring Experiment (GOME) OCIO measurements in the austral and boreal winters 1995 through 1999. *J. Geophys. Res.*, Vol. 106, No. D5, 4971–4989.
- Wagner, T. and U. Platt (1998). Satellite mapping of enhanced BrO concentrations in the troposphere. *Nature*, Vol. 395, 486 – 490.
- Wahner, A., A. Ravishankara, S. Sander, and R. Friedl (1988, November). Absorption cross section of BrO between 312 and 385 nm at 298 and 223 K. *Chem. Phys. Lett.*, Vol. 152, No. 6, 507–512.
- Wahner, A., G. S. Tyndall, and A. R. Ravishankara (1987). Absorption cross section for OCIO as a function of temperature in the wavelength range from 240 - 480 nm. *J. Phys. Chem.*, Vol. 91, 2734–3738.
- Wamsley, P. R., J. W. Elkins, D. W. Fahey, G. S. Dutton, R. C. Volk, C. M. Myers, S. A. Montzka, J. H. Butler, A. D. Clarke, P. J. Fraser, L. P. Steele, M. P. Lucarelli, E. L. Atlas, S. M. Schauffler, D. R. Blake, F. S. Rowland, W. T. Sturges, J. M. Lee, S. A. Penkett, A. Engel, R. M. Stimpfle, K. R. Chan, D. K. Weisenstein, M. K. W. Ko, and R. J. Salawitch (1998). Distribution of halon-1211 in the upper troposphere and lower stratosphere and the 1994 total bromine budget. *J. Geophys. Res.*, Vol. 103, No. D1, 1513–1526.
- Webster, C. R., R. D. May, H. A. Michelson, D. C. Scott, J. C. Wilson, H. H. Jonason, C. A. Brock, J. E. Dye, D. Baumgardner, R. M. Stimpfle, J. P. Koplów, J. J. Margitan, M. J. Profitt, L. Jaeglé, R. L. Herman, H. Hu, G. J. Flesch, and M. Loewenstein (1998). Evolution of HCl in the lower stratosphere from 1991 to 1996 following the eruption of Mt. Pinatubo. *Geophys. Res. Lett.*, Vol. 25, 995–998.
- Weidner, F. (2005). *Development and Application of a Versatile Balloon-Borne DOAS Instrument for Skylight Radiance and Atmospheric Trace Gas Profile Measurements*. Dissertation, Institut für Umweltphysik, Universität Heidelberg.
- Weidner, F., H. Bösch, H. Bovensmann, J. Burrows, A. Butz, C. Camy-Peyret, M. Dorf, K. Gerilowski, W. Gurlit, U. Platt, C. von Friedeburg, T. Wagner, and K. Pfeilsticker (2005). Balloon-borne limb profiling of UV/vis skylight radiances, O₃, NO₂, and BrO: technical set-up and validation of the method. *Atmos. Chem. Phys.*, Vol. 5, 1409–1422.
- Wetzel, G., T. von Clarmann, H. Oelhaf, and H. Fischer (1995). Vertical profiles of N₂O₅ along with CH₄, N₂O, and H₂O in the late Arctic winter retrieved from MIPAS-B infrared limb emission measurements. *J. Geophys. Res.*, Vol. 100, No. D11, 23173–23181.
- Wilmouth, D. M., T. F. Janisco, N. M. Donahue, and J. G. Anderson (1999). Fourier Transform Ultraviolet Spectroscopy of the $A^2\Pi_{3/2} \leftarrow X^2\Pi_{3/2}$ Transition of BrO. *J. Phys. Chem., A*, Vol. 103, 8935–8945.

- WMO (2003). Scientific Assessment of Ozone depletion: 2002, *World Meteorological Organization Global Ozone Research and Monitoring Project, Report 47*.
- Wofsy, S. C., M. B. McElroy, and Y. L. Yung (1975). The chemistry of atmospheric bromine. *Geophys. Res. Lett.*, Vol. 2, 215–218.

Acknowledgements

Finally I would like to express my gratitude to the following people for their support and assistance in making this work a success:

- Prof. Dr. Klaus Pfeilsticker, under whose scientific guidance this work was made possible, for his specialist knowledge and willingness to give so freely of his expertise. He also created a unique and enjoyable working environment.
- Prof. Dr. Frank Arnold for agreeing to take part in the assessment of this work.
- Prof. Dr. Ulrich Platt who gave me the opportunity to carry out the necessary research with academic freedom at the Institut für Umweltphysik.
- My colleagues from the DOAS balloon team - Frank Weidner, André Butz and Harmut Bösch for their company and support during the last years and for proof-reading my thesis - my work would not have been possible without their teamwork and willingness to share their experience and knowledge. Special thanks to André for processing the LPMA data.
Thanks also to the other DOAS balloon team members (former and current) - Hartwig Harder, Richard Fitzenberger and Frieder Ferlemann, who are still willing to give support in technical questions after having left the institute - Ulrike Reichl, Benjamin Simmes, Lena Kritten, Aaron Linder and Martin Hirsekorn for their valued support and company during balloon campaigns.
- All colleagues from the atmospheric chemistry group at the Institut für Umweltphysik for frequent Mensa visits at high-noon, coffee breaks, biscuit discussions and the cooperative atmosphere.
- Martyn Chipperfield from the University of Leeds for providing SLIMCAT model data and for the good and successful cooperation. His input was essential to much of my work.
- Katja Grunow for her meteorological support and her company during balloon campaigns and her unfailing readiness to perform trajectory calculations for us.
- The LPMA balloon team - Claude Camy-Peyret, Pascal Jeseck, Isabelle Pepin, Christian Rouillé, Sebastian Payan, Gaelle Dufour and Yao Té - for the successful cooperation, their support in preparing the LPMA / DOAS payload (especially the sun-tracker) and for processing the LPMA spectra.
- Konstantin Gerilowski and Wolfgang Gurlit for the enjoyable, though sometimes tedious and exhausting, nightshifts with their tealight and midday siestas at ‘Apoolien’.
- Jean Evrard and André Laurens from CNES ‘equipe nacelles pointées’ and the balloon team from Aire sur l’Adour / France, without who the balloon flights would not have taken place.
- Our colleagues from the other balloon teams. Especially Fred Stroh, Andreas Engel and Serhiy Hrechanyy (TRIPLE), Hermann Oelhaf and Gerald Wetzel (MIPAS) for their cooperation and for making their measurements and results available to us.
- Ross Salawitch for his comments on our work and for keeping us updated and involved in the latest developments and findings on stratospheric bromine.
- Florence Goutail, Michel Van Roozendaal and Francois Hendrick for their cooperation on the SCIAMACHY BrO validation.
- Chris Sioris for providing SCIAMACHY BrO limb profiles.
- All my friends, acquaintances and family who accompanied me and gave me support during the last years.
- Dominique Le Cocq, who with her love, sweetness and sweets gave me the necessary energy during the last year. Her comments on my English are especially appreciated.

This work was conducted within ESA contracts AO 146 and AO 465. Funding came from the Bundesministerium für Bildung und Forschung (BMBF), contract DLR-50EE0017.